Towards Multidisciplinary Design Optimization Capability of Horizontal Axis Wind Turbines

by

Michael Kenneth McWilliam
B.Sc., University of Waterloo, 2005
M.Sc., University of Waterloo, 2008

A Dissertation Submitted in Partial Fulfillment of the
Requirements for the Degree of

DOCTOR OF PHILOSOPHY

in the Department of Mechanical Engineering

Towards Multidisciplinary Design Optimization Capability
of Horizontal Axis Wind Turbines

by

Michael Kenneth McWilliam
B.Sc., University of Waterloo, 2005
M.Sc., University of Waterloo, 2008

Supervisory Committee

Dr. Curran Crawford Supervisor Main, Supervisor
(Department of Mechanical Engineering)

Dr. Afzal Suleman, Departmental Member
(Department of Mechanical Engineering)

Dr. Jane (Juan-Juan) Ye, Outside Member
(Department of Mathematics and Statistics)

Supervisory Committee

Dr. Curran Crawford Supervisor Main, Supervisor
(Department of Mechanical Engineering)

Dr. Afzal Suleman, Departmental Member
(Department of Mechanical Engineering)

Dr. Jane (Juan-Juan) Ye, Outside Member
(Department of Mathematics and Statistics)

ABSTRACT

Research into advanced wind turbine design has shown that load alleviation strategies like bend-twist coupled blades and coned rotors could reduce costs. However these strategies are based on nonlinear aero-structural dynamics providing additional benefits to components beyond the blades. These innovations will require Multidisciplinary Design Optimization (MDO) to realize the full benefits.

This research expands the MDO capabilities of Horizontal Axis Wind Turbines. The early research explored the numerical stability properties of Blade Element Momentum (BEM) models. Then developed a provincial scale wind farm siting models to help engineers determine the optimal design parameters.

The main focus of this research was to incorporate advanced analysis tools into an aero-elastic optimization framework. To adequately explore advanced designs with optimization, a new set of medium fidelity analysis tools is required. These tools need to resolve more of the physics than conventional tools like (BEM) models and linear beams, while being faster than high fidelity techniques like grid based computational fluid dynamics and shell and brick based finite element models. Nonlinear beam models based on Geometrically Exact Beam Theory (GEBT) and Variational Asymptotic Beam Section Analysis (VABS) can resolve the effects of flexible struc-

tures with anisotropic material properties. Lagrangian Vortex Dynamics (LVD) can resolve the aerodynamic effects of novel blade curvature.

Initially this research focused on the structural optimization capabilities. First, it developed adjoint-based gradients for the coupled GEBT and VABS analysis. Second, it developed a composite lay-up parameterization scheme based on manufacturing processes.

The most significant challenge was obtaining aero-elastic optimization solutions in the presence of erroneous gradients. The errors are due to poor convergence properties of conventional LVD. This thesis presents a new LVD formulation based on the Finite Element Method (FEM) that defines an objective convergence metric and analytic gradients. By adopting the same formulation used in structural models, this aerodynamic model can be solved simultaneously in aero-structural simulations. The FEM-based LVD model is affected by singularities, but there are strategies to overcome these problems. This research successfully demonstrates the FEM-based LVD model in aero-elastic design optimization.

Contents

List of Tables

List of Figures

ACKNOWLEDGEMENTS

I would like to thank:

My wife, Adriana Johnston, for supporting me throughout this long process and all her patience in the difficult moments.

My supervisor, Curran Crawford, for revealing to me the world of MDO and medium fidelity analysis.

Chapter 1

Introduction

This chapter starts by explaining the motivation of this research in section 1.1. Wind turbine development is an established field and many researchers have already made important contributions to the field, which are discussed in section 1.2. In section 1.3 the author lays out the research vision that underpins the contributions made in this work. These contributions are summarized in section 1.4. This chapter closes with a outline of the thesis in section 1.5.

1.1 Background and Motivation

An inexpensive and reliable energy supply is an important necessity for any developed society. The conventional sources of energy are largely carbon based fuels and to a lesser extent, hydro-electricity and nuclear. There are increasing concerns over these conventional sources. A combination of increased demand and dwindling supply is increasing the cost of carbon based fuels. The Heavy pollution in large population centers is another unattractive consequence. The potential threat of climate change is increasingly seen as a risk associated with fuel combustion. Further growth in hydro-electricity is limited because most viable sites are already developed. Increased utilization of Nuclear energy is possible, however disasters in Chernobyl, Three Mile Island and more recently, Japan, highlight the risk associated with nuclear energy.

Wind turbines are increasingly becoming a popular alternative source of electricity generation [1, 2]. Wind turbines rely on a renewable resource to generate electricity, thus are insensitive to the supply issues plaguing carbon based energy. Furthermore extensive research into the life-cycle costs of wind turbines have demonstrated that

wind turbines generate their embodied energy within 4-8 months of operation with negligible Carbon Dioxide (CO_2) emissions (a major contributor to climate change) [3]. The research by Lenzen and Munksgaard demonstrated that reduced energy and CO_2 emissions are possible by pursuing ever larger turbines. Currently, wind energy is a mature technology in terms of technical reliability, with several corporate entities building and managing wind farms [1]. Research by Tavner *et al.* has demonstrated that the reliability of wind turbines is similar to modern gas turbines and approaching that of steam turbines [4].

There still remain some challenges to future growth [2, 1]. The uncertainty of wind forecasting and other technical issues prevent wide-spread integration into the electricity grid. Environmental issues associated with noise emissions limit where turbines can be built. The economic cost of wind energy also remains a major impediment [1]. Research by Greenblatt et al. [5] demonstrated that natural gas will remain a less expensive energy source even when carbon emissions are taxed. To address the cost issue, the technology of wind turbines must be improved.

Rasmussen and Madsen state that the first and second priorities for wind energy researchers are cost reduction and offshore wind energy respectively [1]. A similar article by Thor and Weis-Taylor state that improved models for aero-elastic stability and adaptive structures should be a high priority for research, both in the short and long-term, in order to achieve the cost reductions [2].

The focused development of modern wind turbine technology started during the 1970s. Since then, many configurations have been tested, including vertical axis configurations and two-bladed horizontal axis turbines [6]. The three-bladed horizontal axis "Danish" wind turbine has proven to be the most cost effective and reliable configuration [7].

Initially, commercial turbines were designed for maximum coefficient of power (C_P, ratio of power generated vs. power available) at a single wind speed [6]. To reflect the variability in the wind resource, designers moved to maximizing the Annual Energy Production (AEP) [6]. With larger and larger turbines being built, the cost of the structure has become increasingly more important. Current turbine designs are being designed based on the minimum Cost Of Electricity (COE) to include structural aspects [6]. The cost of a wind turbine is attributed to the material used to maintain structural integrity, while the electricity generated is strongly dependent on the aerodynamic design. Turbine design based on COE minimization is therefore evolving towards a multidisciplinary approach. The scope of the cost models is not

just limited to the initial capitol costs. Recent work by National Renewable Energy Laboratory (NREL) has developed comprehensive cost models that incorporate manufacturing costs, operation and maintenance, along with the balance of plant costs [8, 9].

The driver of minimum COE is affecting wind turbines in a number of ways. One effective way of reducing turbine cost has been increasing the size of the turbines themselves, thereby increasing the energy produced for every foundation and electrical connection [10, 11]. Considering the amount of wind energy available to a turbine at a given wind speed is fixed [12], reductions in COE will come from a mix of better structural designs and utilizing sites that have better wind resources. The search for better wind resources has prompted increasing interest in offshore wind farms [10]. When developing offshore sites, the economics change considerably and in these cases, the foundations and electrical transmission become the most significant costs [10]. These increased costs have made the economies of scale in wind turbines more substantial. A crucial limit to the size of turbines is structural integrity. Not only will improved structural design reduce the overall cost, it will enable developers to take advantage of sites with better wind resources.

In summary, wind energy is a relatively benign source of electricity available at a reasonable cost, where the winds are strong. Yet, it is important that further cost reductions are achieved. The evolution of turbine design is moving to a more multi-disciplinary approach. Economies of scale and interest in offshore wind farms are driving designers to produce larger turbines. To continue this progression, efficient nonlinear analysis tools are required to create more effective aero-structural designs that are inherently more flexible than current designs [13]. These trends are the primary motivation behind developing improved analysis tools for use in multidisciplinary design optimization.

1.2 Previous Work

This section outlines the contributions that have been made to develop larger more efficient turbines that utilize innovative structural design and multi-disciplinary design optimization. The literature indicates that wind turbine designs are getting larger and the design process is becoming more multi-disciplinary (see section 1.2.1). To achieve larger turbines, engineers need to incorporate load alleviation into the design; section 1.2.2 discusses these contributions. One of the challenges of adopting these

innovative concepts in commercial designs is that conventional analysis techniques are inadequate. Typically, the innovative concept is based on a geometry or property (*e.g.* curved and flexible blades), that is assumed not to exist in the conventional analysis (*e.g.* Blade Element Momentum (BEM) theory assumes straight blades, linear beam theory assumes stiff blades). Section 1.2.3 discusses the conventional analysis techniques along with more advanced methods that could overcome these limitations. Multidisciplinary design can have compounding complexity that makes it difficult for engineers to develop optimal designs. Optimization can help engineers navigate this complexity; accordingly many researchers have already made contributions to wind turbine Multi-disciplinary Design Optimization (MDO). These MDO contributions are discussed in section 1.2.4.

1.2.1 Historical Trends in Wind Turbine Design

Historical trends in wind turbine design show that turbines are likely to increase in size in the future [14]. Historically, this growth has occurred for several reasons: there are economies of scale, the larger turbines are higher and have access to a better wind resource, and larger turbines allows wind farm designers to capture more wind at exceptional locations (*e.g.* at the top of a hill). Although they are starting to reach size and weight limits for onshore installations [15], their growth is sure to continue for offshore applications [10].

Capturing more energy is only one aspect of wind energy development. As outlined in section 1.1, the most important driver is costs. Thus increased energy capture is only beneficial when it is only associated with limited increases in cost. The power of the wind turbine scales with the square of the rotor diameter, while the weight of structurally similar rotors scale with the cube of rotor diameter [15]. Considering these scaling laws one would expect that eventually material costs would dominate and prevent further scaling. However, studies have shown that commercial designs are becoming more efficient and have managed to maintain close to quadratic scaling of weight [14].

Initially, designers adopted more accurate analysis tools that allowed for less conservative designs [11]. More recently, the drive for further improvement has prompted many studies into alternative materials to achieve the desired weight, strength and stiffness properties [16, 17, 18]. At the current scale, limited use of carbon fiber is used to achieve the desired stiffness without the weight penalty of increased material

usage [15] and many manufacturers are turning towards stronger versions of Glass Reinforced Plastic (GRP) for the rest of the blade [14].

These trends show that innovative structural design is an important component to achieving overall COE reductions through larger rotor designs. Further increases in scale will require further innovations in design, prompting much research into advanced design concepts [14, 15] (see section 1.2.2 for more details).

This coupling between increased energy capture and innovative structural design highlights the system interactions that are driving wind turbine design. Jackson *et al.* notes much attention has been given to aerodynamic optimization (e.g. [19]) while little MDO is applied in practice [15]. Both Veers *et al.* and Jackson *et al.* state that aero-elastic tailoring and other load alleviation strategies increasingly deserve more research attention [14, 15]. Accordingly, there has been increasing research given to system engineering [9] and MDO (see section 1.2.4).

1.2.2 Load Alleviation in Wind Turbines

When designing wind turbines, the most stringent constraint is either the fatigue loads or the ultimate loads. Several experiments have demonstrated that unsteady aerodynamics is a strong contributor to this detrimental loading [20]. The actual desirable loads (power-producing rotor torque) compose a small proportion of the overall loads imparted on the machine. Thus there is great potential to reduce the undesirable loads without reducing the overall energy capture [21]. The loads generated at the rotor are applied to all the other turbine components (drive-train, tower and foundation). Barlas and Van Kuik [21] note that the potential cost reductions from load alleviation are small in the blades alone, however, considering the drive-train and tower, the potential is significant, again motivating MDO of the system.

When looking at load reduction, there are two approaches: active control and passive control [22]. The former employs sensors to measure the loads or estimate a future loading state. These measurements are used by a controller to give the appropriate signal to an actuator to alleviate undesirable loading. The work by Barlos and Van Kuik [21] gives an excellent summary of the state of the art in this field. Currently, collective and individual blade pitch control is common, but is too slow to effectively attenuate turbulent loading [21]. Barlos and Van Kuik [21] cite large research projects in Europe that have investigated many different strategies and assessed their potential with numerical simulations. Overall, the authors found

that active flaps were most effective. In some cases the researchers were able to demonstrate potential reduction in fatigue loads by up to 90% in numerical studies. Wind tunnel investigations confirmed many of the conclusions of the numerical work.

An investigation by Johnson et al. [22] looked into the different methodologies that could be employed for active control. In this work they focused on flaps, micro-tabs, plasma jets and boundary layer control. The authors cited flaps and micro-tabs as having the greatest potential for load alleviation. The authors demonstrated that small, efficient and simple micro-tabs can generate nearly the same control authority as flaps. The research by this group lead to the SMART rotor project [23]. In this project researchers outfitted a 1.1 MW wind turbine with flaps on the outer portion of the blades. The investigation employed a combination of accelerometers, fiber optic strain gauges, pressure sensors and pitot tubes for feedback.

One of the major issues with active control strategies is the weight, reliability, cost and engineering resources that are required to employ them in commercial designs. For these reasons, a lot of attention has been paid to passive approaches. The passive strategies rely on applying sophisticated design to engineer a desirable blade response to wind gusts and turbulence. One example is the DAMPBLADE project in Europe [24], in which the authors looked at the potential of materials that exhibited increased damping properties and developed enhanced analysis capabilities for rotors designed with these materials.

Another approach that has received much attention is using coned rotors [25, 26, 27]. The idea behind this concept is that a hinged rotor would eliminate the root bending moments. During gusts, the blades would passively cone in to reduce the projected area and the structural loads. This would enable larger rotors that could capture 55% more energy in low wind situations [25]. Yet several challenges exist for controlling these types of turbines, analysis by Crawford and Platts demonstrated power control cannot be achieved through pitch control. Instead, speed control is required to control the degree of coning. Due to changes in the moment of inertia, the control demands excessive torque from the generator [26].

Conventional analysis tools assume a straight blade. Studies into swept blades have found desirable aero-elastic effects. By sweeping the blade, a gust in the wind will induce a twist towards feather and reduce the loads. A field test by Sandia National Laboratories in conjunction with Knight and Carver demonstrated that sweep twist adaptive blades could be larger without exceeding the bending loads of smaller blades [28]. The field test demonstrated 10-12% more energy than conventional turbines.

A detailed numerical study by Hansen looked at the aero-elastic behavior of swept blades [29]. In this research the author found that the blades attenuated the flap-wise force response in the frequency range around the rotational speed. However, the blade exhibited less damping in the edge wise mode, increasing the potential for aero-elastic instability.

The potential success of sweep-twist coupling has lead The General Electric company (A major wind turbine manufacturer) to patent in-plan blade curvature [30]. The patent is based on mixing both for and aft sweep in the blade to control both the elastic twist for load alleviation, while limiting the total torsion loads at the root of the blade.

A numerical investigation by Dwyer and Bennett [31] looked at improving the aero-elastic response of small turbines with bend twist coupling and sweep twist coupling. Their work was severely hampered by inadequate design tools and could only conduct a series of trade studies. They concluded that there is great potential for aero-elastic tailoring but better analysis tools are required. This work justified the need to develop improved analysis tools.

Bottasso *et. al.* conducted an MDO study into elastic bend-twist coupled blades. Here the anisotropy of blade material is used to cause the blade to feather whenever a gust creates large bending loads. One of the challenges of elastic bend twist coupling is reduced bending stiffness of biased fibers. This reduced stiffness forces the designer to add more material to compensate, which in turn increases the blade weight. They found that applying biased fibers in the skin instead of the spar-cap, bend-twist coupling could be achieved with a smaller weight penalty. Furthermore they found that biased fiber only need to be incorporated in the inner regions of the blade to achieve the desired coupling with the minimum weight overall. Applying a multidisciplinary approach revealed an additional benefit of bend twist coupling. By passively attenuating the loads there was a reduced amount of pitch actuation in the control of the machine. This work is an example of how MDO can reveal system benefits of advanced concepts.

A detailed numerical investigation of aero-elastic coupling was carried out by Wetzel [32]. In this study, 40 paper designs were developed and analyzed in detail. The author focused on using elastic coupling to achieve bend twist coupling and found that maximum coupling is achieved with a modest fiber angle of 20°. A more detailed investigation into the internal stress found in-plane shear exceeded yield limits. The author found a smaller bias angle of 7° gave the best coupling without exceeding

stress limits. The work of Dwyer and Bennett [31] along with Wetzel [32] highlight the importance of advanced analysis tools for engineering load alleviation strategies.

It is interesting to note the work of Maheri *et al.* in developing different design strategies for turbines utilizing load alleviation [33]. In this work the authors explored the use of induced twist as a design variable. This effectively decouples the aerodynamic and structural analysis.

1.2.3 Wind Turbine Design Analysis Methods

In the early days of wind turbine development, the blades were sufficiently stiff that many designers relied on linear beam models [13, 34]. Linear analysis allowed further simplifications by reducing the model complexity through modal analysis [13, 35]. This involves an eigen-value analysis in which the analyst would select the first 3-6 modes and develop the equivalent mass, damping and stiffness matrices for the reduced model (assuming mode shapes do not vary with operating conditions). Interest in large offshore wind turbines is driving engineers to apply nonlinear analysis and more sophisticated aero-elastic models [13].

The work by Zhao *et al.* [36] is an example of some of the research into higher fidelity models without excessive complexity. Here, the author modeled the blade as a chain of rigid bodies connected by cardonic joints. Another example is the work of Yan [37], where a panel code was used for the aerodynamics and a linear shell model for the structure.

Other authors are trying to improve the fidelity in structural design without resorting to complicated FEM models. The work by Malcom and Laird [38] is particularly innovative, where the authors represent the full turbine blade in a three dimensional FEM model. The blade is subjected to a set of fundamental deflections. The resulting force solution is used to determine the equivalent cross section properties. These properties are then used in a simple beam analysis. However, this work suffers from uncertainty associated with the extensive use of statistical analysis.

A more rigorous example of efficient high fidelity analysis is given by Otera and Ponta [39]. Here, the authors applied Variational Asymptotic Beam Section (VABS) analysis to determine the cross section properties. The work is similar to the work used this research, VABS is described in greater detail in chapter 2. This particular work applied some statistical methods where a more rigorous asymptotic analysis could have been applied [40].

A considerable amount of research has addressed structural stability. In response to helicopter aero-elastic experiences, many researchers have examined the possibility of flutter in wind turbine rotors [6]. This subject has received some recent attention for large multi-MW wind turbines. Lobitz [41] used the Theodorsen function to perform a classical flutter analysis and found that flutter would occur at twice the nominal operational speed. This conclusion was confirmed by Hansen [42] with the more sophisticated Beddoes-Leishman dynamic stall model. It should be noted that research cited by Rasmussen *et al.* [43] demonstrated that interacting modes could compromise the flutter stability of large wind turbines. Full turbine analysis is required to resolve this behavior [43].

One issue that is actually quite serious is "stall flutter"; this occurs when the vibration direction is aligned in such a way that the negative lift slope of the blade in stall amplifies the vibrations [43]. Riziotis *et al.* performed a detailed analysis of this issue and found significant edge-wise instability in large stall regulated wind turbines. In this study, variable speed wind turbines were also investigated, where the damping in the generator was found to be sufficient to stabilize the edge-wise modes. Rasmussen *et al.* does highlight that hysteresis in the drive-train can also excite some edge-wise modes. Hansen [42] is credited with developing a simple analytical model for stall vibration that is used to engineer vibration modes that are not sympathetic to stall. These issues are more serious in either constant pitch stall regulated machines or pitch to stall regulated machines. This has prompted commercial turbine manufacturers to use pitch to fine (reduced angles of attack) to regulate the power.

Looking at the blades in isolation gives an unrealistic assessment of turbine dynamics and there is increasing interest in performing full turbine analysis [43]. This is achieved by applying multi-body dynamics [13]. The stability analysis is still based on linearized models, where the Coleman transfer is used to express the blade dynamics in an inertial reference frame [13]. The reader is referred to Bir [44] for more details on the Coleman transfer. One example of this analysis is the work by Hansen [45]; the author developed a nonlinear co-rotational beam model based on the Hamiltonian principle. First, a steady state solution is found for the nonlinear model, then the model is linearized about this solution. The linearized model is augmented with a state space model for the dynamic stall[1]. An eigen value analysis is applied to

[1]Airfoils undergoing dynamic stall are known to exhibit temporal hysteresis in loading [46]. Consequently, models for both aerodynamic [47, 48] and structural [49] applications have been developed.

determine the various modes and their stability properties. It should be noted that Rasmussen *et al.* [43] cites research demonstrating that wake interaction gives some impetus for full wind farm modeling to asses turbine dynamics.

The majority of stability research is based on linear models, although interest in nonlinear dynamics is growing [13]. Nonlinear dynamics are assessed with Lyapunov exponents and to a lesser extent Floquent analysis [50, 13, 43]. In this area Larsen [50] developed custom structural models for the specific purpose of nonlinear stability analysis. The author demonstrated how regions of stability could be identified within a range of potential operational conditions.

In addition to analysis methods, there are several notable efforts in advancing design methods. Conventional turbine design is based on sequential optimization where the aerodynamic aspects are optimized first, followed by structural optimization. For this framework, Bir [51] developed a tool automating preliminary structural design. The LEXPOL project by Collani *et al.* [52] developed a stochastic model for long term turbine loads that could be used to give better results than the traditional safety factor approach. Finally the experimental work of Jensen [53] demonstrated that secondary failure modes (Brazier effect) occur in highly optimized structures and require secondary reinforcement.

This section will conclude with a brief discussion on fatigue methods. In the early years, fatigue evaluation was performed through a frequency analysis [11]. A brief introduction to these methods can be found in an article by Halfpenny [54]. This approach is much more efficient than the current accepted practice of running multiple time domain simulations [55]. However, nonlinear effects have compromised the validity of the frequency approach [11]. The increased complexity associated with offshore applications has prompted renewed interest in these methods; the TURBU program by Van Engelen [56] is an example. Albeit, the target application is highly nonlinear structures, frequency methods could be applied to develop a surrogate model for fatigue. A simplistic example of this is given by Fuglsang *et al.* [57, 58, 59]. Alternatively, the nonlinear effects can still be incorporated through nonlinear frequency domain techniques [60, 61, 62].

1.2.4 Wind Turbine Design Optimization

Optimization has been an important tool for turbine design for many years [6]. The approach to wind turbine design has evolved with the technology. In the early days,

design optimization was discipline specific and focused on engineering performance metrics. For example, in aerodynamic design engineers would focus on maximizing the coefficient of power at a design wind speed [6]. The system performance of a wind turbine is highly coupled, thus, single discipline optimization can lead to suboptimal designs. For example, a small increase in aerodynamic performance may lead to a large increase in costs in the structural design.

It is only recently that multi-disciplinary approaches are being considered in commercial turbines. With larger turbines, structural aspects became increasingly important; to give a more realistic performance metric, designers began aiming to minimize the COE [6]. Given that power generation is based on aerodynamic performance, while the costs are based on material usage and structural considerations, minimizing this objective is inherently multi-disciplinary. Furthermore, incorporating costs into the design objectives leads to more balanced designs that are closer to the optimal overall design. The interest in multidisciplinary design optimization is not just limited to aero-structural optimization. Recently, the NREL has started a systems engineering group to look at wind turbine design in the context of community impact, environmental impact and grid integration [9].

The complexity of taking a multi-disciplinary approach is a common topic in academic literature. An early example is given by Fuglsang and Madsen, where BEM was coupled to a simple modal structural model to evaluate the COE [57]. In this work, the author used a combination of sequential linear programming and the method of feasible directions to find the minimum COE solution. A novel approach presented there was a simplistic surrogate model for fatigue loads that was tuned with a full time domain simulation after a set number of optimization iterations. The cost model was based on a combination of structural loads and component weight.

The work of Xudong *et al* [63] coupled a BEM model with a structural model based on modal analysis. Then applied gradient based optimization algorithms to find the minimum COE solution [63]. The work used component weight to evaluate costs and interpolation curves to approximate the shape of the blade. The use of interpolation curves helped reduce the dimensionality of the problem.

Soren Hjort *et al* [64] presented the most comprehensive framework to date for design optimization. Here, the author attempted to optimize the airfoil profile, the rotor blade chord, twist and thickness, the pitch and speed control schedule and the internal structural design considering aerodynamics, structural mechanics, noise emissions and economics. The author stressed the large dimensionality in play when perform-

ing such a comprehensive optimization. To reduce the dimensions of the design space for each optimization loop, the author used a combination of sequential and multi-level optimization. This resulted in problems with increased noise in the gradient calculations and compromised their application of gradient based optimization.

The work of Crawford *et al.* [65] is another example of a more comprehensive approach to design optimization. As with many other optimization works, the author used BEM for aerodynamics and linear beam models for structural mechanics. This work is unique in attempting to optimize small wind turbines for distributed generation. In off-grid applications, turbine start-up is an important performance metric. Here, the author developed a generator model to evaluate this metric.

An interesting application of MDO is in multi-objective optimization. This allows the user to evaluate the trade-off between different measures of merit. An example of this is given by Benini and Toffolo [66] where it is argued that maximum AEP density is more desirable for building wind farms. The authors applied genetic algorithms with BEM and a simple structural model to evaluate the Pareto front between these quantities.

Site specific design is a popular MDO topic for wind turbine design. The earliest example of site specific design is given by Collecutt and Flay on finding the optimal configuration for turbines in New Zealand [67]. In this work, the authors used semi-empirical studies to determine the rotor diameter and tower height that would minimize COE. Another example of using semi-empirical models is given by Diveux *et al.*, where genetic algorithms were used to evaluate the potential of site specific tailoring [68]. Recently the work of Kenway and Martins [69] applied gradient based optimization with *XFoil*, BEM and linear beam models to show that 3-4% improvement in AEP is possible when site specific optimization is applied.

The work of Thomsen *et al.* [70] along with Fuglsang *et al* [58, 59] performed a detailed investigation on the potential for site specific design. Thomsen *et al.* performed aero-elastic simulations of a single turbine design at 6 different locations to show the wide range of AEP and fatigue loads [70]. Simultaneously, Fuglsang *et al.* developed an optimization code for the purpose of site specific tailoring [58]. The framework used for this work is similar to a framework proposed by Fuglsang and Madsen [57] in 1999. This optimization framework was then applied to site specific turbine designs for the same six sites to determine the best group of design variables for site specific optimization [59].

The work by Jockson *et al.* shows the potential of site specific optimization when a more comprehensive economic model is applied for the region [71]. Here, the authors looked at the California electricity market and found that time of day electricity pricing presented a strong case for building wind turbines with over-sized rotors [71].

A powerful feature of MDO is the ability to fully evaluate different design concepts. Without knowing the optimal performance it is difficult to know for certain the value of a novel concept. Giguere *et al.* coupled BEM with a simple linear beam model to evaluate the most appropriate type of airfoils for stall regulated wind turbines [72]. Including the structural aspects was important to show that a larger blade resulted in less material overall.

Another example of evaluating novel design concepts is given by Crawford and Platts [26]. Allowing the rotor to cone in with gusts and strong wind is an attractive load alleviation strategy. Here, the authors applied a modified BEM simulation along with a linear beam model to evaluate the potential of this concept. By taking a multi-disciplinary approach, the authors were able to identify an undesirable interaction between the rotor and generator.

Due to the iterative nature of design optimization, many applications of optimization used computationally efficient BEM to model the aerodynamics [57, 63, 64, 65, 66, 69, 70, 58, 59, 72, 26]. Accordingly, there has been work in improving these methods for design optimization. The work by Lanzafame and Messina investigated various empirical models for airfoils in stall [73]. Clifton-Smith investigated different tip loss models for optimization applications [74]. More recently McWilliam and Crawford investigated the numerical stability of different solution algorithms for BEM [75].

BEM is not the only aerodynamic model applied in optimization work. Potential flow methods are attractive because they are much more efficient than Reynolds Averaged Navier Stokes (RANS) yet accurately resolve the full three dimensional flow. This has lead several authors to apply vortex methods to find the maximum coefficient of power solution for a wind turbine rotor [76, 77, 78]. In all cases the authors had to make many assumptions on the structure of the wake to make the optimization tractable for analytical optimization. An interesting conclusion from Chattot is that the maximum energy condition given by Betz does not have to be met at all stations and only has to be met on average [77]. Each author gives the conclusion that vortex methods give a better optimal solution than the BEM methods by Gluaert [76, 77, 78]. This shows that higher fidelity methods have the potential

to produce better turbines overall. Unlike BEM theory, potential flow analysis is not limited to straight blades without coning, furthermore, these methods are not plagued by the many correction factors required in BEM. Overall potential flow methods are more predictive and suitable for advanced blade concepts that utilize curvature.

The potential of higher fidelity methods has inspired the use of numerical potential flow methods for MDO. By resolving the three dimensional wake structures, one can evaluate the effect of novel geometry. Advanced methods are also considered for the structural model. Here we look at nonlinear beam models with cross section analysis that considers the full anisotropy of the fiber-reinforced material. By applying advanced models the full potential of many advanced blade design concepts can be determined.

1.3 Research Vision

It is clear by historical trends that wind turbine designs are getting larger. To overcome the challenges of larger turbines, researchers have proposed several concepts (*e.g.* bend twist coupling, curved blades, *etc.*) that cannot be simulated efficiently with existing analysis methods (*i.e.* linear beams assume stiff blades, BEM theory assumes straight blades without coning). Single discipline studies with either grid-based Computational Fluid Dynamics (CFD) or 3 dimensional FEM models could simulate these concepts, yet these tools come with increased development costs (*i.e.* more operator time setting up the models along with greater computational resources to solve the models). To incorporate these advanced concepts into commercial designs there is a need for efficient analysis tools with higher fidelity.

The literature also shows wind turbine design is becoming increasingly more multi-disciplinary. Load reduction in the blades may not just improve the blade structural design, but could provide benefits to the drive-train, tower, control system and even the electricity grid (*e.g.* flexible blades could dampen undesired power fluctuations). When considering the system it may become apparent that more expensive blades will yield the greatest benefits. To realize these potential benefits, MDO techniques should be utilized to couple multiple analysis modules. To help the designer navigate the system complexity, optimization algorithms should be applied. In the context of MDO, expensive analysis techniques become even more expensive (*i.e.* mesh generation needs to be automated because many more solutions are required in optimization), thus MDO increases the need for medium fidelity tools.

This begs the question "given these needs, what MDO framework is required to improve wind turbine design?". First, we need aerodynamic analysis tools that can handle non-straight blades with arbitrary curvature and we need structural models that can resolve material anisotropy and flexible blades. These tools should require, at most, only simple meshes that are easy to generate automatically. These analysis tools should be efficient so they can be used in optimization without prohibitive computational costs. The models should easily couple to form system models that at the very least enable aero-structural analysis, but ideally include control, drive train, tower and possibly, the electricity grid. These tools should provide steady state solutions for estimating AEP. Then, to evaluate extreme loads and fatigue damage, there needs to be efficient ways of simulating unsteady processes within iterative analysis like optimization. All these models should be coupled with optimization algorithms to navigate the system complexity. Finally, to objectively evaluate the costs and benefits of various design features, the optimization should be based on comprehensive cost models that incorporate manufacturing and the optimal environmental conditions in which these turbines will be installed.

It is in the context of this research vision that this author has attempted to improve the engineering design capabilities of wind turbines. Given the expanded scope of system analysis, along with the fastidious attention needed to develop new analysis methods, it is unreasonable to expect this research vision to be accomplished by one person in one PhD. Instead this author has looked to make incremental contributions to this overall goal. To simplify the problem, the author has focused on steady state analysis of aero-structural analysis, with some considerations for the larger system. Despite the simplifications, the contributions of this author can later be extended to larger system analysis with unsteady effects. This later work represents the future of this research and is beyond the scope of this thesis.

1.4 Research Contributions

The overall objective of this research was to expand the MDO capabilities for Horizontal Axis Wind Turbines (HAWTs). The field of MDO is far-reaching, including adapting established analysis techniques for optimization (*e.g.* investigating the numerical stability of BEM theory listed below), to expanding the scope of engineering design through systems engineering (*e.g.* wind farm siting listed below). The follow-

ing is a list of contributions toward an enhanced wind turbine MDO capability that have been made over the course of this thesis work:

Numerical stability of BEM: BEM is an attractive aerodynamic model for optimization due to computational speed. This research discovered how BEM has multiple solution and numerical instabilities that can spoil the numerical convergence (see section 2.3.1 of chapter 2). This research investigated numerical strategies to avoid the instabilities. This work was published in Wind Engineering [75].

Wind farm siting: For a turbine design to be truly optimal it needs to be designed for the environmental conditions of the installation site. Yet turbines are typically designed before sites are identified, thus the engineer is forced to make assumptions a-priori that may not reflect the actual site conditions. Section 5.1 of chapter 5 presents a totally new model for finding the optimal location for wind farms in a large area. This will allow engineers to gather statistics on the most likely conditions for their designs. This models differs from conventional turbine siting models in that it is looking at regions on the scale of $500,000 km^2$, using the wind resource, electrical transmission network, population density and economics to find the optimal sites. This work was published in Renewable Energy [79].

Most of the analysis techniques in recent HAWT optimization literature utilize simplistic analysis tools that are not capable of simulating advanced turbine designs with flexible, non-straight blades and composite layups introducing structural coupling. Accordingly, this research emphasizes the use of medium-fidelity tools. Originally this work was meant to focus on structural aspects using Geometrically Exact Beam Theory (GEBT) and VABS along with a conventional LVD to simulate the aerodynamics. This structural research lead to the following contributions:

Structural sensitivity analysis: Two-stage structural simulations using VABS analysis and nonlinear GEBT is attractive for optimization due to the speed and moderate fidelity. To improve the speed for optimization this author developed analytic adjoint based gradients for both GEBT and VABS theory and then combined them to form a coupled GEBT and VABS structural gradient. This work was used for structural optimization. The gradients and the optimization

is presented in section 5.2 of chapter 5. This work was presented at the AIAA 2012 Structures, Dynamics and Materials Conference [80].

Manufacturing based structural parameterization: In section 5.3 of chapter 5, a new parameterization scheme is presented based on the manufacturing process of wind turbines. This scheme is based on defining slabs of the material similar to the process of carbon/glass fiber layups. Solutions with this scheme lead to well defined designs for manufacturing. This work was presented at the AIAA 2013 Aerospace Sciences Meeting [81].

There are many challenges using conventional LVD methods in design optimization. First Lawton and Crawford [82] demonstrated that conventional LVD fails to give robust and accurate gradients for design sensitivity. Later, the author of this thesis demonstrated that iterative convergence criteria along with slow convergence can lead to significant error in conventional LVD solutions (see section 3.2.1). Section 5.4 documents this thesis author's attempt at MDO with conventional LVD, demonstrating how these problems stalled the progress of the optimization. This work was presented at the 2013 AIAA Aerospace Sciences Meetings [83]. To overcome these challenges this author developed a completely new approach to LVD specifically for aero-elastic optimization. This development lead to several more contributions to the field:

FEM-based LVD: The FEM was used to develop a novel mathematical model for LVD. Unlike conventional LVD, the FEM is used to develop a kinematic description of the wake, where the flow field fidelity is decoupled from the parameterization and computational effort. This allows for local refinement by increasing the number of elements, while at the same time increasing the computational speed by reducing the number of control points. Under certain configurations the new FEM-based LVD is significantly faster than conventional LVD. The FEM is used to develop an objective measure of convergence. This eliminates the uncertainty associated with time-marching LVD and leads to additional contributions listed below. This work is discussed in chapter 3 and has been presented at the AIAA 2013 Structures, Dynamics and Materials Conference [84]; a more updated version was presented at the Science of Making Torque conference and published in Journal of Physics: Conference Series [85]. Currently, two journal publications based on this work are being prepared for

submission. The first presents the method in detail with basic cases and the second explores the various tuning parameters and novel configurations that are capable with this model for wind turbine simulations.

Aero-elastic analysis with LVD: Chapter 4 investigates different algorithms for solving coupled aerodynamic and structural problems with both conventional and FEM-based LVD. This research demonstrates two fixed-point solution algorithms for aero-structural simulations with conventional LVD. Yet these contributions only serve to highlight the advantages of FEM-based LVD. Due to the similarity with structural FEM, the FEM-based LVD model can be tightly coupled with structural FEM problems and solved simultaneously. This avoids the additional iterations associated with the fixed point solution algorithms and makes the FEM-based LVD significantly faster than conventional LVD. A journal paper on this contribution is currently under preparation.

Multi-disciplinary design optimization with LVD: By avoiding time marching and defining an objective measure of convergence, analytic gradients can be defined for FEM-based LVD. These gradients are faster and significantly more accurate than those obtained from finite differencing of conventional LVD. The advantages of FEM-based LVD and the details of the analytic gradients are presented in section 5.5 of chapter 5. Here, the new FEM-based LVD was used in both aerodynamic and aero-elastic optimization. The aerodynamic optimization demonstrated how the accurate gradients lead to optimization solutions with high levels of optimality. Due to the accurate gradients, aero-elastic optimization solutions can be obtained with the FEM-based LVD model. This is a significant improvement over conventional LVD where aero-elastic optimization was not possible. A journal paper on this contribution is currently under preparation.

Figure 1.1 summarizes how these contributions fit into the overall effort to obtain a full, unsteady, medium fidelity, MDO framework. The work started with preliminary studies in MDO. Afterward, the structural analysis tools were developed. Originally, the plan was to incorporate the conventional LVD code developed by Cline and Crawford [86] and Lawton and Crawford [87]. The plan assumed that coupling this model into an MDO framework would not be difficult and this research could proceeded directly to developing unsteady analysis capabilities. However, convergence problems

in the conventional LVD forced the author to abandon these plans. In response to these difficulties, this research developed a totally new LVD formulation based on the FEM specifically for aero-elastic optimization. The remaining tasks to complete the full, unsteady, medium fidelity, MDO framework and the studies therein, represent the future work of this research.

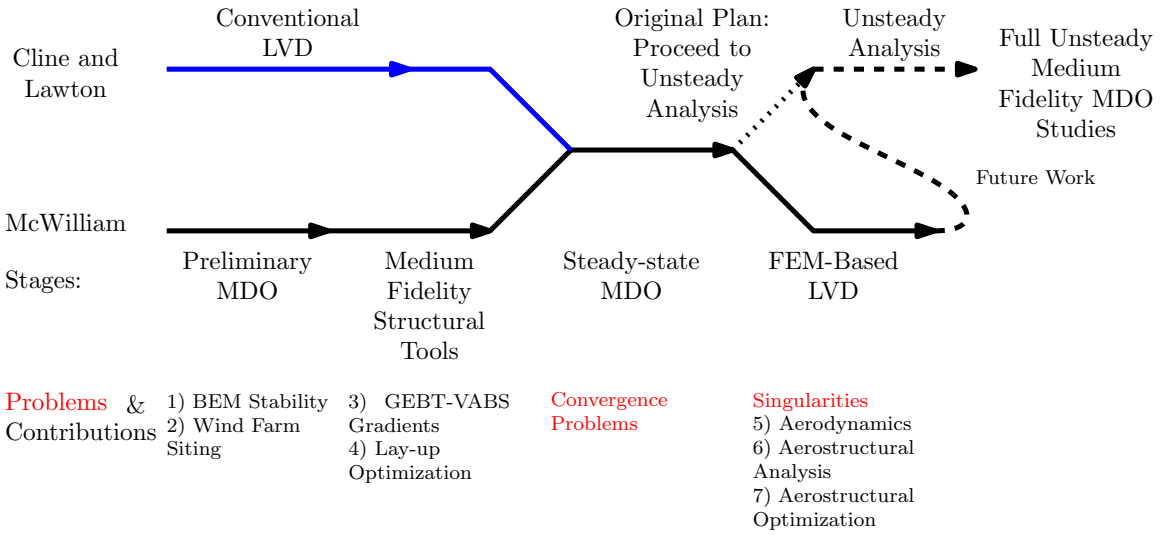

Figure 1.1: Road map of research contributions

1.5 Thesis Outline

This thesis presents work in improving current design methodologies and exploring the design concepts these methods enable. This research emphasizes the development and implementation of medium-fidelity tools that are efficient for optimization, yet with enough fidelity to explore advanced wind turbine design concepts. Chapter 2 outlines different tools that were considered and gives a detailed explanation of the theory behind those tools. The structural aspects are modeled using nonlinear beam theory, several candidate models were investigated and GEBT was selected for this work. The nonlinear beam theory requires cross section stiffness properties. To obtain these properties from cross section geometry and material properties, VABS analysis was employed. This work started by using an existing vortex model for the aerodynamics. This eventually became an important topic in this research so chapter 2 gives a discussion on conventional vortex theory and some of the limitation in

optimization. Chapter 2 closes with a discussion on MDO, where the different MDO frameworks are explained along with the theory behind the sensitivity analysis.

Originally, this research was meant to explore the structural and MDO aspects of optimal wind turbine design. Yet it became apparent that there are significant challenges in applying conventional vortex aerodynamics for numerical wind turbine design optimization. These methods are not widely used in wind turbine engineering and have not matured to the robustness that is required for gradient based optimization. Conventional LVD is typically solved using pseudo time marching algorithms and cannot be converged to arbitrary levels. This makes aero-structural optimization difficult for two reasons. First, the pseudo-time marching solution algorithms used in conventional LVD are not compatible with the solution algorithms in steady state structural models. Thus, aero-elastic coupling requires nested iteration by wrapping a fixed point iteration around the two models to satisfy consistency constraints. The second challenge is conventional LVD does not have a well defined convergence condition; without a convergence condition an analytic gradient cannot be easily defined. Instead, finite differencing must be used. Since conventional LVD cannot be converged to arbitrary levels of precision there is significant error in these gradients. This research shows how these problems made it difficult to obtain converged optimization solutions with LVD.

To overcome these problems, chapter 3 presents a completely new LVD aerodynamic model based on the FEM, suited to gradient based aero-elastic optimization. The new model uses shape functions to describe the configuration in the wake. In steady state these shape functions offer a second definition for velocity, which is used in an objective measure of convergence. This new aerodynamic model can be linearized and solved with the same solution algorithms used for nonlinear structural FEM problems. This chapter presents multiple validations of this method along with grid convergence studies and comparisons with conventional LVD.

Chapter 4 demonstrates how the new FEM-based LVD model is coupled with structural models and used to solve aero-structural problems. The similarity with structural FEM enables the FEM-based LVD to be solved simultaneously with the structural model. This chapter presents comparisons that show this approach is significantly faster than fixed point iteration with conventional LVD.

The overall goal for this research work was design optimization; this work is presented in chapter 5. Several design optimization studies were conducted in this research, each focused on expanding the MDO capabilities for HAWT. The first study

looked at how optimization could be used to find the optimal locations for wind farms. These results could be used to develop optimal turbine designs for a region. The next study developed adjoint based gradients for GEBT and VABS analysis, then applied them in structural optimization. Manufacturing is an important consideration in turbine design; the next study presents a new lay-up parameterizations based on the slabs of material that are layered in the production of a blade. The first attempt at aero-elastic optimization coupled a conventional LVD model with GEBT and VABS in an MDO framework. The optimization failed to produce converged optimization solutions and demonstrated the difficulty of using conventional LVD in optimization. Finally, this chapter is closed by demonstrating the new FEM-based LVD model in optimization. Unlike conventional LVD, analytical gradients are easy to define which eliminates the noise in the sensitivity analysis. These gradients are presented in this chapter along with a simple optimization study demonstrating the efficacy of the new FEM-based LVD for aero-structural design optimization for wind turbines.

Finally, conclusions and recommendations for future work are given in chapter 6.

Chapter 2

Engineering Analysis Tools

The original intent of this research was to couple together established medium fidelity analysis tools for engineering design of wind turbines to create a multi-disciplinary analysis framework. The structural model was based on beam theory, discussed in section 2.1, with an emphasis on nonlinear beam theory to account for the affects of large deformation. Many nonlinear beam theory candidates were investigated; these are discussed in section 2.1.2. The nonlinear beam model requires stiffness properties for a given cross section geometry and materials; these stiffness properties are provided by cross-section analysis, explained in section 2.2. Solving the coupled aerodynamic forces is important for structural optimization. This work explored two options, the first being BEM. Due to the limitations of BEM theory, conventional LVD was used in the initial optimization studies discussed in section 5.4 of chapter 5. These aerodynamic methods are discussed in section 2.3. Optimization was used extensively in this work. There are many considerations when applying MDO techniques: first is the framework (*i.e* how the optimization algorithm interacts with the analysis modules); second the actual algorithm (*i.e.* gradient based vs. heuristic algorithms); finally, in the case of gradient based algorithms used in this work, the sensitivity analysis. These optimization topics are discussed in greater detail in section 2.4.

The majority of this chapter is devoted to analysis methods that have already been established in the literature. The investigation of BEM theory discussed in section 2.3.1 uncovered some new insights into the numerical behavior of BEM. These new insights were published in Wind Engineering [88].

2.1 Structural Beam Theory

Beam theory is applicable to long, slender structures where the cross section dimensions are much smaller than the overall length. The theory simplifies the structural analysis by aggregating the cross-section distributed forces and deformations into integrated cross section quantities. Shell and brick based FEM models will resolve the details of the cross section deformation and forces by introducing many more degrees of freedom. The higher fidelity of these methods come with an additional computational costs to solve these additional degrees of freedom. Since wind turbine blades are very slender, beam theory should give adequate results, while the additional computational costs of high fidelity methods should only provide marginal benefit. Furthermore section 2.2 explains how advanced cross section analysis can introduce the high fidelity cross section effects like warping into beam theory. The ability to efficiently solve the structural dynamics, while maintaining a high level of fidelity has lead to the application of beam theory for the structural models. This research used a combination of linear beam theory discussed in section 2.1.1 and nonlinear beam theory discussed in section 2.1.2.

2.1.1 Linear Beam Theory

Linear beam theory is commonly used in wind turbine design optimization. Accordingly, there are several examples of MDO of HAWT using linear beam theory [57, 59, 13]. The linear structural model can be simplified further through modal analysis. This calculates a family of deflection modes, many of which modes can be ignored, leading to a reduced order model with a small number of state variables. Reduced order models of only 4-6 modes have been shown to give good agreement for wind turbine deformation [13].

The conventional linear Euler-Bernoulli beam theory was applied in this research to understand how advanced aerodynamic models would function in aero-elastic calculations. This model is well established and widely documented in text books; most of the details on this model will not be documented here. The reader should refer to Logan [89] for more details.

This section documents an interpolation scheme for the kinematic description of state. This scheme was required to make the linear beam model compatible for aero-elastic analysis with the advanced aerodynamic models. This scheme will provide the

deformed position and orientation to the aerodynamic model at arbitrary locations along the beam.

Before the interpolation scheme is presented, some definitions need to be given. Element based quantities like reference frames ($\boldsymbol{\lambda}_e$), span parameters (s_e) and element lengths (l_e) are all identified with the subscript $\bullet_e$. In the case of tensor quantities the $\bullet_e$ subscript denotes the element reference frame, and the $\bullet_g$ subscript denotes the global reference frame. Numerical subscripts ($\bullet_1$ or $\bullet_2$) refer to the element nodes and over-bars ($\bar{\bullet}$) denote quantities in the undeformed configuration. Many of the vector quantities are defined in the element reference frame. It is necessary to translate these vectors between this frame and the global frame. This is done through the element rotation matrix $\bar{\boldsymbol{\lambda}}_E$ with equation (2.1) where $\boldsymbol{a}_e$ is an arbitrary vector in the element reference frame and $\boldsymbol{a}_g$ is the same vector in the global reference frame. The element reference frame defines the undeformed orientation of the element where the element x axis is aligned with the element and, in the case of aerodynamic blades, the y axis is aligned with the chord direction.

$$\boldsymbol{a}_e = \bar{\boldsymbol{\lambda}}_E \boldsymbol{a}_g \tag{2.1}$$

In linear beam theory the position at the nodes is given by equation (2.2a), where $\boldsymbol{x}$ is the deformed position, $\bar{\boldsymbol{x}}$ is the undeformed position and $\boldsymbol{u}_e$ is the deflection.

$$\boldsymbol{x}_e = \bar{\boldsymbol{x}}_e + \boldsymbol{u}_e \tag{2.2a}$$

Positions in the element reference frame are tranformed to the global reference frame with equation (2.2b).

$$\boldsymbol{x}_g = \bar{\boldsymbol{x}}_1 + \bar{\boldsymbol{\lambda}}_E^T \boldsymbol{x}_e \tag{2.2b}$$

Angular deflection is given in Euler rotation angles (θ_{xe}, θ_{ye}, θ_{ze}). The angles are defined in the beam element's reference frame. The deformed orientation ($\boldsymbol{\lambda}_e$), defined in the element coordinates, can be calculated from the original undeformed orientation ($\bar{\boldsymbol{\lambda}}_e$) and the angular deformation with equation (2.3a). This definition is only valid with small deflections that occur with stiff beams.

$$\boldsymbol{\lambda}_e = \boldsymbol{\lambda}_{ez} \boldsymbol{\lambda}_{ey} \boldsymbol{\lambda}_{ex} \bar{\boldsymbol{\lambda}}_e \tag{2.3a}$$

where

$$\boldsymbol{\lambda}_{ex} = \begin{bmatrix} 1 & 0 & 0 \\ 0 & \cos\theta_{xe} & -\sin\theta_{xe} \\ 0 & \sin\theta_{xe} & \cos\theta_{xe} \end{bmatrix} \quad (2.3b) \qquad \boldsymbol{\lambda}_{ey} = \begin{bmatrix} \cos\theta_{ye} & 0 & \sin\theta_{ye} \\ 0 & 1 & 0 \\ -\sin\theta_{ye} & 0 & \cos\theta_{ye} \end{bmatrix} \quad (2.3c)$$

$$\boldsymbol{\lambda}_{ez} = \begin{bmatrix} \cos\theta_{ze} & -\sin\theta_{ze} & 0 \\ \sin\theta_{ze} & \cos\theta_{ze} & 0 \\ 0 & 0 & 1 \end{bmatrix} \quad (2.3d)$$

Equation (2.3e) will transform rotation matrices in the element coordinates to the global reference frame.

$$\boldsymbol{\lambda}_g = \bar{\boldsymbol{\lambda}}_E^T \boldsymbol{\lambda}_e \bar{\boldsymbol{\lambda}}_E \quad (2.3e)$$

The axial deflection and twist are interpolated linearly between the two nodes. The Euler-Bernoulli beam theory is based on a small angle approximation where the angular deflection is equivalent to the gradient of the transverse displacement. The interpolation for both the transverse deflection and rotation is based on Hermite interpolating polynomials and the gradients thereof respectively. This leads to the interpolation equations (2.4a) and (2.4b), where the prime (*i.e.* $\bullet'$) denotes a gradient:

$$\boldsymbol{u}_e = P_{h1}(s_e)\boldsymbol{u}_{e1} + l_e P_{h2}(s_e)\boldsymbol{\theta}_{e1} + P_{h3}(s_e)\boldsymbol{u}_{e2} + l_e P_{h3}(s_e)\boldsymbol{\theta}_{e2} \quad (2.4a)$$

$$\boldsymbol{\theta}_e = \frac{1}{l_e} P'_{h1}(s_e)\boldsymbol{u}_{e1} + P'_{h2}(s_e)\boldsymbol{\theta}_{e1} + \frac{1}{l_e} P'_{h3}(s_e)\boldsymbol{u}_{e2} + P'_{h3}(s_e)\boldsymbol{\theta}_{e2} \quad (2.4b)$$

where

$$s_e = \frac{s - s_1}{l_e} \quad (2.4c)$$

$$\boldsymbol{u}_e = \begin{Bmatrix} u_y \\ u_z \end{Bmatrix} \quad (2.4d) \qquad \boldsymbol{\theta}_e = \begin{Bmatrix} -\theta_y \\ \theta_z \end{Bmatrix} \quad (2.4e)$$

$$P_{h1}(s) = 1 - 3s^2 + 2s^3 \quad (2.4f) \qquad P_{h2}(s) = s - 2s^2 + s^3 \quad (2.4g)$$

$$P_{h1}(s) = 3s^2 - 2s^3 \quad (2.4h) \qquad P_{h2}(s) = -s^2 + s^3 \quad (2.4i)$$

2.1.2 Nonlinear Beam Theory

Multiple nonlinear beam theories exist within the literature. The reader is referred to Shabana [90] for a comprehensive review on most of them. For aero-elastic applications it is crucial that any nonlinear beam theory is accurate in resolving the twist deformation. In addition Jung *et al.* [91] demonstrates the importance of resolving shear deformation, cross section warping and material anisotropy in beam dynamics. The fidelity to resolve these effects was used as a criteria in selecting three potential candidates for this work; each will be described below.

The classic nonlinear beam theory is referred to as co-rotational formulation or floating frame of reference formulation [92]. In this formulation beam, deflection is defined within a floating reference frame that follows the rigid body motions of the beam. The deflection is either defined in terms of displacements in the local reference frame or by defining a set of "natural modes". Figure 2.1a shows the kinematics for the natural mode approach. When the displacement approach is taken, the equations of motion become very complicated [93, 50] and suffer from error in various approximations for the beam [93]. The natural modes for simple straight prismatic beams are well known, while for beams with arbitrary curvature and twist it is unclear.

The second theory is Absolute Nodal Coordinate Formulation (ANCF) pioneered by Shabana and Yakoub [94, 95]. The ANCF uses the absolute position of the nodes and gradients of position at the nodes for state variables, see figure 2.1b. There are two versions of this theory. The first uses a three dimensional shape function to define the position of points within the three dimensional volume of the beam [96]. From here, continuum mechanics is applied to determine the deformation gradient and hence strain. With the appropriate constitutive relationships, the stress is then found. Finally, integrating the stress yields the resulting forces. The second version avoids the continuum mechanics approach and uses a one dimensional shape function to define a Frenet frame [97]. From this, the traditional strain measure of a beam is defined and used to determine the resulting forces [98]. Overall, ANCF is attractive because various mathematical decompositions can be applied to make it very efficient for dynamic analysis [99].

The third theory considered here is called Geometrically Exact Beam Theory (GEBT). This theory was originally developed by J. C. Simo [100] and further extended for computer implementation by Simo and Vu-Quoc [101]. In this theory the

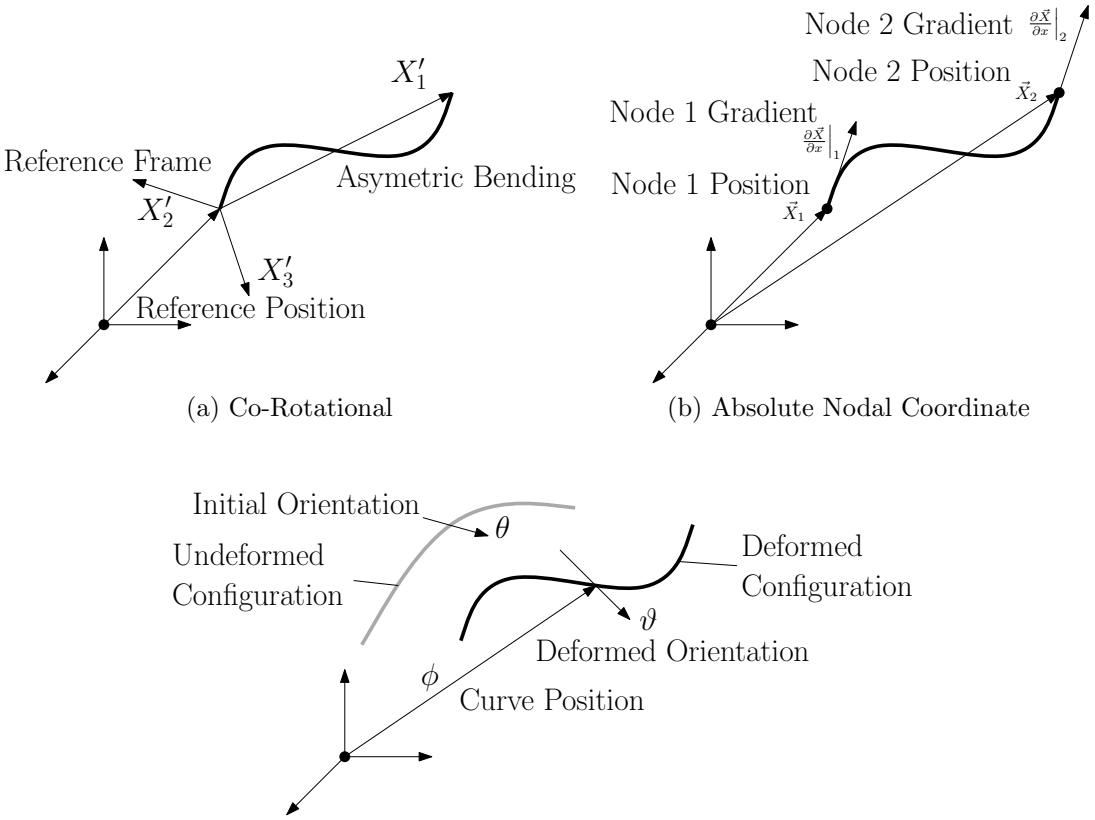

(a) Co-Rotational

(b) Absolute Nodal Coordinate

(c) Geometrically Exact

Figure 2.1: Nonlinear beam kinematics

beam is represented by the position (ϕ) of a reference curve and the orientation of the cross sections (ϑ). An example of the beam kinematics is given in figure 2.1c, where θ is the initial orientation of the cross section.

Another notable version of this theory is the intrinsic equation given by Hodges [102]; these equations are independent of the kinematic and constitutive relationships. Although generality is a desirable quality, Hodges *et al.* [103] demonstrate that the computer implementation leads to many additional equations to incorporate the kinematics and constitution.

By representing the full three dimensional orientation of the beam exactly, the error inherent in approximating curvature is eliminated [102, 93]. The mathematics of three dimensional finite rotations complicates the implementation of GEBT in a

FEM framework [104]. This is due to the fact that rotations are not commutative[1] and do not admit a linear space[2] [104].

At this point, many of the issues associated with finite rotations have been solved [106]. The field of GEBT can be considered mature. Lens and Cardona [107] give an example of a modern computer implementation of GEBT that incorporates an interpolation and integration scheme that does not suffer from the problems of classic GEBT. The implementation in this work is similar. A detailed description of GEBT is deferred to the latter half of this section.

It should be noted that there exists an alternative representation that forgoes much of the complexity of finite rotations by using three three-dimensional orthonormal vectors for the state variables. These vectors describe the axes of the cross section orientation [108, 109]. These additional vectors lead to many redundant degrees of freedom. Betsch and Steinmann [109] use Lagrange multipliers to include the orthonormal constraints into the governing equations, leading to many more equations to solve than classic GEBT. Romero and Armero [108] incorporate the orthonormal constraints directly into the governing equations, maintaining the same dimensionality of classic GEBT. With Romero and Armero's approach, the state variables lose their ortho-normality when descretized and interpolated to intermediate locations. Due to a lack of ortho-normality or the additional complexity of solving more equations, these approaches were not pursued in this work.

Several comparisons have been made between the three different beam theories presented here. Overall, many authors report that locking is a major problem in ANCF beams [106, 110]. Locking occurs when the shape functions do not admit all the required deformation modes. Locking occurs in the other theories, however, simple solutions for both geometrically exact and co-rotational theories have been discovered [92].

Multiple locking issues with ANCF lead to the conclusion that twice as many degrees of freedom are required for ANCF to achieve the same accuracy as the GEBT [106]. Similarly, the article by Schwab and Meijaard [110] compared the co-rotational beam formulation with ANCF and found that alternative ANCF derivations using some subjective judgments are required to get similar accuracy in ANCF. A follow-

[1]To say that rotations are not commutative is to say a rotation of α then β is in general not the same as a rotation of β then α [105]. They are commutative only when α and β are co-axial [105].

[2]To say that rotations do not admit a linear space is to say that a rotation of α then β is in general not equivalent to a total rotation of $\alpha + \beta$ [105]. Only when α and β are co-axial can the total rotation be given by $\alpha + \beta$ [105].

up comparison was made by Dibold *et al.* [111] that refuted many of these claims. However, only the planar version[3] of ANCF was presented in this comparison. These simplifications lead to a very computationally efficient formulation. Furthermore, the comparisons were made with the analysis of cables exhibiting a significant magnitude of high frequency deformation modes.

The comparisons in the literature [106, 110, 111] demonstrate many inaccuracies with ANCF [106, 110] and generally find that the potential computational efficiency is only realized when simulating bodies with the flexibility of cables [111]. Within the co-rotational formulation, there is an element of subjective judgment when developing the strain energy equations [92]. This lack of objectivity detracts from this theory and so will not be used in this work. Due to the objectivity [92], overall accuracy [106] and computational efficiency [106] GEBT has been applied in this work.

Geometrically Exact Beam Theory

This section summarizes the GEBT original proposed by Simo [100]. Figure 2.2a shows the basic kinematic description of a geometrically exact beam. The first state variable is the position (ϕ) of the reference curve in the inertial reference frame at any given point in time and along any generalized position (s) along the curve. The second is the pseudo vector for the cross-section orientation (θ) in the inertial reference frame at any given point in time and position. The direction of the pseudo vector gives the axis of rotation, while the length is the angle in radians.

In geometrically exact beams there is a material reference frame (e_i) attached to the beam cross-section. The rotation tensor Λ rotates a vector from the cross-section reference frame to the inertial reference frame (E_i). The rotation tensor Λ can be determined directly from the orientation vector θ with equation (2.5). The n by n identity matrix is denoted by $\mathbf{I}_n$. The notation of $\beta\times$ is defined as a skew symmetric matrix based on the vector β as shown in equation (2.6).

$$\begin{aligned}\Lambda &= \exp\left(\theta\times\right) \\ &= \mathbf{I}_3 + \frac{\sin|\theta|}{|\theta|}\left[\theta\times\right] + \frac{1-\cos|\theta|}{|\theta|}\left[\theta\times\right]^2 \end{aligned} \tag{2.5}$$

[3]The planar version ignores twist, out-of-plane deformation and only rotation about the out-of-plane axis. Thus, only three modes of deformation are free in this version.

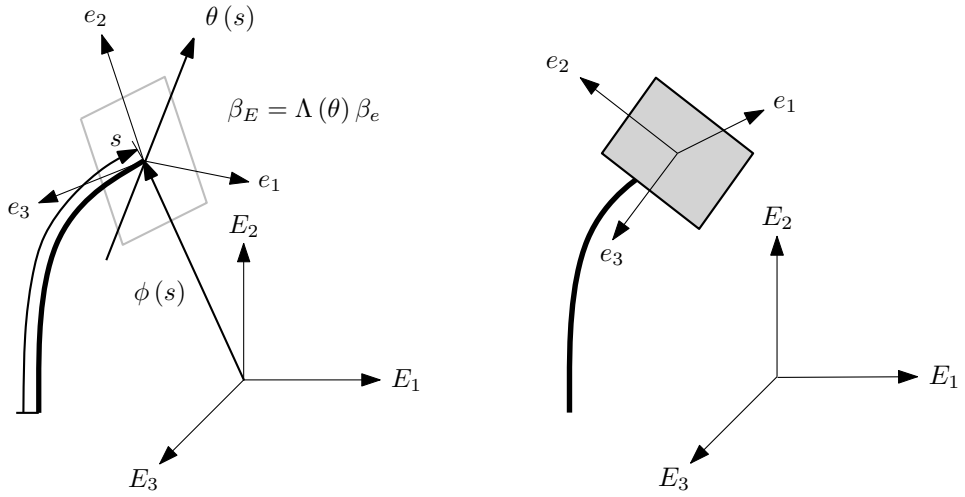

(a) Position and Orientation Kinematics

(b) Rigid and Normal Cross Section

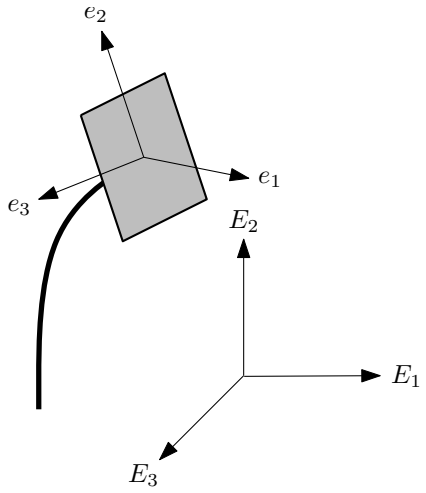

(c) Rigid Cross Section with Shear

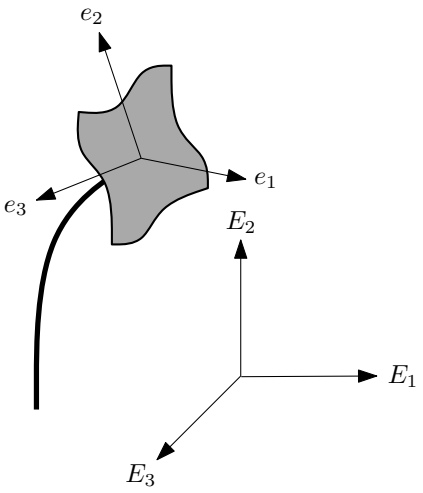

(d) Cross Section with Shear and Warping

Figure 2.2: Geometrically exact beam kinematics

$$\beta\times = \begin{bmatrix} 0 & -\beta_3 & \beta_2 \\ \beta_3 & 0 & -\beta_1 \\ -\beta_2 & \beta_1 & 0 \end{bmatrix} \tag{2.6}$$

Figure 2.2 shows various cross-section kinematics. If the Bernoulli assumption (rigid and normal cross-section) is applied, then the material reference frame is a Frenet frame of the reference curve as shown in figure 2.2b. If the normal assumption is relaxed to give a Timoshenko beam model, then the normal vector of the cross-

section no longer corresponds to the tangent vector of ϕ (thus e_i is no longer a Frenet frame), as shown in figure 2.2d. When the cross-section is assumed rigid, then the material never displaces within this frame. Consequently, the three dimensional strain can be derived based on the position and orientation of the cross-section alone and the problem is fully determined. Finally, if the rigid cross-section assumption is relaxed, the cross-section material is permitted to warp as shown in figure 2.2c. This introduces additional degrees of freedom that need to be constrained by the cross-section analysis. For this work Variational Asymptotic Beam Section (VABS) will be applied.

Simo [100] gives the governing equations in (2.7), where $\mathbf{R}$ is the residual; $\mathbf{n}$ and $\mathbf{m}$ are the internal force and moment stress respectively; $\bar{\mathbf{n}}$ and $\bar{\mathbf{m}}$ are the applied distributed forces and moments respectively. Note the d/ds denotes a square diagonal matrix where the derivative is taken at the diagonal. In a block matrix, an n by n matrix of zeros is denoted by $\mathbf{0}_n$; similar notation is used for vectors.

$$\mathbf{R} = \begin{bmatrix} \frac{d}{ds} & \mathbf{0}_3 \\ -\frac{d\phi}{ds}\times & \frac{d}{ds} \end{bmatrix} \begin{Bmatrix} \mathbf{n} \\ \mathbf{m} \end{Bmatrix} - \begin{Bmatrix} \bar{\mathbf{n}} \\ \bar{\mathbf{m}} \end{Bmatrix} \tag{2.7}$$

The strain energy function Ψ accounts for the blade material and structure. The Laplace of Ψ gives a linearized model relating internal stress and strain in equation (2.8).

$$\begin{Bmatrix} \mathbf{n} \\ \mathbf{m} \end{Bmatrix} = \begin{bmatrix} \Lambda & \mathbf{0}_3 \\ \mathbf{0}_3 & \Lambda \end{bmatrix} \left[\nabla^2\Psi\right] \begin{Bmatrix} \gamma \\ \kappa \end{Bmatrix} \tag{2.8}$$

For geometrically exact beam theory the strain measures in equation (2.9) define the deformation of the beam. The undeformed configuration is represented by Λ_0, ϕ_0 and θ_0.

$$\begin{aligned} \begin{Bmatrix} \gamma \\ \kappa \end{Bmatrix} &= \begin{Bmatrix} \Lambda^T \frac{d\phi}{ds} - \Lambda_0^T \frac{d\phi_0}{ds} \\ \Lambda^T \frac{d\theta}{ds} - \Lambda_0^T \frac{d\theta_0}{ds} \end{Bmatrix} \\ &= \begin{bmatrix} \Lambda^T & \mathbf{0}_3 \\ \mathbf{0}_3 & \Lambda^T \end{bmatrix} \begin{bmatrix} \frac{d}{ds} & \mathbf{0}_3 \\ \mathbf{0}_3 & \frac{d}{ds} \end{bmatrix} \begin{Bmatrix} \phi \\ \theta \end{Bmatrix} - \begin{Bmatrix} \Lambda_0^T \frac{d\phi_0}{ds} \\ \Lambda_0^T \frac{d\theta_0}{ds} \end{Bmatrix} \end{aligned} \tag{2.9}$$

Together with equation (2.7) we get the complete residual expression in equation (2.10) in terms of the the state variables ϕ and θ.

$$
\begin{aligned}
\mathbf{R} \;=\; & \begin{bmatrix} \frac{d}{ds} & \mathbf{0}_3 \\ -\frac{d\phi}{ds}\times & \frac{d}{ds} \end{bmatrix} \begin{bmatrix} \exp(\theta\times) & \mathbf{0}_3 \\ \mathbf{0}_3 & \exp(\theta\times) \end{bmatrix} \left[\nabla^2\Psi\right] \\
& \left(\begin{bmatrix} \exp(-\theta\times) & \mathbf{0}_3 \\ \mathbf{0}_3 & \exp(-\theta\times) \end{bmatrix} \begin{bmatrix} \frac{d}{ds} & \mathbf{0}_3 \\ \mathbf{0}_3 & \frac{d}{ds} \end{bmatrix} \begin{Bmatrix} \phi \\ \theta \end{Bmatrix} - \begin{Bmatrix} \Lambda_0^T \frac{d\phi_0}{ds} \\ \Lambda_0^T \frac{d\theta_0}{ds} \end{Bmatrix} \right) \\
& - \begin{Bmatrix} \bar{\mathbf{n}} \\ \bar{\mathbf{m}} \end{Bmatrix}
\end{aligned} \tag{2.10}
$$

GEBT relies on three dimensional orientation as a state variable. Several schemes have been presented in literature to represent these rotations [108, 109, 92, 105, 112]. There are two common approaches. The first approach is to represent the orientation with quaternion or pseudo vectors [92, 105, 112]. In either case, updating the state variable is complicated because rotations are not communicative and do not admit a linear space [104]. In both cases, a set of update formulas have be developed to transition from state to state [92, 105]. When applying these formulas, care must be taken to avoid singularities [105].

In finite element theory the state variables need to be interpolated to intermediate points. However, finite rotations do not admit a linear space [105]. To overcome this, several authors have proposed various interpolation schemes [104]. The original schemes by Simo and Vu-Quoc [100] suffered from a lack of objectivity and path dependence [113]. Jelenic and Chrisfield [114] developed a scheme that exhibited objectivity and path independence using a co-rotational approach. For each node an incremental orientation is defined and then interpolated.

For steady state simulations the angular velocity of the rotor is a specified constant and the inertial effects from rotation are represented as an external force dependent on radial position. This eliminates the need to resolve additional speed state variables and a variational for the kinetic energy. In these cases, the Newton-Raphson algorithm is employed to solve the state data. In this case, the matrix $\mathbf{K}$ is simply the tangent stiffness and the residual vector $\mathbf{r}$ is augmented with an extra term (r^l) for load control.

Load control is employed to determine solutions in the presence of structural instabilities (e.g. buckling). When load control is applied, the force vector is scaled by λ. The load parameter λ is an additional state variable governed by a user-specified load control equation. An example of a load control equation is given in (2.11). In

this example an outer iteration loop is needed to solve C such that λ is 1.0 for the final solution. For this work it is unlikely any structural instabilities will be encountered. For more information on load control the reader is referred to Krenk [92].

$$r^l = \mathbf{x}^T\mathbf{x} + C(\lambda^2 - 1) \tag{2.11}$$

2.2 Cross Section Analysis

The goal of cross section analysis is to develop a relationship between beam deformation and force measures. The classic approach is based on assuming that the cross section is a rigid plane, solving the strain field, solving the stress field and finally integrating to get the resulting force measures. Hansen [45] gives an example in wind turbine applications. Li [115] demonstrates this procedure for initially curved and twisted beams.

The rigid cross section assumption breaks down for anisotropic or heterogeneous beams [116, 91]. It is widely known that warping (both in-plane and out-of-plane deformation) will occur, affecting the overall force response. Resolving this warping is crucial for aero-elastic applications [91]. Hodges gives a review of many of the different methodologies for solving warping in beams [116]. One can group the different theories into two categories: the analytical or finite element approaches. The analytical approaches attempt to define an "equivalent" simple cross section for a given general cross-section and then apply detailed analytical analysis on the simple cross section [116]. These approaches lack the objectivity and generality inherent in the finite element approaches. It is for these reasons that none of the analytical methods were considered in this research.

When the beam is built with thin laminates, it can be analyzed with classical laminate theory [91, 117]. Jung *et al.* [91] gives a review of the different applications of classical laminate theory for cross section analysis. These approaches are based on the laminates being thin, an assumption that can break down in wind turbine applications near the root of the blade.

A novel approach is given by Malcom and Laird [38], using a three dimensional finite element model of a beam to extract equivalent beam properties. The approach relies on statistical methods to extract beam properties and suffer from uncertainty therein. For this research, this approach was not considered because of the uncertainty

in the analysis. Furthermore, the complexity and computational cost of developing a three dimensional model for every cross section evaluation is undesirable.

Finally, a notable example of the finite element based cross section analysis is given by Giavotto *et al.* [118]. The author applied virtual work principles to develop a variational for an infinitesimal section of the beam. The variational resulted in a second order homogeneous ordinary differential equation. The final solution is a series of Eigen functions. For practicality, the series must be truncated, with no way of determining what terms to truncate to achieve a desired level of accuracy. The presence of more rigorous approaches in the literature ruled out this theory from consideration. What is interesting about this theory, is it demonstrates how surface traction at the ends of the beam affect the warping solution, thus giving insight into the Vaslov beam theory [119, 120].

Hodges and Yu [121] recently introduced Variational Asymptotic Beam Section (VABS), a general finite element based cross section analysis tool for wind turbines. The theory of VABS was developed by Hodges [40] and colleagues [122, 123, 124] and is based on the Variational Asymptotic Method (VAM) [125]. Another notable contribution is by Popescu *et al.* [126], which shows how VAM could be applied to oblique cross sections. The theory is based on approximating the solution to the warping function with a finite element representation of the cross section. Minimizing the full variational for the cross-section requires solving a differential matrix expression. To simplify the problem VAM is used to neglect high order terms and then build up further approximations by adding the next order of terms. For a detailed explanation of the theory, refer to section 2.2.1.

Extensive validation has been performed for VABS making this a well-validated method to adopt. The work of Yu and Hodges [127] demonstrate that VABS can reproduce the well-known elasticity solutions for prismatic isotropic homogeneous beams. For more general anisotropic heterogeneous beams, Yu *et al.* [128] provided a comparison of VABS with three dimensional FEM models in ABAQUS, along with competing theories in literature. In all test cases there was excellent agreement between the VABS solution and the ABAQUS model. Furthermore, the authors demonstrated that the competing theories failed to resolve one phenomenon or another. These conclusions are reinforced by Volovoi *et al.* [129] demonstrating that traditional beam theory and VABS are sufficient for modeling heterogeneous anisotropic beams. Finally, the work of Hodges and Yu [121] validates VABS for wind turbine applications.

The work of Chen *et al.* [130] compared VABS with many available cross section analysis tools for several different types of beams. The comparison found that VABS gave excellent results in all comparisons. Many of the alternatives failed to consistently give reliable results. It is for these reasons that this research work is based on the theory of VABS.

2.2.1 Variational Asymptotic Beam Section Theory

The cross-section analysis involves the strain energy function Ψ. This function can be given in terms of continuum mechanics as shown in equation (2.12a). Note the definition in equation (2.12b) and the vector ε contains the components of the Jauman-Biot-Cauchy strain tensor as shown in equation (2.12c), where J is the determinant of the metric tensor (otherwise known as the Jacobian) and $\mathbf{D}$ is a tensor that relates the stress and strain tensors. The strain energy function includes all the geometric and material information for the beam cross-section.

$$\Psi = \frac{1}{2}\left\langle\left\langle \varepsilon^T \mathbf{D} \varepsilon \right\rangle\right\rangle \tag{2.12a}$$

where

$$\langle\langle \bullet \rangle\rangle \equiv \int_A \bullet \sqrt{J} dA \tag{2.12b}$$

and

$$\varepsilon \equiv \left\{ \begin{array}{cccccc} \varepsilon_{11} & 2\varepsilon_{12} & 2\varepsilon_{13} & \varepsilon_{22} & 2\varepsilon_{23} & \varepsilon_{33} \end{array} \right\}^T \tag{2.12c}$$

The continuum mechanics strain vector is related to the beam strain measures $\bar{\epsilon} \equiv \{\Gamma_1, \mathbf{K}^T\}$ and the cross-section warping w as shown in equation (2.13). Note that Γ_1 is extension strain and $\mathbf{K}$ contains the twist and bending strain measures. The vector θ is the pseudo rotation vector that describes the initial curvature.

$$\varepsilon = \mathbf{B}_a \mathbf{w} + \mathbf{B}_\epsilon \bar{\epsilon} + \mathbf{B}_R \mathbf{w} + \mathbf{B}_l \frac{d\mathbf{w}}{ds} \tag{2.13a}$$

where

$$\mathbf{B}_a \equiv \begin{bmatrix} 0 & 0 & 0 \\ \frac{\partial}{\partial x_2} & 0 & 0 \\ \frac{\partial}{\partial x_3} & 0 & 0 \\ 0 & \frac{\partial}{\partial x_2} & 0 \\ 0 & \frac{\partial}{\partial x_3} & \frac{\partial}{\partial x_2} \\ 0 & 0 & \frac{\partial}{\partial x_3} \end{bmatrix} \quad (2.13b) \qquad \mathbf{B}_\epsilon \equiv \frac{1}{\sqrt{J}} \begin{bmatrix} 1 & 0 & x_3 & -x_2 \\ 0 & -x_3 & 0 & 0 \\ 0 & x_2 & 0 & 0 \\ 0 & 0 & 0 & 0 \\ 0 & 0 & 0 & 0 \\ 0 & 0 & 0 & 0 \end{bmatrix} \quad (2.13c)$$

$$\mathbf{B}_R \equiv \frac{1}{\sqrt{J}} \begin{bmatrix} \theta_1 \left(x_3 \frac{\partial}{\partial x_2} - x_2 \frac{\partial}{\partial x_3} \right) & -\theta_3 & \theta_2 \\ \theta_3 & \theta_1 \left(x_3 \frac{\partial}{\partial x_2} - x_2 \frac{\partial}{\partial x_3} \right) & -\theta_1 \\ -\theta_2 & \theta_1 & \theta_1 \left(x_3 \frac{\partial}{\partial x_2} - x_2 \frac{\partial}{\partial x_3} \right) \\ 0 & 0 & 0 \\ 0 & 0 & 0 \\ 0 & 0 & 0 \end{bmatrix} \quad (2.13d)$$

$$\mathbf{B}_l \equiv \frac{1}{\sqrt{J}} \begin{bmatrix} 1 & 0 & 0 & 0 & 0 & 0 \\ 0 & 1 & 0 & 0 & 0 & 0 \\ 0 & 0 & 1 & 0 & 0 & 0 \end{bmatrix}^T \quad (2.13e)$$

To develop an accurate model for equation (2.12a), a solution for the warping function $\mathbf{w}$ is required. Finite element methods can be used to represent the warping as nodal displacements $\mathbf{V}$ and shape functions $\mathbf{S}$ on a two dimensional area mesh of the cross-section as shown in equation (2.14).

$$\mathbf{w} = \mathbf{S}\mathbf{V} \quad (2.14)$$

With this definition of warping, the strain energy function can be expressed as a quadratic equation, as shown in (2.15).

$$\begin{aligned} 2\Psi &= \mathbf{V}^T \left(\mathbf{E}_{aa} + 2\mathbf{E}_{aR} + \mathbf{E}_{RR} \right) \mathbf{V} + \frac{d\mathbf{V}}{ds}^T \mathbf{E}_{ll} \frac{d\mathbf{V}}{ds} + \epsilon^T \mathbf{E}_{\epsilon\epsilon} \epsilon \\ &\quad + 2 \left(\mathbf{V}^T \left(\left(\mathbf{E}_{a\epsilon} + \mathbf{E}_{R\epsilon} \right) \epsilon + \left(\mathbf{E}_{al} + \mathbf{E}_{Rl} \right) \frac{d\mathbf{V}}{ds} \right) + \frac{d\mathbf{V}}{ds}^T \mathbf{E}_{l\epsilon} \epsilon \right) \end{aligned} \quad (2.15a)$$

where

$$\mathbf{E}_{aa} \equiv \left\langle\left\langle \mathbf{S}^T \mathbf{B}_a^T \mathbf{D} \mathbf{B}_a \mathbf{S} \right\rangle\right\rangle \quad (2.15b) \qquad \mathbf{E}_{a\epsilon} \equiv \left\langle\left\langle \mathbf{S}^T \mathbf{B}_a^T \mathbf{D} \mathbf{B}_\epsilon \mathbf{S} \right\rangle\right\rangle \quad (2.15c)$$

$$\mathbf{E}_{aR} \equiv \left\langle\left\langle \mathbf{S}^T \mathbf{B}_a^T \mathbf{D} \mathbf{B}_R \mathbf{S} \right\rangle\right\rangle \quad (2.15d) \qquad \mathbf{E}_{al} \equiv \left\langle\left\langle \mathbf{S}^T \mathbf{B}_a^T \mathbf{D} \mathbf{B}_l \mathbf{S} \right\rangle\right\rangle \quad (2.15e)$$

$$\mathbf{E}_{\epsilon\epsilon} \equiv \left\langle\left\langle \mathbf{S}^T \mathbf{B}_\epsilon^T \mathbf{D} \mathbf{B}_\epsilon \mathbf{S} \right\rangle\right\rangle \quad (2.15f) \qquad \mathbf{E}_{RR} \equiv \left\langle\left\langle \mathbf{S}^T \mathbf{B}_R^T \mathbf{D} \mathbf{B}_R \mathbf{S} \right\rangle\right\rangle \quad (2.15g)$$

$$\mathbf{E}_{ll} \equiv \left\langle\left\langle \mathbf{S}^T \mathbf{B}_l^T \mathbf{D} \mathbf{B}_l \mathbf{S} \right\rangle\right\rangle \quad (2.15h) \qquad \mathbf{E}_{R\epsilon} \equiv \left\langle\left\langle \mathbf{S}^T \mathbf{B}_R^T \mathbf{D} \mathbf{B}_\epsilon \mathbf{S} \right\rangle\right\rangle \quad (2.15i)$$

$$\mathbf{E}_{l\epsilon} \equiv \left\langle\left\langle \mathbf{S}^T \mathbf{B}_l^T \mathbf{D} \mathbf{B}_\epsilon \mathbf{S} \right\rangle\right\rangle \quad (2.15j) \qquad \mathbf{E}_{Rl} \equiv \left\langle\left\langle \mathbf{S}^T \mathbf{B}_R^T \mathbf{D} \mathbf{B}_l \mathbf{S} \right\rangle\right\rangle \quad (2.15k)$$

The warping solution $\mathbf{V}$ is determined by minimizing equation (2.15a) with respect to $\mathbf{V}$ subject to the constraints given in equation (2.16). These constraints suppress rigid body displacement and axial rotation of the cross-section.

$$\langle\langle \mathbf{S}\mathbf{V} \rangle\rangle = 0 \quad (2.16a)$$

$$\langle\langle x_3 \mathbf{S}\mathbf{V}_2 - x_2 \mathbf{S}\mathbf{V}_3 \rangle\rangle = 0 \quad (2.16b)$$

Minimizing the full form of equation (2.15a) is a formidable task and is not necessary. Many of the parameters in equation (2.15a) are sufficiently small that they could be ignored. This is where the Variational Asymptotic Method (VAM) is applied. First, an ordering scheme is applied to identify the most significant terms. The truncated functional given in equation (2.17) is solved for the first approximation of $\mathbf{V}_0$.

$$2\Psi_0 = \mathbf{V}_0^T \mathbf{E}_{aa} \mathbf{V}_0 + 2\mathbf{V}_0^T \mathbf{E}_{a\epsilon} \epsilon + \epsilon^T \mathbf{E}_{\epsilon\epsilon} \epsilon \quad (2.17)$$

The simplified form in equation (2.17) allows for analytic optimization. The Euler-Lagrange equation for this problem is given in equation (2.18a).

$$\mathbf{E}_{aa} \mathbf{V}_0 + \mathbf{E}_{a\epsilon} \epsilon = \mathbf{H} \Upsilon \xi \quad (2.18a)$$

where

$$\mathbf{H} \equiv \left\langle \left\langle \mathbf{S}^T \mathbf{S} \right\rangle \right\rangle \tag{2.18b}$$

and Υ represents the null space of $\mathbf{E}_{aa}$ which corresponds to the constraints given in equations (2.16). The matrix ξ is a Lagrange multiplier used to enforce the constraint. Solving for ξ gives the problem in equation (2.19), which can be solved using standard methods of linear algebra.

$$\mathbf{E}_{aa}\mathbf{V}_0^\star = -\mathbf{N}^T\mathbf{E}_{a\epsilon}\epsilon \tag{2.19a}$$

where

$$\mathbf{N} \equiv \mathbf{I} - \Upsilon \left(\Upsilon^T \mathbf{H} \Upsilon\right)^{-1} \Upsilon^T \mathbf{H} \tag{2.19b}$$

The role of $\mathbf{N}$ ensures that the source term is orthogonal to the null space of $\mathbf{E}_{aa}$. This allows the matrix $\mathbf{E}_{aa}$ to be made invertible by adding $\Upsilon \otimes \Upsilon^T$ without affecting the final solution. In practice, however, round-off error can cause large errors if $\Upsilon \otimes \Upsilon^T$ is not sufficiently large. This problem is rectified by scaling this additional term to have the same trace as $\mathbf{E}_{aa}$.

The solution of (2.19a) may still violate equation (2.16). To enforce this constraint the solution is multiplied by $\mathbf{N}$ to get the final solution for $\mathbf{V}_0$

$$\mathbf{V}_0 = \hat{\mathbf{V}}_0\epsilon = \mathbf{N}\mathbf{V}_0^\star \tag{2.20}$$

This solution is used to give the first approximation to the strain energy in equation (2.21). Note that the $\mathbf{V}_0^T\mathbf{E}_{aa}\mathbf{V}_0$ is sufficiently small that it can be neglected. The term in the brackets gives the constitutive matrix for the beam.

$$2\Psi_0 = \epsilon^T \left(\hat{\mathbf{V}}_0^T\mathbf{E}_{a\epsilon} + \mathbf{E}_{\epsilon\epsilon}\right)\bar{\epsilon} \tag{2.21}$$

Improved solutions for the constitutive matrix can be achieved by perturbing the solution by V_1 and solving another variational. The second approximation is used to develop the generalized Timoshenko model, which will account for initial curvature and axial gradients of strain. This second model is much more complicated than the first approximation. The second order model was not extensively used in this work, and for the sake of brevity it will not be presented here. The reader is referred to Yu *et. al.* [131].

Neglecting the generalized Timoshenko model introduces a compatibility problem. The GEBT equations rely on a 6x6 constitutive matrix $\mathbf{C}$, while the first approximation (given in equation (2.21)) is based on Euler-Bernoulli strain measures. The constitutive matrix is augmented by giving large stiffness ($100C_{11}$) for the shear strain. With a large stiffness, the shear strain will approach 0 and the Euler-Bernoulli model is recovered.

Once the beam problem is solved, VABS can be used once again to determine the three dimensional strain of the problem. Equation (2.22) can be used to estimate the strain at any point in the cross-section. This three dimensional strain can then be used in any failure model to enforce stress and strain constraints.

$$\varepsilon = \left(\mathbf{B}_a \hat{\mathbf{V}}_0 + \mathbf{B}_\epsilon\right) \bar{\epsilon} \tag{2.22}$$

2.3 Aerodynamic Models

For wind turbine aerodynamics there are two established methods used in industry. The first is BEM theory and the second is grid-based CFD. BEM theory is accurate and efficient, but relies heavily on correction factors and can only simulate simple blade geometries. Section 2.3.1 presents a review of the BEM literature along with investigations that revealed how BEM can have multiple solutions and numerical instabilities that could be detrimental for design optimization.

Grid-based CFD can provide high fidelity solutions for wind turbine flows. These methods are based on creating a grid in the fluid domain and solving a discrete form of the governing equations (*e.g.* the Navier Stokes equations) [132]. These methods are attractive because they can simulate any blade geometry and provide high fidelity solutions. However, grid-based CFD is not well suited for efficient MDO. The computational demands are quite high and most of these methods require cluster computing just to obtain a single solution. Considering that unsteady loads are important in wind turbine design, these computational costs are further exacerbated by the need to perform unsteady analysis. For more information on grid-based CFD in wind turbine research see section 2.3.2.

Established aerodynamic methods are not suitable for efficient MDO of advanced blade designs. BEM does not have the fidelity, while grid based CFD is too expensive. To overcome this limitation a third option is needed. In the early years, the aeronautical industry successfully applied potential flow methods to design aircraft.

Several methods were developed from Nonlinear Lifting Line Theory (NLLT) to panel methods [133]. The simplest of these approaches is NLLT [134, 135, 136, 137] where sectional lift coefficients are used to calculate the bound circulation distribution on the blade. Several authors have applied this technique successfully to simulation wind turbines [138, 139, 86, 140, 141, 142, 143, 144, 145]. This theory is discussed in detail in section 2.3.3.

2.3.1 Blade Element Momentum Aerodynamics

The work presented in this section is adapted from a Wind Engineering publication by the author:

Michael McWilliam and Curran Crawford. The Behavior of Fixed Point Iteration and Newton-Raphson Methods in Solving the Blade Element Momentum Equations. *Wind Engineering*, 35(1):17–31, December 2010

This publication has contributed to further improvement in the BEM methods by Ning [146].

Blade Element Momentum (BEM) theory is widely used to model the aerodynamic performance of wind turbines. The efficiency of these methods has made them common in many design codes. Despite their inherent simplicity, these methods have proven reliable enough for design and certification. Consequently, there is still active research into design methods based on BEM theory [147].

Despite their widespread use, these methods have several shortcomings. Owing to the basic assumptions, they are not suitable for out-of plane blade geometry, like coning and wing-lets. Furthermore, the assumption of radial independence between the sections undermines their validity in unsteady flows. Thus, the methods are limited for modeling yawed flow and highly stalled conditions, often seen in turbine operation. Several models have been proposed in recent history to deal with these issues.

The work of Du and Tangler has addressed the problem of stall delay [148, 149]. Shen has provided alternative models for the tip loss effects [150]. Other researchers have focused more on problems regarding the momentum model. Chaney *et al.* developed a method for incorporating the effects of an expanding wake [151]. Madsen *et al.* compared BEM to actuator disc models to develop two correction models for deviations in the local power coefficients [152]. Haans *et al.* developed an advanced model

for yawed flow [153]. The work of Crawford gave a novel way of modeling coned rotors [154]. Finally, Sharpe incorporated wake rotation effects play in the axial momentum equations [155, 156]. Martinez *et al.* has used the momentum model developed by Sharpe, along with airfoil post stall corrections, to give improved predictions for stall regulated wind turbines [157].

Due to its efficiency, BEM theory is being applied in turbine optimization tools. Xudong *et al.* have successfully applied BEM based optimization to design several wind turbines of various sizes [63]. The early work of Fuglsang *et al.* created a MDO framework with BEM, structural and fatigue models. The objective was to minimize the cost of electricity, with sequential linear programming and the method of feasible directions [57]. The work of Clifton-Smith et. al. applied genetic algorithms with BEM to optimize energy capture and startup time [158, 74]. The work of Benini *et al.* is another example of applying genetic algorithms, in this case it was applied to the multi-objective optimization of a stall regulated wind turbine [66]. The work of Crawford *et al.* applied BEM with a generator model and a low frequency noise model to optimize the turbine for minimal cost of electricity and minimum energy pay back period, with gradient based techniques [65]. Another work by Crawford *et al.* applied gradient based techniques with advanced BEM methods to optimize a unique rotor design that had hinged rotor blades [26]. The importance of convergence is touched upon by Lanzafame, who demonstrated why sources of numerical instability must be reduced in optimization applications [73]. Similarly, the work of Hjort *et al.* showed how poor convergence introduces noise into the optimization. This noise compromised the gradient calculations, thus, undermining any gradient based methods in their study [64].

The typical approach to solving the momentum equations is to analytically reformulate the expression as a fixed point function. Here, the induction at a future iteration is expressed as a function of induction at the current iteration. For the basic BEM equations, this method is both fast and accurate. However, the benefits of a fixed point scheme are diminished in many of these advanced BEM models. The work by Crawford showed that applying the out-of-plane correction models in unsteady simulations slowed the convergence [27]. Furthermore, the implicit definition of induction in the momentum equations given by Sharpe makes it difficult to formulate a fixed point iteration function [155]. Thus, the fixed point iteration scheme may not be suitable as a general solver for all forms of BEM. It is clear that other

numerical techniques need to be investigated to enable the use of all advanced BEM based methods.

When a method is applied in an optimization application, the numerical method must be both stable and efficient for it to be practical [73, 64]. This defines the criteria for evaluating an alternative method. The Newton-Raphson technique has very fast convergence, however it also comes with known instabilities. Fortunately, these instabilities can be detected and dealt with by other methods. Overall, this section investigates numerical methods for solving the BEM equations. First, it explores analytically the predicted behavior of the BEM equations in section 2.3.1. The stability of two numerical methods is then quantified over a range of parameters in section 2.3.1, followed by recommendations for the application of these methods. Speed is not the focus of this investigation; the numerical methods under consideration are fast for most problems, thus we assume that each method already meets the efficiency criteria.

Blade Element Momentum Theory

The approach taken here explores a basic form of the BEM equations. This allows the major trends of the equations to be identified quickly and simply. The equations selected here will have a similar form to the more advanced forms that motivated this work. This similarity will make the conclusions drawn here applicable to other forms of BEM. Many of the conclusions from this study will apply to any monotonic momentum equation. The conservation of momentum requires any such model to be monotonic, hence, these conclusions are universal. Furthermore, only the axial momentum equation is explored, with a simple turbulent wake correction model. Neglecting the tangential component of BEM theory is justified since it has a small influence of the final solution.

The key parameter in solving the momentum equations is the induction at the rotor plane. This affects the angle of attack and all the aerodynamic forces on the blade. The induction solution is achieved when the thrust coefficient of the axial momentum equation (2.23) equals the thrust coefficient of the blade element equation (2.24).

$$C_{tm} = 4a\,(1-a) \tag{2.23}$$

$$C_{tb} = \sigma \left(\frac{W}{V_\infty} \right)^2 c_n \tag{2.24}$$

Both equations give the coefficient of thrust C_t, which is a non-dimensional thrust parameter. The induction is given by a; its effect on equation (2.24) is not obvious but will be shown in the definition of the terms in equation (2.24). The effect of blade size is captured in the solidity term (σ); this is the ratio of blade area to swept area. The effect of the airfoils is captured by the normal force coefficient; this parameter is found with equation (2.25). Here, the sectional coefficient of lift (c_l) and sectional coefficient of drag (c_d) are dependent on the angle of attack (α), which is the difference between the local flow angle (ϕ) and the twist angle (θ) - see equation (2.26) and figure 2.3. The local flow angle is governed by equation (2.27), where λ is the local speed ratio, which is the ratio of the blade speed to the undisturbed wind velocity. The effect of the rotors angular speed is captured by the velocity ratio (W/V_∞); this is the ratio of air speed relative to the blade, to the undisturbed wind speed. This parameter can be given in terms of model variables with either expression (2.28) or (2.29). For the remainder of the discussion, only the first version (2.28) will be considered.

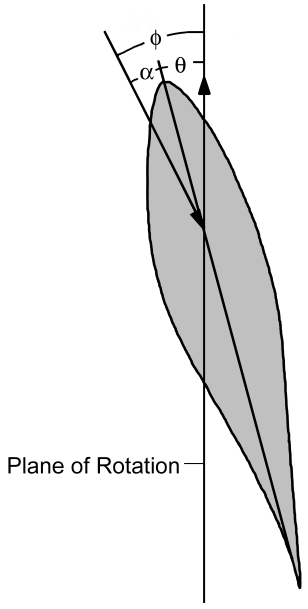

Figure 2.3: Geometric convention for blade element theory

$$c_n = c_l \cos\phi + c_d \sin\phi \tag{2.25}$$

$$\alpha = \phi - \theta \tag{2.26}$$

$$\tan\phi = \frac{1-a}{\lambda} \tag{2.27}$$

$$\frac{W}{V_\infty} = \frac{1-a}{\sin\phi} \tag{2.28}$$

$$\frac{W}{V_\infty} = \frac{\lambda}{\cos\phi} \tag{2.29}$$

The domain of the axial momentum equation (2.23) is limited to low values of thrust before a turbulent wake state is entered. When the thrust is too high, the turbulent wake function (equation (2.30)a) is used instead. The function given here is not strictly based on experimental data or models presented in literature, but selected for its simplicity to illustrate the numerics of the methods. The analytic study will not look at the turbulent wake state leaving its examination to the numerical study in section 2.3.1.

$$C_{tw} = \frac{5.2a + 0.8}{3} \tag{2.30}$$

These equations only give a summary of BEM theory for more details the reader is referred to Burton *et. al.* [156], Manwell *et. al.* [34] and Hansen [35].

Analytic Investigation of BEM Stability

The residual expression, equation (2.31), is given by subtracting equation (2.24) from equation (2.23). This equation is used by a Newton-Raphson iteration algorithm to find a solution for a. Numerical instabilities will occur when the slope of this equation approaches 0. The circumstances for this condition to occur can be investigated by differentiating equation (2.31), to yield equation (2.32).

$$R(a) = 4a\,(1-a) - \sigma\left(\frac{1-a}{\sin\phi}\right)^2 c_n \tag{2.31}$$

$$\frac{dR}{da} = \overbrace{4 - 8a}^{I} + \overbrace{\sigma \left(\underbrace{2\left(1-a\right)c_n}_{A} + \lambda \underbrace{\left(\overbrace{\frac{dc_l}{d\alpha}}^{i} \cos\phi + \overbrace{\frac{dc_d}{d\alpha}}^{ii} \sin\phi + \overbrace{c_d \cos\phi}^{iii} - \overbrace{c_l \sin\phi}^{iv} \right)}_{B} \right)}^{II} \tag{2.32}$$

Term I in equation (2.32) is the gradient of the momentum equation. This term is always positive for any realistic model, including turbulent wake models. The source of the instability is the blade element gradient, labeled as term II. An important property is that solidity acts as an amplifier for this term, thus any negative quantity for the right hand side of II can yield an instability if solidity is scaled properly.

Further insight can be gained by looking where the sum of terms A and B are negative. Term A accounts for the effect of changing W/V_∞. The first component of this term will only be negative when the turbine is reversing the flow. The second component has similar trends and will only be negative when the blade element is applying forces that accelerate the flow. Thus, this term can only contribute to instability when the rotor is operating in off-design conditions. For a well designed turbine, this instability is rare.

The B term accounts for variation in the blade force term. The first variable in this term is the local speed ratio. Like solidity, this term can be considered an amplifier. The remaining terms are dependent on the blade element state. Here the angle of attack has a strong influence. This would give strong coupling to the blade twist and local speed ratio. The first two terms account for the change in lift and drag coefficients. The remaining terms account for variation in the direction of blade forces.

The first term (i) shows that a negative lift slope can lead to instability. This will occur when the blade is stalling at either positive or negative angles of attack. The second term (ii) shows that variation in drag contributes to stability at positive angles of attack, and is detrimental elsewhere. The third term (iii) shows that the actual drag force has a stabilizing effect overall. The fourth term (iv) shows that the lift force can have a stabilizing effect at negative angles of attack, but introduce instability as the flow angle increases and lift forces are high.

The fixed point iteration function for the BEM equations is developed by assuming the flow angle is constant, then solving equations (2.31) for $R(a) = 0$. The fixed point iteration function for the version of BEM presented here is given in equation (2.33).

$$a_{i+1} = f(a) = \frac{1}{\frac{4\sin^2\phi}{\sigma c_n} + 1} \tag{2.33}$$

By explicitly defining induction as a function of blade conditions, the only source of instability is in the lift and drag response of the blade itself. A fixed point iteration will diverge whenever the gradient of the function $f(a)$ has a magnitude of 1 or greater. This condition was applied to equation (2.33) to define the conditions for stability given by equation (2.34). The reader should be aware that both equation (2.33) and (2.34) are invalid beyond the onset of turbulent wake conditions.

$$\begin{cases} \dfrac{dc_n}{d\phi} > \overbrace{\cos\phi c_n}^{I} - \overbrace{\left(\dfrac{\lambda^2 + (1-a)^2}{\lambda}\right)\dfrac{\left(4\sin^2\phi + \sigma c_n\right)^2}{4\sigma\sin^2\phi}}^{II} & \text{for} \quad \sin^2\phi\dfrac{dc_n}{d\phi} > \sin(2\phi)\, c_n \\ 0 < \left(4\sin^2\phi + \sigma c_n\right)^2 & \text{for} \quad \sin^2\phi\dfrac{dc_n}{d\phi} = \sin(2\phi)\, c_n \\ \dfrac{dc_n}{d\phi} < \cos\phi c_n + \left(\dfrac{\lambda^2 + (1-a)^2}{\lambda}\right)\dfrac{\left(4\sin^2\phi + \sigma c_n\right)^2}{4\sigma\sin^2\phi} & \text{for} \quad \sin^2\phi\dfrac{dc_n}{d\phi} < \sin(2\phi)\, c_n \end{cases} \tag{2.34}$$

The inequality given in equation (2.34) shows three conditions. Which equation is active is dependent on a domain constraint. The middle condition can be ignored, as this will only be active when turbulent wake conditions occur and this expression is not valid in any case. The left hand side of all the inequalities is dependent on the variation of the normal force coefficient. Note that $\frac{dc_n}{d\phi}$ is related to airfoil coefficients through equation (2.35). The right hand side of all the conditions is a function of the normal force coefficient. Inspection of equation (2.34) shows that the stability condition is similar to the domain constraint. This means it is likely that the favorable condition will be active, giving a bias towards stability.

$$\frac{dc_n}{d\phi} = \frac{dc_l}{d\alpha}\cos\phi + \frac{dc_d}{d\alpha}\sin\phi + c_d\cos\phi - c_l\sin\phi \tag{2.35}$$

Stability cannot be guaranteed however, since the first condition can be active whenever the normal force gradient is relatively large. Under these conditions, diver-

gence occurs when the normal force coefficient is still large enough that term II is similar in magnitude to term I. This may occur over a wide range of flow angles.

Another source of instability is in the turbulent wake functions. Each turbulent wake model can form a residual expression that could be solved to develop a fixed point function. For the turbulent wake model used here, the fixed point function resembled the quadratic formula. For the equation used in this study, the domain is bounded, and the range is unbounded. Both of these qualities would lead to a diverging solution. Other turbulent wake models would have a different form, with their own unique stability characteristics.

An important point to note is that in a Newton-Raphson iteration, the stability is independent of the momentum model, and strongly dependent on the airfoil characteristics. The stability characteristics of a fixed point scheme are far more complicated and unique for every momentum model or turbulent wake model.

Numerical Investigation of BEM Stability

To expand on the analytic investigation, a set of numerical results were analyzed. The first goal was to identify a) whether multiple solutions to the BEM equations could exist, then b) regions of numerical instability and finally c) how well these regions correlated with the angle of attack. The role of airfoil drag is debatable. Some researchers propose that it should not be used to determine the induction, since the effect of drag in the momentum balance is limited to a narrow region of the wake [34]. Other researchers assume an azimuthal averaged loss of momentum, that includes the effect of drag [27]. To explore the effect of these assumptions, a second set of data was generated, without using the drag coefficient.

The theory described in section 2.3.1 was implemented in a computer program. The theory has four independent variables: blade twist (θ), the local speed ratio (λ), solidity (σ) and axial induction (a). The first three variables are effectively design parameters fixed by section location, rotor speed and inflow conditions, while the last one is a state variable that would be iterated on by a numerical solver.

For a given set of design parameters, the code sampled induction values a between -0.25 and 1.0 inclusive with a step size of 0.001. From that, the code determined the values of equation (2.31) and equation (2.33) at each point. To evaluate stability, finite differencing was applied to obtain the slope of each equation. Locations where the sign

of the residual expression changed were counted as a solution to the BEM equation. These calculations were then applied over a large range of design parameters.

The code used the lift and drag data from eight S800 series airfoils (S801, S809, S810, S812, S813, S814, S815 and S825). The airfoils were chosen for the availability of experimental data over a wide range of angle of attack [159, 160, 161, 162, 163, 164, 165, 166]. A second set of data for a rough leading edge was also used for each airfoil. To prevent angle of attack domain errors, the airfoil data was extrapolated to $\pm 180^\circ$ using methods proposed by the National Renewable Energy Laboratory (NREL) [167]. This extrapolation is common practice in turbine design. Linear interpolation was applied for intermediate α points.

For every airfoil, both clean and rough, regardless of whether drag was used or not, there were regions within the design space where multiple induction solutions existed. Most had 3 unique solutions but some points had up to 5. The regions where multiple solutions exist is given by figure 2.4. Each contour plot is defined by two design variables, while the value is defined by the maximum number of solutions for all the points of the remaining design variable. Figures 2.4a through 2.4c are typical for most airfoils in the study. Here, the results show that the region of multiple solutions is nearly planar within the 3-dimensional space defined by the design parameters. In this region, the design parameters allow the blade element model to follow the momentum model. The BEM equations with the clean S812, rough S814 and rough S815 have multiple solutions over a much wider range of the design space. An example of this is given by figure 2.4d. Thus, no assumptions can be made on where multiple solutions will exist.

Figure 2.5a shows an example of how the thrust models varied with induction to produce multiple solutions. As expected, when multiple solutions occur, it is because the blade element model follows the momentum model for an interval. The slight variations in the airfoil data for this interval result in multiple solutions. The small slope of the residual function could produce unbounded results close to the solution. Figure 2.5b shows how the fixed point function would vary for the same point. As expected, the fixed point function lies on the $y = x$ line. Here, the slope is close to unity, consequently, the solver would exhibit either slow convergence, or divergence.

Neglecting drag in the calculations had little effect on the number of solutions found. Including drag merely altered the region in the design space where multiple solutions could be found. Inspection of these regions showed similar trends to those

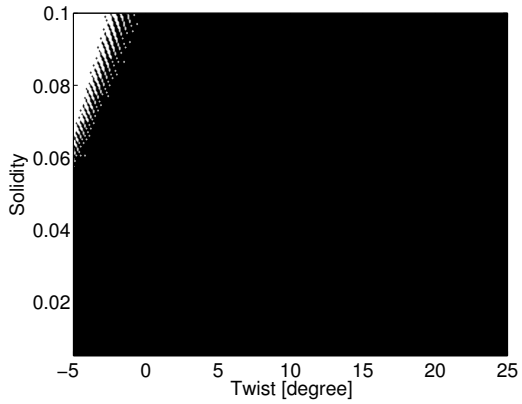

(a) Rough S809 with drag

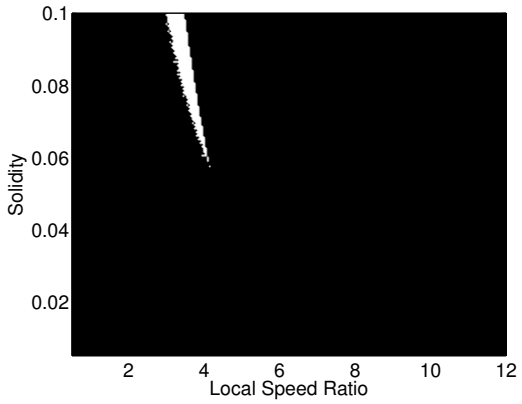

(b) Rough S809 with drag

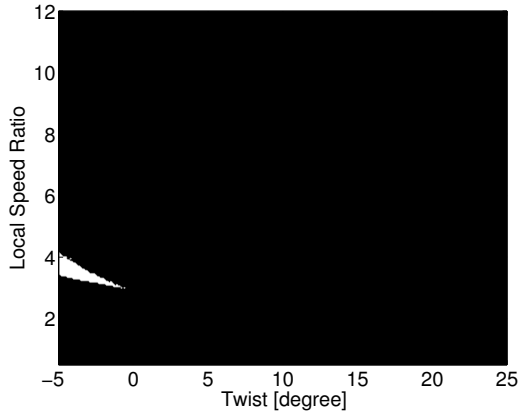

(c) Rough S809 with drag

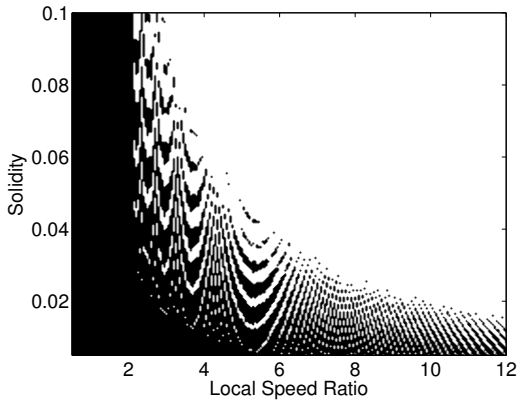

(d) Rough S815 with drag

Figure 2.4: Multiple solution counts over varying range of parameters (1 solution black, 3 solutions white)

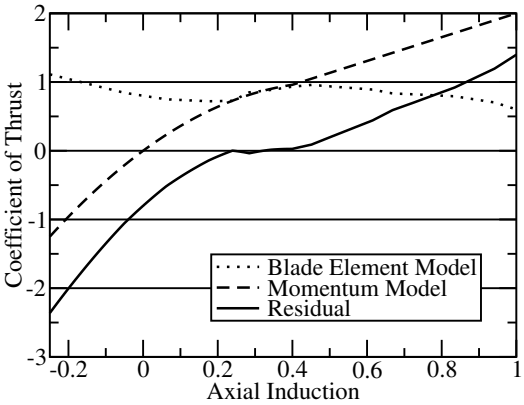

(a) Residual function

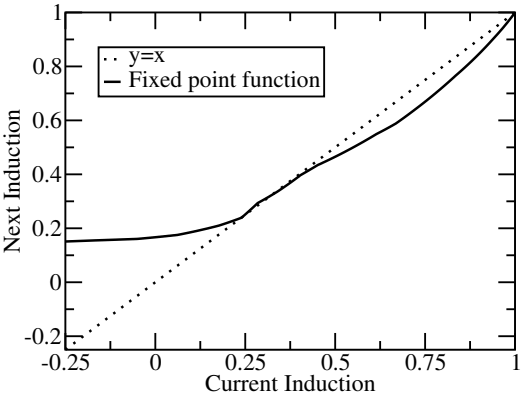

(b) Fixed point function

Figure 2.5: Example of multiple solutions; clean S809 airfoil with drag, $\sigma = 0.0945$, $\lambda = 3.05$ and $\theta = -5^\circ$

shown in figure 2.5. Accordingly, the effect of drag has a minor role in the existence of multiple solutions.

Overall, the blade element equation (2.24) is decreasing with increasing drag and lift, thus multiple solutions only occur when there is a decreasing lift coefficient from stall. The validity of the airfoil data here is in question. First, stall is known to give an unsteady force response. Second, the nature of stall can vary widely due to turbulence and various other conditions. Finally, for wind turbines in particular, the rotational effects are known to delay stall. Thus these regions of multiple solutions coincide with the regions of greatest uncertainty in the actual physics of the aerodynamic models.

Multiple solutions occur when the blade forces vary with induction, similar to how induction (from the wake structure) varies with forces. In other words, the magnitude and slopes are similar, for both the blade element model and the momentum model. Regardless of the uncertainty in the modeling, these situations could occur in reality. Under these circumstances, the induction is weakly dependent on the blade state and the induction would be more strongly affected by local flow conditions. For example, with all other things being constant, after a gust, the flow would settle into a low induction state, while after a lull, a high induction state. Similarly, variation in the stall forces would also cause changes in the induction state. This weak dependence could be a source of error and uncertainty in modeling turbines when the blades are stalling. Along the interval of multiple solutions, the range of induction is between 0.2 and 0.4, with a variation of lift coefficient between 0.7 and 1.0. This causes significant variations in the blade forces. Given the importance of using stall to regulate some wind turbines and in predicting loads during the turbulent conditions when stall is entered, this could be an important insight for the design of wind turbines.

A Newton-Raphson iteration scheme will produce unbounded solutions when the slope approaches 0. The fraction of points that had a residual slope magnitude less than 0.02 was used as a measure of instability. Similarly, when the magnitude of the fixed point function slope is unity or greater, the method will diverge. The percentage of points that exhibited this behavior was used as a measure of instability for the fixed point iteration scheme. Selected results are tabulated in table 2.1. Note the stability measures of each method are not directly comparable, as the nature of the instability is different.

To quantify the various effects present, the average stability of the appropriate set is given in table 2.2. From this data it is clear that the Newton-Raphson iteration stability is sensitive to grit roughness. This is expected, as a roughened leading

Table 2.1: Stability results for selected profiles

	Rough	Ignoring Drag	Mean Instability Newton-Raphson	Mean Instability Fixed Point
S825	Yes	No	14×10^{-6}	0.18
S809	Yes	No	50×10^{-6}	0.21
S813	Yes	No	329×10^{-6}	0.21
S815	Yes	No	414×10^{-6}	0.18
S809	No	Yes	472×10^{-6}	0.22
S813	No	No	840×10^{-6}	0.20
S825	No	Yes	858×10^{-6}	0.18

edge leads to a more gradual stall, confirming the analytical conclusion that this is beneficial to the stability of Newton-Raphson methods. Comparing the effect of including drag in the calculations shows that it has a minor role in stabilizing the calculations. Overall, the stability of the fixed point function has weak dependence on airfoil properties.

Table 2.2: Stability of selected data sets

Data Set	Mean Instability Newton-Raphson	Mean Instability Fixed Point
Clean Leading Edge	553×10^{-6}	0.20
Rough Leading Edge	270×10^{-6}	0.19
Using Drag	400×10^{-6}	0.20
Ignoring Drag	423×10^{-6}	0.20

The location within the design space where instability occurred is shown in figure 2.6. The figure shows contour plots for the Newton-Raphson stability measure. At each point within the contour plot, two design variables are fixed; the plotted value is the average stability for all points of the remaining free design variable. Drag was included in the calculations for all these results. Figure 2.6b shows that instability occurs in a small region defined by both the local speed ratio and solidity. This confirms the importance of these two parameters, as discussed in section 2.3.1. The remaining figures show that high twist is also associated with instability. Here, term A of equation (2.32) is starting to contribute to instability.

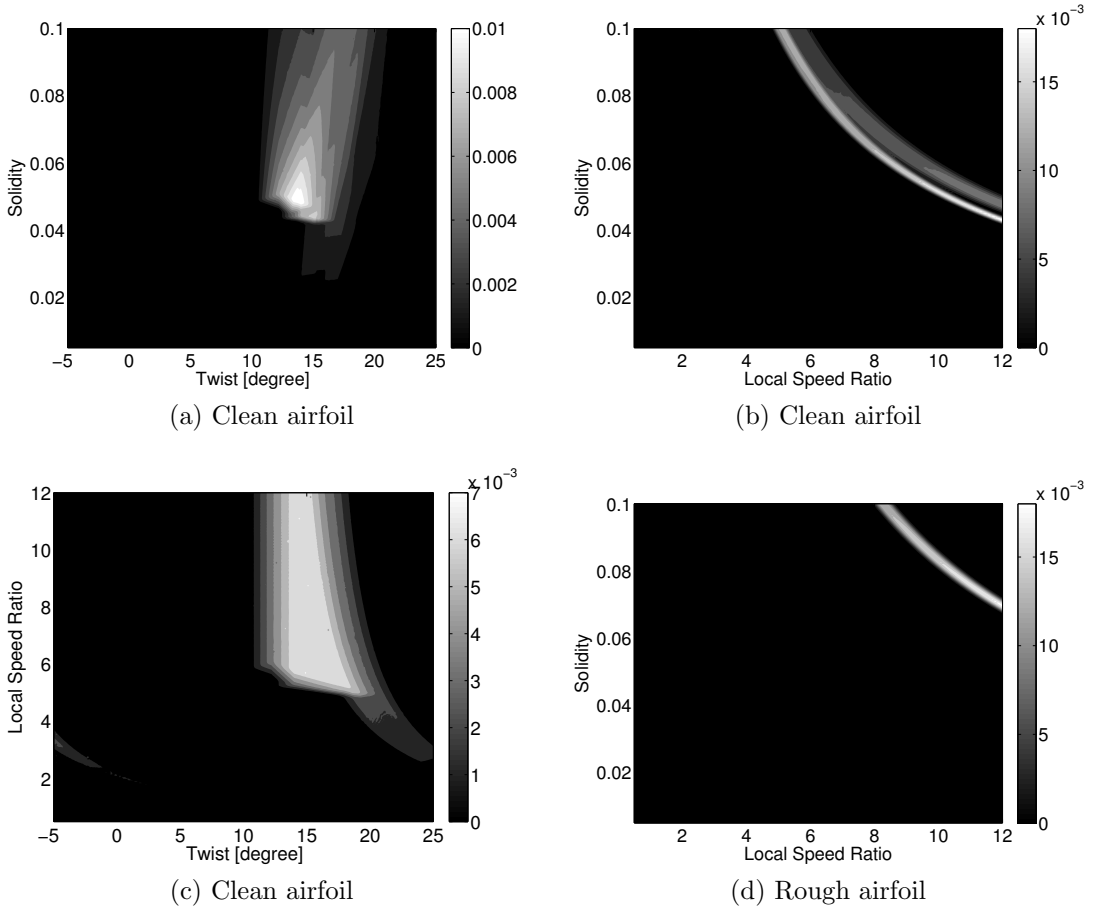

(a) Clean airfoil

(b) Clean airfoil

(c) Clean airfoil

(d) Rough airfoil

Figure 2.6: Mean stability measure for Newton-Raphson method with S813 airfoil

The results given in figures 2.6a through 2.6c are an example of relatively low stability. When the S813 profile has leading edge roughness, the stability improves significantly. The stability region of the roughened S813 profile with respect to local speed ratio and solidity is given in figure 2.6d. Here, the location of the instability is less broad, and shifted towards increased local speed ratio and solidity.

The regions within the design space where the instability occurs for the fixed point iteration function is given in figure 2.7. As before, each sub-figure is a contour plot showing the average stability across the remaining free variable. The plots shown here were generated with rough S813 data, and are typical for the other airfoils.

The results show that the fixed point iteration function has increased stability for small angles of twist and low solidity. The plot shows increased stability for low local speed ratios. When solidity or twist is also low, then increased stability is present at higher local speed ratios. This region of increased stability corresponds well to design

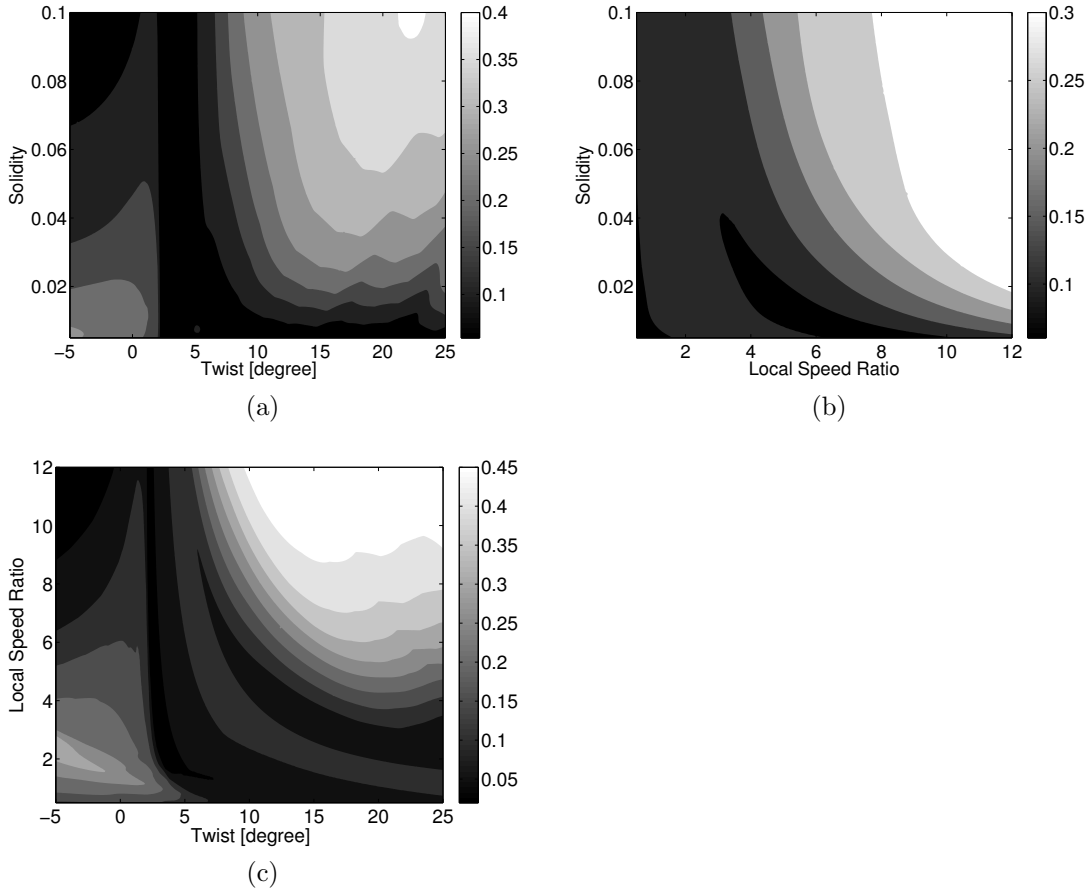

Figure 2.7: Mean stability measure for fixed point method with the rough S813 airfoil

parameters expected in well designed turbines. Despite the seemingly poor stability, this shows that a fixed point scheme is still acceptable for most design applications. However, it is common for most optimization algorithms to test areas in the design space far from the optimum. Accordingly, this algorithm may not be suitable for optimization applications.

To understand how airfoil data affected stability, the angle of attack where instability occurred was recorded for every case. Figure 2.8a shows the frequency of Newton-Raphson instability conditions at various angles of attack for the S813 airfoil. This figure is typical for other profiles. It is clear from these figures that there is a strong correlation to the angle of attack. This confirms that term B is dominant in equation (2.32). The greater frequency for negative angles of attack show that term A from equation (2.32) is also contributing to instability.

The frequency results for the roughened S813 are given in figure 2.8b. It is clear that instability is confined to specific angles of attack. The difference between clean

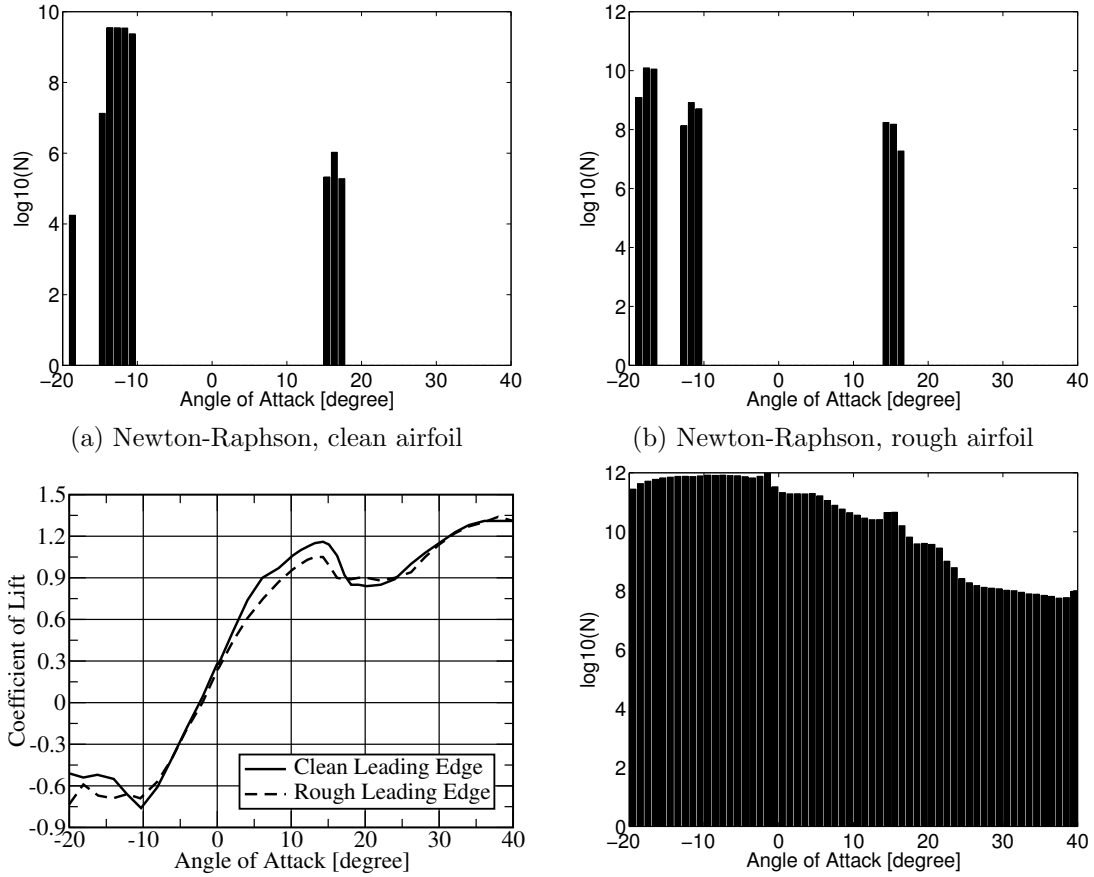

(a) Newton-Raphson, clean airfoil

(b) Newton-Raphson, rough airfoil

(c) S813 Lift Polar

(d) Fixed Point, rough airfoil

Figure 2.8: The frequency of instability for the S813 airfoil

and rough profiles is the magnitude of the frequency and more importantly, the angles where frequency is high. Referring to the lift polar given in figure 2.8c, it is clear that the high frequency of occurrences correspond with negative lift curve slope.

The data for the fixed point iteration scheme showed that the instability would occur for a wide range of angles of attack. The results for the rough S813 airfoil, including drag, are given in figure 2.8d. The instability is strongest for negative angles of attack. This would correspond with the instability region of large twist and high local speed ratio in figure 2.7c. It is important to note that the region of fixed point instability could not be correlated to airfoil polar data.

It was demonstrated in section 2.3.1 that for a Newton-Raphson scheme, the stability had a minor dependence on the momentum equation. Provided that this equation is monotonic, the same stability qualities will exist. Any momentum model

that is not monotonic with respect to induction, violates conservation of momentum, hence it is safe to assume that these stability characteristics are universal.

When applying a fixed point iteration scheme, several algebraic manipulations are applied to both the blade element model and the momentum model. A different fixed point function will be developed for each momentum model and choice of analytic manipulation. This fixed point function will then have its own unique stability characteristics. Thus, for the fixed point iteration scheme, it is difficult to draw any conclusions that apply universally.

The results here show that the Newton-Raphson iteration scheme is more stable for solving BEM equations than the more widely used fixed point iteration scheme. Yet, these results neglect the nature of the instability. The behavior at the instability has similar importance in selecting the appropriate numerical scheme.

When a Newton-Raphson scheme falls into an unstable region, an unbounded result is produced. This demands techniques for handling these exceptions. A common practice is to limit the maximum change in subsequent solutions. To prevent oscillations in the predicted solution, relaxation could be applied. The detriment here is the difficulty in creating an effective technique for handling these exceptions.

Alternatively, when a fixed point scheme is in an unstable region, it is unlikely to give an unbounded prediction. Instead, the scheme will bounce around a range of reasonable values. Under these circumstances, the common practice is to lag the solution after a given number of iterations. The detriment here is that many iterations must pass for these lagging methods to be activated. For a more unstable fixed point function, the method would be much slower.

In both methods, the algorithm must be able to detect when the method is failing and have techniques to handle these situations. The results here show that the stability of the Newton-Raphson scheme is tightly tied to the airfoil profile performance data, and is in a well defined region within the design space. This gives the algorithm many other possibilities to detect unstable regions for the Newton-Raphson scheme. Section 2.3.1 showed the difficulty in identifying the stability characteristics for a fixed point iteration scheme. For the fixed point function here, the user is forced to iterate a set number of times to detect whether the solution needs lagging. Thus, odd designs will significantly slow this method.

This author did not formally investigate any strategies to improve the stability. However, Ning [146] has taken this work further and developed strategies to eliminate the instabilities completely. The conventional BEM equations are based on two inde-

pendent variables (*i.e.* the axial and tangential induction). Ning showed you could cast the problem as a one dimensional parameter search over the flow angle. Guaranteed convergence is achieved through the intermediate value theorem, once two points with opposite sign in the residual are identified. In these cases, the solution is bounded by these two points and convergence is guaranteed merely by reducing this interval down to below the solution tolerance.

2.3.2 Grid-Based Computational Fluid Dynamics

Simulating wind turbines with grid based CFD is an active area of research. These methods are based on a mesh in the fluid domain and solving descretized partial differential equations (see Ferziger [132] for more details). The grid based approach has been applied to solve the Euler equations [69], vorticity transport equations [168] and the RANS equations [169] for wind turbine flows. Refer to White [170] for more information on these governing equations. These methods usually employ various schemes to resolve turbulence. The complexity of simulating turbulence has prompted some researchers to simply ignore it [168]. A more common approach is to apply simple eddy viscosity models [171]. When turbulent effects are important, researchers have applied Large Eddy Simulation (LES) [172]. Some researchers have successfully applied Direct Numerical Simulation (DNS) by using artificially high viscosity to limit the computational requirements in simulating the wind turbine. See Pope [173] for more details on various turbulence modeling techniques.

Grid-based CFD studies can be divided into two groups based on the focus of the research: far-wake flows and near-wake flows. The former group is focused on turbine wake interactions to maximize wind farm efficiency and to understand unsteady loading; the later research is more important for turbine design due to the focus of detailed flow phenomenon at the rotor [174].

One of the challenges in grid-based CFD is the computational effort required to get solutions. This can be controlled through different rotor representations [175]. The simplest is actuator disk models, where the rotor geometry is ignored and the rotor forces are smeared across a disk at the rotor plane. Sorensen *et. al.* [168] presents an actuator disk model based on the vorticity transport equations; the study investigated the different high thrust wake states. An interesting result was the simulation predicted that flow reversal would occur at thrust levels much lower than seen in experiments.

Actuator disk models cannot resolve finite blade effects, prompting much research into actuator line methods [176, 177, 172, 178]. Like the actuator disk models, the actuator line approach still ignores the detailed blade geometry. It differs from actuator disk models by concentrating the blade forces on a line where the blade would exist. Despite neglecting detailed geometry, the actuator line method requires a finer mesh at the actuator line to properly resolve the flow at the blade [178]. These models have lead to several detailed studies in wake aerodynamics. Ivanell *et. al.* [177] presented a DNS simulation with artificially high viscosity that captured the discrete vortex structure in the wake. Troldborg *et. al.* [172] developed an actuator line model with an LES model for turbulence. They investigated the effects of rotation speed on the wake stability and found high Tip Speed Ratio (TSR) lead to wake instabilities. Ivanell *et. al.* [176] used an actuator line model with LES to investigate the stability properties of the tip vortex.

The last class of grid-based CFD are those that resolve the detailed turbine geometry. These models are the most expensive because very small grid cells are required to resolve the boundary layer and a large domain is required to resolve far-field effects [175]. Gomez-Iradi [179] gives an early validation of this approach by simulating the NREL Phase VI rotor over a range of operator conditions. Later, Bechmann *et. al.* [180] simulated the MEXICO experiments over a range of operating conditions. Most of the grid-based CFD studies are focused on investigating three dimensional flow effects on the various wind turbine components. Johansen *et. al.* [181] used grid-based CFD to investigate the benefits of aerodynamic hubs. Johansen and Sorensen [182] used CFD to investigate the effects of wing-lets. Zahle *et. al.* used the overset grid method to investigate rotor-tower interactions. A common topic of study is the three dimensional flow field effects on airfoil loading. Hu *et. al.* [183] performed a numerical study on stall delay and validated this work with hot-wire measurements of a wind tunnel experiment. Johansen and Sorensen [169] developed a method for extracting aerofoil characteristics from three-dimensional flow solutions that can later be used in simple BEM models. Sorensen [184] developed a laminar-to-turbulent transition model for simulating boundary layer flows for wind turbines.

Due to the complexity of generating meshes and the computational requirements, these approaches are rarely seen in wind turbine MDO. One example is given by Kenway and Martins [185]; they employed MDO for site specific shape optimization with the Euler equations.

2.3.3 Lagrangian Vortex Methods

Theory of Lagrangian Vortex Methods

The aerodynamic models used in this research are part of a broad class of methods that will be referred to here as 'super-position methods'. Super-position methods are applicable to incompressible flows that exist at Mach numbers below 0.3 [170]. When a flow is incompressible, it is also divergence free [170]:

$$\nabla \cdot \boldsymbol{u} = \boldsymbol{0} \tag{2.36}$$

With the property in equation (2.36), vector identities can be used to derive the Poisson equation in equation (2.37) [186]:

$$\nabla^2 \boldsymbol{u} = -\nabla \times \boldsymbol{\omega} \tag{2.37}$$

Where the vorticity ($\boldsymbol{\omega}$) is defined in equation (2.38):

$$\omega \equiv \nabla \times \boldsymbol{u} \tag{2.38}$$

Given that equation (2.37) is linear, multiple elementary solutions can be combined in super-position [133]. Typically the elementary solutions used are based on Green's functions [186]. For flows with line vortices, this leads to the Biot-Savart law in equation (2.39) [133], which describes the influence of vortex filaments in the flow field.

$$\boldsymbol{u} = \frac{\Gamma}{4\pi} \int \frac{d\boldsymbol{s} \times \boldsymbol{d}}{\|\boldsymbol{d}\|^3} \tag{2.39}$$

These methods can be simplified further by assuming the flow is also irrotational as defined by equation (2.40) [133]. The irrotational assumption is not too restrictive considering that the vorticity only exists in a very small region defined by the wake of the wing.

$$\nabla \times \boldsymbol{u} = \boldsymbol{0} \tag{2.40}$$

This transforms equation (2.37) into a Laplace equation, where the solution can be described by a potential field [133]. Vorticity is still present in this formulation by assuming that it exists at the boundaries of this Laplace equation [133]. Potential flow leads to additional elementary solutions like sources and doublet's.

The Lifting-Line and Other Wing Representations

What differentiates the different super position methods, is the way that the lifting surfaces are represented. The simplest being lifting-line theory which has been used extensively in this research. Accordingly it deserves an expanded explanation.

Lifting line theory was first used by Ludwig Prandtl [134, 135]. It is based on the Kutta-Joukowski theorem in equation (2.41) that relates how the lift force (L) on the wing is related to a bound circulation (Γ_b) [133]). This allows the wing to be represented as a bound vortex with a given strength (Γ_b). This representation is acceptable for long slender wings with high aspect ratio.

$$L = \rho V \Gamma_b \tag{2.41}$$

Given that circulation is a conserved quantity [170], this generates trailed vorticity in the wake as it varies along the span (see equation (2.42)) [133]. For unsteady flows, additional shed vorticity is generated due to the temporal change in bound vorticity. The work presented in this research focused on steady flows, hence shed vorticity will be ignored.

$$\Gamma_t = \frac{d\Gamma_b}{ds} \tag{2.42}$$

Lifting line theory uses the Biot Savart law in equation (2.39) to determine how the vorticity in the wake induces the flow near the lifting line. The problem is closed by the fact that this induced flow dictates the magnitude of the bound circulation.

The different lifting line methods vary by how the induced flow is used to define the bound circulation. In the original work by Prandtl, a Dirichlet boundary condition was used to enforce no flow passing through the wing at the 1/4 chord position [133]. Prandtl ignored the influence caused by the bound vortices, this limited the theory to wings without sweep or dihedral. Later, Weissenger extended this theory by using the same boundary condition, but moving the control point to the 3/4 chord position [136]. At this position, the control point is affected by the bound vorticity, which made the approach applicable to wings with both sweep and dihedral [136]. These two approaches led to simple models that could be solved analytically with series solutions.

The Dirichlet boundary condition is only acceptable when the wings are at small angles of attack, where stall and other inviscid phenomenon is negligible. A more

modern adaption is given by Phillips and Snyder [137], where the sectional lift coefficients (c_l) are used in conjunction with Kutta-Joukowski theorem to define the bound circulation in equation (2.43). This creates a nonlinear lifting line model where the induced velocity is used to calculate the angle of attack. The angle of attack then defines a sectional lift coefficient, which gives the bound circulation. The effects of stall and other inviscid phenomenon are incorporated through the sectional lift coefficients when they are based on either experiments or numerical methods that include viscous effects. Phillips and Snyder show that this method is acceptable for problems with multiple lifting surfaces that have both sweep and dihedral, making this a general method for simulating systems of slender wings [137].

$$\Gamma_b = \frac{cc_l\|\boldsymbol{w}\|}{2} \tag{2.43}$$

A notable example of the Phillips Snyder model is given by Fluck and Crawford [187], where it was applied to bird wings to evaluate how tip feathers limit induced drag. The lifting line model was composed of multiple branching line segments to represent the main wing and the tip feathers. Viscosity effects were incorporated by using experimentally measured sectional lift coefficients. Despite the complexity of the bird wings the authors were able to demonstrate excellent agreement with experiments.

Lifting line methods are limited to wings with high aspect ratios. For low aspect ratio wings, one needs to take into account the distribution of loading along the chordwise direction. This is achieved by replacing the single bound vortex with a lattice of vortices distributed along the mean chord line. Each of the vortex elements in the wing have their own independent strength, which is controlled by multiple control points on the wing surface [133]. This method is similar to the lifting line method in that the influence of the vorticity from both the lifting line and wake are used to calculate the flow at the lifting surface. Then, the circulation strength is based on Dirichlet boundary conditions applied to control points on the wing [133].

To consider the effect of wing thickness, one can turn to panel methods [133]. Panel methods are based on a set of source and doublet entities distributed across the wing. The source terms will push the flow out to create a region that is not penetrated by the flow. In panel methods, the Dirichlet boundary condition is applied at the surface of the wing. As before, superposition is used to determine the effects of the wake and

wing, which in turn, are used to determine the strength of the sources and doublets [133].

Wind turbine blades are based on long slender wings with high aspect ratios. The extra complexity of either lattice or panel methods is unlikely to give significantly improved solutions. The lifting line methods used in this research are based on the lifting line theory of Phillips and Snyder [137]. Figure 2.9 shows an example of a free-wake lifting line code to simulate a wing and a wind turbine. The wind turbine simulation had three blades, but only one is shown for clarity. The cylinders in figure 2.9b indicate the starting location of a semi-infinite vortex cylinder model.

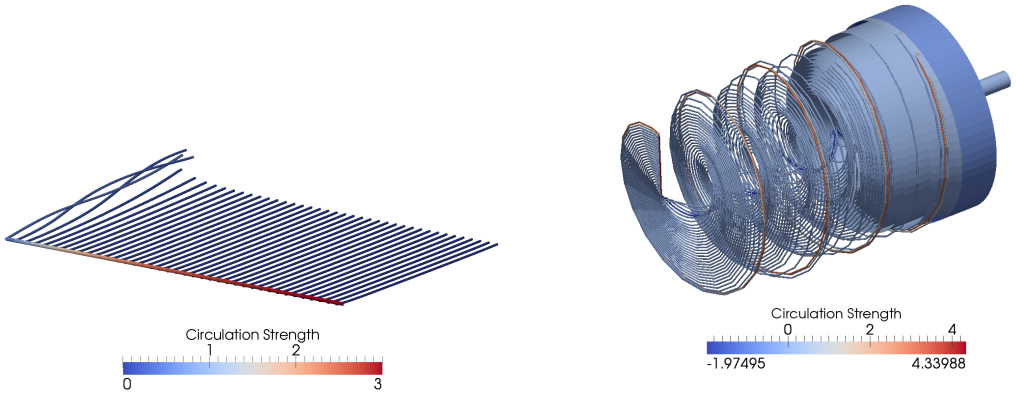

(a) Elliptical Wing (b) Wind Turbine

Figure 2.9: Visualizations of FEM based LVD simulation results

Free-Wake Representations and Instabilities

All the super-position methods depend on some sort of geometric representation of the wake. Most of the classic methods assume a flat vortex lattice system aligned with either the chord direction or undisturbed flow direction [133]. For simple wings, this representation gives good results [133]. By ignoring the flow effects on the wake, one could develop efficient analytical solutions to the bound vortex system [134, 135, 136], or simple nonlinear systems that can easily be solved with Newton iteration [133].

In reality, the vorticity in the wake is a material element and will follow the flow-field [186]. These effects become important when considering novel geometry like wing-lets, or large deflections associated with flexible blades. All the classic super-position methods can be improved by letting the wake evolve with the flow field. These versions are often referred to as 'free-wake' or 'force-free wake' models. This introduces a new complexity to the problem: the position of the wake is dependent

on the local flow field in the wake; which is in turn dependent on the position of the vorticity in the wake. Solving this circular dependency is the greatest challenge in free wake super-position methods.

Typically, this circular dependency is resolved using a time marching algorithm (otherwise known as a fixed point) [133, 188]. At each time step the influence is calculated at all the control points in the wake, then based on that influence and a numerical advection scheme (*e.g.* first order forward Euler in equation 2.44), the wake positions are updated for the next time step. When a steady state solution is desired, the same time marching algorithm is used. In this case it evolves in pseudo time where shed vorticity is ignored and updates to the bound circulation strength apply to the whole wake immediately. A steady-state solution is achieved when changes in state between iterations falls below a specified tolerance. This is referred to as an iterative convergence criteria.

$$\boldsymbol{x}_{i+1} = \boldsymbol{x}_i + \boldsymbol{u}_i \Delta t \tag{2.44}$$

Free-wake models take considerably more computational effort to solve than fixed wake models. This is because every control point in the wake requires an influence calculation from every other element in the system. This leads to a $O(N^2)$ computational scaling. This can be improved to $O(N \log N)$ by lumping distant vortex elements with the fast multi-pole method [86, 87].

All the free-wake methods in the literature known by this author apply a time marching algorithm [86, 87, 145, 189, 190, 191, 192, 188, 140, 141]. This highlights the uniqueness of the FEM-based LVD contribution given in chapter 3. This approach manages to solve the free-wake configuration without time evolution. It introduces a new way of accelerating the influence calculation by lumping the control points in the wake. The details of this model will be deferred to chapter 3.

Time evolution is complicated by the many instabilities in the wake. The first difficulty is the fact that point vortices and vortex sheets are singular at the core [192, 133]. Without careful treatment a wake element can get too close to the core of another vortex element and be pushed into highly distorted and unrealistic configurations [193]. This singularity can be eliminated by considering that viscosity will distribute the vorticity. These core flows are typically based on simple models. One example is given by Van-Garrel [145], who solved the induction from a simple line element in figure 2.10, with equation (2.45). Equation (2.45) is based on the ana-

lytical solution to (2.39) for a line element, this analytical solution is given in Katz and Plotkins [133] and is simplified further by Phillips and Snyder [137]. Van-Garrel incorporated a core model by adding a core radius term (d_c) in the denominator, eliminating the singularity. The Van-Garrel kernel function is used extensively in this research. Other kernel functions exist that employ different core models, these alternative models were not explored in this work because the effect of the core model was considered secondary compared to the challenge of adapting LVD for optimization.

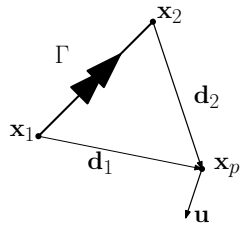

Figure 2.10: Vortex line geometry

$$\boldsymbol{u} = \frac{\Gamma\left(\|\boldsymbol{d}_1\| + \|\boldsymbol{d}_2\|\right)(\boldsymbol{d}_1 \times \boldsymbol{d}_2)}{4\pi\left(\|\boldsymbol{d}_1\|\|\boldsymbol{d}_2\|\left(\|\boldsymbol{d}_1\|\|\boldsymbol{d}_2\| + \boldsymbol{d}_1 \cdot \boldsymbol{d}_2\right) + \left(d_c l\right)^2\right)} \tag{2.45}$$

The instabilities are not limited to just the kernel function. Pure vortex systems are fundamentally chaotic [186]. Furthermore it is known that helical vortex structure (*i.e.* a wind turbine wake structures) can be unstable under different conditions [144, 143, 176]. This has lead to many studies into the stability. Okulov [144] has analytically derived the stability criterion for helical vortex structures with arbitrary number of filaments. Walther *et. al.* [143] gives a numerical investigation where the stability is evaluated based on the vortex pitch, core radius, and the wave number of the perturbation. They concluded that all helical vortex systems will become unstable when the core growth causes the helical vortices to merge (this leads to a Kelvin-Helmholtz instability [186]). Ivanell *et. al.* [176] performed a similar study with grid-based CFD simulation with a LES model for the turbulence. They found the turbulence intensity has an effect on the stability.

These instabilities are problematic for time-marching algorithms because the evolution automatically inherits the natural chaos associated with vortex systems [186]. Many authors have noted the difficulty of obtaining converged solutions due to these instabilities [191, 192, 190, 189, 82, 83]. One could argue given that chaos is natural to vortex flows, that these instabilities should be considered part of the solution. How-

ever, the numerical error caused by the discretization (in both time and space) acts as a perturbation that would not exist in reality [189]. Investigations into the stability of numerical vortex systems have concluded that this numerical error amplifies the chaotic motion beyond levels seen in experiments [189].

This problem has prompted many authors to explore higher order advection schemes. The first was Bagail and Leishman [189], who developed a high order scheme that uses numerical damping to attenuate the high frequency disturbances. Later, Bhagwat and Leishman [190] created a pseudo implicit scheme based on a predictor-corrector approach. Recently, Lawton and Crawford [87] have developed a second order viscous splitting algorithm. Ramos-Garcia *et. al.* [191] successfully applied the Adams-Bashforth algorithm along with the Adams-Bashforth-Moulton predictor-corrector algorithm. Each of these methods are explicit; further improvements could be made by employing implicit methods like the Crank-Nicholson scheme developed by Lawton and Crawford [194].

The difficulties of evolving vortex systems in time highlights the value of the FEM-based LVD contribution presented in chapter 3. By avoiding time evolution, it avoids the problems of instabilities.

Lagrangian Vortex Methods in Wind Energy

Many of the Lagrangian vortex methods have been successfully applied to simulate wind turbine flows. Chattot [77] used a lifting line model with a prescribed wake to optimize the power of wind turbine subjected to a thrust constraint. This work demonstrated the advantages of vortex methods over BEM by showing that the optimal vortex solution will locally exceed the Betz limit, but still preserve the limit over the whole rotor disc.

Lee [142] notes that BEM is not suitable for non-straight blades. In this work, a lifting line model was used for inverse design, where the flow behavior is specified and the lifting line model is applied to calculate the blade shape to produce that behavior. The wake in this model was still constrained, but varied the pitch based on the coefficient of power.

The conventional LVD model used in this research is similar to the free-wake lifting line model given by Van-Garrel [145]. The model developed by Van-Garrel used the core model given in equation (2.45) and evolves the wake with a time marching algorithm using first order forward Euler shown in equation (2.44).

Despite the instabilities, the time marching algorithm is well suited for simulating unsteady flows. This effect is more pronounced in floating offshore wind turbine application due to wave motion being amplified at the rotor. This will produce irregular shaped wakes that cannot be properly resolved with BEM theory. This prompted Sebastian and Lackner [188, 195, 196] to develop a lifting line code specialized for floating offshore applications. An interesting result of this research is that the authors were able to show a wind turbine could extract wave energy due to this motion.

Lifting line models are also well suited for simulating novel blade geometries. An example of this is given by Maniaci [192], where a lifting line model with distributed vortex elements in the wake was used to explore winglet design. This work is unique in the use of distributed vortex elements, which distribute the vorticity over a surface. The advantage here is improved solutions to the induced velocity on the blade and the vortex singularity associated with line elements is eliminated.

Many of the other super-position methods have been successfully applied to wind turbine flows. Dossing [141] used a vortex lattice and a panel method with a free-wake to explore the effect of winglets on wind turbines.

Another example is an aero-elastic panel method by Roura *et. al.* [140]. The wind turbine blade was rigid, structural deflections were incorporated into the model using a stiff hinge at the root to introduce a flapping and torsion motion.

A common misconception with super-position methods is that viscous effects are ignored. However, in many cases, the important effects can be included through models. Ramos-Garcia *et. al.* [191] shows how the effects of the boundary layer can be incorporated into a panel method for wind turbine simulations. The effect of the boundary layer is to displace the inviscid flow away from the surface. A boundary layer model is used to calculate the displacement thickness, then the control points of the panel method are shifted up to the boundary surface between the viscous and inviscid flows.

Schmitz and Chattot [197] developed a coupled Navier-Stokes/Vortex-Panel solver. A grid-based CFD code is used to solve the Navier-Stokes equations near the blade. Then outside the grid-based CFD domain, a panel method is used to simulate the wake flow. This approach is able to go beyond viscous-inviscid matching because it is able to resolve the effects of stall that are important when turbines are operating at low tip speed ratios.

All of these approaches rely on incorporating an additional model to account for the effect of viscosity. However, super-position methods can be developed to im-

plicitly resolve viscous effects [186]. Taking the curl of the Navier stokes equations yields a transport equation for vorticity that includes a diffusion operator dependent on viscosity [186]. This diffusion operator can be transformed into a Lagrangian representation for vortex particles, which is referred to as the particle strength exchange method [186]. This approach leads to a super-position method with fidelity comparable to Navier-Stokes based CFD.

One example of a high fidelity vortex method applied to wind turbine flows is given by Chatelain *et. al.* [198]. The model uses vortex methods to give a solution to the Navier-Stokes equations. Unlike grid-based approaches, this model uses Lagrangian vortex particles to simulate the flow. A Lagrangian update is used to solve the advection. The influence calculation is replaced by a Eulerian fast Poisson solver. This model is capable of LES since vortex elements naturally resolve the large scale turbulent fluctuations, then a particle strength exchange model resolves the sub-grid turbulence.

Limitation of Conventional LVD

Initially, the conventional LVD model used in this research was based on *libAero* developed by Cline and Crawford [86] and later improved by Lawton and Crawford [87]. The model uses the lifting line representation developed by Phillips and Snyder [137] and the free-wake model developed by Van-Garrel [145]. Like similar codes, this model was affected by the natural instabilities inherent in vortex methods, which had an adverse effect on the sensitivity analysis.

Lawton and Crawford [82] explored both the finite differencing and complex step gradient algorithms for LVD. Both of these methods are based on perturbing the design vector and calculating a new solution for comparison. Figure 2.11 shows the histogram of gradient values for the same design variable and the same simulation. The different gradient values are from taking gradients at different iterations in the simulation. This shows that both the gradient algorithms had significant variation from one iteration to the next and the mean of the two algorithms differed considerably.

Figure 2.12, given by Lawton and Crawford [82], shows that this variation is not due to the convergence of the simulation but to the chaotic evolution of vortex systems.

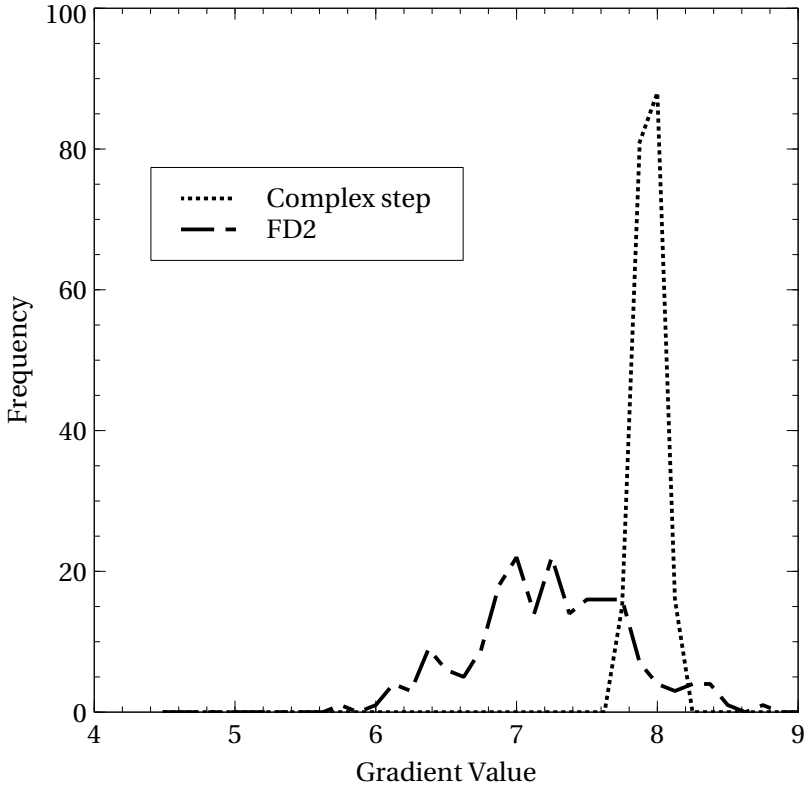

Figure 2.11: Variation in design sensitivity [82]

The challenges of consistently obtaining accurate gradients is tied to the uncertainty of iterative convergence metrics and the chaotic evolution of vortex systems. This is discussed further in section 3.2.1 in chapter 3. In aero-elastic applications, the motion of the blade adds to the instability further degrading the robustness of the gradients and compromising the convergence of the optimization, this is discussed in greater detail in section 5.4 of chapter 5.

2.4 Optimization Methods

For this work, the role of the optimization algorithm is to determine the design parameters that minimize a cost function subject to a set of constraints. The selection of the algorithm is dependent on the nature of the objective function. In a noisy space the objective could exhibit many local minima. In these circumstances, heuristic algorithms (*e.g.* evolutionary algorithms and simulated annealing) work well because they sample regions far from the best known solution in trying to improve [199]. This

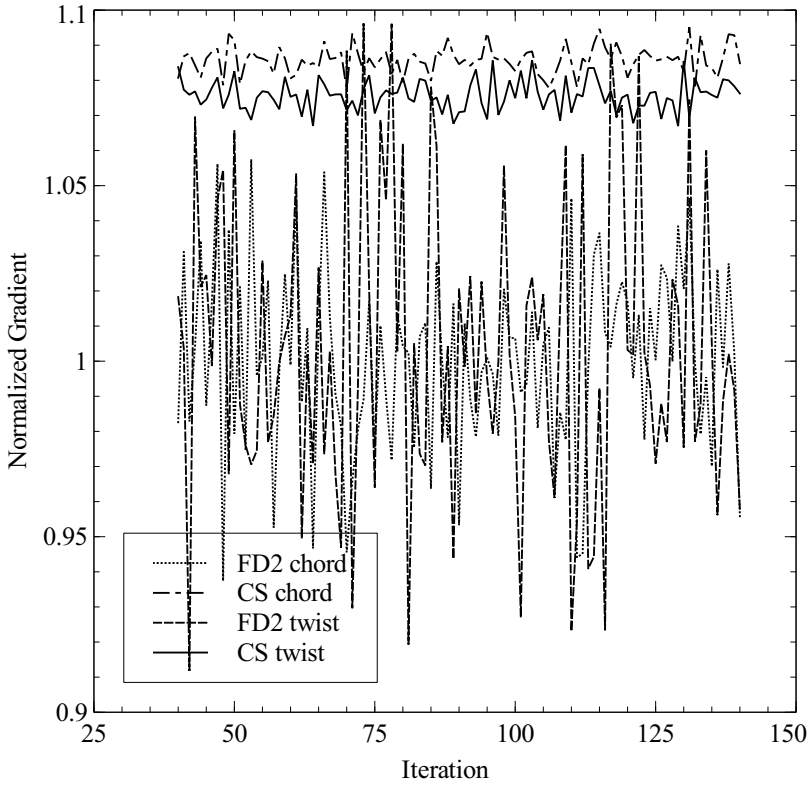

Figure 2.12: Gradient value vs. Iteration [82]

robustness comes at a cost. Typically these algorithms require many more function evaluations than gradient based methods. Consequently, this work will apply gradient based methods.

Gradient based methods use gradient information to determine the direction to search for the optimal solution [200]. Once a direction is known, a one dimensional line search is used to find the optimal solution [200]. Introducing constraints require more sophisticated algorithms. The one being used in this research is Sequential Quadratic Programming (SQP) [200]. The algorithm will use subsequent function evaluations to build an estimate of the Hessian matrix. When the Hessian is sufficiently built up, the algorithm approaches second order convergence [200]. In SQP the constraints are represented by linear functions. The reader is referred to Vanderplaats [200] and Hestenes [201] for more reading on optimization algorithms for structural applications. The SQP algorithm used in this work has been developed by Lawrence *et al.* [202], this implementation is referred to as the CFSQP algorithm.

2.4.1 MDO Optimization Frameworks

Two optimization frameworks were used in this work. The first is called Single Discipline Feasible (SDF), the algorithm is given in figure 2.13a. In the analysis stage of SDF only one discipline is considered at one time. This creates two optimization loops where only design parameters specific to a particular discipline are optimized at any given time. The alternative is to employ the Multiple Discipline Feasible (MDF) as shown in figure 2.13b. In this algorithm, both aerodynamic and structural disciplines are considered simultaneously. In the analysis, a full aero-elastic solution is achieved in a nested iteration loop. All the design parameters are considered in the outer optimization loop.

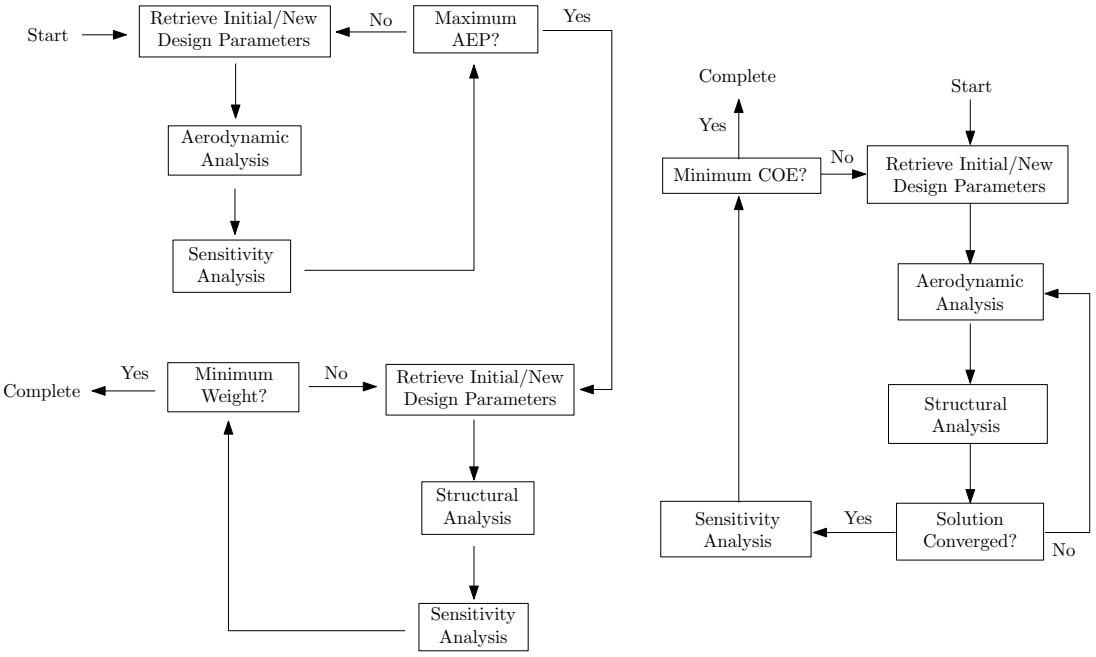

(a) Single-Discipline Feasible (b) Multi-Discipline Feasible

Figure 2.13: The algorithms of various optimization frameworks

The algorithms in figure 2.13 are given in abstract terms. Each of the analysis modules has multiple alternatives. For example, the sensitivity analysis could employ finite difference, complex step or adjoint methods. Evaluating different methods within the same framework will demonstrate the relative merits of the different analysis methods.

The algorithms presented in figure 2.13 are not the only frameworks available in MDO literature. The reader is referred to Park [203] for more information on the

different frameworks. For the current application, the MDF framework is a natural fit. Explorations with any other framework is beyond the scope of this work and is unlikely to afford any advantage.

2.4.2 Sensitivity Analysis

The simplest approach for approximating a gradient is the finite difference method, see equation (2.46). This method is based on a truncated Taylor series expansion. The magnitude of step parameter h must be selected carefully. If it is too small the two terms in the numerator begin to approach similar values, and subtraction errors enter the computation. This source of error is referred to as rounding error. If h is too large, then the error of neglecting the second term ($O\left(h^2\right)$) begins to dominate. This error is referred to as truncation error. The uncertainty in an optimal size of h forces practitioners to conduct studies to determine an acceptable value of h [204].

$$\frac{df}{dx} = \frac{f\left(x+h\right) - f\left(x\right)}{h} + O\left(h^2\right) \tag{2.46}$$

To overcome the problem of an optimal selection of h, researchers have developed alternative methods [204] as given in (2.47). Similar to (2.46), this method is based on a series expansion and introduces truncation error. By eliminating the subtraction operation, this method does not suffer from rounding error. Thus, h only needs to be small enough (typically less than 10^{-5}) to make truncation error negligible [204]. To apply this method, the user must define several transcendental functions (like log) for complex types. See the thesis by Martins [204] for more details.

$$\frac{df}{dx} = \frac{Im\left\{f(x+hi)\right\}}{h} + O\left(h^2\right) \tag{2.47}$$

The Taylor series expansions in the imaginary domain can lead to approximations to second derivatives, however these approximations introduce a subtraction error. To address this problem, Fikes and Alonso [205] developed another method based on Dual and Hyper-Dual numbers. Dual numbers are similar to complex numbers except $i^2 = 0$. For first order gradients, the formula (2.47) still applies. The benefit of this method is that the real component holds the function value without any error from the complex part, obviating the need for two function evaluations. In their paper [205], all the elementary mathematical operators are defined for this number type.

For second order derivatives, hyper dual numbers are needed. For this work, second order derivatives are not required, thus are not discussed here.

The adjoint method was pioneered by Jameson [206, 207, 208]. In sensitivity analysis, there is a user defined objective or constraint function J. In sensitivity analysis the objective and constraint function receive the same treatment, thus these terms will be used interchangeably. The function J is dependent on generalized state variables (x) and generalized design variables (y). When the system is constrained by the governing equation in (2.48), the sensitivity of the objective to a design variable is given by equation (2.49).

$$\mathbf{R}\left(x, y\right) = 0 \tag{2.48}$$

$$\begin{aligned}
\frac{dJ}{dy} &= \frac{\partial J}{\partial y} + \int \left\{\frac{\partial J}{\partial x}\right\}^T \left\{\frac{dx}{dy}\right\} d\mathcal{D} && \text{(2.49a)}\\
&= \frac{\partial J}{\partial y} + \int \left\{\frac{\partial J}{\partial R}\right\}^T \left[\frac{\partial R}{\partial x}\right] \left\{\frac{dx}{dy}\right\} d\mathcal{D} && \text{(2.49b)}\\
&= \frac{\partial J}{\partial y} + \int \left\{\frac{\partial J}{\partial R}\right\}^T \left\{\frac{\partial R}{\partial y}\right\} d\mathcal{D} && \text{(2.49c)}
\end{aligned}$$

The $\frac{\partial R}{\partial x}$ term is a linearization of the governing equations with respect to the state equations. In general, this is a second order tensor that is a differential operator. For the remainder of this section, it will be denoted as ∇R. The integral is taken over the domain $\mathcal{D}$, where R is defined. The vector $\left\{\frac{\partial J}{\partial R}\right\}$ is typically referred to as the adjoint vector or Lagrange multiplier. In this thesis it is denoted as ψ for short. Similarly, $\frac{dx}{dy}$ will be denoted as χ.

When calculating gradients in the forward mode (equation (2.49a)), one is accounting for the governing equations by solving (2.50) for every design variable.

$$\nabla R \chi = \left\{\frac{\partial R}{\partial y}\right\} \tag{2.50}$$

For problems where the number of design variables is much greater than the number of objectives, this can be very expensive. The alternative is to propagate the gradient information backwards using equation (2.49c). When propagating the gradients backwards, the governing equations are accounted for by solving the adjoint equation (2.51) denoted as ∇R^*.

$$\nabla R^* \psi = \left\{ \frac{\partial J}{\partial x} \right\} \tag{2.51}$$

If R is a linear equation, then the adjoint is merely a transpose of ∇R. In linear structural analysis, ∇R is typically self-adjoint. In these cases the derivation of the adjoint operator is trivial [204]. However if R is nonlinear or differential, then the process is more complicated. Giles and Pierce [209, 210] demonstrate adjoint methods using the concept of duality. First the governing equations are linearized, in this case, standard rules of calculus apply for the linearization. Taking the adjoint is performed by proving (2.52), when R is nonlinear or differential the equations cannot be written out in matrix form as they are here. In these cases, the term on the right hand side of $[\partial R/\partial x]$ are distributed within the linearized equation. The goal is to isolate χ from ∇R such that it could be expressed as an inner product resulting in $\chi^T \nabla R^* \psi$ result. At this point, there is a differential operator on the left hand side with ψ distributed within.

$$\int \psi^T \nabla R \chi d\mathcal{D} = \int \chi^T \nabla R^* \psi d\mathcal{D} \tag{2.52}$$

When ∇R is differential, integration by parts must be applied to isolate χ. This introduces the boundary terms ($\mathcal{B}$) when differential in space and the initial and terminal terms ($\mathcal{T}$) when differential in time. For the proof in equation (2.52) to be valid these terms must vanish. This vanishing condition is used to define the boundary, initial and terminal conditions of the adjoint equation ∇R^*. An example is in inviscid flow, here the only free variable at the boundary is pressure. Thus, any boundary objective can only be expressed as functions of pressure. Both Giles and Pierce along with Jameson discuss this extensively [209, 208].

When applying this method to unsteady problems the approach is similar. One can treat time as an additional independent variable of the domain and apply equation (2.52) [211]. In deriving the adjoint equation, additional terminal conditions are created. The user then integrates the adjoint equation backwards in time to solve the adjoint variables.

In general, the computational effort for solving the adjoint is similar to the physical equation. The benefit of the adjoint method is that those solutions can then be applied for every term in the gradient vector. If there are more design variables than objective and constraint expressions, this method is superior to the methods described above.

In aero-elastic optimization there are multiple constraints for material stress and strain throughout the entire blade. Applying a separate constraint for every point on the blade would introduce many more objectives than design variables. To aggregate these constraints, the Kreisselmeier-Steinhauser (KS) function can be applied to approximate the maximum stress and strain [212]. With the KS function the number of design variables (approximately 100-300) will exceed the number of objectives (approximately 3-5) making the wind turbine blade optimization problem ideal for adjoint methods.

The derivation of the adjoint equation can be based on the continuous or discrete versions of R giving the continuous and discrete version of the adjoint equation respectively [213]. Nadarajah and Jameson [213] compared the two approaches for an inviscid flow problem. In this example, both methods gave satisfactory results, however the continuous adjoint equation contributes to faster convergence in optimization applications. Bueno-Orovio *et al.* [214] applied the discrete boundary equation to the Burgers Equations and discovered that it could introduce non-physical behavior.

For the linear structural problem, the application of the adjoint method is almost trivial [204]. The adjoint equation is merely the transpose of the stiffness equation. For nonlinear structural dynamics, Trier *et al.* [215] demonstrated that the linearized equations of motion can be used to derive the adjoint equations. The resulting adjoint equation is dependent on the point of linearization, thus needs be continuously updated as the state evolves. Wang and Yu [216] have made progress in deriving the adjoint equation for a simplified form of GEBT.

The thesis by Martins [204] demonstrates the application of the adjoint method for coupled systems. When applying the adjoint for a coupled system of equations (e.g. aero-elastics), multiple sets of governing equations and associated state variables are involved. In the case of aero-elastics there is an equation and state data for both the aerodynamic and structural aspects. Here the sensitivity is dependent on the solution of (2.53). The symbols $\mathcal{A}$ and $\mathcal{S}$ represent the governing equations for aerodynamics and structural dynamics respectively. Similarly, the variable x_a and x_s are the aerodynamic and structural state data respectively.

$$\begin{bmatrix} \frac{\partial \mathcal{A}}{\partial x_a} & \frac{\partial \mathcal{A}}{\partial x_s} \\ \frac{\partial \mathcal{S}}{\partial x_a} & \frac{\partial \mathcal{S}}{\partial x_s} \end{bmatrix} \begin{Bmatrix} \frac{dx_a}{dy} \\ \frac{dx_s}{dy} \end{Bmatrix} = - \begin{Bmatrix} \frac{\partial \mathcal{A}}{\partial y} \\ \frac{\partial \mathcal{S}}{\partial y} \end{Bmatrix} \tag{2.53}$$

The adjoint can be derived by treating the matrix in equation (2.53) as the ∇R operator in (2.52). Giving the adjoint equation in (2.54), where ψ_a and ψ_s are the adjoint variables for the aerodynamic and structural equations.

$$\begin{bmatrix} \left[\frac{\partial \mathcal{A}}{\partial x_a}\right]^T & \left[\frac{\partial \mathcal{S}}{\partial x_a}\right]^T \\ \left[\frac{\partial \mathcal{A}}{\partial x_s}\right]^T & \left[\frac{\partial \mathcal{S}}{\partial x_s}\right]^T \end{bmatrix} \begin{Bmatrix} \psi_a \\ \psi_s \end{Bmatrix} = - \begin{Bmatrix} \frac{\partial J}{\partial x_a} \\ \frac{\partial J}{\partial x_s} \end{Bmatrix} \tag{2.54}$$

Martins [204] demonstrated that the coupled adjoint equations can be formulated as shown in equation (2.55). The last terms on the right-hand side could be based on previous iterates of the other equation in a lagged fashion. This showed that equation (2.54) can be solved with the same algorithm used to solve coupled governing equations.

$$\underbrace{\left[\frac{\partial \mathcal{A}}{\partial x_a}\right]^T \psi_a = -\frac{\partial J}{\partial x_a}}_{\text{Aerodynamic Adjoint Equation}} - \left[\frac{\partial \mathcal{S}}{\partial x_a}\right]^T \psi_s \tag{2.55a}$$

$$\underbrace{\left[\frac{\partial \mathcal{S}}{\partial x_s}\right]^T \psi_s = -\frac{\partial J}{\partial x_s}}_{\text{Structural Adjoint Equation}} - \left[\frac{\partial \mathcal{S}}{\partial x_s}\right]^T \psi_a \tag{2.55b}$$

Chapter 3

Finite Element Method Based Lagrangian Vortex Dynamics

An early version of the work presented in this chapter was presented at the 2013 AIAA Structural Dynamics and Materials conference:

Michael K. McWilliam, Stephen Lawton, and Curran Crawford. An implicit model for lagrangian vortex dynamics for horizontal axis wind turbine design optimization. In *AIAA 2013 Structures, Dynamics and Materials conference*, 2013

Stephen Lawton is credited in the AIAA publication for providing results demonstrating the poor convergence properties of conventional LVD. These results were not used in this chapter. Later, an improved version was presented at the 2014 Science of Making Torque from Wind:

Michael K McWilliam and Curran Crawford. Finite element based lagrangian vortex dynamics model for wind turbine aerodynamics. *Journal of Physics: Conference Series*, 524(1):012127, 2014

The work presented in this chapter has improved the model further since the *Journal of Physics: Conference Series* publication.

This chapter presents a new Lagrangian Vortex Dynamics (LVD) formulation based on the Finite Element Method (FEM). The motivation for this work is to address several limitations with conventional LVD listed below.

1) **High computational complexity:** The computational complexity[1] is due to coupling between the time step and the element size since the physical size of the influencing elements is governed by the time-step. Thus, small elements require small time steps and vice-versa. This scaling is further exacerbated since the required number of time steps for a given wake length scales with $1/\Delta t$.

2) **Inherent uncertainty with iterative convergence:** If a simulation exhibits slow convergence it will end prematurely with an erroneous solution.

3) **The numerical evolution in time is fundamentally unstable:** Pure vortex systems are fundamentally chaotic [186]. Time marching algorithms adopt this chaotic behavior and numerical error in the discretization amplifies it further.

4) **Multiple solutions are required in aero-elastic simulations:** LVD requires lifting line positions from the structural model, while the structural model requires the aerodynamic forces from LVD. Ideally these two models could be converged simultaneously, yet in practice, this introduces more noise [83]. Instead the user is forced to solve multiple alternating aerodynamic and structural solutions in a Gauss-Siedel iteration.

5) **Path dependency prevents fast convergence in iterative schemes:** In most optimization and Gauss-Siedel routines previous numerical solutions are used to accelerate the convergence of simulations. Yet the solutions of time marching algorithms exhibit path dependency that, in practice, will foul the convergence of these methods.

6) **Numerical noise produces erroneous gradients:** In optimization and design applications it is useful to gather sensitivity information. Conventional numerical schemes such as finite differencing tend to amplify the error in the noise [82], while the use of a time marching evolution with iterative convergence criteria makes it difficult to derive compatible analytic gradient schemes.

The presentation of the new FEM-based LVD will show how this formulation addresses each one of these limitations.

[1] Computational complexity is how the computational effort scales with the number of elements. In conventional LVD it scales cubically with the number of elements. First, the Biot-Savart calculation has $O(N^2)$ complexity and must be executed every time step. Then, the algorithm must execute a minimum of N time steps for the full length of the wake. Overall this leads to $O(N^3)$ complexity

This chapter starts by describing the new LVD formulation in section 3.1. Unlike conventional LVD, the new FEM-based LVD approach has separate mesh parameters for the trailing vorticity streak-lines and influencing elements. Section 3.2 presents several convergence studies to show how all these parameters affect the speed and accuracy of wind turbine simulations. This model is validated with the classical analytic solution for an elliptically loaded wing, experimental measurements of multiple wings and a wind turbine in section 3.3.

3.1 The Improved Finite Element Formulation

The new FEM-based LVD is not a new mathematical theory for fluid mechanics, it is still based on the same governing equations used in conventional LVD. For the sake of brevity, these equations will not be repeated here. The reader should refer back to section 2.3.3 in chapter 2. What sets this method apart from conventional LVD is the numerical parameterization and the algorithms used to solve the system.

The new formulation is based on a nonlinear lifting line vortex model with a free wake. The lift coefficients for the lifting line are based on either experimental measurements or computational results for two dimensional lift coefficients for a range of attack angles and Reynolds numbers. The induction is calculated with the Van-Garrel vortex element given in equation (2.45). This formula incorporates a core model with a radius d_c, which is initially set to the airfoil thickness and then grows at a constant rate. The resident time of the vorticity in the wake is so short that the effect of the core radius growth is negligible.

The formulation presented here is for steady state solutions, where only the trailing vorticity is considered. However, this formulation can easily be extended for unsteady simulations.

The formulation is based on two new innovations that together create a totally new numerical scheme for simulating vortex dominated flows. First, is a Finite Element (FE) description of state discussed in section 3.1.1 that decouples the spatial and temporal discretization and allows for local refinement. The next contribution is the use of an error function to define the convergence. Gradients of this error function can then be used to solve the equations discussed in section 3.1.2. The linearized system is defined in section 3.1.3. Finally, section 3.1.4 describes how all the relevant equations are combined in a solution algorithm to solve the model. Together these innovations address many of the issues of conventional LVD.

3.1.1 The Finite Element Description of State

The first deficiency of conventional LVD is addressed by adopting a different kinematic description for the wake structure (see figure 3.1). Instead of focusing on individual influencing element end-points, the set of three-dimensional streak-lines are parameterized using a FE description based on a set of shape functions $\eta_j(\tau)$ and control points $\boldsymbol{X}_{xj}$ for any vortex age τ. The position along the streak-line is related to the vortex age through equation (3.1a). These streak-lines are broken up into sections and share end points with adjacent sections. These sections will be referred to as 'basis sections' while the control points $\boldsymbol{X}_{xj}$ will be referred to as 'points'. This FE description gives the user two ways of refining the streak-line; the user can chose to use many short basis sections with simple shape functions or longer basis sections with high-order shape functions. In steady state flows this description also provides a definition for the vortex velocity shown in equation (3.1b).

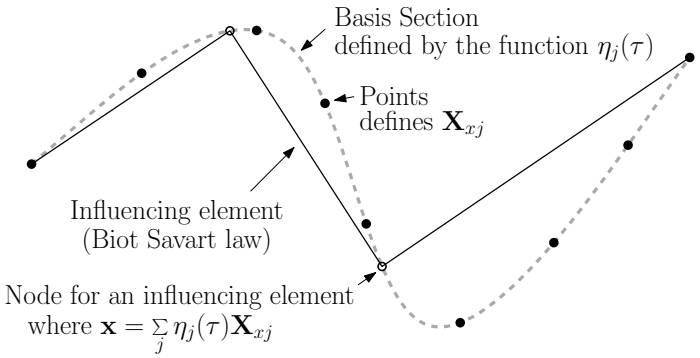

(a) Chain of quadratic bases with 3 influence elements

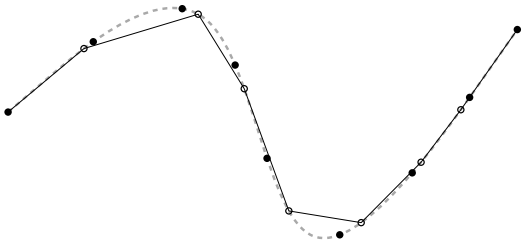

(b) A refined influence configuration with more elements

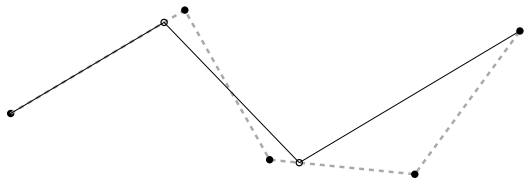

(c) Reduced number of state variables with a chain of linear bases

Figure 3.1: Influencing elements (black-solid) connected to basis sections (grey-dashed)

$$\boldsymbol{x} = \sum_j \eta_j(\tau)\boldsymbol{X}_{xj} \qquad (3.1a) \qquad\qquad \dot{\boldsymbol{x}} = \sum_j \dot{\eta}_j(\tau)\boldsymbol{X}_{xj} \qquad (3.1b)$$

The shape function is meant to approximate the solution and can have a large influence on the final configuration. In addition to the order of the interpolating polynomial, one can select different types of polynomials. The Lagrange polynomial is the simplest; it is based on interpolating between points. One problem with Lagrange polynomials is they only enforce C^0 continuity at the end-points. This can lead to a kink at the basis section end-points. Hermite interpolating polynomials are parameterized by both position and gradients. This enables C^1 continuity to be enforced at the end points of the basis sections. For a more detailed investigation on these effects the reader should refer to section 3.2.3.

For the special case of rotating wings (*i.e.* wind turbines), the wake will form into a helix with cylindrical geometry. In this special, case the solution can be improved by performing the FEM interpolation in a cylindrical coordinate system. The control points $\boldsymbol{X}_{ij}$ give the axial, radial and angular position coordinates. Equations 3.1a and 3.1b are applied as usual, and then these results are transformed to a Cartesian coordinate system for the various other calculations. This approach is advantageous because it preserves the cylindrical curvature of the helix. Section 3.2.3 gives a detailed discussion on the benefits of cylindrical interpolation.

The theoretical foundation of FEM is the use of shape functions to approximate the solution. This implies it is the space curve in equation (3.1a) (not the influencing elements) that describe the locations of vorticity. This leaves open different approaches for calculating the influence associated with this curve. The challenge is integrating (2.39) over an arbitrary space curve, which is something not easily achieved analytically and was not attempted. Another approach, which forgoes the use of elements completely, would simply apply numerical quadrature of equation (2.39) directly. This essentially lumps the vorticity onto points, which can be viewed as an approximation of the original space curve (*i.e.* a smooth curve can be represented by a sequence of points). The influence calculation could be improved by approximating the space curves with line segments. Then the influence can be calculated with the analytical solution in (2.45). It is only through the application of this line-segment approximation that the model incorporates the influencing elements shown in figure 3.1. Here, the space curve in equation (3.1a) is defining the end-points of the influencing elements. This improves upon the point approximation by distributing the vorticity along the line, but ignores the effects of curvature.

Decoupling the influence element discretization from the control point discretization gives another opportunity for accelerating the computational speed. It is well

known that structural models with a FE parameterization can be accelerated by using an optimal set of basis functions; this has lead to very fast reduced order models based on modal analysis. By introducing the FE parameterization here, there is now a potential that LVD models can be accelerated in a similar way once an optimal set of basis functions is identified. Section 3.2.2 discusses the potential of applying a basis function approach to accelerating the convergence.

3.1.2 The Error Function

The second innovation in this new model is the use of an error function to define and solve the problem. The error function associated with the bound circulation strength on the blade (shown in equation (3.2a)), is based on Weissigner Lifting Line Theory (WLLT). Equation (3.2a) is defined for the whole lifting line, but is currently evaluated at the mid-point of each lifting line element (see equation (3.2b)). This could be extended by defining an integral along the lifting line and evaluating it with numerical quadrature.

$$r_\Gamma \equiv \Gamma - \frac{cc_l\|\boldsymbol{w}\|}{2} \qquad (3.2a) \qquad\qquad R_{\Gamma i} = r_\Gamma|_{s=middle} \qquad (3.2b)$$

The error function for the wake is based on the fact that vortex elements follow the local flow field (*i.e.* are force-free). This means the velocity of any fluid element must be equal to the local flow field; any difference is an error in the solution. This error is shown mathematically in equation (3.3a) in a rotating reference frame where $\boldsymbol{\Omega}$ describes the angular velocity of the rotor, $\boldsymbol{x}_0$ is a point on the rotation axis, $\boldsymbol{u}_\infty$ is the wind speed and $\boldsymbol{u}_\gamma$ is the influence from all the vorticity in the flow field.

$$\boldsymbol{r}_x \equiv \dot{\boldsymbol{x}} + \boldsymbol{\Omega} \times (\boldsymbol{x} - \boldsymbol{x}_0) - \boldsymbol{u}_\infty - \boldsymbol{u}_\gamma \qquad (3.3a)$$

The error function in equation (3.3a) is defined continuously for every point along the trailing filaments (*i.e.* basis sections). This error is mapped to scalars by applying the Galerkin projection (see equation (3.3b)) of the error (*i.e.* $\boldsymbol{r}_x(\tau)$) onto the weighting function $\zeta_j(\tau)$; typically the shape function for state (*i.e.* $\eta_j(\tau)$) is used for the weighting function. Equation 3.3b gives a corresponding error for each control point, where the subscript j refers to the control points. The integral is approximated with numerical integration. The integration points and the associated weights are denoted by τ_k and w_k respectively. In this work the integrals are approximated with Gauss

quadrature[2] (see Logan [89] for more details). One point quadrature was used with linear basis sections[3], while three point quadrature gave best results for quadratic and cubic basis sections.

$$\boldsymbol{R}_{xj} = \int_{\tau_0}^{\tau_f} \zeta_j(\tau)\boldsymbol{r}_x(\tau)d\tau \approx \sum_k \zeta_j(\tau_k)\boldsymbol{r}_x(\tau_k)w_k \tag{3.3b}$$

3.1.3 The Linearized System

To solve and/or take gradients of the system, it is necessary to define a linearized version of the system that takes the form given in (3.4a), where the state vector ($\boldsymbol{X}$) is defined in equation (3.4b), the residual vector ($\boldsymbol{R}$) is defined in (3.4c) and the Jacobian ($[\boldsymbol{J}]$) is defined in (3.4d). The overhead bar denotes a linear approximation. Due to nonlinearity in the system (*e.g.* the airfoil lift curves, influence kernel function, *etc.*) the linearized system needs to be updated whenever the state vector is changed.

$$\bar{\boldsymbol{R}} = \boldsymbol{R}|_{X_0} + [\boldsymbol{J}]\,\Delta\boldsymbol{X} \tag{3.4a}$$

$$\boldsymbol{X} \equiv (\ \Gamma_1 \quad \Gamma_2 \quad \cdots \quad \boldsymbol{X}_{x1}^T \quad \boldsymbol{X}_{x2}^T \quad \cdots\ )^T \tag{3.4b}$$

$$\boldsymbol{R} \equiv (\ R_{\Gamma 1} \quad R_{\Gamma 2} \quad \cdots \quad \boldsymbol{R}_{x1}^T \quad \boldsymbol{R}_{x2}^T \quad \cdots\ )^T \tag{3.4c}$$

$$[\boldsymbol{J}] \equiv \frac{\partial \boldsymbol{R}}{\partial \boldsymbol{X}} \tag{3.4d}$$

Before the derivation of the linearized residual is given, some notation needs to be introduced. A 3-component column vector $\boldsymbol{a}$ defines a skew-symmetric matrix $[\boldsymbol{a}\times]$ according to:

$$[\boldsymbol{a}\times] = \begin{bmatrix} 0 & -a_3 & a_2 \\ a_3 & 0 & -a_1 \\ -a_2 & a_1 & 0 \end{bmatrix} \tag{3.5}$$

[2]Gauss quadrature will give an exact solution to the integral of a polynomial of specified order with a minimum number of sampling points [89]

[3]This is equivalent to mid-point rule in simple integration and implicit Crank-Nicolson for temporal integration in time marching codes

The derivative of the column vector magnitude with respect to the vector itself is given by:

$$\frac{\partial \|\boldsymbol{a}\|}{\partial \boldsymbol{a}} = \frac{\boldsymbol{a}^T}{\|\boldsymbol{a}\|} \tag{3.6}$$

The derivation of the Jacobian will be split into two parts: First the linearization of the strength residual ($[\boldsymbol{J}_{\Gamma i}]$), then the linearization of the advection residual ($[\boldsymbol{J}_{xj}]$). Both of these Jacobian matrices are linearized with respect to the state vector which contains both the vortex strength on the lifting line and the control point positions the free wake. Together these matrices are combined to give the system Jacobian (*i.e.* $[\boldsymbol{J}] = \begin{bmatrix} \boldsymbol{J}_{\Gamma i}^T & \boldsymbol{J}_{xj}^T \end{bmatrix}^T$). The linearization of the strength residual is based on taking the gradient of equation 3.2b:

$$\begin{aligned} [\boldsymbol{J}_{\Gamma i}] &= \frac{\partial R_{\Gamma i}}{\partial \boldsymbol{X}} = \frac{\partial r_{\Gamma i}}{\partial \boldsymbol{X}} \\ &= \frac{\partial \Gamma}{\partial \boldsymbol{X}} - \left(\frac{c}{2}\right)\left(\|\boldsymbol{w}\|\frac{\partial c_l}{\partial \alpha}\frac{\partial \alpha}{\partial \boldsymbol{w}} + \left(\frac{\partial c_l}{\partial Re}\left(\frac{\rho c}{\mu}\right) + \frac{c_l}{\|\boldsymbol{w}\|}\right)\boldsymbol{w}^T\right)\frac{\partial \boldsymbol{w}}{\partial \boldsymbol{X}} \end{aligned} \tag{3.7a}$$

The relative velocity $\boldsymbol{w} = \boldsymbol{u}_\infty + \boldsymbol{u} - \boldsymbol{v}$ includes $\boldsymbol{u}_\infty$ the undisturbed fluid velocity, $\boldsymbol{u}$ the influence and $\boldsymbol{v}$ the velocity of the blade. Assuming that $\boldsymbol{u}_\infty$ and $\boldsymbol{v}$ are independent of state, then the linearization can be simplified further.

$$[\boldsymbol{J}_{\Gamma i}] = \frac{\partial \Gamma}{\partial \boldsymbol{X}} - \left(\frac{c}{2}\right)\left(\|\boldsymbol{w}\|\frac{\partial c_l}{\partial \alpha}\frac{\partial \alpha}{\partial \boldsymbol{w}} + \left(\frac{\partial c_l}{\partial Re}\left(\frac{\rho c}{\mu}\right) + \frac{c_l}{\|\boldsymbol{w}\|}\right)\boldsymbol{w}^T\right)\frac{\partial \boldsymbol{u}}{\partial \boldsymbol{X}} \tag{3.7b}$$

Given that $\hat{\boldsymbol{c}}$ and $\hat{\boldsymbol{t}}$ are unit vectors in the chord and thickness direction respectively, $\partial\alpha/\partial\boldsymbol{w}$ is given by:

$$\frac{\partial \alpha}{\partial \boldsymbol{w}} = \frac{\left(\hat{\boldsymbol{t}}\cdot\boldsymbol{w}\right)\hat{\boldsymbol{c}}^T - \left(\hat{\boldsymbol{c}}\cdot\boldsymbol{w}\right)\hat{\boldsymbol{t}}^T}{\left(\hat{\boldsymbol{t}}\cdot\boldsymbol{w}\right)^2 + \left(\hat{\boldsymbol{c}}\cdot\boldsymbol{w}\right)^2} \tag{3.7c}$$

The first term in equation (3.7b) is simply a row vector of 0's with a 1 at the appropriate entry because the strength Γ is contained in the state vector $\boldsymbol{X}$. All that remains is the linearization of the influence $\boldsymbol{u}$; since the influence also affects the residual in the wake that derivation will be deferred for now.

The derivation for the linearized advection residual proceeds as follows, where $\boldsymbol{\Omega}$ is the rotation rate when simulating rotating wings (*i.e.* wind turbines or propellers):

$$
\begin{aligned}
[\boldsymbol{J}_{xj}] &= \frac{\partial \boldsymbol{R}_{xj}}{\partial \boldsymbol{X}} = \sum_k \zeta_j(\tau_k) \frac{\partial \boldsymbol{r}_x(\tau_k)}{\partial \boldsymbol{X}} w_k \\
&= \sum_k \zeta_j(\tau_k) \left(\frac{\partial \dot{\boldsymbol{x}}}{\partial \boldsymbol{X}} + [\boldsymbol{\Omega}\times] \frac{\partial \boldsymbol{x}}{\partial \boldsymbol{X}} - \frac{\partial \boldsymbol{u}}{\partial \boldsymbol{X}} \right) w_k
\end{aligned} \tag{3.8}
$$

The linearization of $\boldsymbol{x}$ and $\dot{\boldsymbol{x}}$ are based on equations (3.1a) and (3.1b) respectively:

$$
\frac{\partial \boldsymbol{x}}{\partial \boldsymbol{X}_{xj}} = \eta_j(\tau) \tag{3.9a}
$$

$$
\frac{\partial \dot{\boldsymbol{x}}}{\partial \boldsymbol{X}_{xj}} = \dot{\eta}_j(\tau) \tag{3.9b}
$$

The linearization of the flow field is based on linearization of the Biot-Savart Law shown below, where $\partial \boldsymbol{u}/\partial \boldsymbol{X}|_n$ is the linearization of the influence from a single element.

$$
\frac{\partial \boldsymbol{u}}{\partial \boldsymbol{X}} = \sum_{n=1}^{N} \left. \frac{\partial \boldsymbol{u}}{\partial \boldsymbol{X}} \right|_n \tag{3.10a}
$$

In this system only the Van Garrel elements (defined in equation (2.45)) are used; its linearization is given in (3.10b) where the subscript n denotes an individual element and the numeric subscripts denote the vectors in figure 2.10.

$$
\begin{aligned}
\left. \frac{\partial \boldsymbol{u}}{\partial \boldsymbol{X}} \right|_n &= \frac{\partial \boldsymbol{u}_n}{\partial \Gamma_n} \frac{\partial \Gamma_n}{\partial \boldsymbol{X}} + \left(\frac{\partial \boldsymbol{u}_n}{\partial \|\boldsymbol{d}_{1n}\|} \frac{\partial \|\boldsymbol{d}_{1n}\|}{\partial \boldsymbol{d}_{1n}} + \frac{\partial \boldsymbol{u}_n}{\partial \boldsymbol{d}_{1n}} \right) \left(\frac{\partial \boldsymbol{d}_{1n}}{\partial \boldsymbol{x}_{1n}} \frac{\partial \boldsymbol{x}_{1n}}{\partial \boldsymbol{X}} + \frac{\partial \boldsymbol{d}_{1n}}{\partial \boldsymbol{x}_{pn}} \frac{\partial \boldsymbol{x}_{pn}}{\partial \boldsymbol{X}} \right) \\
&\quad + \left(\frac{\partial \boldsymbol{u}_n}{\partial \|\boldsymbol{d}_{2n}\|} \frac{\partial \|\boldsymbol{d}_{2n}\|}{\partial \boldsymbol{d}_{2n}} + \frac{\partial \boldsymbol{u}_n}{\partial \boldsymbol{d}_{2n}} \right) \left(\frac{\partial \boldsymbol{d}_{2n}}{\partial \boldsymbol{x}_{2n}} \frac{\partial \boldsymbol{x}_{2n}}{\partial \boldsymbol{X}} + \frac{\partial \boldsymbol{d}_{2n}}{\partial \boldsymbol{x}_{pn}} \frac{\partial \boldsymbol{x}_{pn}}{\partial \boldsymbol{X}} \right) \\
&\quad + \frac{\partial \boldsymbol{u}_n}{\partial \|\boldsymbol{l}_n\|} \frac{\partial \|\boldsymbol{l}_n\|}{\partial \boldsymbol{l}_n} \left(\frac{\partial \boldsymbol{l}_n}{\partial \boldsymbol{x}_{1n}} \frac{\partial \boldsymbol{x}_{1n}}{\partial \boldsymbol{X}} + \frac{\partial \boldsymbol{l}_n}{\partial \boldsymbol{x}_{2n}} \frac{\partial \boldsymbol{x}_{2n}}{\partial \boldsymbol{X}} \right)
\end{aligned} \tag{3.10b}
$$

Many of the terms are expressed below in equations (3.10c) through (3.10j).

$$
\frac{\partial \boldsymbol{u}_n}{\partial \Gamma_n} = \frac{\left(\|\boldsymbol{d}_{1n}\| + \|\boldsymbol{d}_{2n}\| \right) \left(\boldsymbol{d}_{1n} \times \boldsymbol{d}_{2n} \right)}{4\pi \left(\|\boldsymbol{d}_{1n}\| \|\boldsymbol{d}_{2n}\| \left(\|\boldsymbol{d}_{1n}\| \|\boldsymbol{d}_{2n}\| + \boldsymbol{d}_{1n} \cdot \boldsymbol{d}_{2n} \right) + \left(d_{cn} \|\boldsymbol{l}_n\| \right)^2 \right)} \tag{3.10c}
$$

$$\frac{\partial \boldsymbol{u}_n}{\partial \|\boldsymbol{d}_{1n}\|} = \frac{\Gamma_n \left(\boldsymbol{d}_{1n} \times \boldsymbol{d}_{2n}\right)}{4\pi \left(\|\boldsymbol{d}_{1n}\|\|\boldsymbol{d}_{2n}\| \left(\|\boldsymbol{d}_{1n}\|\|\boldsymbol{d}_{2n}\| + \boldsymbol{d}_{1n} \cdot \boldsymbol{d}_{2n}\right) + \left(d_{cn}\|\boldsymbol{l}_n\|\right)^2\right)} - \frac{\Gamma_n \|\boldsymbol{d}_{2n}\| \left(2\|\boldsymbol{d}_{1n}\|\|\boldsymbol{d}_{2n}\| + \boldsymbol{d}_{1n} \cdot \boldsymbol{d}_{2n}\right) \left(\|\boldsymbol{d}_{1n}\| + \|\boldsymbol{d}_{2n}\|\right) \left(\boldsymbol{d}_{1n} \times \boldsymbol{d}_{2n}\right)}{4\pi \left(\|\boldsymbol{d}_{1n}\|\|\boldsymbol{d}_{2n}\| \left(\|\boldsymbol{d}_{1n}\|\|\boldsymbol{d}_{2n}\| + \boldsymbol{d}_{1n} \cdot \boldsymbol{d}_{2n}\right) + \left(d_{cn}\|\boldsymbol{l}_n\|\right)^2\right)^2} \tag{3.10d}$$

$$\frac{\partial \boldsymbol{u}_n}{\partial \boldsymbol{d}_{1n}} = \frac{-\Gamma_n \left(\|\boldsymbol{d}_{1n}\| + \|\boldsymbol{d}_{2n}\|\right) [\boldsymbol{d}_{2n}\times]}{4\pi \left(\|\boldsymbol{d}_{1n}\|\|\boldsymbol{d}_{2n}\| \left(\|\boldsymbol{d}_{1n}\|\|\boldsymbol{d}_{2n}\| + \boldsymbol{d}_{1n} \cdot \boldsymbol{d}_{2n}\right) + \left(d_{cn}\|\boldsymbol{l}_n\|\right)^2\right)} - \frac{\Gamma_n \|\boldsymbol{d}_{1n}\|\|\boldsymbol{d}_{2n}\| \left(\|\boldsymbol{d}_{1n}\| + \|\boldsymbol{d}_{2n}\|\right) \left(\boldsymbol{d}_{1n} \times \boldsymbol{d}_{2n}\right) \otimes \boldsymbol{d}_{2n}}{4\pi \left(\|\boldsymbol{d}_{1n}\|\|\boldsymbol{d}_{2n}\| \left(\|\boldsymbol{d}_{1n}\|\|\boldsymbol{d}_{2n}\| + \boldsymbol{d}_{1n} \cdot \boldsymbol{d}_{2n}\right) + \left(d_{cn}\|\boldsymbol{l}_n\|\right)^2\right)^2} \tag{3.10e}$$

$$\frac{\partial \boldsymbol{u}_n}{\partial \|\boldsymbol{d}_{2n}\|} = \frac{\Gamma_n \left(\boldsymbol{d}_{1n} \times \boldsymbol{d}_{2n}\right)}{4\pi \left(\|\boldsymbol{d}_{2n}\|\|\boldsymbol{d}_{1n}\| \left(\|\boldsymbol{d}_{2n}\|\|\boldsymbol{d}_{1n}\| + \boldsymbol{d}_{2n} \cdot \boldsymbol{d}_{1n}\right) + \left(d_{cn}\|\boldsymbol{l}_n\|\right)^2\right)} - \frac{\Gamma_n \|\boldsymbol{d}_{1n}\| \left(2\|\boldsymbol{d}_{2n}\|\|\boldsymbol{d}_{1n}\| + \boldsymbol{d}_{2n} \cdot \boldsymbol{d}_{1n}\right) \left(\|\boldsymbol{d}_{2n}\| + \|\boldsymbol{d}_{1n}\|\right) \left(\boldsymbol{d}_{1n} \times \boldsymbol{d}_{2n}\right)}{4\pi \left(\|\boldsymbol{d}_{2n}\|\|\boldsymbol{d}_{1n}\| \left(\|\boldsymbol{d}_{2n}\|\|\boldsymbol{d}_{1n}\| + \boldsymbol{d}_{2n} \cdot \boldsymbol{d}_{1n}\right) + \left(d_{cn}\|\boldsymbol{l}_n\|\right)^2\right)^2} \tag{3.10f}$$

$$\frac{\partial \boldsymbol{u}_n}{\partial \boldsymbol{d}_{2n}} = \frac{\Gamma_n \left(\|\boldsymbol{d}_{1n}\| + \|\boldsymbol{d}_{2n}\|\right) [\boldsymbol{d}_{1n}\times]}{4\pi \left(\|\boldsymbol{d}_{1n}\|\|\boldsymbol{d}_{2n}\| \left(\|\boldsymbol{d}_{1n}\|\|\boldsymbol{d}_{2n}\| + \boldsymbol{d}_{1n} \cdot \boldsymbol{d}_{2n}\right) + \left(d_{cn}\|\boldsymbol{l}_n\|\right)^2\right)} - \frac{\Gamma_n \|\boldsymbol{d}_{1n}\|\|\boldsymbol{d}_{2n}\| \left(\|\boldsymbol{d}_{1n}\| + \|\boldsymbol{d}_{2n}\|\right) \left(\boldsymbol{d}_{1n} \times \boldsymbol{d}_{2n}\right) \otimes \boldsymbol{d}_{1n}}{4\pi \left(\|\boldsymbol{d}_{1n}\|\|\boldsymbol{d}_{2n}\| \left(\|\boldsymbol{d}_{1n}\|\|\boldsymbol{d}_{2n}\| + \boldsymbol{d}_{1n} \cdot \boldsymbol{d}_{2n}\right) + \left(d_{cn}\|\boldsymbol{l}_n\|\right)^2\right)^2} \tag{3.10g}$$

$$\frac{\partial \boldsymbol{u}_n}{\partial \|\boldsymbol{l}_n\|} = -\frac{\Gamma_n 2 d_{cn}^2 \|\boldsymbol{l}_n\| \left(\|\boldsymbol{d}_{2n}\| + \|\boldsymbol{d}_{1n}\|\right) \left(\boldsymbol{d}_{1n} \times \boldsymbol{d}_{2n}\right)}{4\pi \left(\|\boldsymbol{d}_{2n}\|\|\boldsymbol{d}_{1n}\| \left(\|\boldsymbol{d}_{2n}\|\|\boldsymbol{d}_{1n}\| + \boldsymbol{d}_{2n} \cdot \boldsymbol{d}_{1n}\right) + \left(d_{cn}\|\boldsymbol{l}_n\|\right)^2\right)^2} \tag{3.10h}$$

$$\frac{\partial \boldsymbol{d}_{1n}}{\partial \boldsymbol{x}_{pn}} = \frac{\partial \boldsymbol{d}_{2n}}{\partial \boldsymbol{x}_{pn}} = \frac{\partial \boldsymbol{l}_n}{\partial \boldsymbol{x}_{2n}} = \boldsymbol{I} \tag{3.10i}$$

$$\frac{\partial \boldsymbol{d}_{1n}}{\partial \boldsymbol{x}_{1n}} = \frac{\partial \boldsymbol{d}_{2n}}{\partial \boldsymbol{x}_{2n}} = \frac{\partial \boldsymbol{l}_n}{\partial \boldsymbol{x}_{1n}} = -\boldsymbol{I} \tag{3.10j}$$

3.1.4 The Solution Algorithm

Figure 3.2 shows an example of how computational elements are arranged to simulate the flow around a single wind turbine blade. In this figure the blade is modeled by

four lifting line elements of strength Γ_i. The error $R_{\Gamma i}$ of these elements is evaluated at the mid-points shown by the squares. A basis section (shown as a grey dashed line) is trailing from the end point of each lifting line element; the position of these basis sections is governed by the control points $\boldsymbol{X}_{xj}$, which are associated with error $\boldsymbol{R}_{xj}$. A set of influencing elements (shown by the black solid lines) are attached to each basis section (see figure 3.1 for the different ways basis section are combined with influencing elements). The primary state variables are the lifting line strength Γ_i and the control points $\boldsymbol{X}_{xj}$, each with a corresponding error $R_{\Gamma i}$ and $\boldsymbol{R}_{xj}$ respectively.

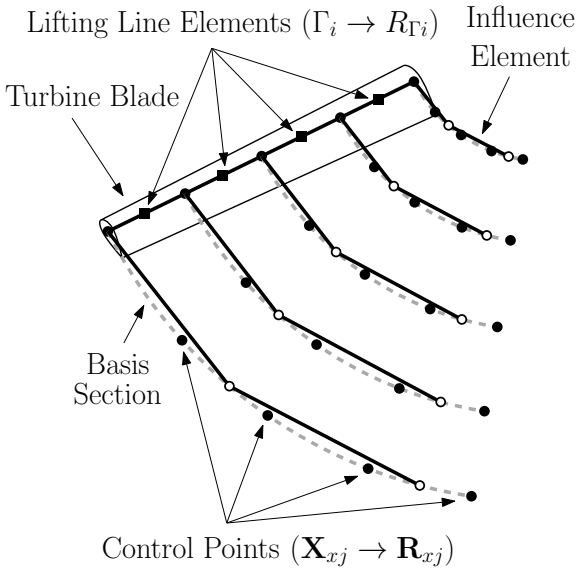

Figure 3.2: Schematic of an FEM based LVD simulation

By defining error functions (*i.e.* equation (3.2b) and (3.3b)) one can formulate the system as a root finding problem as shown in equation (3.11) where the goal is to solve the state vector $\boldsymbol{X}$ such that the error $\boldsymbol{R}$ is $\mathbf{0}$.

$$\boldsymbol{R}(\boldsymbol{X}) = \mathbf{0} \tag{3.11}$$

The most compelling feature of this new formulation is the fact that the problem can be formulated in the form of equation (3.11). Many problems across multiple disciplines are formulated as a nonlinear root solving problem like this. As such there is already a large body of research for different types of algorithms for problems of this form, the most important being the solution algorithms. Many algorithms

were explored, but the most effective has been the Newton iteration with adaptive relaxation shown in algorithm 1.

The Newton algorithm relies on an optimal relaxation parameter β. To calculate the optimal relaxation, a search algorithm shown in algorithm 2 is employed. This algorithm is similar to the Armijo back-tracking line search. The standard Armijo algorithm assumes that residual evaluations are relatively expensive and it is better to expend computational effort on finding a better search direction [202]. However in the FEM-based LVD model all elements affect all the other elements which leads to expensive Jacobian evaluations. Instead, the line search algorithm used here uses many residual evaluations to get the best solution. When relaxation is required, the algorithm uses a back-tracking search to find the interval that contains the optimal solution. Once the interval is identified, previous function evaluations can be used to define a quadratic approximation. The minimum of that quadratic approximation is then taken as the solution. For more information on line search algorithms see Vanderplaats [200].

In general algorithm 1 is not capable of efficiently solving all problems. This algorithm performed poorly when there were a large number of elements on the blade causing influencing elements in the wake to be in close proximity. Simulations with large element spacing could still give poor solver performance when the length of the wake was very long.

To understand the source of the difficulties an in-depth study was conducted on a series of problems that consistently exhibited poor solver performance. Figure 3.3 shows one of these examples. In this case 16 elements were used to represent the rotor from the MEXICO experiments [217]. Then each trailing filament was simulated with 120 18° elements (*i.e.* 6 rotor revolutions), with 120 linear basis sections in a Cartesian reference frame. No far-wake model was employed in this simulation. In figure 3.3 'Search Fraction' refers to β used in the line search and the 'Solution Length' refers to the norm of $\Delta \boldsymbol{X}$ (*i.e.* solution of the linearized system).

Figure 3.3 shows two distinct intervals (*i.e.* around iteration 75 and between iterations 300 and 750) where the solver was making negligible improvement in the system residual. It is clear that in these intervals the search fraction is very small in response to a large solution vector. The large search vector suggests the Jacobian

[4]The optimal relaxation parameter β is solved with one parameter optimization shown in algorithm 2.

[5]Quadratic minimum is based on the minimum point in a quadratic curve fit

Algorithm 1 Newton iteration with adaptive relaxation for FEM based LVD

Select the initial guess $\boldsymbol{X}_{(0)}$
$\boldsymbol{R}_{(0)} \leftarrow$ Calculate Residual($\boldsymbol{X}_{(0)}$)
while $\|\boldsymbol{R}_{(i)}\| > \epsilon$ **do**
  $[\boldsymbol{J}] \leftarrow$ Calculate Jacobian($\boldsymbol{X}_{(i)}$)
  Solve the linear system $[\boldsymbol{J}]\,\Delta\boldsymbol{X} = -\boldsymbol{R}_{(i)}$ for $\Delta\boldsymbol{X}$
  Update the state vector with optimal relaxation[4] $\boldsymbol{X}_{(i+1)} = \boldsymbol{X}_{(i)} + \beta\Delta\boldsymbol{X}$
  $\boldsymbol{R}_{(i+1)} \leftarrow$ Calculate Residual($\boldsymbol{X}_{(i+1)}$)
end while

function Calculate Residual($\boldsymbol{X}$)
  for all lifting line elements **do**
    $\boldsymbol{u} \leftarrow$ Calculate Influence($\boldsymbol{x}$) ▷ $\boldsymbol{x}$ is a lifting line position
    Calculate the angle of attack (α) and Reynolds number (Re)
    Based on α and Re interpolate experimental data to get cl
    Calculate the error with equations (3.2a) and (3.2b)
    Assign the error to the corresponding entry in the vector $\boldsymbol{R}$
  end for
  for all control points in the wake **do**
    Initialize corresponding entries in the vector $\boldsymbol{R}$ to $\boldsymbol{0}$
    for all integration points (*i.e.* τ_j) in equation (3.3b) **do**
      $\boldsymbol{u} \leftarrow$ Calculate Influence($\boldsymbol{x}$) ▷ Position $\boldsymbol{x}$ based on equation (3.1a)
      Calculate the velocity of the flow element $\dot{\boldsymbol{x}}$ ▷ using equation (3.1b)
      Calculate the local error with equation (3.3a)
      Calculate the weighted error according to equation (3.3b)
      Add the weighted error to the corresponding entries in the vector $\boldsymbol{R}$
    end for
  end for
  return the fully populated error vector $\boldsymbol{R}$
end function

function Calculate Influence($\boldsymbol{x}$)
  $\boldsymbol{u} \leftarrow \boldsymbol{u}_\infty$ ▷ Initialize with the free stream wind velocity
  for all influencing elements **do**
    Calculate $\boldsymbol{u}_{\gamma i}$ at $\boldsymbol{x}$ with equation (2.45)
    $\boldsymbol{u} \leftarrow \boldsymbol{u} + \boldsymbol{u}_{\gamma i}$
  end for
  return the influence $\boldsymbol{u}$
end function

Algorithm 2 Optimal line search algorithm

Given $\boldsymbol{X}_0$, $\|\boldsymbol{R}_0\|$, $\Delta\boldsymbol{X}$ and β_i ▷ Initial β is the last solution or 1
Solve β where $\|\boldsymbol{R}(\boldsymbol{X}_0 + \beta\Delta\boldsymbol{X})\|$ is minimum
$\beta_1 \leftarrow \beta_i$
$R_1 \leftarrow \|\boldsymbol{R}(\boldsymbol{X}_0 + \beta_1\Delta\boldsymbol{X})\|$
if $\beta_i = 1$ and $R_1 < 0.5\|\boldsymbol{R}_0\|$ **then**
  return β_i ▷ Un-relaxed Newton solution is acceptable
end if
if $\beta_1 < 1$ **then** ▷ Start search in larger β
  $\beta_2 \leftarrow \min(\beta_1\alpha, 1.0)$ ▷ Golden ratio is used for expansion ration α
  $R_2 \leftarrow \|\boldsymbol{R}(\boldsymbol{X}_0 + \beta_2\Delta\boldsymbol{X})\|$
  if $R_2 < R_1$ and $\beta_2 < 1$ **then** ▷ Optimal solution at larger β
    $\beta_3 \leftarrow \min(\beta_2\alpha, 1.0)$
    $R_3 \leftarrow \|\boldsymbol{R}(\boldsymbol{X}_0 + \beta_3\Delta\boldsymbol{X})\|$
    while $\beta_3 < 1$ and $R_3 < R_2$ **do** ▷ Continue search with larger β
      $\beta_1 \leftarrow \beta_2$, $R_1 \leftarrow R_2$, $\beta_2 \leftarrow \beta_3$, $R_2 \leftarrow R_3$
      $\beta_3 \leftarrow \beta_2\alpha$
      $R_3 \leftarrow \|\boldsymbol{R}(\boldsymbol{X}_0 + \beta_3\Delta\boldsymbol{X})\|$
    end while
    if $\beta_3 = 1$ and $R_3 < R_2$ **then** ▷ Solution interval found
      return 1
    else
      return QUADRATIC MINIMUM(β_1,R_1,β_2,R_2,β_3,R_3)[5]
    end if
  end if
  $\beta_3 \leftarrow \beta_2$, $R_3 \leftarrow R_2$, $\beta_2 \leftarrow \beta_1$, $R_2 \leftarrow R_1$
else
  $\beta_3 \leftarrow \beta_1$, $R_3 \leftarrow R_1$
  $\beta_2 \leftarrow \beta_3/\alpha$
  $R_2 \leftarrow \|\boldsymbol{R}(\boldsymbol{X}_0 + \beta_2\Delta\boldsymbol{X})\|$
end if
repeat ▷ Search smaller β values
  $\beta_1 \leftarrow \beta_2/\alpha$
  $R_1 \leftarrow \|\boldsymbol{R}(\boldsymbol{X}_0 + \beta_1\Delta\boldsymbol{X})\|$
  if $R_1 > R_2$ **then** ▷ Solution interval found
    return QUADRATIC MINIMUM(β_1,R_1,β_2,R_2,β_3,R_3)
  end if
  $\beta_3 \leftarrow \beta_2$, $R_3 \leftarrow R_2$, $\beta_2 \leftarrow \beta_1$, $R_2 \leftarrow R_1$
until $\beta_1 < \beta_{min}$
return Failure Code

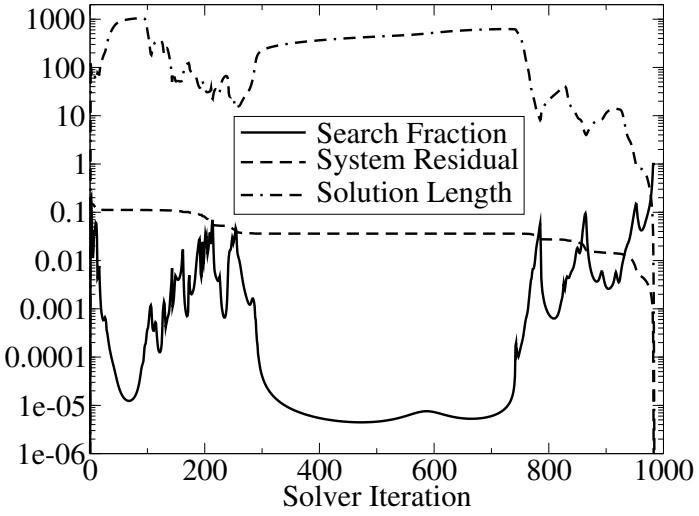

Figure 3.3: Example of poor solver performance

is nearly singular. For 10 different iterations the condition number of the Jacobian was calculated with a singular value decomposition. The condition number ranged between $7,500$ and $1.5 \cdot 10^6$ which shows the Jacobian can be nearly singular, but with double precision number types would still give acceptable solutions.

To understand what parts of the system contribute to the large search vector, the system was divided into partitions. One for the lifting line strength and another for each trailing filament. Figure 3.4 shows the proportion each partition contributes to the total search vector. It is clear that in these stalled intervals the solver is only making significant changes on a small part of the system.

Concentrating the solver on a small portion of the system would be acceptable if the residual in these regions decreased. However this is not the case. The optimal line search algorithm is based on finding the minimum system residual. At that optimal search length there will be regions where the residual is decreasing, and other regions where it is increasing with respect to β. Figure 3.5 shows how the residual for the different partitions varies with search length when a near singular solution is used in the search. The figure shows that at the optimal search length for the system, the residual in the partitions associated with the singular mode actually increased beyond the original level. The effect of near singular conditions is to move residual from the system to the regions of associated with the singularity. This in-turn will exacerbate the singularity further.

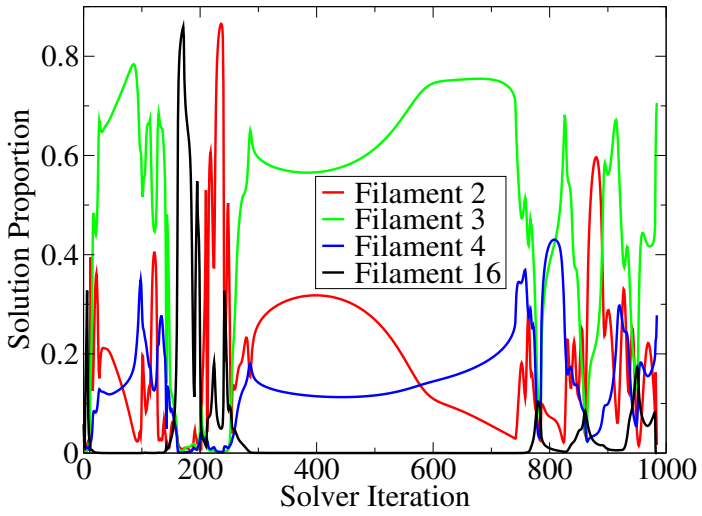

Figure 3.4: The proportions of the solution vector

Singular value decompositions of the Jacobian were computed to gain further insights on how the near singular Jacobian affects the system. One example is given in figure 3.6 where the state vector associated with the smallest singular value was added to the original configuration. Comparing figures 3.6b with 3.6a shows the singular mode is associated with the same partitions in figure 3.4. This confirms the role of near singular conditions leading to poor solver performance. Many near singular conditions were visualized in the same way. In general the singularity occurred at the end of the wake near filaments with large strength. Furthermore, the singularities would occur more often around the strong root filament than the tip filament. To obtain accurate results on the blade only a short portion of the wake needs to be resolved. However, truncated wakes introduce distortion. Using far-wake models with short resolved wakes has helped avoid singularities due to long wakes. There are limits though, very short resolved wakes can lead to errors in the solution.

The role of singularities in solver stall suggests the solver can be improved with algorithms that are not sensitive to singularities. One attractive algorithm is the Levenberg-Marquardt update [218, 219] shown in equation (3.12). It is clear that singularities can be eliminated from the system by increasing the numerical tuning parameter γ. When γ is small, the search direction is similar to a Newton update, when it is large the search direction is similar to a steepest descent update. However, in practice this algorithm would only make good progress in the first few iterations and then quickly the performance would drop-off. Unlike the full Newton update the

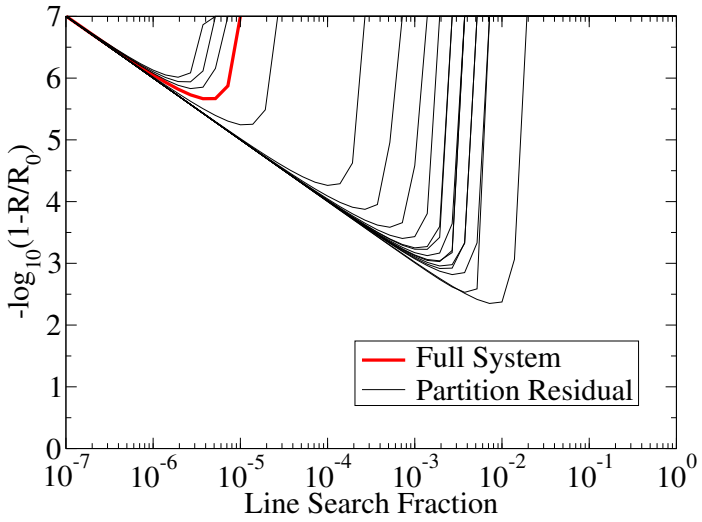

Figure 3.5: Search performance with near singular solutions

Levenberg-Marquardt algorithm was never able to find the solution to any problem. Furthermore the Levenberg-Marquardt algorithms tended to push the system into configurations where the condition number in the Jacobian had increased. In these cases further improvements with either the Levenberg-Marquardt or the full Newton algorithm was nearly impossible. Thus, in general best performance is achieved when the full Newton algorithm is used throughout the solution process.

$$\Delta \boldsymbol{X} = \left[\boldsymbol{J}^T \boldsymbol{J} + \gamma \boldsymbol{I}\right]^{-1} \boldsymbol{J}^T \boldsymbol{R} \tag{3.12}$$

Since Levenberg-Marquardt algorithm performed poorly, solver performance can only be improved by avoiding near singular conditions. A Jacobian will have a small singular value when changes in the state in a particular direction will only produce small variations in the residual. The key to avoiding singular conditions is to understand all the different scenarios where this condition will arise and to have strategies to avoid them.

The singular mode visualizations showed that all singularities occurred in the wake, indicating that equation (3.3b) is the source of these near singular conditions. There are three components to equation (3.3b): the velocity of the element, the state independent flow field (*i.e.* the wind), and the state dependent flow field (*i.e.* the influence calculation from Biot-Savart law). Since state independent contributions are ignored in the Jacobian, the singularities are born out of interactions between

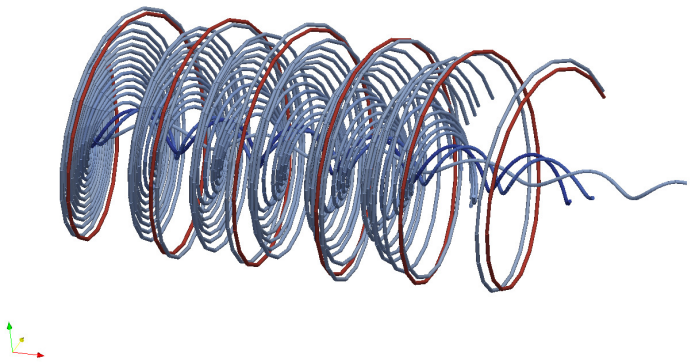

(a) Original configuration

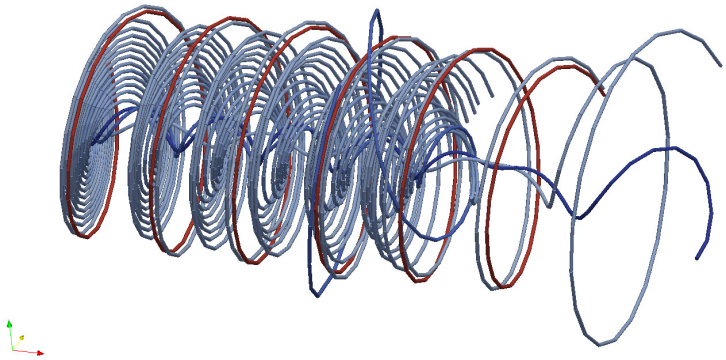

(b) Original with singular mode

Figure 3.6: The singular mode of the solution vector

the element velocity and state dependent flow-field. In other words, the solver can reduce the residual by aligning the element velocity to the flow field or it can adjust the influence configuration such that the flow field is aligned to the element. When the system is in a configuration where the changes due to these two strategies are in nearly equal and opposite in direction then singularities occur.

One example where the solver is faced with opposing effects is in the strength state on the lifting line. The residual on the lifting line will force strength to change in a particular direction, however this strength is an important parameter in the Biot-Savart law for the advection residual. This singularity can be removed by solving the wake separately from the lifting line strength. This algorithm involves making a

small change to the lifting line strength, then solving the wake configuration before making another update to the lifting line strength. This is similar to the load-stepping algorithms used in the nonlinear structural FEM problems.

Separating the lifting line strength update from the wake update is still not sufficient to avoid all singularities. Due to the velocity term, the position of the down stream elements depend on the positions of upstream elements. There is a tendency where updates are integrated down the length of the wake. Singularities can arise when updates in the near wake oppose the updates in the far-wake. To overcome these singularities the wake is broken up into partitions by filament age. Since residual tends to move downstream, best performance is achieved by updating the near wake first, then moving down stream. The partitions need to be overlapped to suppress distortions at the partition boundaries.

Again partitioning the wake will not completely eliminate singularities. The singularities seem to be strongly associated with Biot-Savart based influence, which produces a strong influence very close the to the element. The near-field influence can be attenuated by increasing the core radius (d_c in equation (2.45)). This has led to singular conditions being suppressed in stubborn problems. In this case the influence calculation will only use an enlarged core-radius when calculating the influence at a position in the wake. This way the influence on the lifting line is not directly effected by the enlarged radius, only indirectly due to a different wake configuration at the solution. Attenuating the near-field influence should not affect the axial induction over a large region, but it will reduce the degree of vortex roll-up around strong filaments. Vortex roll-up is not important in wing simulation [133] and should not be important in wind turbine simulations. When near-field effects are desired, the original small-core radius solution can still be recovered from the large core-radius solution because the solution of the large core-radius simulation is a good initial guess for the original small core-radius simulations. With this initial the original small core solution can be obtained with little difficulty.

Without the singularity avoidance strategies only small simple problems can be solved with algorithm 1 on the full system. When algorithm 1 fails to solve the full system, the next best approach is to apply the circulation strength stepping algorithm. When algorithm 1 fails to solve the wake, then the wake is partitioned and updated in parts. Finally, when singularities occur in the wake solve the core radius is enlarged. At the time of writing all problems that have originally failed without singularity avoidance, could be solved once these strategies were applied to varying degrees.

Each of these strategies will speed up the analysis for near singular problems, however in cases where no singularities occur these strategies slow down the analysis due to unnecessary iterations. For obtaining single solutions the user can simply employ these additional strategies as necessary. However in optimization this process needs to be automated. The solver can detect near singular conditions when the β solution to algorithm 2 falls below a specified value. This has been successfully applied to automatically transition from the full system to the strength stepping algorithm. Then again to transition from the full wake solve to a partitioned wake solve. In iterative schemes where the solver is starting from a previous solution, these two strategies are sufficient to avoid singularities.

The automated scheme does not work for all problems. Sometimes the line search for a full system update will find the minimum system residual at a high relaxation factor. As shown in figure 3.5 this can lead to increases in the residual for a small region and force that part of the system into strange configurations that neither singularity avoidance strategy can over-come. In these cases the solver must re-started from the beginning and use the circulation strength stepping algorithm throughout the whole solution process.

3.1.5 Advantages of the new formulation

The new formulation addresses the limitations of conventional LVD listed at the beginning of this chapter. The kinematic description described in section 3.1.1 addresses the first limitation:

1) Independent number of control points and influence elements: Since a position on a streak-line can be evaluated at any age, this parameterization places no restrictions on the number of influencing elements used to represent a vortex filament (*e.g.* figure 3.1b). Similarly since the nodes of the influence element are not constrained to the control points defining the streak-line, control points can either be added for improved path fidelity or removed to accelerate the computations (*e.g.* figure 3.1c). Overall this leads to reduce computational complexity compared to conventional LVD[6].

The error function described in section 3.1.2 addresses the second limitation:

[6]The number of control points in conventional LVD is coupled to the number of elements. By decoupling these quantities the computational scaling is improved. For more details see section 3.2.2.

2) The level of convergence is well defined: The model is considered solved when the algorithm finds a set of lifting line strengths (*i.e.* Γ_i) and control point positions (*i.e.* $\boldsymbol{X}_{xj}$) where the error in equation (3.2b) and equation (3.3b) approaches 0 for all lifting line elements and control points respectively. There is no uncertainty in a convergence criteria defined by equations (3.2b) and (3.3b) because it is only dependent on the current state.

Adopting the Newton based solution algorithms described in section 3.1.4 addresses many more deficiencies:

3) The instabilities are eliminated by avoiding time evolution: The instabilities of conventional LVD are rooted in the chaotic time evolution of vortices. Since the solution is evolved based on the Jacobian (instead of the time evolution) these instabilities are eliminated[7].

4) The aerodynamic and structural models can be solved simultaneously: Both linear and nonlinear structural models take the same form as equation (3.11). Typically a relaxed Newton iteration similar to the one shown in algorithm 1 is used to solve nonlinear structural models. Thus this new aerodynamic formulation can be tightly coupled[8] to the structural model and solved in a single Newton iteration. This improves upon conventional LVD by eliminating the additional Gauss-Siedel iteration required to resolve consistency constraints.

5) Faster convergence without path dependency: Since the solution in the new formulation is defined by equation (3.11) the solver should arrive to the same solution regardless of initial guess. This is beneficial in optimization routines because previous numerical solutions can be used as the initial guess in algorithm 1 and reducing the number of iterations required to get the next solution[9].

[7] It may seem counter-intuitive that the FEM-based LVD is stable while the underlying governing equations are not necessarily stable. The Newton algorithm simply finds a solution where the configuration should not change in time $d\bullet/dt = 0$ (where $\bullet$ is some arbitrary state variable). However, this does not guarantee that the solution is stable in time, if $d^2\bullet/dtd\bullet \geq 0$ then the solution will easily diverge from the solution. In contrast, given that a solution where $d\bullet/dt = 0$ may exist, there is no guarantee that the time evolution of the system will approach this solution from an arbitrary configuration. See Khalil [220] for more details on stability theory.

[8] When the aerodynamic and structural models are tightly coupled the state vector $\boldsymbol{X}$ and residual vector $\boldsymbol{R}$ contain terms from both the aerodynamic and the structural model. This leads to a formulation where the fully coupled system takes the form in equation (3.11) and can be solved as a single system.

[9] In gradient based optimization the changes in the system become small where previous solutions are very close to the next solution

The items 3 and 5 above should improve accuracy for gradient calculations based on finite differencing. Yet finite differencing requires a solution to equation (3.11) for every design variable. This fact highlights another benefit of casting LVD into the form in equation (3.11):

6) Fast and analytic gradients can be obtained: When the system is expressed in the same form as equation (3.11) adjoint based gradient algorithms can solve all the design sensitivities by solving a linear system similar to the Jacobian. For more details on adjoint methods see section 2.4.2 in chapter 2 or Giles and Pierce [210]. This is a dramatic improvement over finite differencing where algorithm 1 is executed for each design variable which in-turn requires multiple solutions to the Jacobian.

In summary the overall advantages to this new formulation is it provides the required reliability for optimization with several options to make the overall process faster. The reliability comes from the ability to locally refine the model for accuracy; a well defined error measure; and a solution algorithm that is not based on chaotic time evolution. The solution algorithm adds extra computational loads since it requires solutions to the Jacobian. Yet this formulation can be accelerated by reducing the number of control points in less critical regions. When considering the overall aeroelastic optimization process further efficiencies can be found by tightly coupling the aerodynamic and structural model; using previous numerical solutions to accelerate convergence; and relying on adjoint methods to calculate design sensitivities.

3.2 Wind Turbine Results

This work was motivated by the challenges of incorporating conventional LVD into gradient based optimization. To demonstrate these challenges sections 3.2.1 demonstrates how error evolves with conventional solution algorithms and gives an estimate of the error associated with iterative convergence.

The remaining sections are devoted to demonstrating the capabilities of the new FEM based LVD method. Section 3.2.2 presents several convergence studies to understand the effects of many of the grid parameters in the new FEM-based LVD method. The FEM interpolation is controlled by the choice of basis functions and coordinate system, section 3.2.3 compares Lagrange and Hermite interpolating polynomials within both Cartesian and Cylindrical coordinate systems. Section 3.2.4

demonstrates the different ways a FEM based LVD model can be terminated with far-wake models and fixing the physical length of the wake[10]. Section 3.2.5 demonstrates how the FEM-based LVD method uses a merged vortex filament model to have highly resolved flow fields along the blade with only minimal amount of elements in the wake.

All the simulations in this section are based on the MEXICO wind tunnel experiments [217]. The Mexico experiments tested a 4.5m diameter rotor and collected surface pressure and Particle Image Velocimetry (PIV) measurements that tracked the tip vortex positions making this data set ideal for validating LVD simulations. The experiments provided measurements for several operating conditions, this section only simulated the design conditions at $15m/s$, additional operating conditions are presented in the the validation section (see section 3.3.3).

3.2.1 Residual of Conventional LVD

A system residual can be defined for conventional LVD simulation by taking the norm of equations (3.2b) and (3.3b) applied to all lifting line elements and wake nodes respectively. The node locations for the time marching solution are taken to be control point locations in an equivalent FEM parameterization (*i.e.* a linear basis section for each element). Figure 3.7 shows the residual of a time marching simulation that had 8 span-wise elements on the lifting line. Initially, the wake had no elements; for the first 1000 iterations 5° elements were added to the wake. After the wake stops growing, the solver evolves the positions of a finite length wake.

Initially, figure 3.7a shows the residual growing because elements are being added to a transient flow field. Once the wake stops growing, the error decays for approximately 300 iterations. The effects of numerical noise is apparent from the small chaotic fluctuations throughout the simulation. For the first 1300 iterations this error has no impact on the overall trend. However, after 1300 iterations, large chaotic fluctuations begin to appear and eventually the simulation is overwhelmed and begins to diverge. This shows that large conventional LVD simulations cannot be converged arbitrarily. Furthermore, the small scale noise that is present throughout can lead to erroneous gradients, because typical gradient algorithms like finite-differencing are very sensitive to small variations.

[10]Fixing the physical length is something that can not be easily achieved with conventional LVD methods

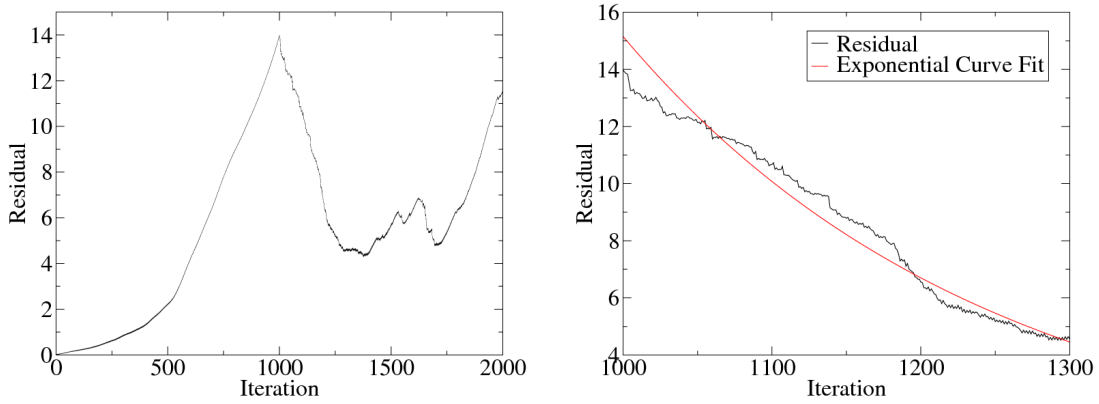

(a) Residual behavior over solve (b) Zoom of residual decay

Figure 3.7: Conventual LVD residual for growing (1000 iterations) then iterating wake

The residual decay through iteration 1000 to 1300 demonstrates best-case performance of the conventional algorithm. From figure 3.7b a decay rate of 0.4% was estimated with an exponential curve fit. Assuming that convergence metrics follow a similar exponential trend, an expected error can be estimated for solutions defined by iterative convergence. First, it is assumed that the evolution of the convergence metric can be approximated by (3.13a) where C is the convergence metric, C_0 is the initial value and C_∞ is the true solution.

$$C = C_\infty + C_0 \exp r_c n \tag{3.13a}$$

In conventional LVD with iterative convergence a solution is obtained when condition (3.13b) is met.

$$\frac{dC}{dn} < \epsilon_c \tag{3.13b}$$

Combining (3.13a) and (3.13b) an upper bound estimate for the error can be defined in terms of the tolerance and decay rate.

$$\begin{aligned} C_0 r_c \exp r_c n &< \epsilon_c \\ r_c(C - C_\infty) &< \epsilon_c \\ C - C_\infty &< \frac{\epsilon_c}{r_c} \end{aligned} \tag{3.13c}$$

Assuming similar decay rates for the convergence metrics, the error in the final solution for this simulation would be approximately 250 times the iterative convergence tolerance. This suggests smaller iterative error tolerance is required to overcome the additional error due to slow decay. Yet, the presence of small scale noise gives a lower bound to this tolerance, otherwise the condition in (3.13b) would never be met. Furthermore, equation (3.13c) shows that the numerical behavior of the solver will affect the final solution. This can be problematic in optimization or design applications when different configurations with different decay rates are being compared. Since these simulations cannot be converged arbitrarily, it is difficult to control or limit the error to ensure different solutions are comparable.

Smaller LVD simulations, with fewer vortex elements in the wake, show improved behavior. Figure 3.8 shows the residual for a simulation identical to the one in figure 3.7, except that it is started with 288 elements in the wake, in a helical configuration, with no additional elements added. As before, the simulation shows an initially growing residual; in this simulation this is caused by the growth of initial transient motion of the wake. The peak residual occurs at time step 283 after which the error decays as the transients advect out of the simulation. The simulation settled into a stable oscillation after 360 iterations (the full simulation completed 2000 iterations). Smaller simulations exhibit better stability overall, however, the numerical noise is relatively more significant leading to increased error in the gradient calculations. Again, this makes it very difficult to use these models in design and optimization applications.

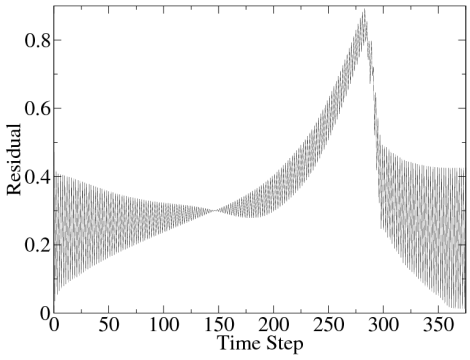

Figure 3.8: The residual of conventional LVD with a static wake of 288 elements

3.2.2 Convergence Studies

Influencing Element Size Convergence Study

Figure 3.9 shows the results for a study that varied the size of the elements from 2 degrees to 24 degrees. The wind turbine simulation used 8 elements on the blade, 4 revolutions in the resolved wake, a cylindrical far-wake model and 24 basis sections with Hermite interpolating polynomials. Figure 3.9a shows improved agreement with smaller elements. Figure 3.9c and 3.9d show this improvement is due to improved agreement in the bound circulation near the tip and wake expansion respectively.

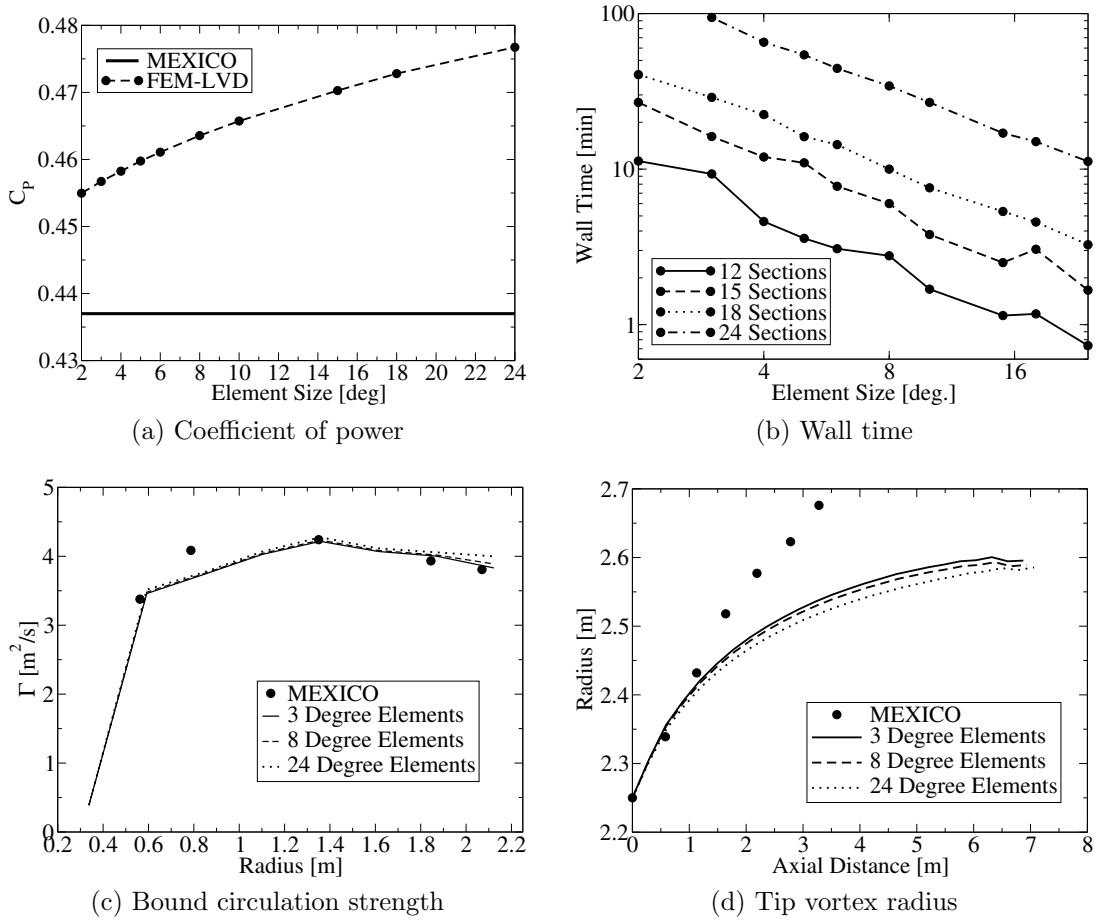

(a) Coefficient of power

(b) Wall time

(c) Bound circulation strength

(d) Tip vortex radius

Figure 3.9: Element size convergence study

Figure 3.9b shows the time required to solve these simulations. Power law regression of the trend lines in figure 3.9b confirms that the FEM simulation time scales linearly with the number of elements, which is a significant improvement over conventional LVD simulations with cubic scaling. Without an objective convergence metric

in conventional LVD, it is difficult to compare solution times directly. The results in section 3.2.1 demonstrate that the residual will increase until the solver completes the same number of time steps as elements in the truncated wake. This suggests that the number of time steps required to achieve optimal convergence in a conventional LVD simulation is proportionate to the number of elements in the truncated wake. In place of a defined solution time, the ratio of time steps completed by the solver vs. the number of elements in the wake is used as an estimate to the level of completion in a conventional LVD simulation. Figure 3.10 shows the time step ratio achieved within the solution time of the equivalent FEM based LVD simulation. Two different conventional LVD configurations were compared, the first started with a growing wake, the second started with a pre-initialized wake. These configurations were compared with FEM based LVD simulations with a variable number of basis sections. The numbers in the series name indicate the number of basis sections used in the FEM-based LVD simulation. The results in figure 3.10 show that FEM based LVD simulations are much faster than conventional LVD simulations when small elements are used.

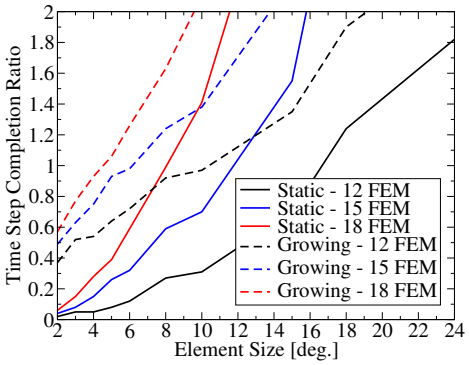

Figure 3.10: Completion comparison vs. element size

The linear complexity proves that the FEM formulation reduces the computational complexity with the number of elements. Unlike conventional LVD which has $O(N^3)$ scaling with the number of elements, the FEM-based LVD model has improved scaling in two ways. First, the Biot-Savart calculation is not required at every element in FEM-based LVD. Instead it is only required at M integration points, where the number of integration points scale with the number of control points. This leads to $O(NM)$ complexity every iteration where $M < N$. Second, since the solution algorithm does not rely on time marching, the number of iterations required does

not necessarily scale with the number of elements. The linear complexity in figure 3.9b shows the number of solver iterations is insensitive to the number of elements. However, the wake length convergence study will show this reduced complexity is not universal. When more elements are added to achieve a physically longer wake, more control points are required and the solver requires more iterations to solve the larger wake; thus cubic scaling still occurs.

Basis Section Convergence Study

Figure 3.11 shows the effect of varying the number of basis sections in a simulation. The FEM-based LVD simulations had 8 elements on the blade and resolved 4 revolutions of the wake with 288 influencing elements for each trailing filament. The basis sections used Hermite interpolating polynomials. The wake was terminated with a vortex cylinder far-wake model. Figure 3.11a shows that the number of basis sections only effects the results when there are less than 15 basis sections and there are not enough control points to properly resolve the solution. Figure 3.11b shows that using a small number of basis sections can improve the solution times dramatically. Improvements in solver speed are very important in optimization when multiple functions evaluations are required.

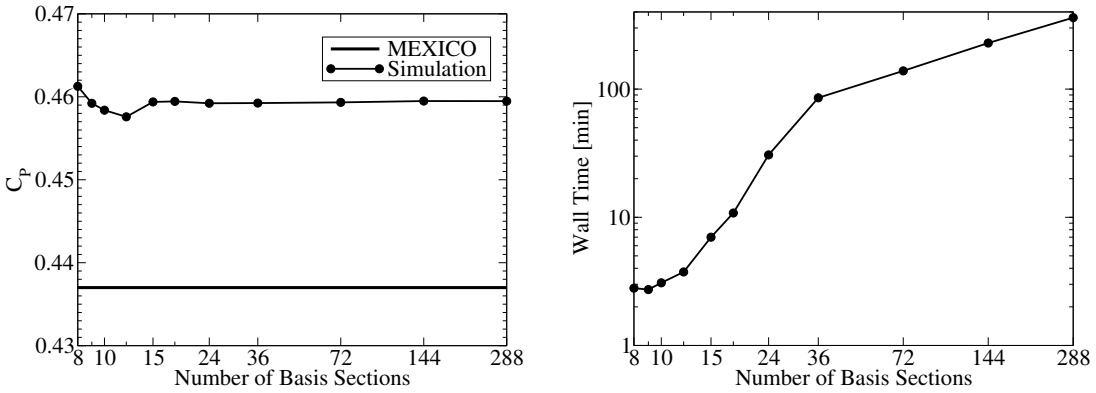

(a) Coefficient of power (b) Wall time

Figure 3.11: Basis section convergence study

Wake Length Convergence Study

Figure 3.12 shows the effects of varying the length of the resolved wake. These simulations had 8 elements on the span. In the wake, 6 basis sections with Hermite interpolating polynomials were used for each rotor revolution. The elements in the

wake are 18° in size, which corresponds to 20 elements per wake revolution. The simulations employed a cylindrical far-wake model to compensate for the truncated wake. Figure 3.12a shows that increasing the length of the resolved wake past 3 rotor revolutions does not have a significant effect on the flow at the rotor. Figure 3.12b confirms that the near wake flow is preserved when a shorter resolved wake is used with a far-wake model. Figure 3.12c shows the simulation time scales with the cube of the number of elements according to power law regression.

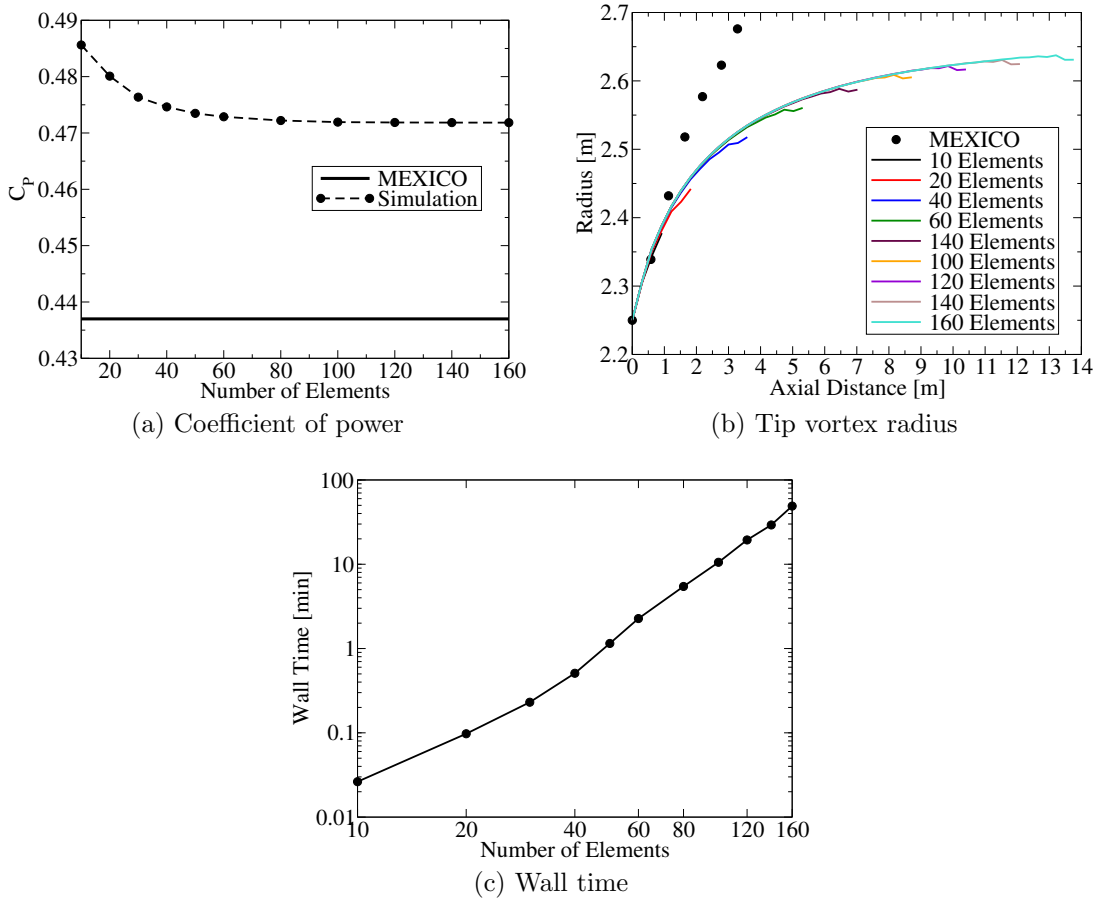

(a) Coefficient of power

(b) Tip vortex radius

(c) Wall time

Figure 3.12: Wake length convergence study results

Span-wise Convergence Study

The number of elements along the blade was varied to give the results in figure 3.13. The greatest variation in bound circulation strength occurs near the root and the tip of the blade. To adequately capture these effect, it is common practice to use a cosine spacing on the blade. However, in FEM-based LVD simulations this can

lead to singular conditions. To avoid this, these simulations used regular spacing in all cases. Each trailing filament in the free wake was modeled with 80 influencing elements to resolve 4 rotor revolutions. All the simulations used 16 basis sections for each trailing filament with Hermite interpolating polynomials. The free wake was terminated with semi-infinite vortex cylinders in the far-wake. Figure 3.13a shows that the C_P convergence is achieved with 23 elements. Adding elements to the blade did not give improved C_P agreement because the overall magnitude in bound circulation (figure 3.13c) and wake expansion (figure 3.13d) seems insensitive to span-wise resolution. Figure 3.13b shows how the simulation time varies with the number of elements, A power law curve fit shows $O\left(n^{2.6}\right)$ scaling in time. Hence the majority of the additional computation time is due to the increase in both integration points and influencing elements. The effect of more elements is noticed in the strength distribution in figure 3.13c, where more elements give improved resolution in the bound circulation. Starting at 23 elements, it is clear that the tip loss is starting to be resolved. With tip loss, there are multiple vortices in the tip region with significant strength causing roll-up to be resolved as waves in figure 3.13d.

3.2.3 Vortex Position Interpolation

Large basis sections in wind turbine simulations can introduce significant error in the vortex position due to the FE interpolation in the wake. To demonstrate these errors several simulations with different interpolation schemes were used to model 4 revolutions of a wake without a far-wake model. The Lagrange results in figure 3.14a[11] exemplify the errors introduced with quadratic Lagrange polynomials in a Cartesian reference frame. The plot shows that with larger basis sections, large oscillations start to form and the mean radius is reduced. Figure 3.14b shows that this error prevents grid converged C_P solutions until 24 basis sections.

The dips are caused by interpolation in a Cartesian reference frame[12], while these dips are exacerbated by the C^1 discontinuities at the boundaries of the basis sections. These discontinuities are caused by the first and second terms of equation (3.3a) (the two dominant terms). The second term resembles a sinusoid which is easily approximated by the first term when C^1 continuity is not enforced at the boundaries of the basis sections.

[11] The distortions are exaggerated by the unequal scaling on the axis

[12] A straight line in a Cartesian space connecting two points on a circle has a radial position less than the radius of the circle.

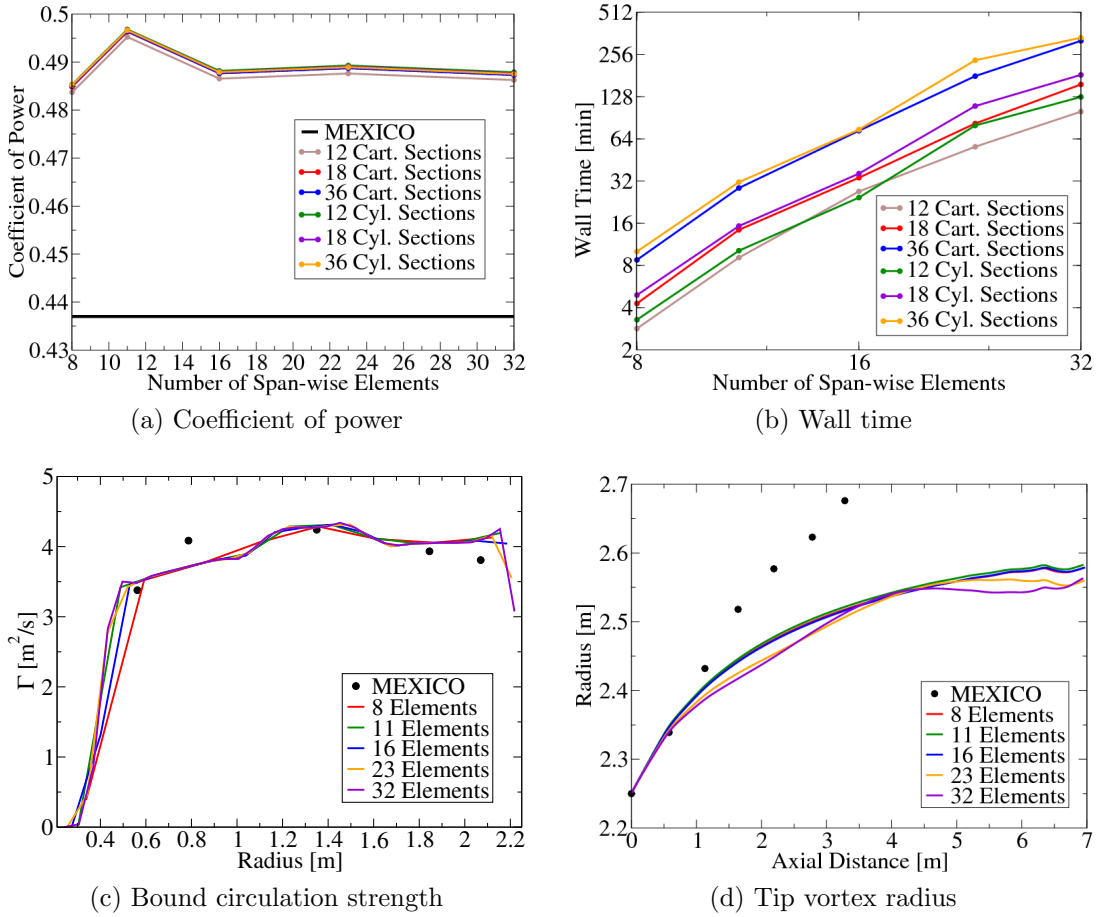

(a) Coefficient of power

(b) Wall time

(c) Bound circulation strength

(d) Tip vortex radius

Figure 3.13: Span-wise convergence study results

The Hermite results in figure 3.14 show the same simulation except C^1 continuity is enforced with Hermite interpolating polynomials. The Hermite data in figure 3.14a show reduced distortion in the vortex position. The Hermite results in figure 3.14b show the C_P starts to diverge at the same grid resolutions as the Lagrange polynomial, but the level of divergence is significantly less.

The Cylindrical results in figure 3.14 show the effect of interpolating quadratic Lagrange polynomials in a cylindrical coordinate system. Figure 3.14a show no distortion in the position when interpolating in a cylindrical coordinate system and the cylindrical results in figure 3.14b shows significantly less C_P divergence at the larger grid spacings. However, solving the system in the cylindrical coordinate system is more expensive for the solver because the solver must use circulation strength stepping strategy to overcome solver stall.

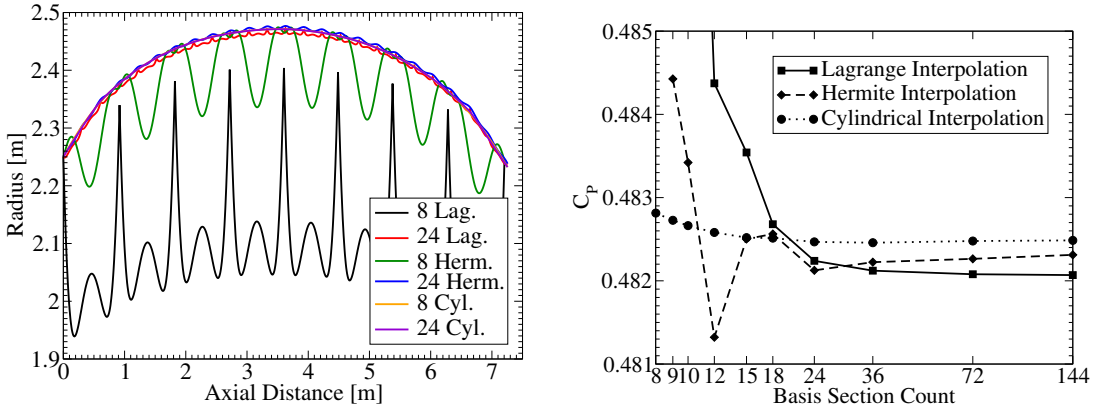

(a) Vortex radius (b) Coefficient of power

Figure 3.14: Errors due to vortex position interpolation

Interpolation with Lagrange polynomials in a Cartesian reference frame produces large distortions in the wake and poor grid convergence. Interpolation with Hermite interpolating polynomials can reduce the distortions and give better grid convergence but errors still exist. For best results, interpolation within a cylindrical reference frame removes all distortions, however, simulations with Cylindrical interpolation can be slower. Thus most simulations used Hermite interpolating polynomials in a Cartesian reference frame.

3.2.4 Free Wake Termination

Figure 3.15 shows results for the different ways the resolved wake can be terminated in the FEM based LVD model.

The simple termination case is where no far-wake model is used and the axial positions are free to float. Figure 3.15a shows that the C_P solution can be improved by using a vortex cylinder model (see [27] for vortex cylinder solution) attached at the ends of the vortex filaments. The vortex cylinder solution is based on the resolved vortex pitch, which is calculated using linear regression. Figure 3.15a shows the number of regression points has little impact on C_P, but figure 3.15b shows more points adds to the solution time.

Figure 3.15c shows that the transition from a discrete vortex element to a diffuse vortex cylinder can introduce a small distortion in the vortex position. This distortion can be mitigated by introducing a small vortex spiral between the resolved filament and the cylinder model. Figure 3.15b shows this spiral transition is expensive.

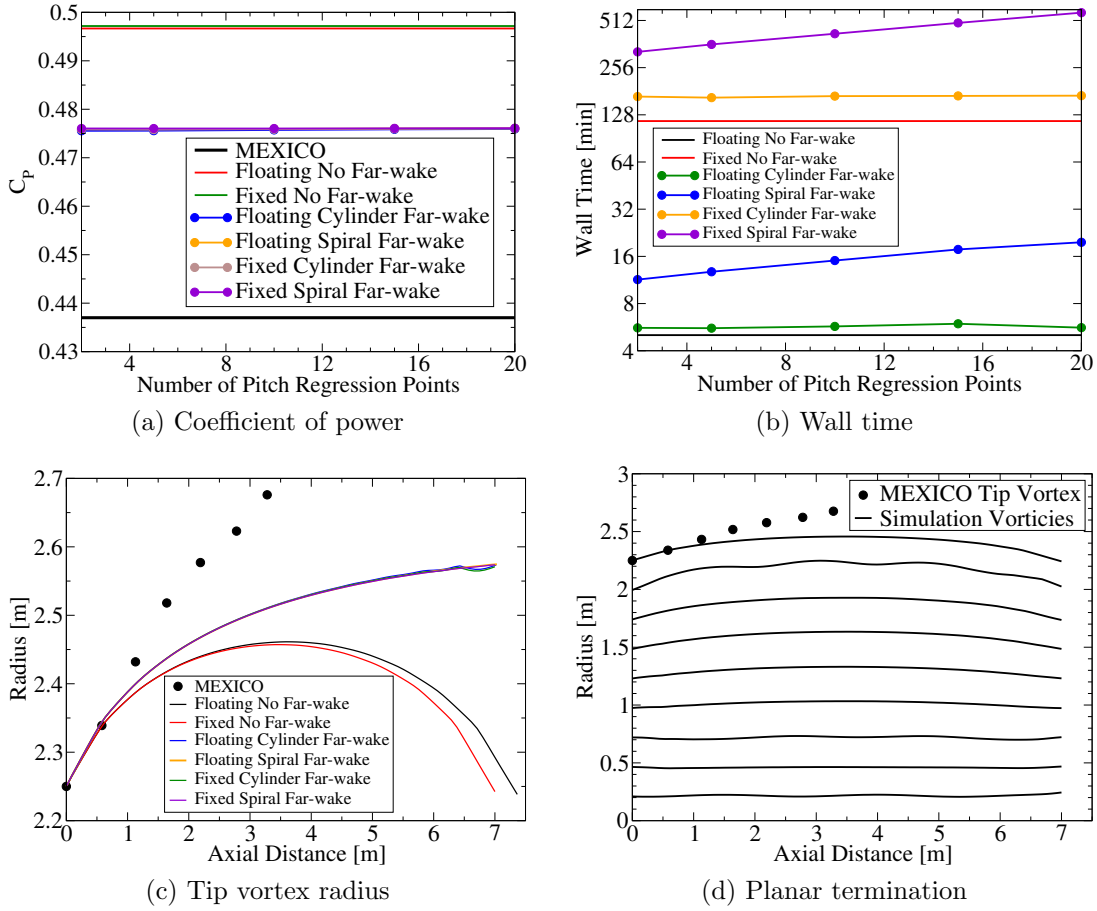

(a) Coefficient of power

(b) Wall time

(c) Tip vortex radius

(d) Planar termination

Figure 3.15: Comparison of wake termination cases

Another potential source of distortion is caused by the axial induction in the wake, which leads to mid-span filaments terminating early. The conditions that follow these filaments (*i.e.* a far-wake model or the absence of vorticity) could negatively influence the remaining resolved wake. The FEM based LVD model allows one to fix the axial position where filaments are terminated; in these cases the age of the vortex filament becomes a free variable. Figure 3.15d shows a vortex filament solution with a fixed termination at 7m. Figures 3.15a and 3.15c show fixed termination has little impact on the results. Figure 3.15b shows this condition complicates the solution process and requires many more iterations, making this approach unattractive.

Overall, the results in figure 3.15 show the best configuration for accuracy and solution time is a vortex cylinder model with 2 pitch regression nodes and no spiral transition.

3.2.5 Merged Filaments

In wind turbine wakes it is common for the strong vorticity trailed at the wake to roll-up into a single cloud of vorticity. Simulating that cloud with multiple filaments is expensive and offers little advantage in resolving the flow at the blade. The simulations can be improved by merging the filaments and only simulating a pair of filaments. This is possible in conventional LVD, however, in this case the elements are merged in discrete operation that could effect the evolution of the wake. By avoiding time evolution the FEM-based LVD method avoids these discrete changes to the wake and solves the system, while maintaining the same merged filament configuration throughout.

The starting position of the merged filament ($\boldsymbol{x}_m$) is based on a strength weighted average of the end positions of the source filaments ($\boldsymbol{x}_i$) as shown in equation (3.14). The weighting used in the average must be positive to ensure the merged position is near all the other positions[13]. It has been observed that the filaments will roll up around the strongest filament. To achieve this in the merging, the weights have been squared. Another benefit of this weighting function (as oppose to $|\Gamma_i|$) is the absence of discontinuities when the system is linearized.

$$\boldsymbol{x}_m = \frac{\sum \Gamma_i^2 \boldsymbol{x}_i}{\sum \Gamma_i^2} \tag{3.14}$$

The strength is merged simply by summing all the contributions of the merged filaments, as shown in equation (3.15). This approach is only valid when all the filaments in the sum (Γ_i) are of the same sign because merging a mix of positive and negative filaments will reduce the total amount of vorticity, which violates Helmholtz laws of vorticity conservation [186]. This is an acceptable limitation for simulating existing design because the maximum strength is typically in the center of the blade and decreases monotonically to either end. However this can be a problem when simulating strange configurations required by an optimization algorithm.

$$\boldsymbol{\Gamma}_m = \sum \Gamma_i \tag{3.15}$$

An important variable for employing merged filaments is the distance downstream where merging is initiated. Too short and there is error, too long and the solver becomes slow. The MEXICO wind turbine, at design conditions, was used to evaluate

[13] A mix of positive and negative weights would cause the merged position to approach the origin

the effect of this variable. Fifteen elements were use on the blade. Then sixteen trailing filaments were then merged into two filaments and the elements in the wake were 15°. The distance downstream where merging was initiated was varied from 1/6, up to 19/6 of a revolution. Sixty degree quadratic Lagrange polynomial basis sections were used for all the filaments. The merged filaments extended far enough back to resolve a total of 4 rotor revolutions. The wake was terminated at a vortex cylinder model. Figure 3.16 shows a visualization of one solution.

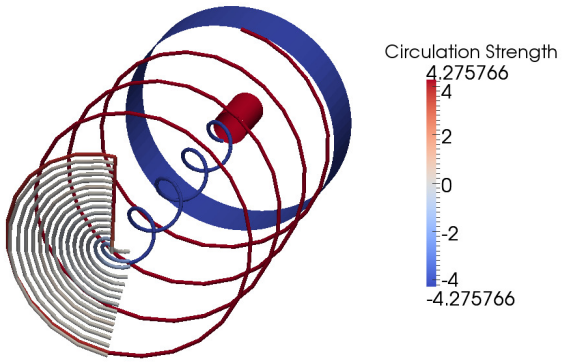

Figure 3.16: Visualization of merged filaments

Figure 3.17a shows a comparison with selected merged filament simulations with MEXICO measurements. Overall the results are very close to a highly resolved wake, which together gave good agreement with MEXICO. All the merged simulation results are within 2% of each other. The results show there is an improved solution by moving the merge location from 1/6 to 1/2, but merging further downstream has a diminished effect.

The effect on solver time is shown in figure 3.17b. For short fully resolved portions, the effect of additional elements is modest. However, when the fully resolved wake starts to approach 3 revolutions, solver stall starts to have a more dramatic affect on the solution speed. Thus merged filaments are beneficial not only for reducing the number of computational elements, but also for avoiding solver stall.

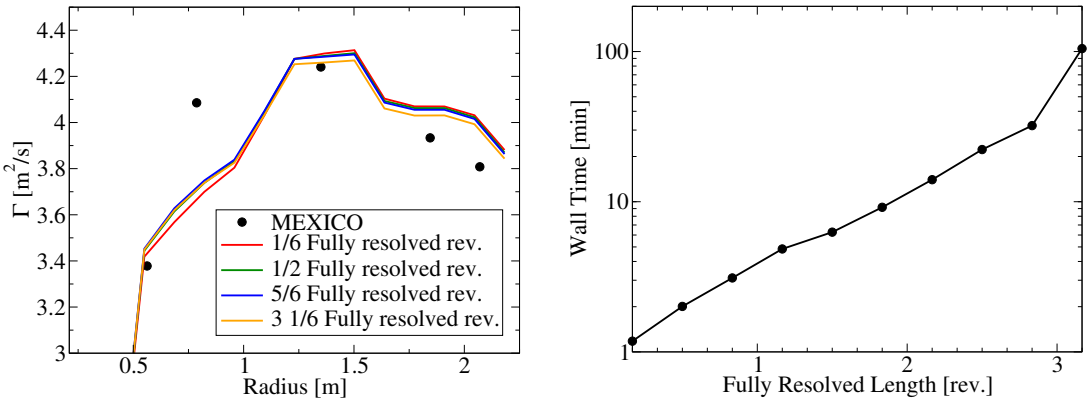

(a) Bound circulation strength (b) Wall time

Figure 3.17: Merged trailing filament results

3.3 Validation

This section gives a series of validation test cases where the FEM based LVD simulation is used to simulate an elliptically loaded wing (section 3.3.1), several experimentally tested wings (section 3.3.2) and a wind turbine under different operating conditions (section 3.3.3).

3.3.1 Elliptical Wing

The new FEM based LVD method was used to simulate a $20m$ wing with an elliptical circulation distribution, with a center span circulation strength of $3m^2/s$, in a $15m/s$ flow. The semi-span was simulated with 40 regularly spaced elements along the span. Symmetry was used to resolve the effect of the other half of the wing. The simulated wake was $40m$ long, with 250 regularly spaced elements for each trailing filament in the wake. The wake had a varying number of Hermite polynomials for the basis sections to explore the potential of reduced order models. Figure 3.18a shows all the simulations produced the same constant downwash as expected with an elliptical distribution [133]. The deviations near the tip are due to the lack of lifting line elements. The results show little difference between the different basis section solutions, suggesting that 4-5 basis sections are sufficient to resolve the flow field along the wing.

Two different conventional LVD configurations were used to simulate the wing for comparison purposes. The first starts with no elements in the wake and then grows the wake until it is fully populated, after which the algorithm evolves a fixed length

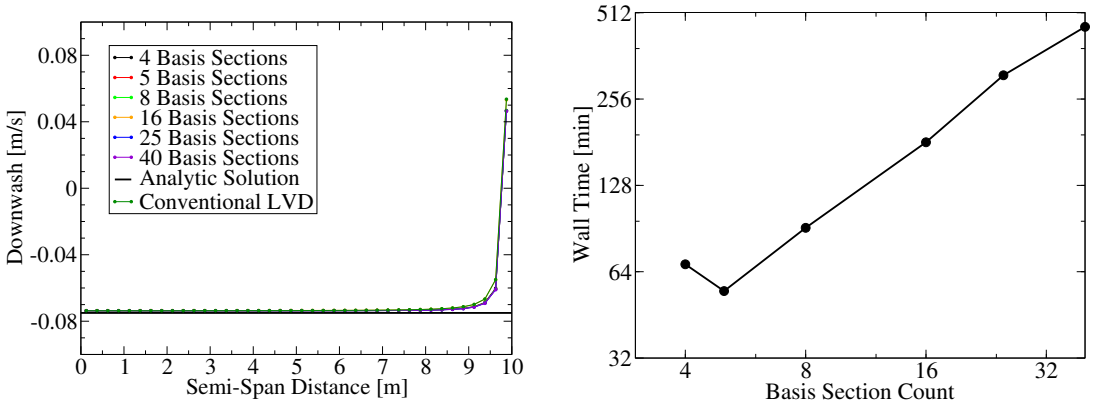

(a) Downwash solution (b) Wall time

Figure 3.18: FEM based LVD simulation results of an elliptical wing

wake. The second conventional configuration starts with full wake initially flat and adds no additional elements. The time step was chosen to give the same element length as the FEM based LVD simulation. The growing version of the conventional LVD simulation required a minimum of 250 iterations to fully grow the wake and expel the initial transients. When the conventional LVD simulation starts with an initial wake, 250 time steps are still required for the initial transients to advect out of the system. Both conventional configurations produced similar results. Only the growing wake solution is shown in figure 3.18. The conventional LVD produced results similar to the FEM-based LVD solution, with a negligible under-prediction of the downwash solution when compared with the FEM-based LVD results. Since both the conventional and the FEM simulations are based on the same governing equations, this confirms that the deviations at the tip from the FEM-based LVD are not due to the FEM formulation itself, but due to the poor grid resolution.

Figure 3.18b gives the time required to obtain each solution. Without a well defined convergence metric in conventional LVD, it is difficult to compare solution times between the FEM based LVD model and the conventional solution algorithms. Instead table 3.1 gives the number of iterations obtained with the conventional solution algorithm within the wall time of the simulation in figure 3.18b. The table shows that all the FEM solutions with less than 25 basis sections are faster than the conventional growing wake simulations, and all the FEM simulations are faster than the conventional static wake simulations.

Table 3.1: Iterations completed in the conventional LVD simulations within FEM solution times

FEM Basis Section Count	Conventional Growing Wake	Conventional Static Wake
4	172	26
5	160	21
8	190	36
16	239	72
25	291	123
40	350	182

3.3.2 Experimental Validation with Wings

The FEM based LVD simulation was compared with two wind tunnel experiments with wings. The first comparison, shown in figure 3.19a, shows good agreement between the simulation and experimental measurements by Mcalister and Takahashi [221] which measured the coefficient of lift using pressure taps on an untwisted rectangular wing. The different measurements were due to multiple tests with different tip geometries, which maintained the same rectangular plan-form, but modified the shape when viewed from the front. The FEM-based LVD model cannot resolve three dimensional geometry, so it is compared to all the measurements simultaneously. The simulation of this wing used experimental airfoil lift coefficients given by Sheldahl and Klimas [222] for a wide range of Reynolds number and angle of attack. The FEM-based LVD used 14 elements along the span. Each trailing filament use 60 influencing elements with 8 basis sections with Hermite interpolating polynomials.

Figure 3.19b shows acceptable agreement of a twisted, tapered, swept wing simulation with experiments by Mendelsohn and Brewer [223]. This simulation used 21 elements along the span. Each filament in the wake was modeled with 90 influencing elements on 4 basis sections with Hermite interpolating polynomials. The simulation used airfoil coefficients from XFoil. Error in the lift coefficients from XFoil would lead to circulation strength error, which would further exacerbate the lift coefficient errors due to errors in the downwash.

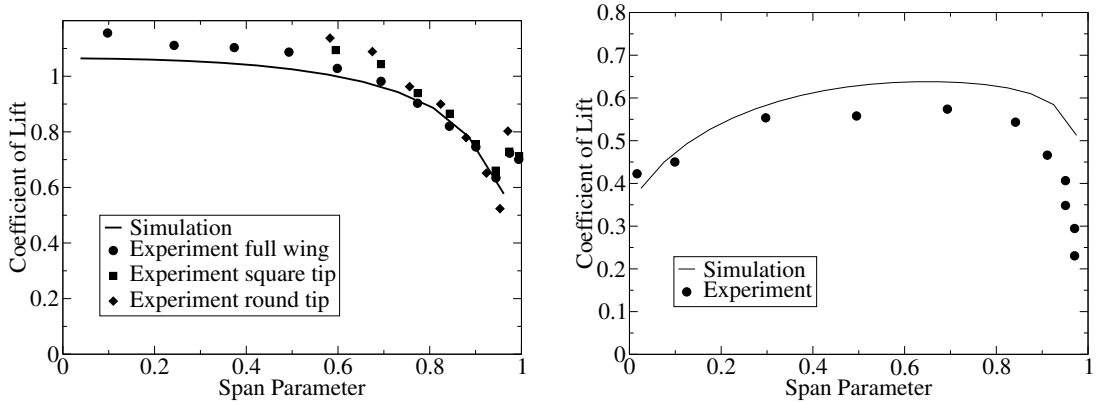

(a) Rectangular wings (b) Swept wings

Figure 3.19: Comparison of FEM based LVD simulation with wing experiments

3.3.3 Experimental Validation with Wind Turbines

The primary application of this code is to simulate wind turbines. For wind turbine validation the MEXICO wind tunnel experiments [217] provide an excellent collection of data for validation. The FEM-based LVD model was used to simulate the MEXICO rotor at 3 different wind speeds. The first is $10m/s$ representing high thrust conditions; the second is $15m/s$, the design wind speed and represents optimal conditions; the third is $24m/s$, a high velocity for the rotor and will lead to stall on the blade. Each of the FEM-based LVD simulations used 16 elements on the blade. Each trailing filament in the wake was 4 revolutions long, with 80 influencing elements and 36 basis sections in the wake with Hermite interpolating polynomials. The wake terminated with a vortex cylinder far-wake model.

The simulations are compared to experimental results in figure 3.20. Overall, the simulations show good agreement with the experiments. However, the simulation tends to over-predict the C_P and C_T slightly, whereas the over-prediction in C_P at $10m/s$ is significant. At high thrusts, wind turbine wakes are known to break down into a turbulent state [168]. Since a steady flow field is implicitly enforced in the formulation, the simulation is not able to adequately resolve the turbulent wake state. This error is acceptable considering turbines are designed to avoid extreme turbulent wake states. This simulation showed excellent agreement in the bound circulation, except at $24m/s$, where the blade is stalled over most of the span. The lift coefficients used in the simulation were based on 2-D experimental measurements without rotational effects. The source of the error could be due to rotational effects, which are known to change the stall behavior [224, 183, 225, 226]. Overall, the simulation was

able to match the wake expansion in the near wake; further downstream, the simulation under-predicted the wake expansion. This discrepancy is common in many other simulations of the MEXICO rotors with both grid based CFD and other lifting line codes [227]. Despite these errors the comparison shows the FEM-based LVD gives adequate predictions of wind turbine performance.

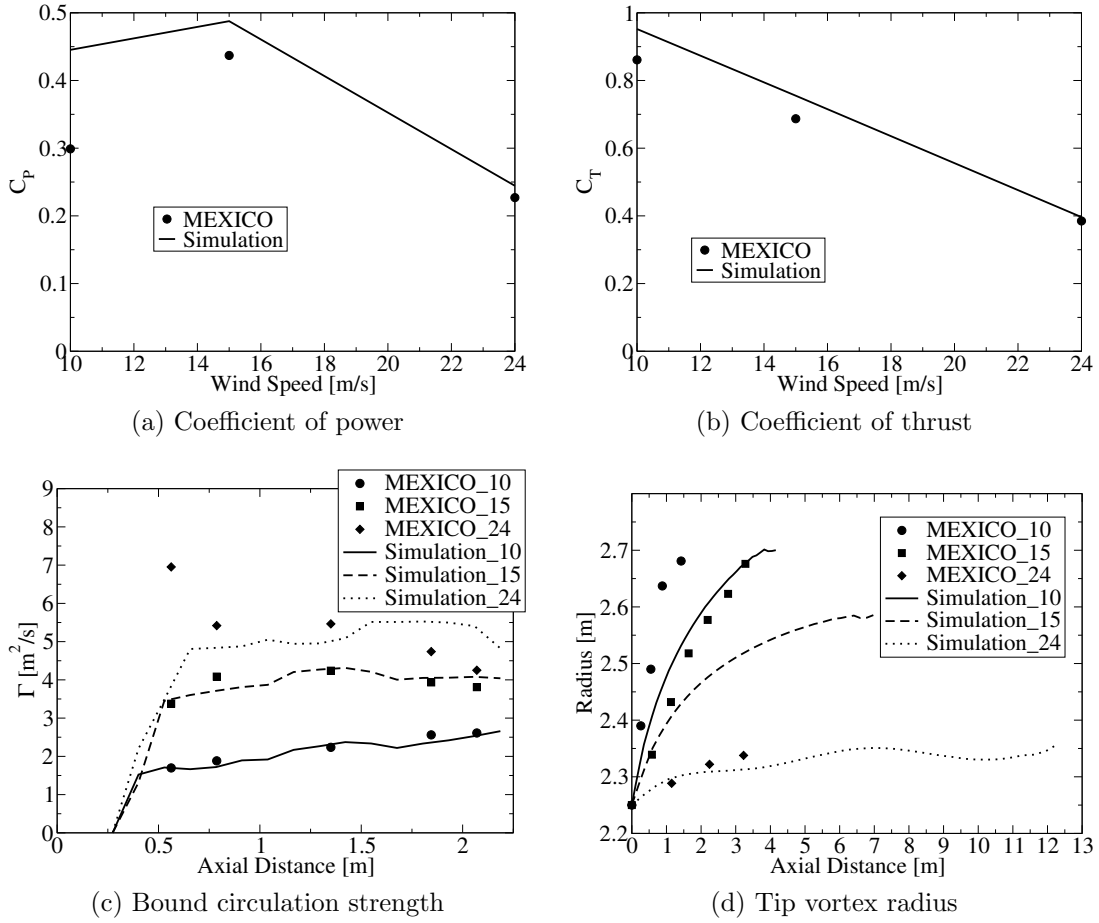

(a) Coefficient of power

(b) Coefficient of thrust

(c) Bound circulation strength

(d) Tip vortex radius

Figure 3.20: Wind turbine validation

Chapter 4

Aero-Elastic Analysis

One of the objectives for developing an FEM based LVD model was to avoid Gauss-Seidel iteration to obtain a coupled aerodynamic structural solution with LVD. The new FEM based LVD method was coupled with a linear beam model and used to solved the steady state aero-elastic solution of a wind turbine. As a comparison the same problem is solved with two different fixed point iterations with conventional LVD.

4.1 Theory

This section is devoted to extending the theory given in chapter 3 to develop a coupled model of an aero-structural system.

4.1.1 Aero-Structural Coupling

The structural model defines how the blade will deform based on applied forces and structural properties. The aerodynamic model contributes to the applied forces thus the coupled structural model is dependent on aerodynamic state variables. Similarly, since the bound circulation strength is dependent on angular deformation and the trailed vortex system is dependent on the blade positions, the aerodynamic model is also dependent on the structural model. This section will show how this coupling is introduced in the simulations.

The structural model is assumed to provide a position and orientation at any point along the span. These results are defined by equation (4.1a) for the positions and

equations (4.1b) through (4.1d), which give the direction vector for the cross section reference frame.

$$\boldsymbol{x} = \boldsymbol{b}_x(s) \qquad (4.1a) \qquad \hat{\boldsymbol{c}} = \boldsymbol{b}_c(s) \qquad (4.1b)$$

$$\hat{\boldsymbol{t}} = \boldsymbol{b}_t(s) \qquad (4.1c) \qquad \hat{\boldsymbol{s}} = \boldsymbol{b}_s(s) \qquad (4.1d)$$

In the purely aerodynamic model, the lifting line positions ($\boldsymbol{X}_p$) were assumed constant; in the coupled model, these positions are substituted with equation (4.1a). The angle of attack was calculated based on the relative flow vector and the cross section reference frame. The effect of angular deformation is introduced into the aerodynamic model by using the cross section reference frame given in equations (4.1b) through (4.1d).

The linearized aerodynamic model in chapter 3 is not affected by using (4.1a) since this model is already linearized about the vortex positions. However, the linearized angle of attack needed to be modified as shown in equation (4.2) to account for variations in the cross section reference frame.

$$\frac{\partial \alpha}{\partial \boldsymbol{X}} = \frac{\left(\hat{\boldsymbol{t}} \cdot \boldsymbol{w}\right) \hat{\boldsymbol{c}}^T \frac{\partial \boldsymbol{w}}{\partial \boldsymbol{X}} - \left(\hat{\boldsymbol{c}} \cdot \boldsymbol{w}\right) \hat{\boldsymbol{t}}^T \frac{\partial \boldsymbol{w}}{\partial \boldsymbol{X}} + \left(\hat{\boldsymbol{c}} \cdot \boldsymbol{w}\right) \boldsymbol{w}^T \frac{\partial \hat{\boldsymbol{t}}}{\partial \boldsymbol{X}} - \left(\hat{\boldsymbol{t}} \cdot \boldsymbol{w}\right) \boldsymbol{w}^T \frac{\partial \hat{\boldsymbol{c}}}{\partial \boldsymbol{X}}}{\left(\hat{\boldsymbol{t}} \cdot \boldsymbol{w}\right)^2 + \left(\hat{\boldsymbol{c}} \cdot \boldsymbol{w}\right)^2} \qquad (4.2)$$

The aerodynamic model affects the structural model through the aerodynamic forces. Equation 4.3 gives the aerodynamic forces per length, where $\hat{\boldsymbol{l}}$ and $\hat{\boldsymbol{d}}$ are the directions of the lift and drag forces respectively.

$$\boldsymbol{f}_a = \frac{1}{2} \rho \boldsymbol{w}^2 c \left(C_l \hat{\boldsymbol{l}} + C_d \hat{\boldsymbol{d}} \right) \qquad (4.3)$$

The lift and drag directions are defined by equations (4.4) and (4.5):

$$\hat{\boldsymbol{l}} = \hat{\boldsymbol{t}} \cos\alpha - \hat{\boldsymbol{c}} \sin\alpha \qquad (4.4)$$

$$\hat{\boldsymbol{d}} = \hat{\boldsymbol{c}} \cos\alpha + \hat{\boldsymbol{t}} \sin\alpha \qquad (4.5)$$

Similarly, the coefficient of pitching moment is used to get the distributed torsion on the blade as shown in equation (4.6).

$$\boldsymbol{m}_a = \frac{1}{2}\rho \boldsymbol{w}^2 c C_m \hat{\boldsymbol{s}} \tag{4.6}$$

Equation 4.7 shows how these distributed forces and moments are integrated over the beam with shape functions to get the equivalent nodal forces and moments.

$$\boldsymbol{F}_a = \int \eta(s) \left\{ \begin{array}{c} \boldsymbol{f} \\ \boldsymbol{m} \end{array} \right\} ds \tag{4.7}$$

The linearized forces are given in equation (4.8):

$$\frac{\partial \boldsymbol{F}_a}{\partial \boldsymbol{X}} = \int \eta(s) \left\{ \begin{array}{c} \frac{\partial \boldsymbol{f}}{\partial \boldsymbol{X}} \\ \frac{\partial \boldsymbol{m}}{\partial \boldsymbol{X}} \end{array} \right\} ds \tag{4.8}$$

where the distributed forces and moments are linearized as follows:

$$\begin{aligned} \frac{\partial \boldsymbol{f}_a}{\partial \boldsymbol{X}} &= \rho \boldsymbol{w} c \left(C_l \hat{\boldsymbol{l}} + C_d \hat{\boldsymbol{d}} \right) \frac{\partial \boldsymbol{w}}{\partial \boldsymbol{X}} \\ &\quad + \frac{1}{2}\rho \boldsymbol{w}^2 c \left(\left(\hat{\boldsymbol{l}} \frac{\partial C_l}{\partial \alpha} + \hat{\boldsymbol{d}} \frac{\partial C_d}{\partial \alpha} \right) \frac{\partial \alpha}{\partial \boldsymbol{X}} + \left(\hat{\boldsymbol{l}} \frac{\partial C_l}{\partial Re} + \hat{\boldsymbol{d}} \frac{\partial C_d}{\partial Re} \right) \frac{\rho c}{\mu} \frac{\partial \boldsymbol{w}}{\partial \boldsymbol{X}} \right) \\ &\quad + \frac{1}{2}\rho \boldsymbol{w}^2 c \left(C_l \frac{\partial \hat{\boldsymbol{l}}}{\partial \boldsymbol{X}} + C_d \frac{\partial \hat{\boldsymbol{d}}}{\partial \boldsymbol{X}} \right) \end{aligned} \tag{4.9}$$

$$\frac{\partial \boldsymbol{m}_a}{\partial \boldsymbol{X}} = \rho \boldsymbol{w} c C_m \hat{\boldsymbol{s}} \frac{\partial \boldsymbol{w}}{\partial \boldsymbol{X}} + \frac{1}{2}\rho \boldsymbol{w}^2 c \left(\left(\frac{\partial C_m}{\partial \alpha} \frac{\partial \alpha}{\partial \boldsymbol{X}} + \frac{\partial C_m}{\partial Re} \frac{\rho c}{\mu} \frac{\partial \boldsymbol{w}}{\partial \boldsymbol{X}} \right) \hat{\boldsymbol{s}} + C_m \frac{\partial \hat{\boldsymbol{s}}}{\partial \boldsymbol{X}} \right) \tag{4.10}$$

4.1.2 Solving the Aero-structural system with conventional LVD

To demonstrate the advantages of the FEM based LVD model over conventional LVD models for aero-elastic problems, the conventional LVD was used to solve aero elastic problems. The coupling described in section 4.1.1 still applies for conventional models, the differences lie in the solution algorithm. This section explains the solution algorithm of solving the conventional LVD model simultaneously.

Since the solution algorithm differs for the structural model, the two are models solved separately within a fixed point iteration as shown in figure 4.1. The simulation starts by calculating the forces and updating the beam configuration. Then, the new

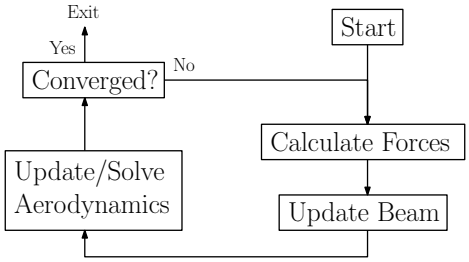

Figure 4.1: Schematic of the aero-elastic fixed point iteration for conventional LVD

lifting line configuration is passed to the aerodynamic model where the aerodynamic state is either updated or solved completely. The full system is considered solved when the difference in state between subsequent steps is within acceptable tolerance.

For flexible beams this solution algorithm is prone to unstable oscillations where the beam will oscillate back and forth between iterations. To overcome this problem relaxation is applied to the structural update. The aerodynamic model can either be solved completely or stepped one iteration at a time. When solved completely the oscillations are mitigated, but relaxations can still be used to accelerate the convergence. Updating the aerodynamic configuration with a single iteration can be less stable, however it can also lead to faster simulations.

4.1.3 Solving the Aero-structural system with FEM based LVD

The advantage of the FEM based LVD is the similarity to structural FEM problems. Solving the coupled system relies on defining a linearized aero-structural system model that can be solved with the solution algorithms explained in section 3.1.4. This section discusses how the structural system augments the aerodynamic system.

The beam model is based on a set of structural state variables ($\boldsymbol{X}_s$). The structural state variables augment the aerodynamic state variables (X_a) to define a system state vector given in equation 4.11.

$$\boldsymbol{X} = \left\{ \begin{array}{c} \boldsymbol{X}_s \\ \boldsymbol{X}_a \end{array} \right\} \tag{4.11}$$

The structural model is assumed to have nonlinear residual function ($\boldsymbol{R}_s$) which augments the aerodynamic residual ($\boldsymbol{R}_a$) to give a residual for the full aero-structural system as shown in equation (4.12).

$$\boldsymbol{R} = \left\{ \begin{array}{c} \boldsymbol{R}_s \\ \boldsymbol{R}_a \end{array} \right\} \tag{4.12}$$

To solve this full system in a single Newton iteration a system Jacobian is needed. It is assumed that the structural model defines a Jacobian with respect to structural state variables ($\boldsymbol{J}_{ss}$) this is used to augment the purely aerodynamic Jacobian ($\boldsymbol{J}_{aa}$) defined in chapter 3 as shown in equation (4.13).

$$\boldsymbol{J} = \left[\begin{array}{cc} \boldsymbol{J}_{ss} & \boldsymbol{J}_{sa} \\ \boldsymbol{J}_{as} & \boldsymbol{J}_{aa} \end{array} \right] \tag{4.13}$$

In the coupled system there are two more Jacobian terms, the first $\boldsymbol{J}_{sa}$ is the linearization of the structural residual with respect to aerodynamic state variables, the second $\boldsymbol{J}_{as}$ is the linearization of the aerodynamic residual with respect to structural state variables. These additional terms are a result of the coupling between the two models. Equation (4.13) are equation (4.2) are combined to define $\boldsymbol{J}_{as}$ with respect to lifting line positions and reference frames orientations. The $\boldsymbol{J}_{sa}$ Jacobian is defined by equation (4.8). Note equation (4.8) also includes additional terms to $\boldsymbol{J}_{ss}$ due to linearization with respect to lifting line positions and the cross section reference frames.

Together equations (4.11), (4.12) and (4.13) defines a linearized system in equation (4.14) that can be solved with the solution algorithms explained in section 3.1.4. When the circulation strength stepping algorithm is used in a aero-elastic simulation, the updates to the beam occur with the updates in strength.

$$\boldsymbol{R} = \boldsymbol{R}_0 + \boldsymbol{J}\boldsymbol{X} \tag{4.14}$$

Coupling with a linear Euler Bernoulli beam model

The linear beam model used in this work is taken from Logan [89], it is based on Euler Bernoulli beam theory for isotropic materials. This is a classic beam model and the full detail will not be presented here. This is a linear model and it has a constant stiffness matrix ($\boldsymbol{K}$) for strain, this is used in the residual definition given

in equations 4.15. Since the aerodynamic forces depend on a nonlinear aerodynamic model, the coupled structural residual is nonlinear.

$$\boldsymbol{R}_s = \boldsymbol{K}\boldsymbol{X}_s - \boldsymbol{F}_s(\boldsymbol{X}) \tag{4.15}$$

The structural Jacobian for the residual definition in (4.15) is given in equation (4.16).

$$\boldsymbol{J}_s = \boldsymbol{K} - \frac{\partial \boldsymbol{F}_s(\boldsymbol{X})}{\partial \boldsymbol{X}} \tag{4.16}$$

4.2 Results

Both the conventional and the FEM-based LVD models were used to solve the steady state deformed aero-structural solution of the NREL 5MW reference wind turbine [228]. This turbine is merely a paper design that defines both aerodynamic and structural properties. In both cases the rotor was represented by 32 elements on the blade. The wake had 96 15° elements in the wake to resolve 4 rotor revolutions and terminated with a cylindrical far-wake model. In the FEM-based LVD simulations the wake had 96 Hermite interpolating basis sections defined in a cylindrical reference frame. In all cases the linear beam model was used for the structural model.

Section 4.2.1 evaluates the convergence behavior of conventional LVD in aero-structural analysis. Then in section 4.2.2 aero-structural analysis is demonstrated with the FEM-based LVD model.

4.2.1 Aero-Structural analysis with conventional LVD

The two aero-structural analysis algorithms were applied to solve the NREL 5-MW wind turbine. Figure 4.2 shows the iterative convergence of the beam state, strength state and the wake state. For comparison the plot shows the convergence of conventional LVD without a beam. The 'Aero-Struct Step' trend lines are from the algorithm where the aerodynamic model is merely updated once between structural updates, in this case the beam and aerodynamics are co-evolved. The 'Aero-Struct Solve' trend lines are from the algorithm where the aerodynamic state was reinitialized and solved completely after each beam update. Since the wake is reinitialized the beam cannot introduce distortions in the wake.

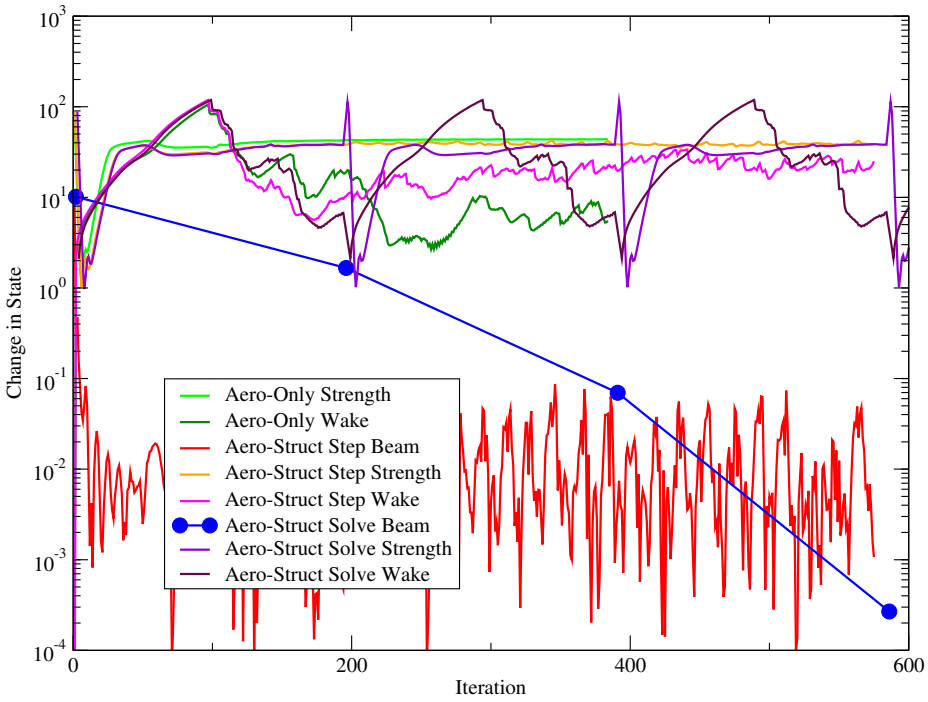

Figure 4.2: Iterative convergence of aero-structural conventional LVD

The strength solution for all simulations would settle into a stable oscillation at the inboard stations. Increasing the strength at the root filament decreased the angle of attack in the adjacent station. Due to the lower angle of attack the next iteration would updated that station with a lower strength. The induction from the root strength would drop off and the angle of attack would increase again. Fluctuations in strength would drive similar fluctuations in stations further out until the azimuthal component of the flow was strong enough to suppress this oscillation. To suppress this effect relaxation was applied to the strength updates, however relaxation only served to delay the onset of the oscillation. Visualization showed this strength oscillation has a minor impact the wake updates.

Comparing the iterative convergence in the wake between the 'Aero-Only' and 'Aero-Struct Step' trend lines shows the influence the beam has when the two models are co-evolved. The changes in the beam state are very small, however the chaotic nature of LVD tends to amplify these small disturbances, leading to poor convergence in the wake overall.

Changes in the beam state in the 'Aero-Struct Solve' simulations fell to 0.0 after 4 beam updates, however it still took nearly 600 iterations to reach this point. This

algorithm is best for structural convergence, but also the most expensive. Despite the good convergence for the structural model, this algorithm would still be plagued by the same convergence problems in the aerodynamics.

4.2.2 Aero-Structural analysis with FEM-base LVD

Figure 4.3 shows the FEM-based LVD solution with the deformed blade. It is clear that the blade is bent backwards and the vortex system has adjusted to this deformation.

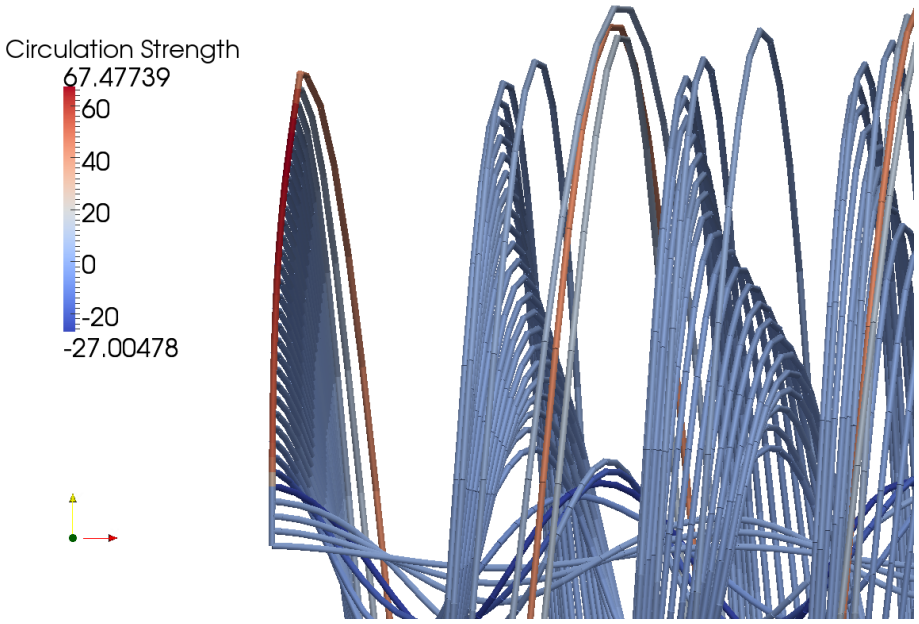

Figure 4.3: FEM-based LVD aero-structural visualization

Figure 4.4 compares the aerodynamic results of a FEM-based LVD simulation with and without the structural model, they are labeled as 'Aerodynamic Only' and 'Aero-Structural' respectively. The aero-structural solutions from the conventional LVD simulations are included for comparison. The 'Classic Step' trend lines are from the conventional LVD simulation where the beam is co-evolved and the 'Classic Solve' trend lines are from the conventional LVD simulation where the aerodynamics are reinitialized and solved completely after each beam update.

Figure 4.4a shows when the structural effects are included, the power increases at the inboard sections. It seems the beam deformation is causing the axial induction

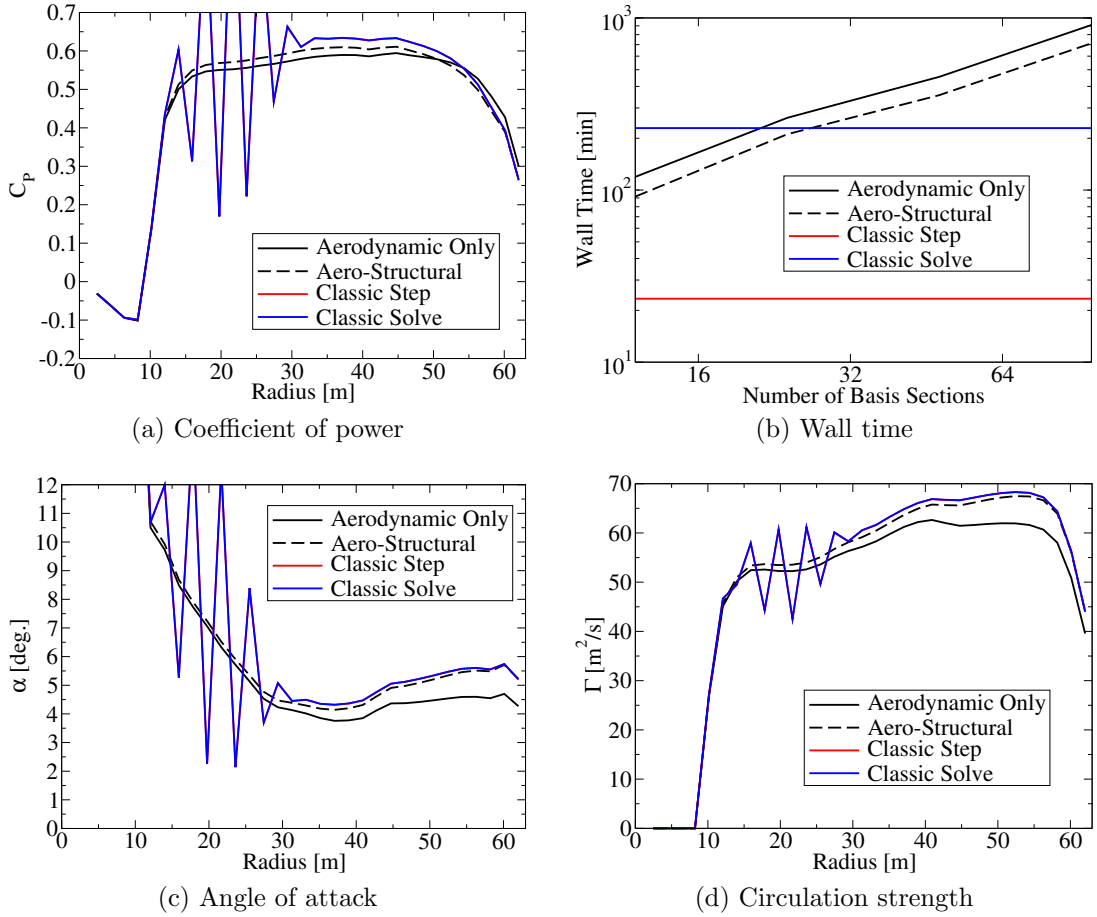

(a) Coefficient of power

(b) Wall time

(c) Angle of attack

(d) Circulation strength

Figure 4.4: FEM-based LVD aerodynamic results from aero-structural simulation

to drop off at these stations. However, for the outboard stations the blades are no longer normal to the flow and the power is reduced. Figure 4.4c demonstrates the importance of aero-structural analysis. The aerodynamic model imparts a small torsion force onto the blades due the coefficient of moment from the airfoil (*i.e.* c_m). In these simulations it was assumed the shear center is located at the quarter chord point. The results shows this torsion leads to a twist deformation of 1° at the tip where the most power is generated. The aerodynamic forces are highly sensitive to the angle of attack, so this small torsion leads to a noticeable increase in circulation strength shown in figure 4.4d.

The results in figure 4.4 of the two conventional LVD simulations shows almost identical solutions. However there are differences between the conventional and FEM-based solutions. The effect of oscillations in the flow-field at inboard sections is clearly present in all the results. At outboard sections the conventional LVD gives good

agreement with the aero-structural FEM simulations. However, the conventional LVD simulations predicted higher angles of attack which translates into higher C_P and circulation strengths.

Figure 4.5 shows the structural results from all the LVD aero-structural simulation. The aero-structural results for the conventional LVD simulations are included with the same naming convention as before. Figures 4.5a and 4.5b shows that the thrust forces dominate over the torque forces. Both plots clearly show that structural deformation affected the aerodynamic forces, confirming the importance of aero-elastic analysis in wind turbine design. In this simulation gravity forces are ignored because they cannot be included in axis-symmetric simulations. If gravity was included the azimuthal forces would be significantly larger when the blade was horizontal. Due the large thrust forces and the lower flap-wise bending stiffness figure 4.5c shows blades experience much larger deformation in the downstream direction. Finally 4.5d shows the internal moments in the beam. Note that flap-wise and edge-wise refer to the moments in the cross-section reference frame, due to twist in the blade some of the outboard flap-wise moment becomes edge-wise in the inboard sections. The internal moments are the loads that can lead to material failures in the blade, most of these moments are concentrated at the root where the cross sections are made extra thick to mitigate the stress.

Comparisons between the FEM-based and conventional LVD simulation results in figures 4.5a and 4.5b shows similar trends as before. The two conventional simulations produced nearly identical results; the effects of the flow field oscillations is clearly present; the force magnitudes are greater at the outboard sections due to a higher angles of attack. Comparing the beam deflections and internal moments there is little difference between either conventional or FEM-based LVD simulations.

Figure 4.4b compares the solution time of all the aero-elastic simulation methods. The conventional LVD simulations lack an objective convergence metric, instead the solution time is estimated based on the number of time steps. For the 'Classic Step' simulation the wall time is based on 192 updates to both the beam and the aerodynamics. For the 'Classic Solve' simulation the wall time is based on 192 aerodynamic updates after the 4th structural update. The figure shows the co-evolving conventional LVD simulation is the fastest of all the algorithms, however it gives the poorest convergence. With a low number of basis sections the FEM-based LVD simulations solved within a similar wall time as the 'Classic Solve' conventional LVD simulation. With increasing number of basis sections the FEM-based LVD simulations become

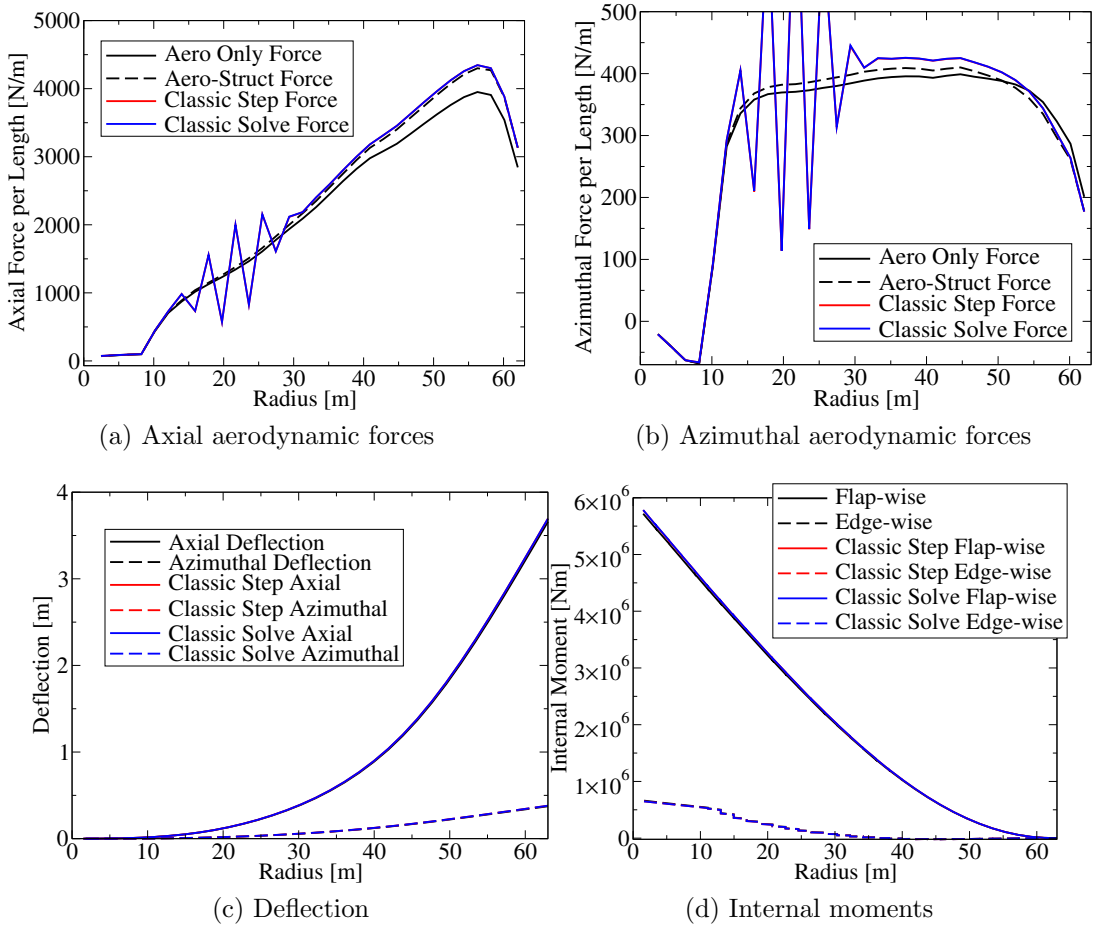

(a) Axial aerodynamic forces

(b) Azimuthal aerodynamic forces

(c) Deflection

(d) Internal moments

Figure 4.5: FEM-based LVD structural results from aero-structural simulation

significantly more expensive compared to the conventional simulations. This shows the importance of using a reduced number of basis sections to obtain solutions quickly. The figure shows the FEM-based LVD simulation without the beam is slower than with the beam. Both the FEM based simulations relied on circulation strength stepping algorithms with partitioned wakes. The aerodynamic only simulations required more circulation strength updates to converge the simulation. This shows the structural model is relatively inexpensive and introduces a beneficial interaction between the structural and aerodynamic model in the solver algorithm.

Chapter 5

Multidisciplinary Design Optimization

This chapter presents multiple advancements in wind turbine Multi-disciplinary Design Optimization (MDO). MDO is more than simple design optimization of a single component with a single discipline, there are two important aspects. First is the multi-disciplinary design analysis. Wind turbines operate in a system where design decisions in one discipline or component will impacts on other disciplines and components. To understand these effects MDO tries to expand the scope of the analysis. The first study in section 5.1 is an example of expanding the scope by applying optimization in conjunction with geographic information to identify the optimal sites for wind farms. To reduce transportation costs wind turbine manufacturers already build multiple facilities around the world. It is only natural for each of these facilities to build wind turbines specific for the region. The wind farm siting model could help designers identify the region specific parameters for the facilities wind turbine design.

An expanded scope introduces complexity, which leads to the second aspect of MDO, the use of optimization to navigate this complexity. Optimization is used in MDO to automatically find optimal configurations. When applied to the full system, optimization can identify system benefits and take advantage of inter-disciplinary interactions that are not always obvious. Yet, optimization introduces additional challenges in adapting analysis methods for optimization. Section 5.2 is one example where adjoint based gradients were developed for the structural analysis. Then in section 5.3 structural optimization was adapted to consider manufacturing aspects.

This chapter closes with two examples of MDO where aero-structural optimization was applied to design optimal wind turbine blades. The first is given in section 5.4 where conventional LVD aerodynamic analysis was coupled to the GEBT and VABS structural analysis. The study serves as an example of the challenges of MDO. Both the aerodynamic and the structural models were used successfully in single discipline optimization. Yet, when combined the inter-disciplinary interactions lead to increased errors in the gradients that prevented convergence in the optimization. This lead the development of FEM-based LVD model presented in chapter 3. The second MDO study in section 5.5 evaluated the new FEM-based LVD model in MDO. The focus of this study was how the new FEM-based LVD would behave in aero-structural optimization. To simplify the analysis a simple linear beam model was used for the structural model. The analytic gradients of FEM-based LVD lead to excellent convergence in the optimization. However the FEM-based LVD model suffers from occasional singularities in the Jacobian that prevents convergence in the analysis. This caused the delays in the optimization due to singularity avoidance strategies outlined in chapter 3.

5.1 Regional Scale Wind Farm Siting Model

The work presented in this section is adapted from a Renewable Energy publication by the author:

M. K. McWilliam, G. C. van Kooten, and C. Crawford. A method for optimizing the location of wind farms. *Renewable Energy*, 48:287–299, June 2013

Wind energy development is sensitive to environmental factors such as the wind resource, access to the electrical grid and the population distribution. Understanding how these factors may affect wind farm development is important for policy makers, electricity system operators, developers and wind turbine manufacturers who want to design wind turbines specifically tailored for a given region. The ability to predict the location of future wind farms will benefit each of these stake-holders.

Voivontas *et al.* [229] and Varela *et al.* [230] demonstrate the importance of Geographic Information Systems (GIS) in wind farm development. Planning organizations use GIS to develop Decision Support Systems (DSS) to determine whether a proposed wind farm development should be approved or not. Many of these systems are based on research by Baban and Parry [231] who conducted a survey to

understand the important factors for wind farm development. This work has inspired many similar studies. Rodman and Meentemeyer [232] created maps of California to protect sensitive ecosystems from development. Lejeune and Feltz [233] developed a decision support system for wind policy development in Belgium. Rasado *et al.* [234] give an example of a very sophisticated approach to developing a DSS, where wind resource assessment tools like WASP and sophisticated logic is used to develop the maps. These examples are only a small sample of studies applying GIS in assessing the impact of wind farm development.

The application of GIS as a predictive tool is most common in wind farm design. Ozturk and Norman [235] represented the wind farm space as a grid and used a greedy improvement heuristic methodology to find the turbine placement that maximized profit. Grady *et al.* [236] applied genetic algorithms and the Jensen wake model [237] to maximize production with the least number of turbines, while Mora *et al.* [238] used evolutionary algorithms to select the turbine, tower and location that maximized the net present value. Marmidis *et al* [239] applied multi objective optimization and Monte Carlo simulations to determine turbine locations that maximized production and minimized installation costs.

DSS and the wind farm design models represent two similar bodies of work that only differ in scale and application. The former is used for large regions but neglects to seek out optimal locations while the latter optimizes wind farm configuration over a small region. The current study combines the contributions of both bodies of research and develops a model that will optimally place wind farms within a large region. As with other DSSs we assess multiple factors to the suitability of a proposed wind farm location in a large region. Our approach differs by incorporating these factors into an overall economic cost function; accordingly not all factors typically included in other DSSs can be included. Similar to the wind farm design models, we employ optimization algorithms. However the shear scale of the problem makes the same heuristic methods in wind farm design models impractical. Instead this work employed gradient based methods to find optimal solutions. The computational load is further reduced by making assumptions on individual turbine placements.

The purpose of this work is to provide a new approach to wind farm siting at a large scale, as a preliminary screening tool. Later stages of wind park design could then use more detailed models to optimize the placement of individual turbines within a farm. The mathematical models used for each aspects are presented in section 5.1.1. The province of Alberta Canada is used as a case study in section 5.1.2. The case study

is used to evaluate the model sensitivity to the wind resource, population density and the transmission network. The research is meant to illustrate how the model can be applied to evaluate energy policy and explore region specific turbine design optimization.

5.1.1 The Wind Farm Siting Model

The goal of the wind farm siting model is to predict the latitude (ϕ) and longitude (θ) within a large region where a wind farm should optimally be built. The locations of previous optimal wind farm solutions can be included to determine the location of next best wind farm. In addition, the model predicts the optimal wind farm radius (R) and the spacing between installed turbines (X_t). The underlying assumption is that wind farm developers will build the project that will produce electricity at minimum cost. This assumption casts the prediction into an optimization framework.

Gradient based optimization algorithms are employed. An important criteria of these algorithms is the existence of continuous gradients with respect to the state variables. While gradient based algorithms are highly sensitive to local minima, we develop mathematical models specifically to guarantee smooth derivatives and have mechanisms to limit local minima solutions.

Wind Farm Geometry

When studying a large region, with potentially large wind farms, care is needed to account for earth curvature effects and the distribution of environmental properties within the wind farm. It is assumed that a wind farm will occupy a circular region. The wind farm radius will vary throughout the solution process because the radius is a state variable in the optimization. When the wind farm radius is large the geographic variation of various properties within the wind farm will influence the cost. Furthermore outer portions of the wind farm may encroach on the region of interest boundary. To account for the effect of a large wind farm region various wind farm properties are calculated at many points within the region. The relative locations of these internal points is shown in figure 5.1. Similarly, the points around the border in figure 5.1 are used to ensure the whole wind farm stays within the region of interest.

The relative distance between points is constant and scales with the wind farm radius. The set of points in figure 5.1 are denoted as (x_i, y_i). These points need to

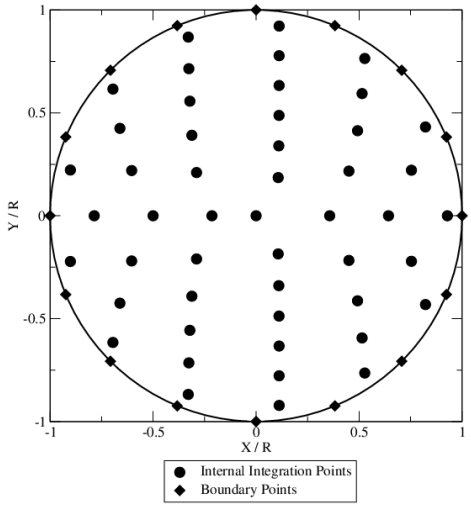

Figure 5.1: Border and integration points within a wind farm

be related to corresponding latitude (ϕ_i) and longitude (θ_i) through equations (5.1) where R_s is the radius of the earth. The curvature of the earth effects the distance given by an increment in longitude. As the position approaches a pole a unit of longitude approaches zero distance. To account for this effect the cosine function in equation (5.1b) reflects the surface distance associated with increments in longitude.

$$\phi_i = \phi + \frac{180 y_i R}{\pi R_s} \tag{5.1a}$$

$$\theta_i = \theta + \frac{180 x_i R}{\pi R_s \cos\left(\frac{\pi\phi}{180}\right)} \tag{5.1b}$$

Geographic Information

This work assumes that geographic information can be represented by a grid of points $\{(\phi_{gi}, \theta_{gi})\}$. Each of these grid points will have a set of attributes to describe the wind resource, population or any other geographic information.

The constraint of continuous derivatives limits the way geographic information is represented. A typical approach would involve developing piece-wise smooth interpolation functions between points of known information. This approach fails to give any mechanisms to smooth out local minima. Instead the weighted average in equation (5.2) is used to determine the generalized attribute a at a location of interest. Here a_i denotes the attribute defined at grid point i with the corresponding weight w_i. The

solution is made continuous by making a dependent on the attribute values at every grid point.

$$a = \frac{\sum a_i w_i}{\sum w_i} \tag{5.2}$$

The weighting function (w_i) biases the result to the nearest point as shown in equation 5.3 where r is the distance between the grid point and the point of interest. The influence of local minima is controlled by varying the numerical constants P and Q. The role of these parameters is discussed further in section 5.1.1.

$$w_i = \exp\left(-\left(\frac{r_i}{Q}\right)^P\right) \tag{5.3}$$

The distance is given by equation (5.4) where the $\hat{\bullet}$ terms represent the point of interest. This definition of distance is based on a tangent plane defined at a latitude of $\tilde{\phi}$, where in general $\tilde{\phi} = \hat{\phi}$. This definition of r_i maintains the same physical unit as the R_s parameter.

$$r_i = \sqrt{\left(\frac{R_s \pi \cos\left(\frac{\pi\tilde{\phi}}{180}\right)\left(\hat{\theta} - \theta_{gi}\right)}{180}\right)^2 + \left(\frac{R_s \pi \left(\hat{\phi} - \phi_{gi}\right)}{180}\right)^2} \tag{5.4}$$

Region Definition

The region of interest is defined by the outer border of the region, within that region there may be an area where wind farms could not be built. These sub-regions could be lakes, existing wind farms or reserved land. The region of interest cannot be defined by a simple path because of the presence of these sub-regions. Instead equation (5.2) is used to define the region of interest. The generalized attribute for the border is denoted by b_i, where i denotes grid points. The points where a turbine can be built are valued -1 and all other points are valued 1.

The result of equation (5.2) is b_j where j denotes a specific boundary points in figure 5.1. The model is constrained such that the largest b_j value is less than 0. To avoid multiple inequality constraints the Kreisselmeier-Steinhauser function shown in equation (5.5) [212] is used to lump the constraints. Here the parameter ϱ is used to control how close equation (5.5) approximates the maximum.

$$\max(b_j) \approx \frac{1}{\varrho} \log\left(\sum \exp(\varrho b_j)\right) \tag{5.5}$$

In the optimization problem the region constraint is as follows:

$$\frac{1}{\varrho} \log\left(\sum \exp(\varrho b_j)\right) \leq 0 \tag{5.6}$$

Wind Farm Cost Model

The cost of the electricity (c) is a common metric for wind farm development. This metric is the ratio of annualized cost (C_a) to annual energy production (E_a):

$$c = \frac{C_a}{E_a} \tag{5.7}$$

The annualized cost is given by equation (5.8), where C_i is the initial cost, r is the expected annual rate of return for the project, L is the life time in years and C_o is the annual operation and maintenance cost.

$$C_a = C_i \frac{r(1+r)^L}{(1+r)^L - 1} + C_o \tag{5.8}$$

For wind farm projects a bulk of the cost is associated with the initial development. The initial cost is further broken down into components as shown in equation (5.9). The fixed cost component (C_f) accounts for things like the wind resource study, legal fees and other preliminary development work. Then there is a cost proportional to the number of turbines (N) that accounts for the turbine purchase and the construction costs, the proportionality is denoted as (C_t). The electrical transmission cost between the wind farm and the electricity grid is dependent on the distance (R_e) and the proportionality constant (C_e). The effect of installed capacity on the transmission cost is neglected in this work. Finally, there is a cost associated with the electricity infrastructure within the wind farm. This cost is proportional to the number of turbines, desired turbine spacing and the proportionality constant C_x.

$$C_i = C_f + C_t N + C_e R_e + C_x N X_t \tag{5.9}$$

The economic equations demonstrate how the environmental conditions affect the cost. Each will be discussed in turn in this section starting with the annual

energy production calculation, the transmission distance model and finally how the population density affect the number of turbines built through a micro-siting model.

Annual Energy Production

The Annual Energy Production (AEP) is based on the product of average turbine power and hours in the year. The average power is based on the probability that the turbine will experience various wind speeds and the power output at those wind speeds. To get an accurate prediction the calculation needs to be corrected for turbine height and wake effects. These corrections are discussed first.

The height of the turbine will influence energy production. Turbines placed at a higher elevation experience a stronger wind, and thus are more productive. This influence is referred to as wind shear. A common model for wind shear is the power law in equation (5.10) [34]. Here V_t is the wind speed experienced by the turbine, V_0 is the wind speed at the wind resource height, H_t is the height of the wind turbine and H_0 is the defined height for the wind resource. The shear exponent S defines the severity of the wind shear, with a value of 1/7 acceptable for most ground surfaces.

$$\frac{V_t}{V_0} = \left(\frac{H_t}{H_0}\right)^S \tag{5.10}$$

Proximity to other turbines also influences turbine output. The wake of upstream turbines will reduce the apparent wind for downstream turbines. These wake effects are dependent on the desired turbine spacing parameter. The wake model by Jensen [237] provides an explicit model for the wind deficit deep within a wind farm. This model is given in equation (5.11), where D is the turbine diameter and α is a turbulence parameter. For most wind farms a turbulence parameter of 0.1 is acceptable. The equation gives the ratio of the wind speed for a downstream turbine (V_f) to the undisturbed wind speed (V_0).

$$\frac{V_f}{V_0} = 1 - \frac{2D^2}{3\left(D + 2\alpha X_t\right)^2 - D^2} \tag{5.11}$$

Equations (5.10) and (5.11) are used to modify the probability distribution. For most wind resources the Weibull distribution has been found to be good approximation over annual yearly time scales [156]. The modified Weibull distribution is given in equation (5.12) where V_i is a wind speed of interest. The distribution is defined by the scale parameter λ_j and the shape parameter κ_j.

$$\Phi_{ij} = \frac{\kappa_j}{\lambda_j} \left(\frac{V_i}{\left(\frac{V_t}{V_0}\right)\left(\frac{V_f}{V_0}\right)\lambda_j} \right)^{\kappa_j - 1} \exp\left(- \left(\frac{V_i}{\left(\frac{V_t}{V_0}\right)\left(\frac{V_f}{V_0}\right)\lambda_j} \right)^{\kappa_j} \right) \tag{5.12}$$

The shape and scale parameters define the wind resource and are geographically distributed. This distribution is represented in a similar way as the region definition. Here a shape and scale attribute is assigned to each of the grid points. Equation (5.2) is then used to calculate the shape and scale parameter for a given location.

The annual energy produced is dependent on the power (P_i), which is defined for each wind speed of interest. This power is used with equation (5.12) to define the average power with equation (5.13).

$$\bar{P}_j = \sum \Phi_{ij} P_i \tag{5.13}$$

To account for different $\bar{P}_j$ within the wind farm, the average of all the integration points is calculated with equation (5.14) where N_i is the number of integration points.

$$\bar{P} = \frac{\sum \bar{P}_j}{N_i} \tag{5.14}$$

Given average power, AEP is given by equation (5.15) where the assumed number of hours in a year is based on a four year average.

$$E_a = 8766 N \bar{P} \tag{5.15}$$

Electrical Transmission Network

The influence of the electrical transmission network is defined by R_e the minimum distance between the wind farm and a transmission line. First a model is needed to define the distance between a given transmission line and the wind farm. Then an analytical formula is used to determine the transmission line that gives the minimum distance solution.

The electrical transmission network is defined by a set of line segments. Each line segment is defined by a start point $(T_\theta, T_\phi)_{0i}$ and end point $(T_\theta, T_\phi)_{Ei}$. The distance to the start point of a given line segment can be decomposed by a parallel component ($r_\parallel$) and a perpendicular component ($r_\perp$) through equations (5.16).

$$r_{\parallel} = \frac{\pi R_s \left(\cos\left(\frac{\pi\tilde{\phi}}{180}\right) (\theta - T_{\theta 0i}) (T_{\theta Ei} - T_{\theta 0i}) + (\phi - T_{\phi 0i}) (T_{\phi Ei} - T_{\phi 0i}) \right)}{180\sqrt{(T_{\theta Ei} - T_{\theta 0i})^2 + (T_{\phi Ei} - T_{\phi 0i})^2}} \tag{5.16a}$$

$$r_{\perp} = \frac{\pi R_s \left(\cos\left(\frac{\pi\tilde{\phi}}{180}\right) (\theta - T_{\theta 0i}) (T_{\phi Ei} - T_{\phi 0i}) - (\phi - T_{\phi 0i}) (T_{\theta Ei} - T_{\theta 0i}) \right)}{180\sqrt{(T_{\theta Ei} - T_{\theta 0i})^2 + (T_{\phi Ei} - T_{\phi 0i})^2}} \tag{5.16b}$$

The distance metric is based on a tangent plane that is defined at the latitude $\tilde{\phi}$. For transmission distance $\tilde{\phi}$ is defined by equation (5.17).

$$\tilde{\phi} = \frac{\phi}{2} + \frac{T_{\phi 0i}}{4} + \frac{T_{\phi Ei}}{4} \tag{5.17}$$

The actual distance of the transmission line to the wind farm will have the same perpendicular component. However, when the wind farm is directly perpendicular the line segment, no parallel component is needed. Thus when $r_{\parallel}$ is less than the segment length $\|T\|$, the actual parallel component is zero. Similarly, when $r_{\parallel}$ is greater then the segment length, the connection only needs to be made at the end of the segment. In this case the parallel component is reduced by the segment length.

Equations (5.16) along with the piece-wise treatment of the parallel component introduce a discontinuity into the gradient. To smooth over these discontinuities the parallel and perpendicular components are approximated as shown in equation (5.18). Here ϵ is numerical smoothing parameters that should be small; for this work it is 0.01.

$$R_{\parallel} = \frac{1}{2}\left(\sqrt{r_{\parallel}^2 + \epsilon} - \sqrt{\left(r_{\parallel} - \|T\|\right)^2 + \epsilon} - \|T\| \right) \tag{5.18a}$$

$$R_{\perp} = \sqrt{r_{\perp}^2 + \epsilon} \tag{5.18b}$$

These equations contribute to the actual transmission length in equation (5.19).

$$R_{ei} = \sqrt{R_{\parallel}^2 + R_{\perp}^2} \tag{5.19}$$

The weighted average formula in equation (5.2) is used to find the minimum distance R_e. In this calculation the attribute variable a_i is replaced by R_{ei}, the distance r_i in the weighting function (5.3) is also replaced with the distance R_{ei}.

Micro-siting

The micro-siting model is meant to approximate the number of turbines that could be built within the wind farm region. This depends on the turbine spacing and the locations of sensitive noise receptors. Wind farm developers must place turbines sufficiently far away from these receptors that the noise is kept within acceptable limits. This in effect removes land adjacent to residential areas that could otherwise be considered for wind farm development and thus limits the number of turbines that could be built.

The influence of noise receptors is dependent on how they are distributed. It is unreasonable or impractical for all receptor locations to be known within a very large region. Instead the population density is used to estimate the number of receptors in a given region. The population density is represented by attributes attached to grid points. For each integration point, equation (5.2) is used to calculate the density. The density of all the integration points is then averaged to get the effective density for the wind farm.

In general people tend to cluster. More than one person will live in a house, and multiple houses will be built within close proximity. This effect will make the number of noise receptors less than the number of people. The assumed cluster factor is a parameter that can be tuned to calibrate the model. For this study, it was assumed that the receptor density was equal to the population density.

The micro-siting model is based on the assumption that both the wind turbines and noise receptors will be distributed in a close pack configuration. This assumption allows one to define a unit cell as shown in figure 5.2. The unit cell is defined by the triangle. A noise receptor is located at the vertices of the triangle. The large circles around the vertices represent the required setback distance. The turbines are placed in the center of the smaller circles, the diameter of the smaller circles is the desired turbine spacing. The micro-siting model assumes increased likelihood that the turbines in the center of the cell will be built, while those within the setback circle will not be built.

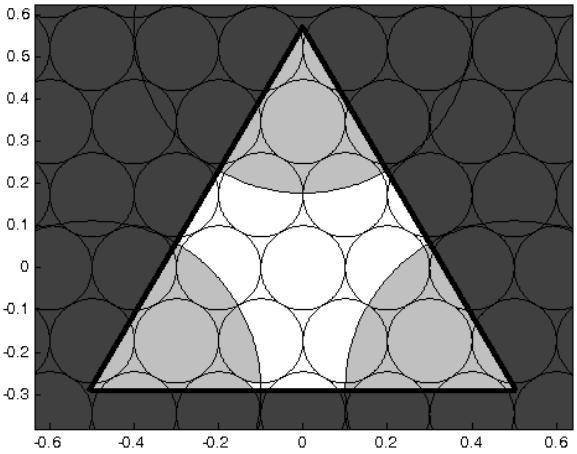

Figure 5.2: A unit cell within the micro-siting model

It is assumed that the relative position of receptors and turbines within one unit cell is repeated throughout the entire wind farm. The total number of turbines is then based on the product of turbines within a unit cell and the number of unit cells within the wind farm. Thus, the micro-siting model is based on predicting the number of turbines within one unit cell (n).

To simplify the problem a non-dimensional noise distance (s) and a non-dimensional turbine spacing (d) are defined by equations (5.20) and (5.21) respectively. This definition is based on an assumed receptor spacing given by equation (5.22), where ρ is the receptor density for the wind farm.

$$s \equiv \frac{X_s}{X_p} \tag{5.20}$$

$$d \equiv \frac{X_t}{2X_p} \tag{5.21}$$

$$X_p = \sqrt{\frac{2}{\sqrt{3}\rho}} \tag{5.22}$$

The micro-siting model is based on three scenarios. The first is assumes a densely populated area where the land is relatively crowded and any turbine built would likely be within a noise offset limit. This scenario occurs when s is greater than $1/\sqrt{3}$. Assuming that no turbines will be built in this case would introduce a discontinuity in the derivative. Instead it is assumed that there is still a probability that a single

turbine will be built in the center of the unit cell. The turbine built in the city of Toronto Canada is an example that turbines can be built in densely populated regions. The probability (Ψ) this turbine will be built is based on the cumulative normal distribution given in equation (5.23). The standard deviation parameter σ is another parameter that can be used to tune the micro-siting model.

$$\Psi = \frac{1}{2}\left[1 + \operatorname{erf}\left(\frac{1-\sqrt{3}s}{\sqrt{6}\sigma}\right)\right] \tag{5.23}$$

In sparsely populated areas there are two more scenarios. The first assumes the spacing of turbines is sparse enough that noise limits would not affect the development. This scenario is likely true for many developments and occurs when d is greater than s. In these circumstances, it is assumed that the noise receptors will not prevent the construction of a single turbine. In this situation n is based on a ratio of effective area per turbine and unit cell area.

Finally there is a case where it is desirable to pack turbines very close together. In these circumstances the noise offset limits will prevent some turbines from being built. The number of turbines built is still based on the ratio of effective turbine area to unit cell area. This ratio is then multiplied by a ratio of unit cell area to available development area. The available development area is equal to the unit cell area minus the area within the offset limits. The available development area solution is based on three geometric scenarios, resulting in a piece-wise solution.

A micro-siting model based on multiple piece-wise geometric models is not acceptable for optimization. In this case, the number of turbines and the gradients are both discontinuous. To overcome this problem, an approximation based on a set of geometric parameters, shown in equations (5.24) through (5.27), is used.

$$\tilde{s} = \frac{\operatorname{bnd}\left(\sqrt{3}s\right)}{\sqrt{3}} \tag{5.24}$$

$$\tilde{d} = \tilde{s}\operatorname{bnd}\left(\frac{d}{\tilde{s}}\right) \tag{5.25}$$

$$\tilde{\vartheta} = \arccos\left(\operatorname{bnd}\left(\frac{1}{2\tilde{s}}\right)\right) \tag{5.26}$$

$$\tilde{\varphi} = \arccos\left(\operatorname{bnd}\left(\frac{\tan\tilde{\vartheta}}{2\tilde{d}}\right)\right) \tag{5.27}$$

The bnd operator is 0 when the argument is less than 0, 1 when the argument is greater than 1, and takes the value of the argument when the argument is between 0 and 1. The formal definition is given in equation (5.28) with the approximation given in equation (5.29). As before the ϵ parameter is a numerical constant and is set to 0.01 for this work.

$$\mathrm{bnd}\left(x\right) \equiv \begin{cases} 0 & : x < 0 \\ x & : 0 \leq x \leq 1 \\ 1 & : 1 < x \end{cases} \tag{5.28}$$

$$\mathrm{bnd}\left(x\right) \approx \frac{1}{2}\left(\sqrt{x^2+\epsilon} - \sqrt{\left(x-1\right)^2+\epsilon} + 1\right) \tag{5.29}$$

These approximated parameters are used in equation (5.31) to determine the unit cell solution for the whole s and d domain. Note that the probability Ψ is still based on the original definition of s given in equation (5.20).

$$\begin{aligned} n &= \frac{\Psi^3}{2\sqrt{3}d^2} \\ &\times \left(\frac{\sqrt{3}}{4} - \left(\frac{\pi}{2} - 3\tilde{\vartheta}\right)\left(\tilde{s}-\tilde{d}\right)^2 - \frac{3\tan\tilde{\vartheta}}{4} + \left(\frac{3\pi}{2} - 3\tilde{\vartheta} - 3\tilde{\varphi} + \frac{3}{2}\sin\left(2\tilde{\varphi}\right)\right)\tilde{d}^2\right) \end{aligned} \tag{5.30}$$

The result from equation (5.31) is used to determine the total number of turbines with equation (5.31).

$$N = \frac{4n\pi R^2}{\sqrt{3}X_p^2} \tag{5.31}$$

Optimization

The optimization algorithm is meant to solve the problem in equation (5.32). The first constraint ensures that all solutions are within the region of interest. The second constraint reflects the fact that most projects are subjected to capacity constraints due to regulation, electrical transmission capacity, financing limits or numerous other reasons. The problem was solved using Sequential Quadratic Programming (SQP), which is a gradient based algorithm provided by Lawrence *et al.* [202].

$$\begin{array}{ll} \text{Minimize} & \text{Cost of electricity (equation (5.7))} \\ \text{Subject to} & \text{Region constraint (equation (5.6))} \\ & \text{Capacity constraint } N \leq 10 \end{array} \tag{5.32}$$

Numerical Smoothing

The goal for any optimization problem is to determine the global minimum. When the objective function contains many local minima, there is no algorithm that can guarantee a globally optimal solution. The best that can be achieved is merely approaching a solution close to the global optimum.

Gradient based methods are particularly sensitive to local minima. In general the algorithm will find the nearest local minima to the start point. When the objective function is particularly noisy, the final solution will be highly sensitive to the starting point. Without the appropriate numerical conditioning these algorithms do not give acceptable solutions.

When the objective is noisy, heuristic methods like tabu search or evolutionary algorithms are known to perform well. These methods rely on an element of randomization to prevent the algorithm from getting trapped at a local minima. By neglecting gradient information the algorithm requires many more function evaluations for the randomization to eventually locate a converged solutions. This quality is undesirable because of the excessive computational resources. Numerical smoothing is applied so efficient gradient based algorithms are still applicable.

Numerical smoothing suppresses small scale variation in the objective function. When the small scale variations are suppressed, the algorithm will respond to large scale variations and find the general area where the global minimum is likely to occur. When this area is identified, multiple solutions started from this area should give results that are close to the global optimum.

The weighting function (5.3) in equation (5.2) controls the level of numerical smoothing. The Q parameter is an effective length scale, all the points within Q will be weighted considerably higher than all other points. The variations that occur within Q will be averaged out. Any local minimum created by this variation would be suppressed.

In equation (5.3) the exponent P controls how strongly the data within Q are averaged. When P is small then the closest point is selected, when P is large then

nearly all points within Q are weighted equally. For this work P takes on values of 1 or 2.

5.1.2 Application of the Optimal Wind Farm Model

The province of Alberta in Canada was chosen to demonstrate the wind farm siting model. In Alberta the electricity market is de-regulated providing much information about the electricity grid. In the South a strong wind resource has prompted many developers to build wind farms. Accordingly, this is a good case to investigate how well this model performs.

The entire province is region of interest. Land along the southwest border is mountainous and not appropriate for wind farm development, and thus removed from the region of interest. The Canadian wind atlas was used to obtain wind resource data at 50m shown in figure 5.3 [240]. Figure 5.3 shows the mean wind energy density calculated by the wind atlas. The data are provided as wind speed histograms. An optimal Weibull probability distribution curve fit was used to determine the scale and shape parameters from the histograms.

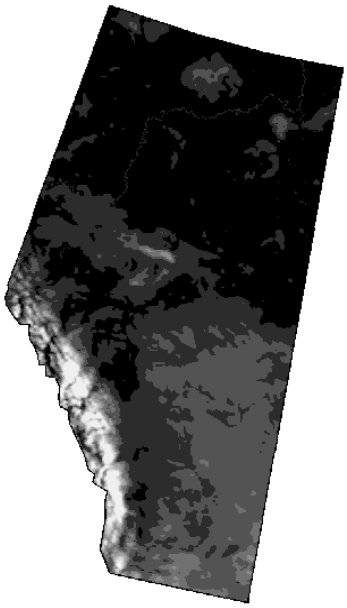

Figure 5.3: Map of average wind resource, ranges between $0W/m^2$ (black) to $300W/m^2$ (white)

Population data for Alberta are available by census divisions from Statistics Canada [241]. This data along with the geographic definition of the census division were used to create the population density map given in figure 5.4.

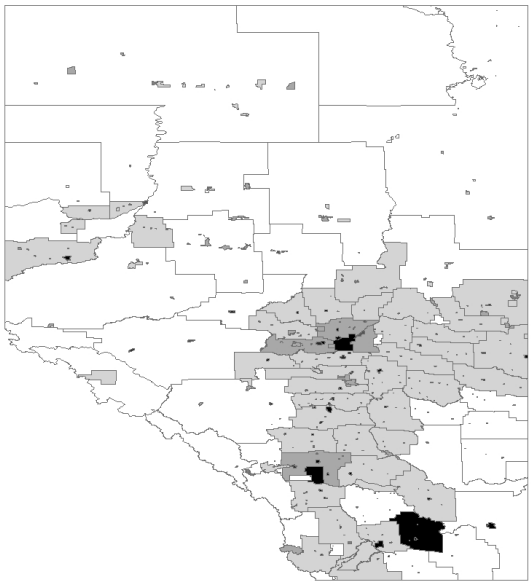

Figure 5.4: Alberta population density (darker shades indicate increasing density)

The geographic location of the electrical transmission network in Alberta was obtained from the Alberta Electric System Operator [242], which divides the province into six regions. Maps of these regions were used to generate the electrical tranmission map shown in figure 5.5.

Given that our purpose is primarily to demonstrate the method developed above, wind turbine performance and various economic parameters were chosen arbitrarily. Figure 5.6 shows the wind turbine power curve used in this work. Table 5.1 gives the parameters for the various cases used in this study.

For each case listed in table 5.1 several solutions were obtained, depending on the values of the Q and P parameters used in the Weibull scale and shape factor calculations. The the Q parameter took values of 5, 28, 150 and 794 km, while P took values of 1 and 2. The Q and P values used for all other calculations were 5 km and 1 respectively. Solutions also differed by starting location, for each case simulations were started from either a common Northern, Eastern, Southern or Western point. The different combinations of parameters led to a total of 32 simulations for each case.

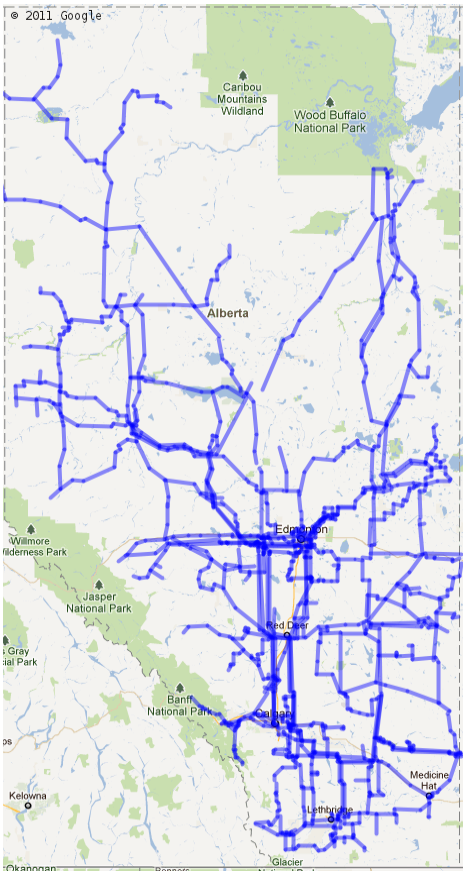

Figure 5.5: Alberta transmission

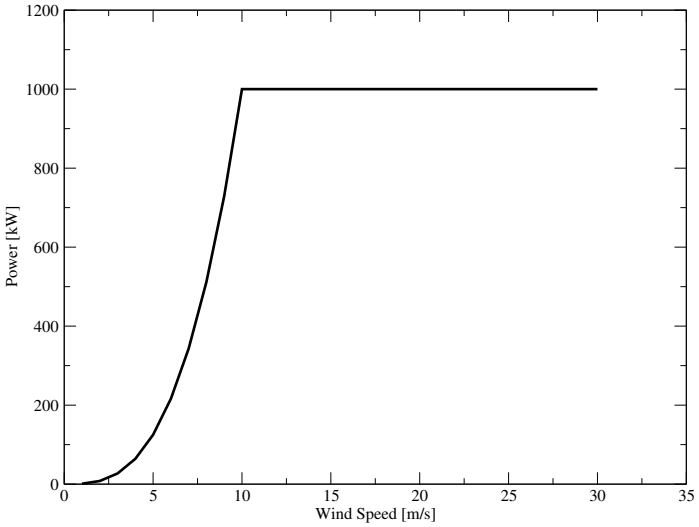

Figure 5.6: Wind turbine power curve

Table 5.1: Optimization parameters by case, (Differences from the base case given in **bold**)

Case	Base	AEP	Transmission	Noise
Lifetime (L)	20 years	20 years	20 years	20 years
Annual Interest Rate (r)	10%	10%	10%	10%
Wind Farm Overhead Cost (C_f)	\$5 mil.	\$5 mil.	\$5 mil.	\$5 mil.
Cost per turbine (C_t)	\$3 mil.	\$3 mil.	\$3 mil.	\$3 mil.
Transmission Cost per km (C_e)	\$100,000	**\$1,000**	**\$1 mil.**	\$100,000
Spacing Cost per km (C_x)	\$10,000	\$10,000	\$10,000	\$10,000
Annual Cost (C_o)	\$50,000	\$50,000	\$50,000	\$50,000
Offset Limit (X_s)	450.0 m	**100.0 m**	450.0 m	**550.0 m**
Turbine Diameter (D)	80.0 m	80.0 m	80.0 m	80.0 m
Turbine Height (H_t)	80.0 m	80.0 m	80.0 m	80.0 m

Numerical Smoothing

This section addresses the effectiveness of numerical smoothing in avoiding local attractors. Numerical smoothing is built into the weighting function (5.3). The parameters Q and P control the level of numerical smoothing with Fourier analysis applied to quantify how various values of Q and P suppress local minima.

Any spatially distributed discrete set of quantities (*eg.* average power $\bar{P}_j$) can be represented by an average quantity added to a series of trigonometric functions; see equation (5.33). The Fourier transform is used to solve the amplitude (A_{ij}) of the sine terms. The set of sine magnitudes reveal the frequency content of variations. A general region of good wind is strongly dependent on the low frequency components, while the local minima are governed by the high frequency components. The goal of the numerical smoothing is to suppress the high frequency components, while preserving the local frequency content.

$$f(x,y) = \bar{f} + \sum_{i}^{N_i} \sum_{j}^{N_j} A_{ij} \sin(\omega_{xi} x + \phi_{xi}) \sin(\omega_{yj} y + \phi_{yj}) \tag{5.33}$$

The wind resource affects the average power of the turbines which in-turn affects the annual energy production (*ie* AEP). To evaluate the spatial distribution of the wind resource equation (5.13) was evaluated over several points.

To get a better understanding of numerical smoothing a frequency based study focused on an area in the South East corner of Alberta. The area is approximately 212 km East to West and 334 km North to South. A 512 by 512 grid of points was sampled with various values of Q and P for the scale and shape factors. The approximate grid spacing is 534m. Figure 5.7 shows a typical result of a Fourier transform, darker colors represent a smaller amplitude. High frequency content is represented in the top right and low frequency content in the lower left.

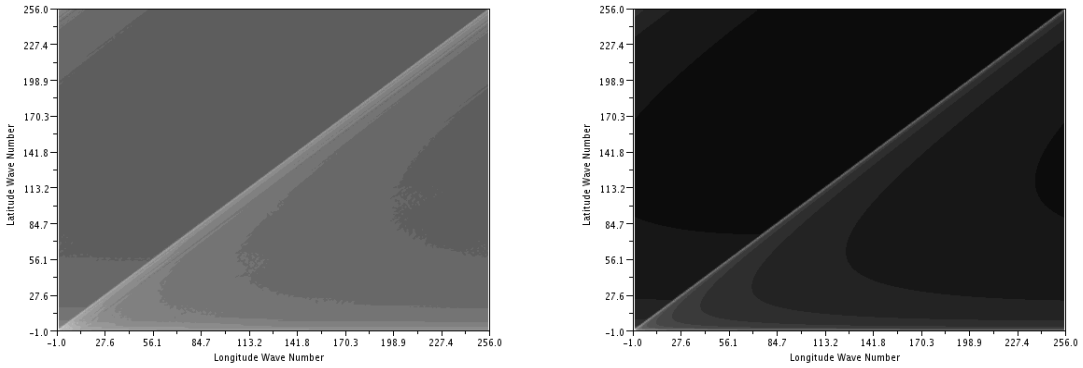

(a) 5 km for Q and 1 for P

(b) 794 km for Q and 2 for P

Figure 5.7: Fourier contour plots

The Fourier analysis was applied to 34 combinations of Q and P. Every result produced a plot similar to that given in figure 5.7. To get a better understanding of the filter parameters the Fourier solution where $\omega_{xi} = \omega_{xj}$ are plotted in figure 5.8. Overall, the figure confirms that larger values of Q give increased attenuation and for larger P values reduced attenuation.

It is interesting to note that the solution is approaching $A = A_0 k^{-1}$ for increasing values of Q. This solution corresponds to a tilted plane; thus the filtering successfully removes any local minima and maxima. The peaks in the $Q = 5$ series demonstrate the existence of local extrema in the solution. Comparing the $P = 1$ and $P = 2$ at $Q = 5$ shows that higher values of P preserves more of the low frequency content.

Figure 5.9 shows the Alberta wind resource subjected to various levels of filtering. Figure 5.9a gives a high level of fidelity, while increasing values of Q effectively blur the resource further and further. At $Q = 150$ km there are only 2 local maxima and at $Q = 794$ km all local maxima are filtered away confirming the results of the Fourier analysis.

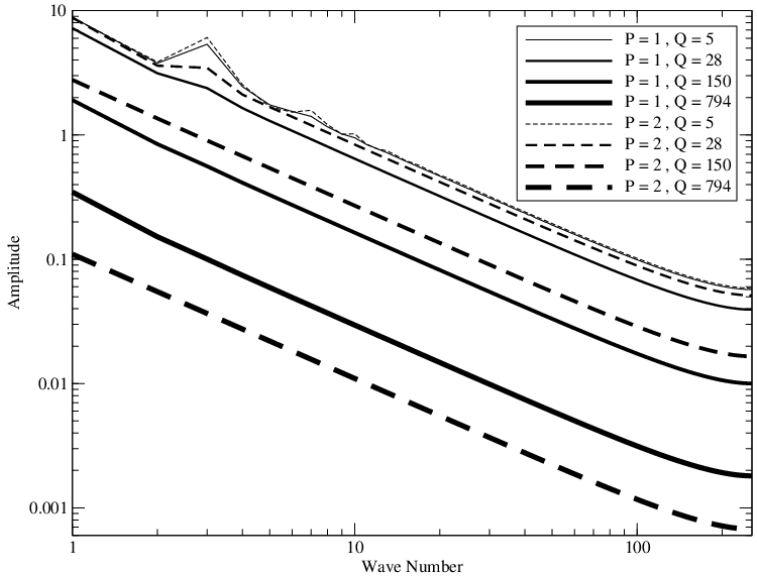

Figure 5.8: Frequency amplitude at common wave number

Discovering the optimal wind farm configuration is based on a sequence of phases, each with one or more wind farm siting simulation, where each subsequent phase is based on less aggressive numerical smoothing. When nothing is known about a region the the filtering in figure 5.9d or 5.9c would direct the optimization to the south from nearly any starting point. Subsequent optimization based on the filtering in figure 5.9b would refine the solution further. The final solution would be based on the filtering in figure 5.9a where distortion is minimized. When the model is used to gather a family of strong possibilities a collection of unique starting points about the last solution could be used in the latter phases to seek out multiple solutions. This phased approach will be demonstrated in articles that discuss the various applications of this model.

The effect of numerical smoothing is demonstrated by comparing the solutions of the base case and the AEP case. In the AEP case significantly cheaper transmission cost and permissive noise limits make the wind farm profitability more dependent on the AEP than all other factors. It is expected that these solutions will seek out regions of maximum AEP. Since the Q parameter was varied only for the Weibull shape and scale parameter the numerical smoothing would only affect the AEP calculations. Thus numerical smoothing should have a greater impact on the AEP case.

Four different starting points were selected, they are shown in figure 5.10 with green icons along with red icons for the final solution. It is clear that many of the

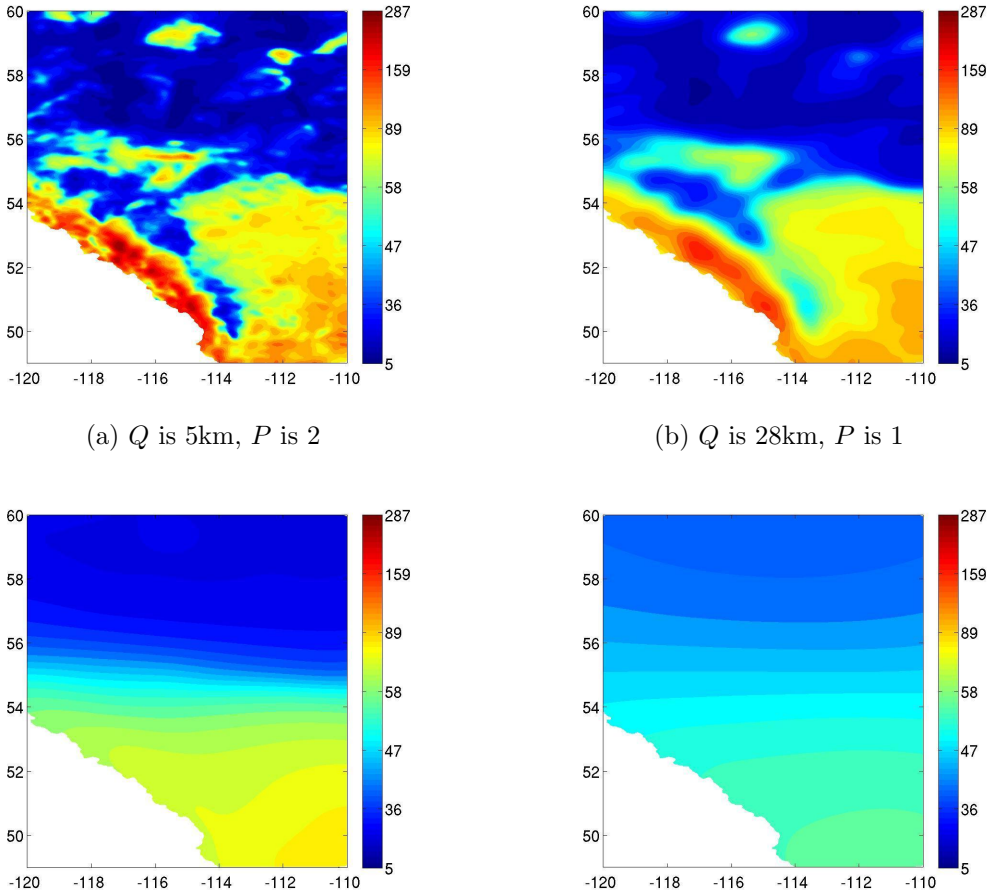

(a) Q is 5km, P is 2

(b) Q is 28km, P is 1

(c) Q is 150km, P is 1

(d) Q is 794km, P is 1

Figure 5.9: Alberta wind resource in W/m^2 with filtering

solutions based on the AEP case (figure 5.10b) moved towards the southeast corner of the province. Figure 5.9 shows that this area has a good resource under most applications of numerical smoothing. When the base case parameters are used, the local minima are influenced by the transmission lines and population distribution. Since these parameters are not smoothed the solution is still affected by local minima and does not travel far distances.

To demonstrate this difference in smoothing sensitivity the linear curve fit of the distance between the starting and end points is graphed against Q in figure 5.11. The slope of this curve fit is taken as the smoothing sensitivity parameter given in table 5.2. It is clear that the AEP seeking case is much more sensitive. Figure 5.11 shows that the distance decreases in the base case for values of Q greater than 150km. Figure

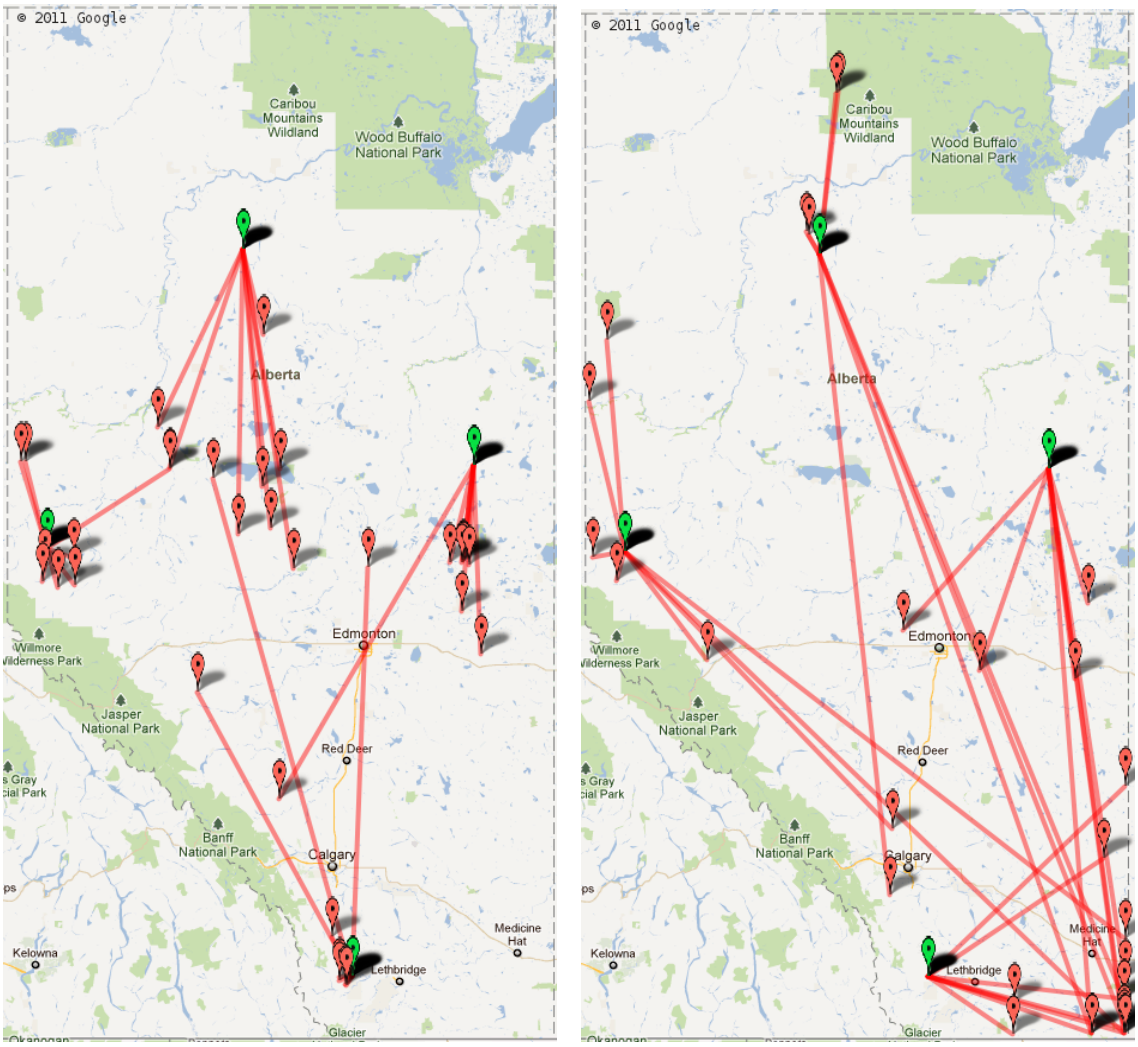

(a) Base Case (b) AEP Case

Figure 5.10: Wind farm locations, lines connect starting positions in green to solutions in red

5.8 shows that all variation is attenuated equally past $Q = 28$, with increasing Q the wind resource solution approaches the mean everywhere. This mean approaching trend is evident by comparing figure 5.9c and 5.9d. As the wind resource approaches the mean everywhere the optimal location has decreased dependence on the wind and becomes more sensitive to other factors. This demonstrates the importance of suppressing other factors when using aggressive numerical smoothing.

One may be tempted to apply the same numerical smoothing to population density. The influence of population is highly nonlinear, once the density reaches a certain

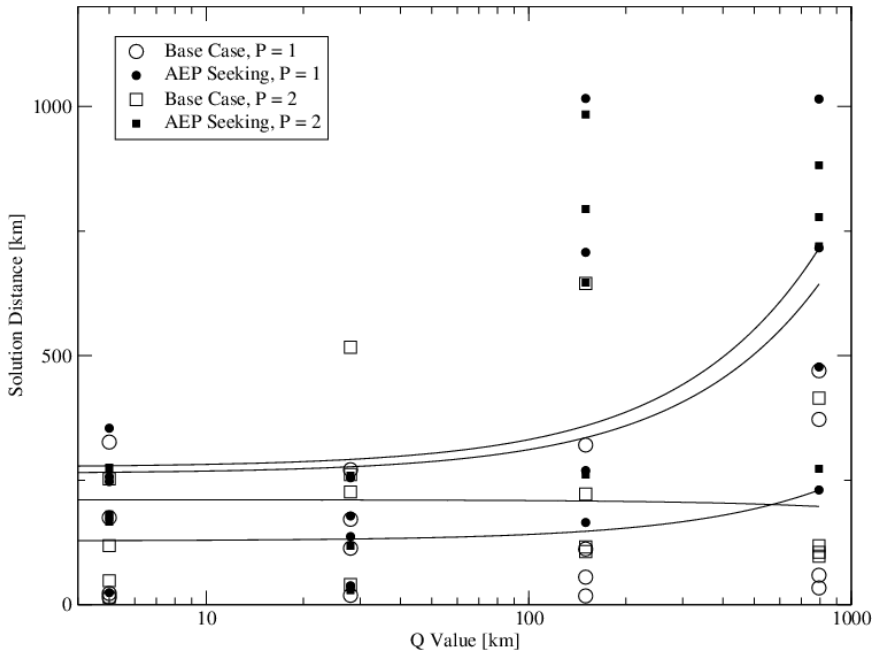

Figure 5.11: Solution distance vs. Q

Table 5.2: Smoothing sensitivity

Cases	$P = 1$	$P = 2$
Base Case	0.128	-0.017
AEP Seeking	0.479	0.553

threshold the number of turbines allowed approaches zero and the wind farm costs become asymptotic. If the population for the region is large enough that the average population density is above this threshold, then the solution becomes highly sensitive to people and moves away from crowded regions. In this case the "blurring" effect of numerical smoothing on population is concealing pockets where an optimal wind farm could be located. In the early phases it is recommended that optimization is based on AEP (equation (5.13)) or economic parameters are selected to suppress the influence of population and possibly transmission.

Sensitivity to Transmission

To evaluate the sensitivity to transmission infrastructure the cost of transmission was increased from \$100,000 per km to \$1,000,000 per km. All other parameters were identical to the base case. Figure 5.12b shows the new solutions with the expensive

transmission along with the transmission lines. Figure 5.12a shows that the base case solutions typically converged on top of a transmission line. With less expensive transmission the base case optimization was able to seek better solutions in regions further from the starting point. Increasing the transmission cost increases the model sensitivity to the local minima along the transmission lines; thus increasing the importance of numerical smoothing for transmission effects.

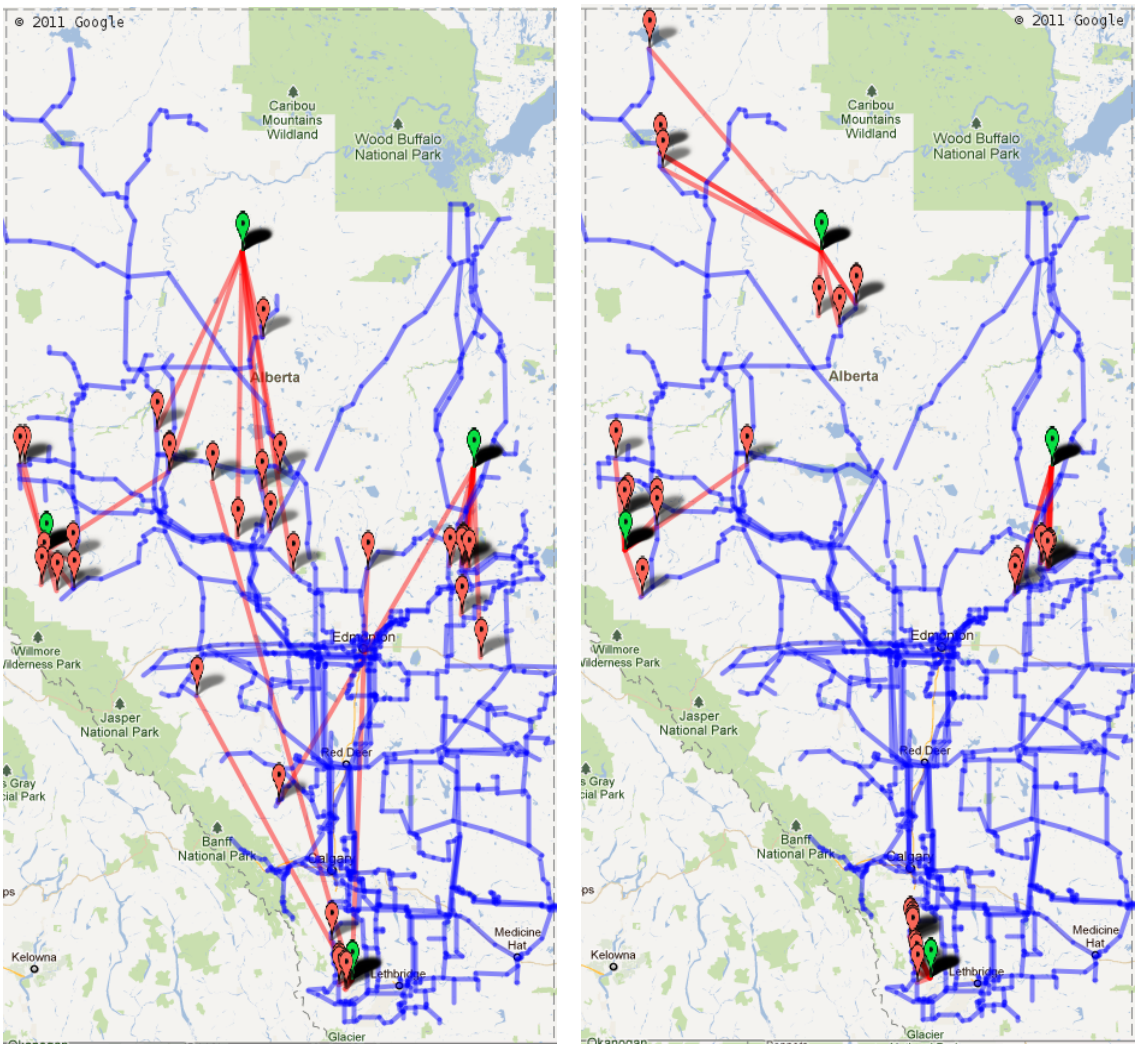

(a) Base Case (b) Tranmission Case

Figure 5.12: Wind farm locations, lines connect starting positions in green to solutions in red

The differences between the base case and transmission case cannot be attributed local minima alone. Within the results there are cases where the expensive transmission solutions achieved a shorter transmission line at the expense of improved

AEP. When four outliers are neglected from the results, the expensive transmission case decreased the minimum distance to a transmission line by 16%. On average the AEP of the expensive transmission results were 10% lower, thus transmission cost is preventing the optimization from seeking better wind resources.

In the four outliers the expensive transmission solution is significantly further from transmission than in the base case. These discrepancies occur when there is a stronger wind resource in the opposite direction of the transmission line nearest to the starting point. In the base case the optimization was able to move in the direction of the stronger wind resource and eventually find a converged solution at a different tranmission line. While the expensive transmission solution failed to reach any transmission line because the costs of a decreasing wind resource prevented further movement towards the nearest transmission line.

Sensitivity to Population

To evaluate the sensitivity to population, the noise offset limit of the base case was increased from 450m to 550m. Comparison between figures 5.13a and 5.10a show clearly that the optimal solutions are kept away from the densely populated southern region. The solutions from the only Southern starting point move towards the mountains where the population is reduced.

On average the optimal solutions were located in regions with an 8% reduction in receptor density. By cutting off regions that had a slightly higher population, there was a 1% reduction in the AEP leading to a 3% increase in wind energy cost.

These results demonstrate how this model could be applied to evaluate noise regulations or the potential performance of new turbine designs. However these conclusions are dependent on the assumptions of the micro-siting model. The micro-siting model needs to be calibrated with existing wind farm developments before any reliable conclusions can be drawn.

Sensitivity to Wind Resource

To confirm the model sensitivity to wind resource a set of optimization solutions were solved based on an objective of maximum average power (equation (5.13)). Those solutions are given in figure 5.13b. Comparison with figure 5.10b demonstrates that when all other influences are suppressed the optimization approaches the maximum

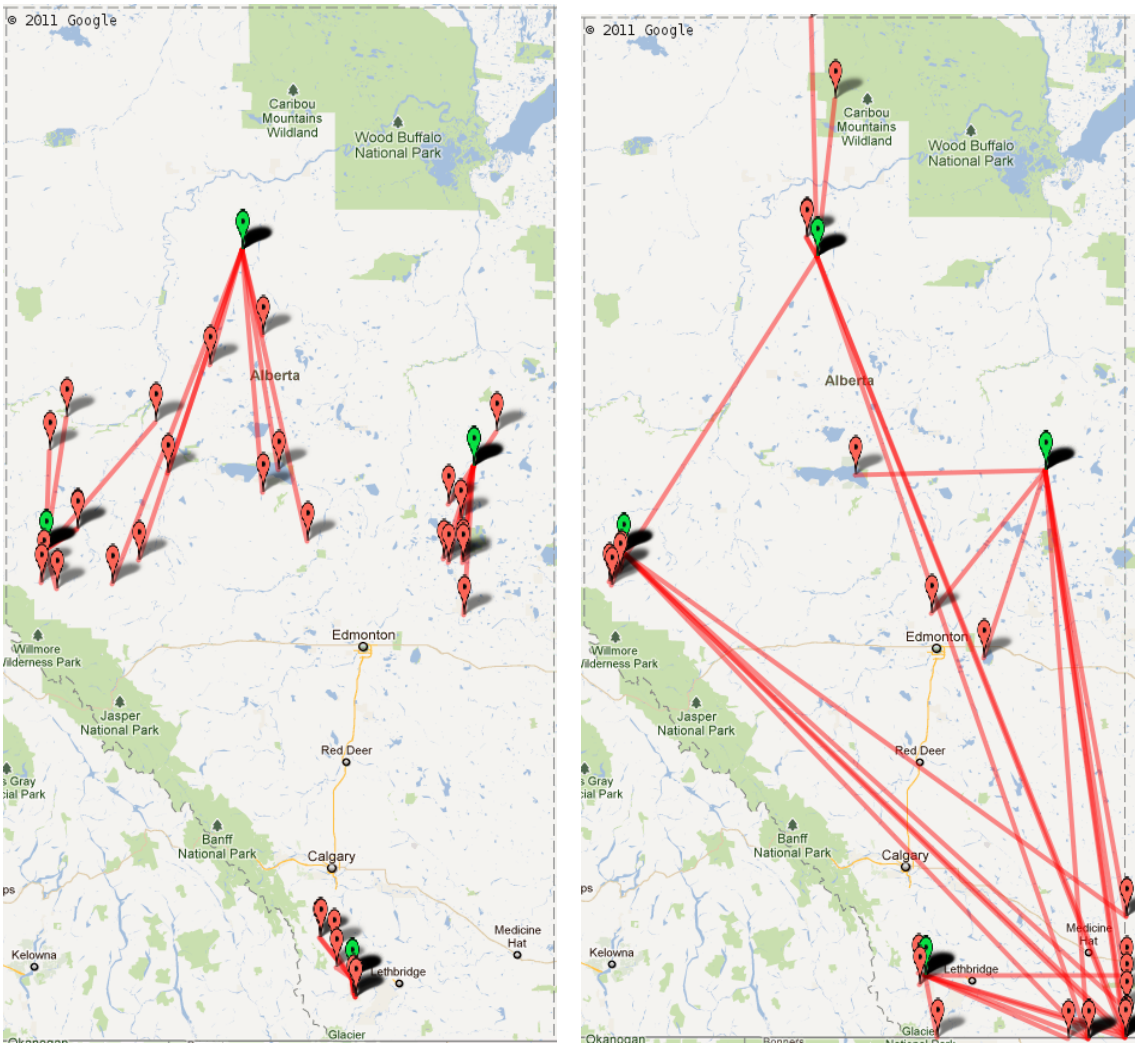

(a) Noise Case (b) Maximum AEP

Figure 5.13: Wind farm locations, lines connect starting positions in green to solutions in red

power solution. The comparison also demonstrates that the small influence of transmission and population does affect the model enough to give different results.

5.2 Structural Optimization with Adjoint Gradients

The work presented in this section is adapted from a 2012 AIAA Structural Dynamics and Materials conference paper:

Michael K. McWilliam and Curran Crawford. Adjoint Based Sensitivity Analysis for Geometrically Exact Beam Theory and Variational Asymptotic Beam Section Analysis with Applications to Wind Turbine Design Optimization. In *53rd AIAA Structures, Structural Dynamics and Materials Conference, April 23-26 2012, Honolulu Hawaii*, April 2012

Currently several advanced wind turbine design concepts are being explored by researchers. In general these concepts are based on reducing damaging fatigue loads by creating adaptive blades. There are strategies that apply sweep [28, 29], coning [25, 26, 27] and biased fiber orientations [31, 32] to aero-elastically tailor blades in order to minimize structural loads. Tools more advanced than Blade Element Momentum (BEM) methods and linear structural analysis are required to properly study these concepts in wind turbine design analysis.

To model the wind turbine blade, the Geometrically Exact Beam Theory (GEBT) pioneered by Simo [100] is well suited to capture geometric nonlinearity crucial in many load alleviation strategies. Currently GEBT is a mature theory now that issues associated with objectivity [104, 113] and temporal integration have been resolved [243, 244, 245]. Multi-dimensional Finite Element Methods (FEM) are capable of resolving the nonlinear dynamics, however the methods require considerably more degrees of freedom to resolve similar fidelity. Accordingly the computational cost detracts from this approach consequently is not considered for this work.

Industrial wind turbine blades are made from fiber reinforced plastic. These materials have anisotropy that can be engineered to give desirable cross section properties. To accurately determine the effect of material anisotropy the cross section warping needs to be solved. Variational Asymptotic Beam Section (VABS) analysis has been developed by Hodges and colleagues [40, 39, 121, 246, 126, 126, 124, 122, 123] to account for the affect of warping. Others have evaluated the accuracy compared to full three dimensional finite element models and analytical solutions [40, 128] demonstrating excellent agreement. Similarly VABS was compared with other cross section analysis methods and found in all cases it was superior [130]. For these reasons VABS has been incorporated into the optimization framework presented here.

These advanced design concepts rely on an expanded design space presenting a challenge to design optimization and analysis. The computational cost of sensitivity analysis based on forward propagating algorithms (e.g. finite difference) scale with the number of design variables. The work of Hjort *et al.* [64] demonstrated that

the computational cost of finite difference methods limited the sophistication and complexity that could be incorporated in design optimization.

Adjoint methods pioneered by Jameson [206] manipulate the physical governing equations of systems so that gradient information is propagated backwards from the objective equation to the design variables. The benefit of these methods is that the computational cost is proportional to the number of objectives and relatively insensitive to the number of design variables. The challenge is manipulating the governing equations to admit adjoint based sensitivity analysis. Trier *et al.* [215] has demonstrated how these methods are applied for nonlinear structural dynamics. Triers contribution did not address the challenges of finite rotations present in GEBT. Recently Wang and Yu [216] have developed the adjoint equations for two dimensional GEBT. Again by simulating the plane problem the challenges associated with three dimensional finite rotations are avoided.

The work presented here demonstrates the development of the adjoint equations for the fully nonlinear, three dimensional GEBT. The GEBT adjoint equations rely on intermediate gradients that depend on the cross section model. To alleviate computational loads in these models the adjoint equations for VABS has been derived. Special attention has been given to sensitivity analysis typical in wind turbine design.

This work is based on GEBT and VABS described in section 2.1.2 and section 2.2.1 of chapter 2 respectively. The adjoint methods are described in section 2.4.2 of chapter 2. Section 5.2.1 describes how the analysis tools are combined to obtain the weight, stress and deflection. This section then gives the derivation of the adjoint sensitivity for both GEBT and VABS analysis. The algorithms were applied to determine the minimum weight design of a wind turbine blade at a single operating point. The algorithms were compared against the finite difference algorithm for computational speed and the final optimization solution in section 5.2.2.

5.2.1 Methodology

Objective Evaluation

Figure 5.14 demonstrates the flow of information to calculate the objective and constraint information. First the mesh module will use the design variables to solve the blade weight and generate the **E** matrices. Then VABS will use this information to determine the warping function and constitutive matrix. Then GEBT will use the constitutive matrix to determine the beam deflection and beam strain. Next VABS

will use the warping solution and the beam strain to determine the three dimensional strain. Finally, the failure model uses the three dimensional strain to calculate a failure metric ($\hat{\sigma}$).

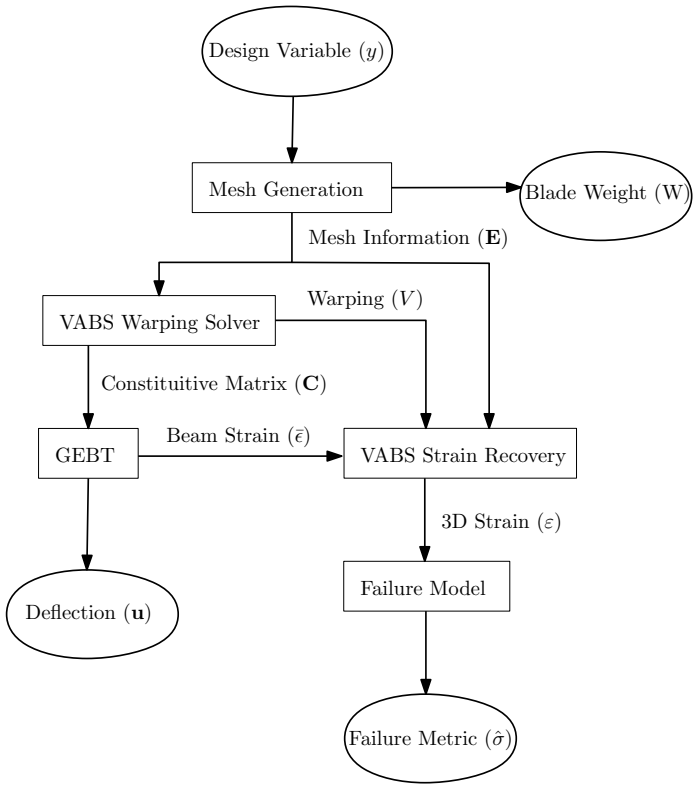

Figure 5.14: The algorithm for function evaluations

Adjoint Based Sensitivity Analysis

Adjoint based sensitivity analysis is broken into three sub-topics. First, the adjoint equations for GEBT are derived. Then the adjoint equations for VABS are derived. Finally, this section closes by discussing the two ways these equations can be coupled to solve the design sensitivities.

The adjoint sensitivity is based on the adjoint theory presented in section 2.4.2 in chapter 2. The following sections will derive the adjoint based sensitivity for GEBT and VABS theory. The general steps taken are as follows:

1. Linearize the governing equations, as shown in section 5.2.1.

2. Derive the adjoint equation as shown in section 5.2.1 and 5.2.1.

3. Determine the objective sensitivity to state variables. This is the source term in the adjoint equation (2.51) and is required before an adjoint solution can be found. Central differencing was used to calculate this gradient.

4. Solve the adjoint equation. All the adjoint equations are linear and can be solved with standard methods in linear algebra.

5. Once the adjoint solution is found, the sensitivity of the residual expression is required to solve the final sensitivity with equation (2.49c). Again central differencing was used to calculate this gradient.

Adjoint Equations for Geometrically Exact Beam Theory

Since GEBT is a nonlinear theory the derivation of the adjoint equations is given in two steps. The first step linearizes the equations; then the adjoint equations are derived from the linear model.

Geometrically exact beam theory is a nonlinear model based on finite rotations. The perturbations of the state variables could be defined in multiple ways [112], each resulting in different linearized equations.

The linearization is complicated by the presence of finite rotations. Finite rotations do not admit a linear space, that is to say a rotation of θ then a perturbation ϑ does not result in a final orientation vector of $\theta + \vartheta$. The linearization can be applied in terms of the orientation parameters directly (i.e. $\partial R/\partial\theta_i$) or an incremental perturbation (i.e. $\partial R/\partial\vartheta_i$). Linearization in terms of ϑ is more intuitive as these directions are configuration independent. To be consistent a perturbation of $\mathbf{u}$ is applied on ϕ, in this case the final position is $\phi + \mathbf{u}$.

Simo and Vu-Quoc [101] give the linearization of the internal energy. They define the linearization of strain as equation (5.34).

$$\begin{Bmatrix} \delta\gamma \\ \delta\kappa \end{Bmatrix} = \begin{bmatrix} \frac{d}{ds} & \frac{d\phi}{ds}\times \\ \mathbf{0}_3 & \frac{d}{ds} \end{bmatrix} \begin{Bmatrix} \delta\mathbf{u} \\ \delta\vartheta \end{Bmatrix} \tag{5.34}$$

This leads to the material tangent stiffness equation in (5.35).

$$\mathbf{K}_m = \begin{bmatrix} \frac{d}{ds} & \mathbf{0}_3 \\ -\frac{d\phi}{ds}\times & \frac{d}{ds} \end{bmatrix} \begin{bmatrix} \Lambda & \mathbf{0}_3 \\ \mathbf{0}_3 & \Lambda \end{bmatrix} \left[\nabla^2\Psi\right] \begin{bmatrix} \Lambda^T & \mathbf{0}_3 \\ \mathbf{0}_3 & \Lambda^T \end{bmatrix} \begin{bmatrix} \frac{d}{ds} & \frac{d\phi}{ds}\times \\ \mathbf{0}_3 & \frac{d}{ds} \end{bmatrix} \tag{5.35}$$

Similarly Simo and Vu-Quoc [101] give the geometric stiffness as (5.36).

$$\mathbf{K}_g = \begin{bmatrix} \frac{d}{ds} & \mathbf{0}_3 & \mathbf{0}_3 \\ \mathbf{0}_3 & \frac{d}{ds} & \mathbf{I}_3 \end{bmatrix} \begin{bmatrix} \mathbf{0}_3 & \mathbf{0}_3 & -\mathbf{n}\times \\ \mathbf{0}_3 & \mathbf{0}_3 & -\mathbf{m}\times \\ \mathbf{n}\times & \mathbf{0}_3 & \mathbf{n}\otimes\frac{d\phi}{ds} - \left(\mathbf{n}\cdot\frac{d\phi}{ds}\right)\mathbf{I}_3 \end{bmatrix} \begin{bmatrix} \frac{d}{ds} & \mathbf{0}_3 \\ \mathbf{0}_3 & \frac{d}{ds} \\ \mathbf{0}_3 & \mathbf{I}_3 \end{bmatrix} \tag{5.36}$$

Together these equations give the linearized model as shown in equation (5.37).

$$\delta\mathbf{R} = (\mathbf{K}_m + \mathbf{K}_g)\,\delta\epsilon \tag{5.37}$$

The development of the adjoint equations is similar to the approach taken by Trier *et al.* [215]. Before the adjoint can be derived for equation (5.37) the adjoint operator for each sub-matrix needs to be defined. Most of the matrix terms in the first matrix of equation 5.37 are algebraic where the adjoint is simply the transpose. The contributions of $\mathbf{K}_m$ (equation (5.35)) and $\mathbf{K}_g$ (equation (5.36)) make $\mathbf{K}$ a differential operator. The adjoint of these matrices and respective boundary terms are given in equations (5.39) and (5.40).

$$\begin{aligned} \int \psi^T \mathbf{K}_m \chi d\mathcal{D} &= \int \chi^T \mathbf{K}_m^* \psi d\mathcal{D} + \mathcal{B}_m \\ &= \int \chi^T \begin{bmatrix} -\frac{d}{ds} & \mathbf{0}_3 \\ -\frac{d\phi}{ds}\times & -\frac{d}{ds} \end{bmatrix} \begin{bmatrix} \Lambda & \mathbf{0}_3 \\ \mathbf{0}_3 & \Lambda \end{bmatrix} [\nabla\Psi]^T \begin{bmatrix} \Lambda^T & \mathbf{0}_3 \\ \mathbf{0}_3 & \Lambda^T \end{bmatrix} \begin{bmatrix} -\frac{d}{ds} & \frac{d\phi}{ds}\times \\ \mathbf{0}_3 & -\frac{d}{ds} \end{bmatrix} \psi d\mathcal{D} \end{aligned} \tag{5.38}$$

and

$$\begin{aligned} \int \psi^T \mathbf{K}_g \chi d\mathcal{D} &= \int \chi^T \mathbf{K}_g^* \psi d\mathcal{D} + \mathcal{B}_g \\ &= \int \chi^T \begin{bmatrix} -\frac{d}{ds} & \mathbf{0}_3 & \mathbf{0}_3 \\ \mathbf{0}_3 & -\frac{d}{ds} & \mathbf{I}_3 \end{bmatrix} \begin{bmatrix} \mathbf{0}_3 & \mathbf{0}_3 & -\mathbf{n}\times \\ \mathbf{0}_3 & \mathbf{0}_3 & -\mathbf{m}\times \\ \mathbf{n}\times & \mathbf{0}_3 & \mathbf{n}\otimes\frac{d\phi}{ds} - \left(\mathbf{n}\cdot\frac{d\phi}{ds}\right)\mathbf{I}_3 \end{bmatrix}^T \begin{bmatrix} -\frac{d}{ds} & \mathbf{0}_3 \\ \mathbf{0}_3 & -\frac{d}{ds} \\ \mathbf{0}_3 & \mathbf{I}_3 \end{bmatrix} \psi d\mathcal{D} \end{aligned} \tag{5.39}$$

Together these equations lead to the definition of $\mathbf{K}^*$ in equation (5.40) which is simply the transpose of the tangent stiffness matrix.

$$\mathbf{K}^* = \mathbf{K}_m^* + \mathbf{K}_g^* \tag{5.40}$$

The adjoint equation is shown in equation (5.41).

$$\mathbf{K}^{*}\psi = \frac{\partial J}{\partial x} \tag{5.41}$$

Once ψ is solved, equation (2.49c) can be used to get the sensitivities.

Adjoint Equations for Variational Asymptotic Beam Section Analysis

This section derives the adjoint equations for VABS analysis. There are two intermediate objectives of VABS analysis, each requiring a unique set of adjoint equations. The first set calculates the design sensitivity of the constitutive matrix. The second set calculates the design sensitivity of the three dimensional strain. This second set of equations has dependency on state variables of GEBT. In general the VABS adjoint equations would have to account for variations in the beam state variables. However, when integrated with the GEBT adjoint equations this variation can be ignored.

The derivation of the adjoint equations proceeds first by defining the objective equation for $\mathbf{C}$ (equation (5.42)).

$$\mathbf{C} = \mathbf{E}_{a\epsilon}^{T}\mathbf{N}\mathbf{V}_{0}^{\star} + \mathbf{E}_{\epsilon\epsilon} \tag{5.42}$$

Second, we define the residual expression for VABS analysis (equation (5.43)).

$$\mathbf{R}_{C} = \mathbf{E}_{a\epsilon}\mathbf{V}_{0}^{\star} + \mathbf{N}^{T}\mathbf{E}_{a\epsilon} \tag{5.43}$$

Next, we define the three supporting gradients, $\partial\mathbf{C}/\partial y$ in equation (5.44),

$$\frac{\partial \mathbf{C}}{\partial y} = \frac{\partial \mathbf{E}_{a\epsilon}}{\partial y}\mathbf{N}^{T}\mathbf{V}_{0}^{\star} + \mathbf{E}_{a\epsilon}\frac{\partial \mathbf{N}}{\partial y}^{T}\mathbf{V}_{0}^{\star} + \frac{\partial \mathbf{E}_{\epsilon\epsilon}}{\partial y} \tag{5.44}$$

$\partial R/\partial y$ in equation (5.45)

$$\frac{\partial \mathbf{R}_{C}}{\partial y} = \frac{\partial \mathbf{E}_{aa}}{\partial y}\mathbf{V}_{0}^{\star} + \frac{\partial \mathbf{N}}{\partial y}^{T}\mathbf{E}_{a\epsilon} + \mathbf{N}^{T}\frac{\partial \mathbf{E}_{a\epsilon}}{\partial y} \tag{5.45}$$

and $\partial\mathbf{C}/\partial\mathbf{V}_{0}^{\star}$ in equation (5.46)

$$\frac{\partial \mathbf{C}}{\partial \mathbf{V}_{0}^{\star}} = \mathbf{E}_{a\epsilon}^{T}\mathbf{N} \tag{5.46}$$

Applying the identity (2.52) gives the adjoint equation as shown in equation (5.47).

$$\mathbf{E}_{aa}\psi = \mathbf{N}^T\mathbf{E}_{a\epsilon} \tag{5.47}$$

By equation (2.19a) it is clear the solution for ψ is $-\mathbf{V}_0^\star$. Substituting these results in equation (2.49c) gives the final sensitivity solution in equation (5.48).

$$\frac{d\mathbf{C}}{dy} = \mathbf{V}_0^{\star T}\frac{\partial \mathbf{E}_{aa}}{\partial y}\mathbf{V}_0^\star + \frac{\partial \mathbf{E}_{\epsilon\epsilon}}{\partial y} + \left(\frac{\partial \mathbf{E}_{a\epsilon}^T}{\partial y}\mathbf{N}\mathbf{V}_0^\star + \mathbf{V}_0^{\star T}\mathbf{N}\frac{\partial \mathbf{E}_{a\epsilon}}{\partial y}\right) + \left(\mathbf{E}_{a\epsilon}^T\frac{\partial \mathbf{N}}{\partial y}\mathbf{V}_0^\star + \mathbf{V}_0^{\star T}\frac{\partial \mathbf{N}^T}{\partial y}\mathbf{E}_{a\epsilon}\right) \tag{5.48}$$

The derivation of the adjoint equations will be based on the objective in equation (5.49a) because it allows for a simple definition of the $\partial J/\partial V$ gradient.

$$\Phi = \mathbf{B}_a\mathbf{N}\hat{\mathbf{V}}_0^\star + \mathbf{B}_\epsilon \tag{5.49a}$$

$$\varepsilon = \Phi\bar{\epsilon} \tag{5.49b}$$

The governing equation and supporting gradient $\partial R/\partial y$ have already been defined in equations (5.43) and (5.45) respectively. Next, the supporting gradient $\partial\Phi/\partial y$ is defined in equation (5.50),

$$\frac{\partial \Phi}{\partial y} = \frac{\partial \mathbf{B}_a}{\partial y}\mathbf{N}\hat{\mathbf{V}}_0^\star + \mathbf{B}_a\frac{\partial \mathbf{N}}{\partial y}\hat{\mathbf{V}}_0^\star + \frac{\partial \mathbf{B}_\epsilon}{\partial y} \tag{5.50}$$

and the other supporting gradient $\partial\Phi/\partial\hat{\mathbf{V}}_0^\star$ is defined in equation (5.51).

$$\frac{\partial \Phi}{\partial \hat{\mathbf{V}}_0^\star} = \mathbf{B}_a\mathbf{N} \tag{5.51}$$

Applying the identity in equation (2.52) leads to the adjoint equation in (5.52).

$$\mathbf{E}_{aa}\psi^\star = \mathbf{N}^T\mathbf{B}_a^T \tag{5.52}$$

Solving the solution of (5.52) directly will result in errors because the matrix $\mathbf{E}_{aa}$ has a null space. This means that $\psi^\star$ will have a deterministic component (particular solution) and an indeterminant component (homogeneous solution). Equation (5.53) is used to suppress the indeterminant component.

$$\psi = \mathbf{N}\psi^\star \tag{5.53}$$

The ψ solution and the other supporting gradients can be substituted into equation (2.49c) to the get sensitivity with equation (5.54).

$$\frac{d\Phi}{dy} = \frac{\partial \mathbf{B}_a}{\partial y}\mathbf{N}\hat{\mathbf{V}}_0^\star + \mathbf{B}_a\frac{\partial \mathbf{N}}{\partial y}\hat{\mathbf{V}}_0^\star + \frac{\partial \mathbf{B}_\epsilon}{\partial y} - \psi^T\left(\frac{\partial \mathbf{E}_{aa}}{\partial y}\mathbf{V}_0^\star + \frac{\partial \mathbf{N}}{\partial y}^T\mathbf{E}_{a\epsilon} + \mathbf{N}^T\frac{\partial \mathbf{E}_{a\epsilon}}{\partial y}\right) \quad (5.54)$$

In general, variations in $\bar{\epsilon}$ would have to be incorporated into the sensitivity analysis. However, in this application $d\varepsilon/dy$ sensitivity calculation is an intermediate step where the GEBT state variables are held constant. Under these circumstances, variations in $\bar{\epsilon}$ can be ignored giving the final sensitivity in equation (5.55).

$$\frac{d\varepsilon}{dy} = \left(\frac{\partial \mathbf{B}_a}{\partial y}\mathbf{N}\hat{\mathbf{V}}_0^\star + \mathbf{B}_a\frac{\partial \mathbf{N}}{\partial y}\hat{\mathbf{V}}_0^\star + \frac{\partial \mathbf{B}_\epsilon}{\partial y} - \psi^T\left(\frac{\partial \mathbf{E}_{aa}}{\partial y}\mathbf{V}_0^\star + \frac{\partial \mathbf{N}}{\partial y}^T\mathbf{E}_{a\epsilon} + \mathbf{N}^T\frac{\partial \mathbf{E}_{a\epsilon}}{\partial y}\right)\right)\bar{\epsilon} \quad (5.55)$$

Finally, this strain sensitivity can be used to find the sensitivity of a failure metric $\hat{\sigma}$ using a Frechet derivative for $d\hat{\sigma}/d\varepsilon$ and shown in (5.56).

$$\frac{d\hat{\sigma}}{dy} = \frac{d\varepsilon}{dy}\frac{d\hat{\sigma}}{d\varepsilon} \quad (5.56)$$

Coupled Adjoint Sensitivity Analysis

The objective of adjoint based sensitivity analysis is to reduce the dependency of computational load on design variables. The work presented here gives two sets of adjoint equations; the first is for the beam; the second for the cross section analysis. This presents two possible algorithms.

The first will shift design variable dependency out of the beam model. The benefit of the first algorithm allows the model to perform cross section analysis at many locations along the blade without having a large impact on the design sensitivity. However, this algorithm is still sensitive to the number of design variables in a given cross section.

The second algorithm retains the GEBT adjoint equations and further shifts the design variable dependency out of the beam cross-section analysis. This eliminates the design variable sensitivity both along the blade and within the cross-section. This algorithm enables rich cross section descriptions at many locations along the blade.

Figure 5.15 shows the flow of information when performing GEBT adjoint based sensitivity analysis. Finite difference (as indicated by the dashed and dotted lines) is still used extensively throughout the framework. In this algorithm the VABS analysis will still calculate the expensive warping solution for every design variable.

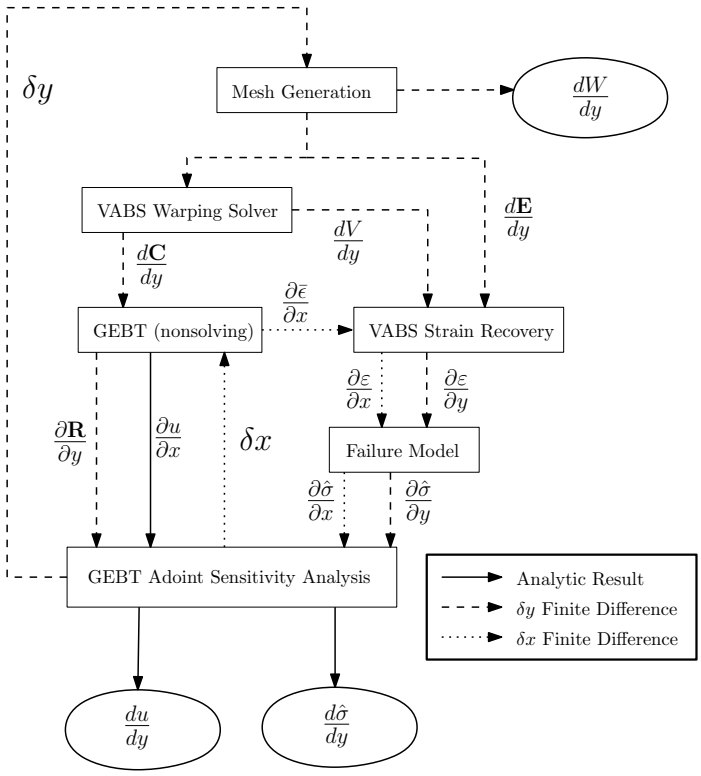

Figure 5.15: The algorithm for GEBT adjoint based sensitivity

The key benefit is the nonlinear implicit equations of GEBT do not have to be solved for every design variable. In theory, eliminating nested iteration loops can have a strong benefit to performance. However, this iteration converges rapidly from the small perturbations of finite difference, so this benefit is limited.

The second algorithm (Figure 5.16) tries to overcome the computational expense in the VABS analysis. Here the VABS adjoint equations are included into the framework. This eliminates the need to solve multiple solutions for the warping function.

The governing equations of VABS analysis provide simple analytic expressions for gradients with respect to the warping. Finite difference algorithms are still used extensively throughout the framework. Simple finite difference algorithms can be used to calculate gradients based on design variables (δy) and beam state variables (x)

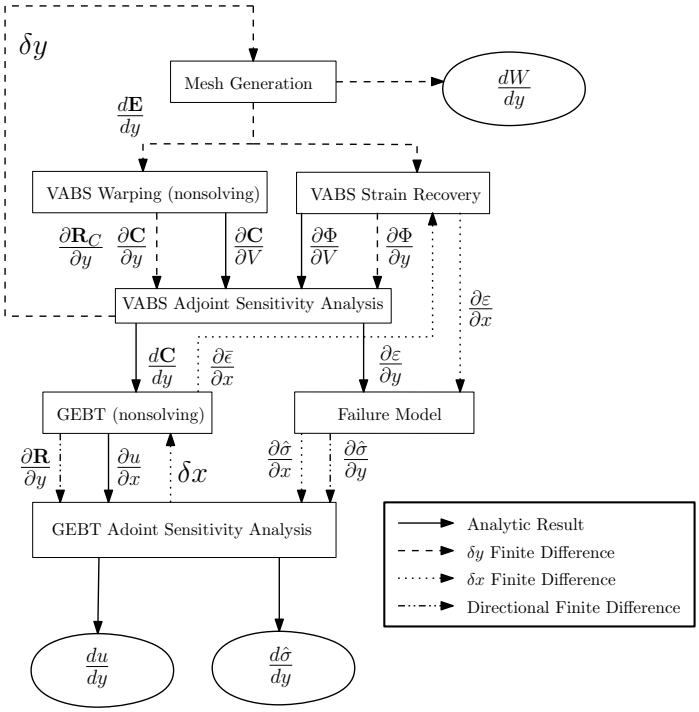

Figure 5.16: The algorithm for GEBT and VABS adjoint based sensitivity

directly. Sensitivities dependent on $\partial \mathbf{C}/\partial y$ and $\partial \varepsilon/\partial y$ are evaluated with directional finite difference as shown in equation (5.57).

$$\frac{\partial f(\alpha)}{\partial y} \approx \lim_{h \to 0} \frac{f\left(\alpha + h\frac{\partial \alpha}{\partial y}\right) - f(\alpha)}{h} \tag{5.57}$$

5.2.2 Results and Discussion

The finite difference gradient algorithm and the algorithms given in figure 5.15 and 5.16 were implemented in a C++ program. Gradient calculations were performed on multiple problems with varying number of design variables. The computational load of the various operations is discussed in section 5.2.2. These algorithms were used in simple optimization problems to evaluate differences in performance, this is discussed in section 5.2.2.

Computational Load of Gradient Evaluations

Figure 5.17 shows the gradient evaluation time for the different algorithms. All the algorithms seem to have a strong dependence on the number of design variables. The

results of a linear regression are given in table 5.3. The results show that the GEBT adjoint algorithm has the largest sensitivity while the FULL adjoint algorithm has the smallest sensitivity.

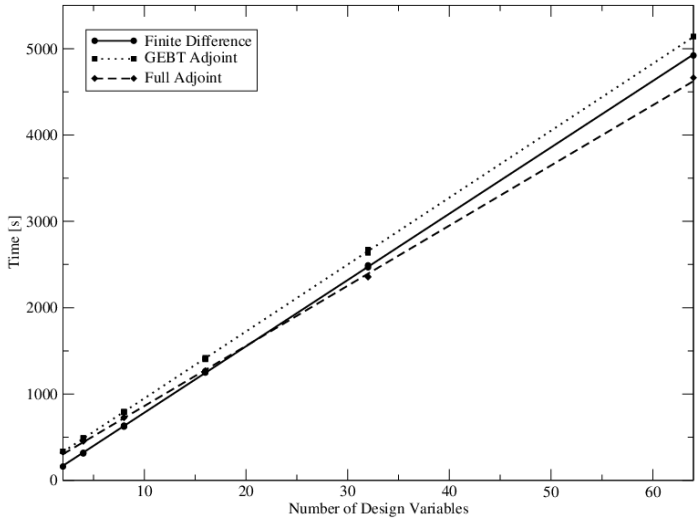

Figure 5.17: Computation time of gradient algorithms

Table 5.3: Curve fit results

Algorithm	Slope [s]	Intercept [s]
Finite Difference	76.8	15.7
GEBT Adjoint	69.7	163.9
Full Adjoint	77.5	174.3

The results in table 5.3 show that all algorithms have significant dependence on the number of design variables. All algorithms rely on finite difference gradients applied to the mesh generation, linking the VABS elements to the new mesh, calculating all the **E** matrices and the **N** matrix. Table 5.4 shows the time and percentage of time consumed by these steps for the largest gradient calculation. It is clear that most of the numerical work is consumed calculating the **N** matrix. This calculation involves a matrix product of a $4 \times n$ and $n \times 4$ matrices and a triple matrix product of a $n \times 4$, 4×4 and $4 \times n$ matrices where n is the number of state variables in the VABS calculation. These multiplications are performed by a matrix library that is much less efficient than other libraries like BLAS [247]. Calculating the **E** matrices

involves a significant amount of computational time. These calculations use the same inefficient library and create unnecessary copies of intermediate results. In future implementations the computational cost of calculating the **E** and **N** matrices will be reduced by using optimized code.

Table 5.4: Computation time of selected calculations

Calculation	Finite Difference [s]	GEBT Adjoint [s]	Full Adjoint [s]
Mesh Calculation	24 (0.5%)	24 (0.5%)	24 (0.6%)
Mesh Linkage	7 (0.1%)	7 (0.1%)	8 (0.2%)
Calculating **E**	824 (16.7%)	823 (16.0%)	793 (18.4%)
Calculating **N**	1796 (36.3%)	1826 (35.6%)	1917 (44.4%)
Solving (2.19a)	2233 (45.1%)	2236 (43.6%)	

Another factor contributing to a similar performance is the reduced time in a GEBT calculation during finite difference gradient calculations. Figure 5.18 shows the average computation time for the GEBT module in both a function evaluation and the gradient calculations. The results show a large difference between function evaluation time and the gradient evaluation time. The GEBT time decreases with an increasing number of design variables. This is based on the initial residual of the GEBT equations. For the function evaluation, the initial residual is large and requires many iterations to converge. In a finite difference perturbation it is small and converges much faster. Increasing the number of design variables introduced variables that had diminishing affect on the initial residual, causing further increases in speed. Overall, the finite difference algorithm performed better than expected because of faster convergence.

The timing results can still demonstrate the potential benefits of adjoint methods. Figure 5.19 shows the computation time in the GEBT module for all the algorithms. The finite difference algorithm requires multiple solutions to a linearized equations, while the adjoint algorithms only need to solve a similar system of equations twice.

Figure 5.20 shows the computation time in the VABS module for each of the algorithms. Since the finite difference algorithm is used in the GEBT adjoint algorithm there is no difference in the computation time. Comparing these algorithms to the FULL adjoint algorithm demonstrates the benefit of cutting out the VABS matrix solution. All the algorithms exhibit sensitivity to the number of design variables be-

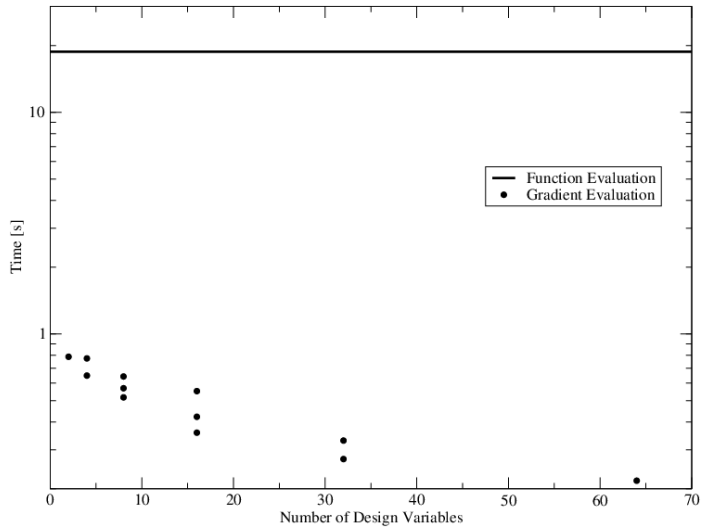

Figure 5.18: Computation time of GEBT calculations

cause the timing results include the calculations of the **E** and **N** matrices as discussed in section 5.2.2.

The adjoint equations improve the speed by cutting out some of the iterative methods and the matrix solutions. However these methods require additional computations. The timing results from the two largest adjoint methods are presented in table 5.5.

Table 5.5: Computation time of additional adjoint calculations

Calculation	GEBT Adjoint	Full Adjoint [s]
GEBT Adjoint Source Term ($\partial J/\partial x$)	179s	181s
Solving the GEBT Adjoint Equation	84.4ms	85.4ms
Calculating the final GEBT Sensitivity	2.24ms	2.29ms
Solving the VABS Adjoint Equation		2.43s
Performing the Frechet Gradients		1.98s

Table 5.4 shows that the additional costs of the GEBT adjoint source term is about 6 times greater than the cost savings of eliminating the multiple matrix solutions. The cost of the finite difference algorithm in calculating the adjoint source term is far more expensive because the number of GEBT state variables is much greater than the number of design variables. This additional cost can be reduced by using analytic gradients, which will discussed further below.

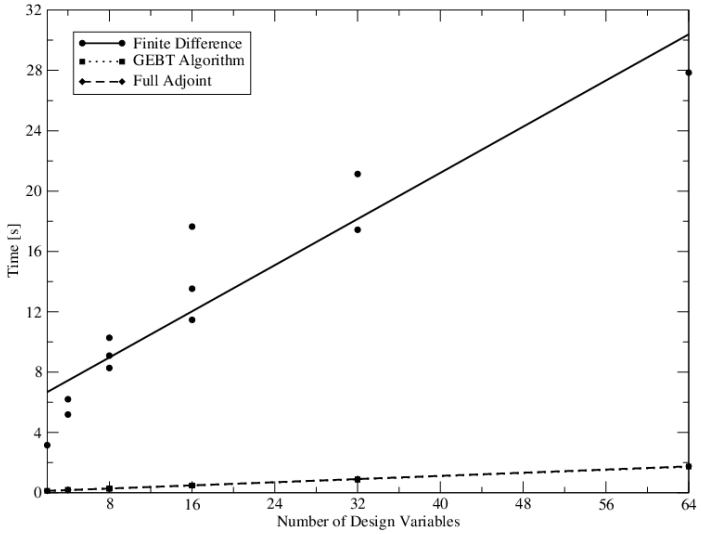

Figure 5.19: Computation time within the GEBT module

There is no additional cost calculating the source term for the VABS adjoint equation because they are intermediate results in the function evaluation. Overall the additional costs of the VABS adjoint algorithm are insignificant compared to the savings from avoiding the VABS solution. This net benefit contributes to the improved timing of the full adjoint algorithm.

Improving the calculation time of the $\partial J/\partial x$ source term will improve both adjoint algorithms. Finite difference algorithms were used for these calculations, however these calculations admit an analytic solution. First the source term for the deflection objective is trivial, it is merely a vector filled with zeros except for a 1 in the deflection coordinate of interest. The source term for the failure metric is given in equation (5.58). The last two matrices ($[\partial\varepsilon/\partial\epsilon]$ and $[\partial\epsilon/\partial x]$) are intermediate results from the function evaluation. The first matrix can be derived by linearizing the failure model.

$$\frac{\partial\sigma}{\partial x} = \left[\frac{\partial\sigma}{\partial\varepsilon}\right]\left[\frac{\partial\varepsilon}{\partial\epsilon}\right]\left[\frac{\partial\epsilon}{\partial x}\right] \tag{5.58}$$

Optimization Results

The sensitivity algorithms were applied to a simple structural optimization problem based on the MEXICO experiments [217]. The original rotor was made from machined aluminum and had a peak power coefficient at 15m/s. Commercial wind turbines are made from glass reinforced plastic and operate at peak power coefficients at wind

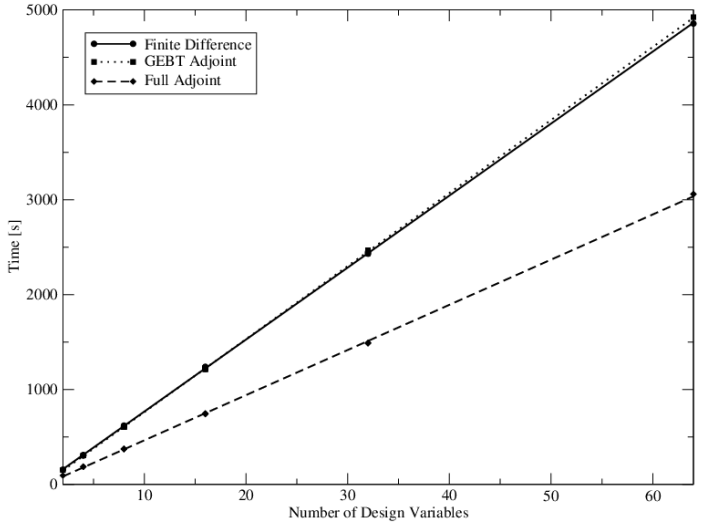

Figure 5.20: Computation time within the VABS module

speeds of approximately $7m/s$. The optimization algorithm was used to solve the optimal commercial equivalent.

The objective for the optimization is to minimize the weight of the blade. This solution is subjected to two constraints. The first limits the tip deflections to 3.5cm and the second applies the Tsai-Hill [248] failure model to avoid material failure. The assumed lay-up is uniaxial glass fiber reinforced plastic. The optimization neglected all the IEC 61400 [249] load cases and only considered steady operation in a 7m/s wind. The measured forces of the MEXICO experiment were scaled by a factor of $7^2/15^2$. The internal structure is based on an 'I-Beam' cross section as shown in Figure 5.21. The optimization problem was solved with a Sequential Quadratic Programming (SQP) algorithm by Lawrence *et al* [202].

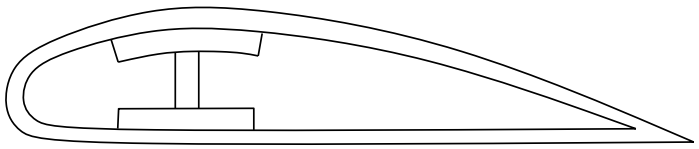

Figure 5.21: 'I-Beam' cross-section

The design variables specified the cross section geometry at specific locations along the blade. These design parameters were interpolated along the blade using cubic splines. Design variables were added by increasing the number of locations along the blade and the number of variables in the cross section.

The cross-section analysis was applied at multiple locations along the blade. The results of this analysis were then interpolated to intermediate locations. Applying VABS analysis at multiple locations gives better results at the expense of increased computational load. To explore this trade-off, cases with two, four and eight evaluation points were explored. Cases where the number of design variables exceeded the number of cross-sections were ignored because every local minimum would have multiple solutions.

The average optimal weight for a common number of design variables is given in figure 5.22. In the 'GEBT Adjoint' algorithm, only the GEBT adjoint equations were incorporated into the sensitivity analysis. In the 'Full Adjoint' algorithm both the GEBT and VABS adjoint equations were incorporated into the sensitivity analysis. These algorithms were compared to the 'Finite Difference' algorithm, where central differencing was applied to the function evaluation as discussed in section 5.2.1. Figure 5.22 shows that more design variables will improve the solution. The results show that all sensitivity algorithms give similar results. Table 5.6 shows that any difference in the adjoint algorithms is either lower or negligible.

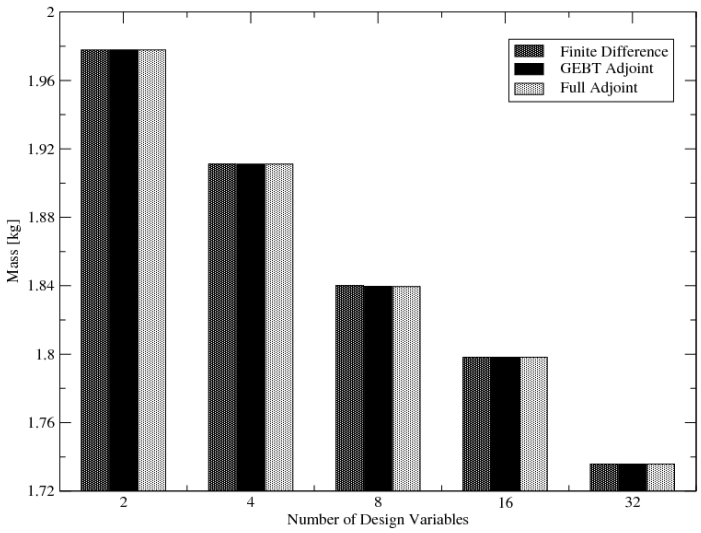

Figure 5.22: Average weight vs. number of design variables

Most design variables converged on the specified boundary (side constraint) that gave the minimum weight. The only exception was the spar-cap thickness. Figure 5.23 shows the spar cap thickness solution for selected problems. The number of cross sections indicate the number of VABS calculations along the span, the number of variables indicate the number of span-wise locations where design variables were

Table 5.6: Average weight difference compared to finite difference

Number of Design Variables	GEBT Adjoint	Full Adjoint
2	-1.53×10^{-8}	-6.91×10^{-9}
4	1.50×10^{-8}	3.19×10^{-6}
8	-4.47×10^{-4}	-4.94×10^{-4}
16	2.14×10^{-10}	1.24×10^{-9}
32	5.34×10^{-11}	1.22×10^{-10}

specified. The solutions with more than two design variables show an increasing thickness until $r/R \approx 0.2$ then decreasing to the minimum thickness. At the root, the chord length is reducing. To maintain adequate stiffness the spar cap thickness must increase. The effect of increasing design variables is evident in the qualitative differences between solutions.

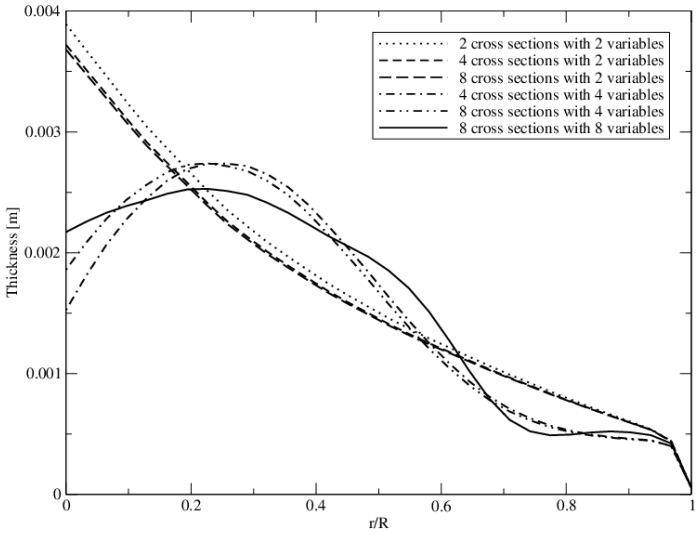

Figure 5.23: Optimal spar-cap thickness

Figure 5.24 reports the average CPU time vs. the number of design variables. The trend lines indicate that for a large number of design variables the full adjoint algorithm is the fastest. Surprisingly, the trend shows that the GEBT adjoint algorithm will be faster than finite difference algorithms with more than 35 design variables.

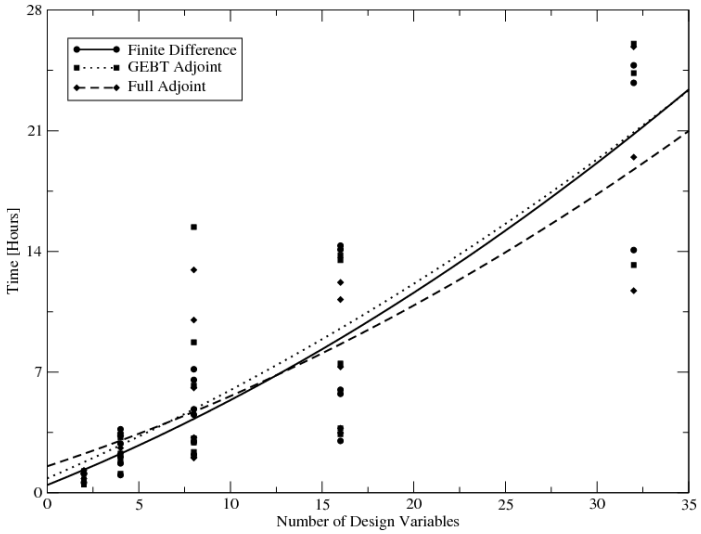

Figure 5.24: Optimization time vs. number of design variables

5.3 Composite Lay-up Optimization

The work presented in this section is adapted from a 2013 AIAA Annual Sciences Meeting conference publication:

Michael K. McWilliam and Curran Crawford. Composite lay-up optimization for horizontal axis wind turbine blades. In *AIAA 51st Aerospace Sciences Meeting*, 2013

Design optimization is an attractive tool to help improve structural design [6]. Within literature there exist numerous design optimization studies, however, little attention has been given to structural aspects [15]. Some of the simplest studies looked at turbine configuration parameters like rotor diameter and hub height; these studies avoided physical models by using statistical curve fits of existing turbines [67, 68]. Several studies neglected structural considerations completely and focused on aerodynamics [71, 76, 77, 78, 19]. Other studies neglected structural aspects in the modeling but estimated the blade cost based on the root bending moments and a simple cross section strength model [72, 66]. Then other studies incorporated structural dynamics in the physical model but still base structural properties on existing turbines [57, 58, 59, 63]. Only a minority of optimization studies included structural design variables into the set of decision variables for optimization [26, 185, 65, 64, 250, 251]. Finally, there are examples of design optimization based on structural mechanics alone; these studies are possible when the surface geometry and a design loads are prescribed [252, 253, 80].

In design optimization there is a trade-off between model fidelity and computational efficiency. Several MDO studies would use a modal representation of the blade to minimize the degrees of freedom [57, 58, 59, 63]. Another approach is to neglect time domain analysis and use linear beam models with iso-tropic cross-section analysis [26, 185, 65]. Applying MDO techniques to divide the optimization makes higher fidelity methods feasible [64, 251]. Bottasso was able to use unsteady nonlinear beam theory along with three-dimensional shell models using multi-level optimization techniques [250, 251].

The work of Buckney *et al* [252] and Pirrera *et al* [253] were able to show that improvements could be made by rotating the neutral axis to be better aligned with the dominate load. The topology based optimization of Buckney *et al* [252] showed there is a case for trailing edge reinforcement. The higher fidelity shell model of Pirrera *et al* [253] demonstrated that buckling constraints push the spar towards the trailing edge on inboard sections.

Within wind turbine literature there are many design concepts that rely on unique composite lay-ups. Design studies of large multi-megawatt wind turbines by both Joosse *et al* [16] and Griffin and Ashwill [17] concluded that Carbon Fiber Reinforced Plastic (CFRP) can potentially reduce the cost of wind turbines. These results have prompted Paquette *et al* [254] to perform physical and field testing on CFRP blades. Coupling has been shown to reduce fatigue damage with little impact on the AEP [255]. This coupling is introduced into the blade by laying up fibers at an angle away from the blade axis [32, 256]. A notable example is given by Bottasso *et al* [250] where a MDO framework revealed that bend-twist coupling reduces the actuation on the pitch motors.

The the structural design parameterization scheme affects what type of designs can be resolved in the optimization. Within the wind energy literature there lacks parameterization schemes suitable for lay-up optimization. There are two common schemes, the most common is using Bezier splines [26] or polynomial splines [185, 251, 250] to smoothly distribute geometric parameters (*eg* spar-cap thickness) along the blade with minimal number of design variables. There are several limitation with this approach; this scheme does not allow an intermediate transition location to be a decision variable, instead it is set as a fixed parameter and multiple optimization solutions are required [251]. There is difficulty in controlling the taper ratio *a-priori* (*ie* the distance between ply-drops, see Samborsky *et al* [18] for more details) instead multiple solutions are required to find feasible designs [251]. Finally this method is not

well suited when multiple layers are under consideration because these interpolated splines do not commonly admit regions of constant span-wise thickness.

A second less common approach is specifying design parameters at fixed locations along the blade [64]. With careful implementation this scheme can specify layer by layer properties across multiple span-wise locations. However this comes at a cost; for the same design resolution this scheme requires many more design variables than the interpolation curves. When gradient based optimization is used this approach fails to give accurate gradients with respect to variations in the span-wise locations of various transitions.

The problem of lay-up optimization is not unique to wind turbines, this is an active research area in itself [257, 258, 259, 260, 261, 262]. There are two dominate approaches to parameterizing lay-up schedules [260]. The first (referred to as the 'layer-by-layer' approach) is directly specifying the thickness and fiber angle at each layer directly. The second relies on classical lamination theory where laminate properties can be expressed as "lamination parameters" [257] which are integrals integrals of layer geometry and angles alone. The lamination parameter approach gives a convex space with at most 12 design variables for the lay-up optimization. Yet solutions based on this scheme require an inverse calculation to determine the lay-up schedule that gives the equivalent parameters [260]. Then by lumping the laminate properties it is difficult to assess the strength in the optimization [260].

The layer-by-layer approach has some limitations; first there are many more design parameters; second this approach is known to yield multiple local optima [260]. The large number of design variables can be compensated by using gradient based optimization [260, 259] or using response surfaces [260, 258]. When the problem is computationally inexpensive then heuristic techniques (*eg* genetic algorithms) can be applied to avoid local optima [261, 262].

This section explores a new lay-up parameterization scheme specifically developed for wind turbine lay-up design optimization. This new scheme is inspired by wind turbine manufacturing techniques and bears some similarity to the 'layer-by-layer' approach. The two dimensional cross section mesh is always aligned with the laminate plies. The position along the span of any transition can easily be made a decision variable. The number of design variables is reduced by lumping layer properties together. Finally an analytic description of the geometry has been developed to give continuous gradients.

The numerical model used to simulate and optimize wind turbines is described in section 5.3.1. Section 5.3.1 describes the parameterization scheme where the issue of local optima is discussed. Section 5.3.2 presents optimization results with the parameterization scheme..

5.3.1 Methodology

The structural model used in this section is based on the nonlinear beam model discussed in section 2.1.2 coupled with the cross-section analysis discussed in section 2.2.1 discussed in chapter 2. The optimization algorithm used in this study is the CFSQP algorithm provided by Lawrence *et al* [202]. It is a gradient based SQP algorithm. In the sensitivity analysis adjoint methods are used to limit the computational load due to numerous design variables. Adjoint algorithms are sensitive to the number of objectives so the KS function [212] in equation (5.5) is used to lump stress and strain constraints. Additional details of the optimization algorithms are discussed in section 2.4 in chapter 2.

Lay-Up Parameterization

There are two aspects to the lay-up parameterization. The geometry at various cross-sections needs to be meshed for VABS analysis. A geometry and meshing algorithm for VABS analysis has been developed where the mesh is aligned with the layers to avoid the smearing of material properties seen in other work [39]. The second component is parameterizing the geometry and material throughout the blade.

The cross section geometry is based on a curvilinear coordinate system as shown in figure 5.25. The offset distance (ζ) from the outer mold line is the first ordinate to this system. Curves of constant offset are aligned with the composite plies. The position on the curve is given by the ratio (η) of distance from the trailing edge to the total length of the path.

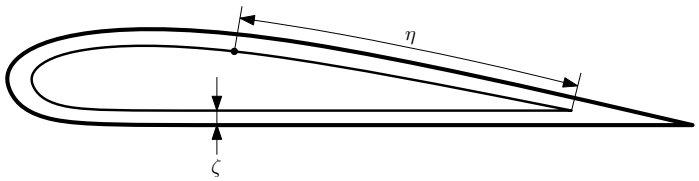

Figure 5.25: Cross-section coordinate system

This coordinate system becomes degenerate when ζ becomes too large. At this point two offset curves have collided. In reality this is impossible because this would require two regions of material to be coincident. Solving the maximum ζ is calculated *a-priori* by calculating successive offsets until a collision occurs. This introduces a geometric constraint where all offsets are constrained to be less than ζ_{max}.

This coordinate system is used to define the mesh of the skin and spar caps. Shear webs are created by connecting opposite points with two parallel lines. The mesh in this region is composed of intermediate parallel lines and connecting regularly spaced points along those lines.

Calculating the offset curves is not trivial and a subject of much research [263, 264, 265, 266]. The approach taken here uses the points that define the outer mold line to define a polygon. The offset curves are based on polygons that approximated the offset polygon from the outer polygon. These polygons are approximate because the true offsets have vertex collisions that give discontinuous gradients. Instead smooth analytic relationships are used to define how the edge lengths vary with offset. Finally the offset polygon is transformed into a smooth curve by interpolating points with splines.

The cross section design is based on a predefined topology based on boxes. These boxes can be parameterized based on height and position within the ζ and η coordinate system. Once the box configuration is set, the mesh is generated with a regular grid of points within the ζ and η coordinate system.

Figure 5.26 shows an example of the airfoil cross section mesh near the root of the blade. Figure 5.26a gives the full view, with a close-up near the spar-cap and trailing edge in figures 5.26b and 5.26c respectively. In this example the spar-cap used two separate layers with a different thickness, but the same number of cells in the mesh to demonstrate how the algorithm respects material boundaries in figure 5.26b. Overall the algorithm gave high quality meshes, however near the trailing edge the geometry changes dramatically over a small η leading to the distortions in figure 5.26c. This distortion would have a small effect on the edge-wise bending stiffness, however typically the trailing edge is not used for structural reinforcements, thus this distortion is acceptable.

All that remains is the defining the thickness, position and material properties of the box. This is where the lay-up parameterization scheme comes into play.

The parameterization scheme is inspired by the natural geometry of fiber reinforced parts. In wind turbines long slender sheets are layered to create spar-caps or

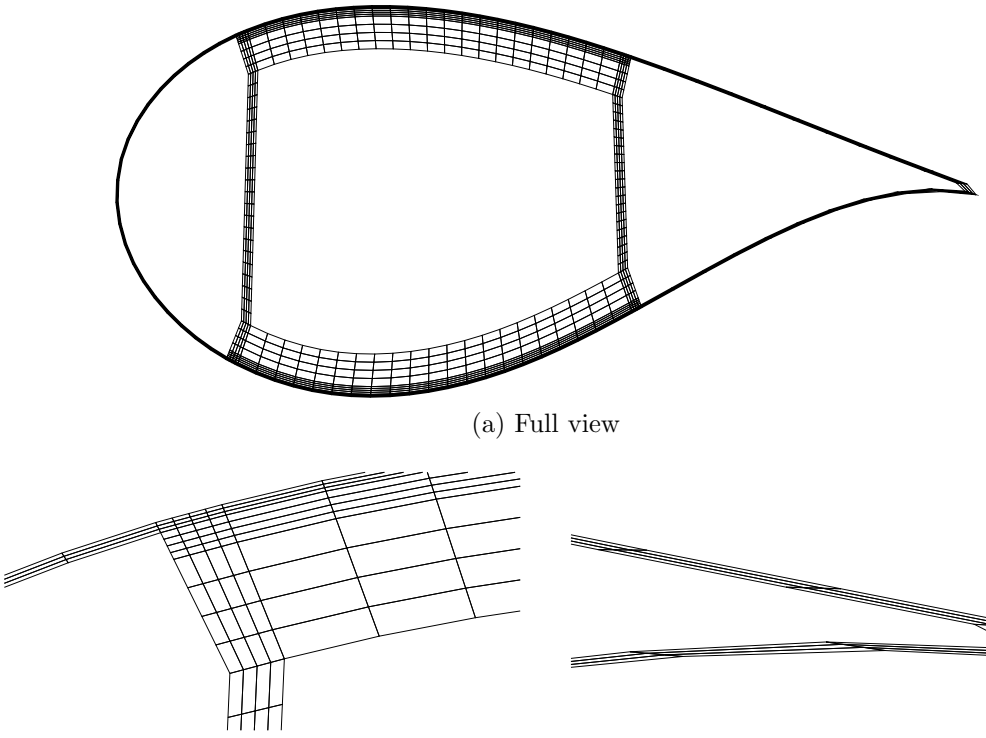

(a) Full view

(b) Spar-cap close-up

(c) Trailing edge close-up

Figure 5.26: Airfoil cross section mesh

shear-webs. Variable thickness along the blade is achieved by tapering the material through ply-drops at either end of the sheets. Viewed from the side the lay-up would look like a set of trapezoids stacked upon each other as shown schematically in figure 5.27a.

Each trapezoid can be parameterized by the span-wise locations of the inboard and outboard tapered (ply-drop) regions, and the thickness as shown in figure 5.27b. Any limits on the taper ratio can be enforced by ensuring the corners on either side of a taper are separated by a distance proportional to the thickness.

Since the composite sheets can be shaped before being placed the spar-caps can have a smooth variation in width and chord wise position. This design freedom is controlled by splines ($g_{i0}(r)$ and $g_{i1}(r)$) as shown in figure 5.27c.

A second set of parameters are needed to describe the material properties as shown in figure 5.28. Span-wise variation is controlled by the start and end of the angled transition line. Unlike the layer by layer scheme, this scheme is not parameterizing individual layers, instead it is grouping layers together to have a common angle definition. The fiber angle can be specified as a constant through the thickness or as a

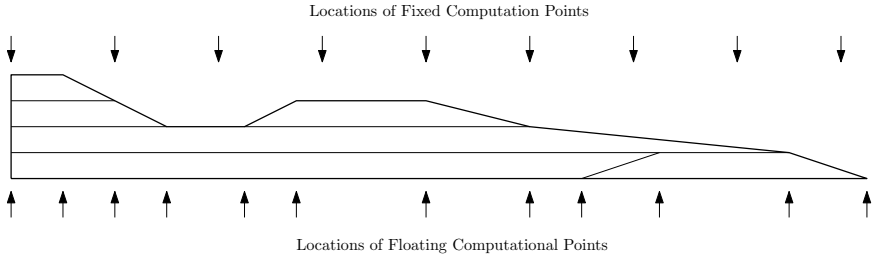

(a) Side view schematic

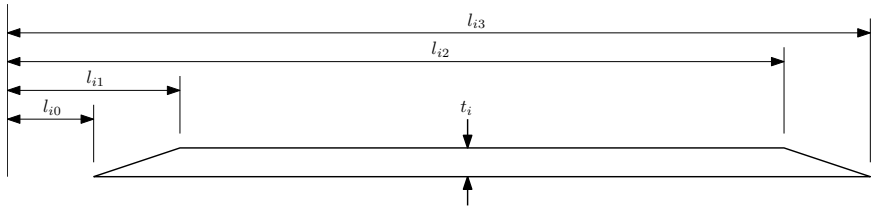

(b) Trapezoid parameterization

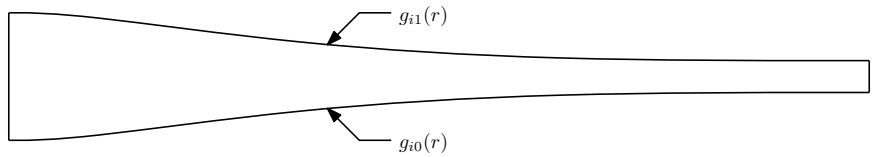

(c) Width parameterization

Figure 5.27: Structural geometry parameterization

function as thickness as shown in figure 5.28. To prevent fiber cracking layers of ±45° are inserted into intermediate locations. Initially it is not necessary that the ±45° layers in the numerical model correspond to layers in the real lay-up. Instead they are present to to resolve their influence. Since this lay-up is merely representative the relative thickness of the layers does not change. Then as converged solutions are obtained the layers can be rearranged to correspond to realistic lay-ups.

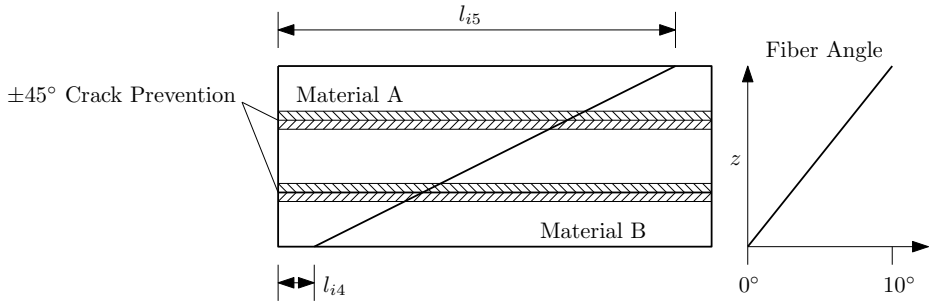

Figure 5.28: Constitutive parameterization

The typical approach of calculating the stiffness of a blade involves cross section analysis at each of the fixed locations shown at the top of figure 5.27a. This approach fails to accurately calculate how changes in span-wise locations will affect the objectives. A set of floating calculations points (bottom of figure 5.27a) are introduced to capture this affect. These calculation points move with the transition points. The results of the cross-section analysis is interpolated to intermediate locations.

The higher fidelity of this scheme is meant to refine existing designs. A limitation of this scheme is the number of trapezoids and their constitution needs to specified *a-priori*. This topology can be selected based older designs, optimization results using simpler parameterization schemes and/or engineering judgment. In this research optimization results based on interpolating splines is used to define the topology.

As with other layer-by-layer type parameterization schemes this parameterization is expected to have local optima. The local optima are typically 90° apart in fiber angle. Existing designs and other studies [32, 256] are evidence that the global optima is close to blade aligned fibers. Thus the problem of local optima is not expected when the initial fiber angle is 0°. Another local optimal can occur if too many trapezoids are used. This local optima is avoided by grouping the layer properties within a trapezoid section thus minimizing the number of trapezoids.

5.3.2 Optimization Studies and Results

Each investigation will involve optimization. To explore the challenges of larger blades the Sandia National Laboratories have developed a paper design of a 100m blade that meets all the International Electrotechnical Commission (IEC) 61-400 design constraints [267]. The authors concluded that the blade is too heavy to be economically competitive. This design represents an excellent design case to explore new concepts. Both investigations explored the design of the spar cap. The spar cap was manufactured with a base layer of uni-axial glass fibers.

The original design used a box spar in the outer portion of the blade. At the inboard locations an extra shear web was added at the trailing edge. The design specified a mix of uni-axial and ±45° layers for the main structural components. For the initial exploration of this parameterization scheme the lay-up design was simplified. In this work a box spar was used throughout the whole cross section. For the skin and shear webs only uni-axial fibers were used.

In all studies the objective was to minimize the volume of the blade. The analysis looked at a single operating point of steady wind at 8m/s. A Lagrangian Vortex Dynamics code was used to solve the aerodynamic forces. These forces were solved once for the original configuration and held constant in the optimization. A 1.4m tip deflection constraint was applied to all the problems. The root bending moment stress was constrained with a safety factor of 10. The spar cap geometry was constrained to fit within the blade.

Spar Cap Thickness

The first optimization study compares the performance of the new parameterization scheme to the conventional spline based parameterization. For all cases the material had not fiber bias and only glass-epoxy was used. The only thing that was varied was the thickness of the spar caps.

Increasing the number of design variables will lead to better designs. To explore this effect a low and high resolution design was developed. The low resolution spline design used only 4 points while the high resolution spline had 8 points. The low resolution spar cap design had two slabs with 4 design variables as shown in figure 5.29a. While the high resolution design had three slabs with 9 design variables as shown in figure 5.29b.

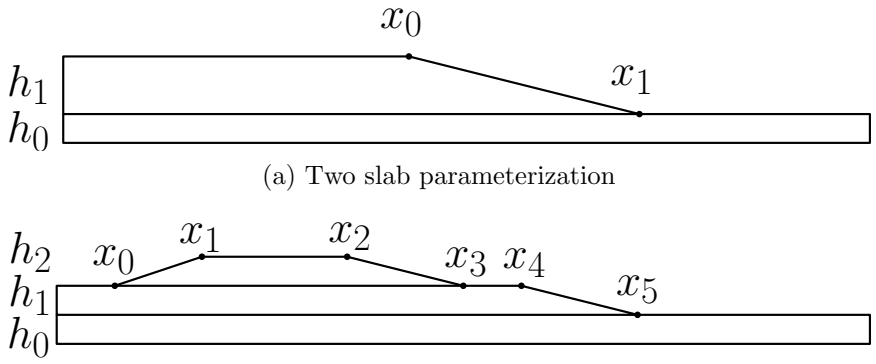

(a) Two slab parameterization

(b) Three slab parameterization

Figure 5.29: Parameterization for slab based thickness optimization

Table 5.7 shows the optimal volume of each optimization result. The results show that the slabs managed to find better design giving volumes less than the best spline based result. Surprisingly the two slab optimization result is better than the three slab result. The three slab parameterization becomes the two slab when the third

thickness is minimized. This indicates additional slabs introduce local minimum in the design space. This is something that needs to be explored in future work.

Table 5.7: Spar-cap thickness optimization results

Parameterization	Volume $[m^3]$
4 Variable Spline	175.4
8 Variable Spline	175.1
Two Slab (4 Variables)	125.4
Three Slab (9 Variables)	144.3

Figure 5.30 shows the thickness solution for the optimization. The spline based optimization tends to add extra material mid-span and removes material at the root. However the slab based parameterization is showing that keeping material at the root allows for less material at the outer portions giving a smaller blade overall. The three slab optimization was initialized with a thick third slab to mimic the spline based optimization results. Since that slab started out thick it worked on the span wise position instead of adjusting the thickness. Thus, the local minimum are introduced because the thickness can be adjusted in two ways.

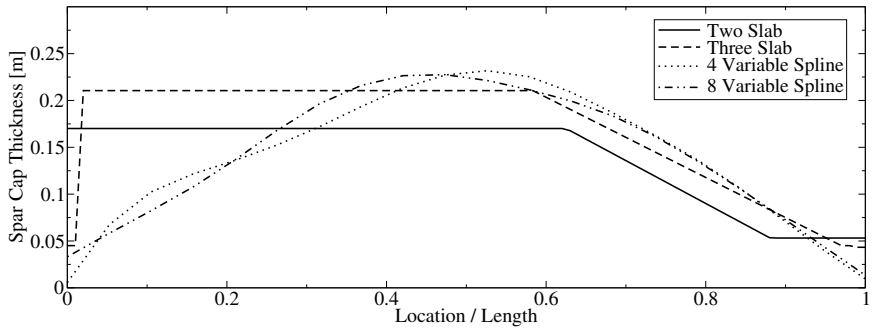

Figure 5.30: Slab thickness solution

Fiber Angle Optimization

Classic parameterization schemes cannot easily specify different material properties at different locations within the laminate. Since this parameterization scheme is based on stacked slabs of material it naturally handles this. To demonstrate this property optimization was applied to determine the optimal fiber angle and material thickness for a blade with bend twist coupling. The optimization was based on the two slab

parameterization. Two additional design variables were added for the fiber angle in the top and bottom slabs as shown in figure 5.31. To maintain bend-twist coupling the average coupling was constrained to 0.2 as shown in equation (5.59).

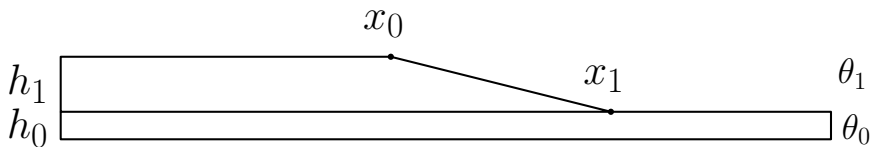

Figure 5.31: Fiber angle parameterization

$$\gamma = \frac{1}{L}\int \frac{C_{45}}{\sqrt{C_{44}C_{55}}}dx = 0.2 \tag{5.59}$$

There are two challenges in the bend-twist coupled design. The first is maintaining the coupling coefficient constraint in equation (5.59). The second is maintaining the tip deflection constraint. These two goals are mutually exclusive. Table 5.8 shows the optimization achieved these goals by having one slab with a large bias angle to give the coupling, while the other slab has a low bias angle to maintain the stiffness. To meet both constraints figure 5.32 shows that extra material was required.

Table 5.8: Fiber angle optimization results

Volume $[m^3]$	148.9
Bottom Slab Angle [degree]	12.3
Top Slab Angle [degree]	2.8

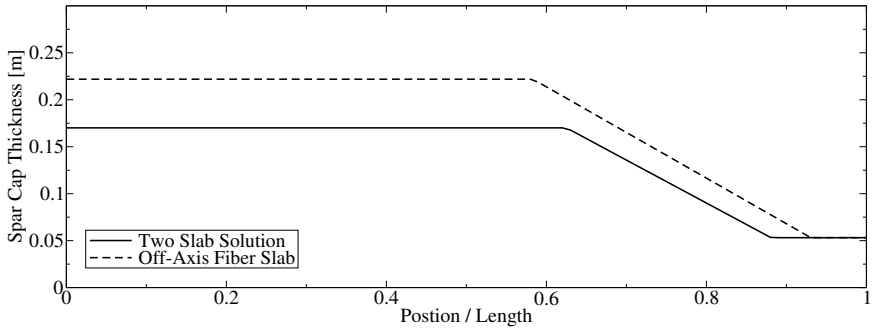

Figure 5.32: Fiber angle optimal blade thickness

Glass-Carbon Blade Optimization

The parameterization scheme allows material properties to be varied in a span-wise direction. To demonstrate this capability we investigated the optimum design of a glass carbon fiber hybrid blade. The spar cap was made with carbon fiber at the outer portion of the blade. Two additional design variables were introduced to control the span-wise location of the glass to carbon transition in both the top and bottom blade. This parameterization is shown in figure 5.33. Carbon fiber is introduced into a blade to increase the stiffness. To explore this case optimization was performed over a range of small tip deflection constraints. To account for the relative difference in cost, the volume of carbon was penalized four times more than the volume of glass.

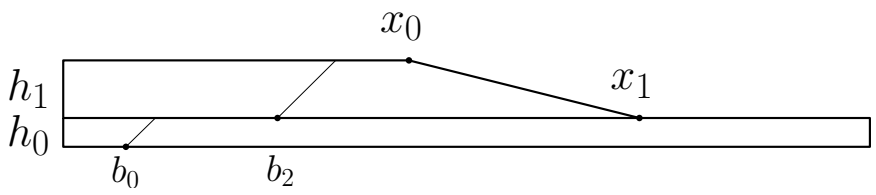

Figure 5.33: Glass-carbon blade parameterization

Table 5.9 shows that carbon can make the blade smaller and stiffer. With the 1m tip deflection the overall volume is less than all other optimization results. Figure 5.34a shows that this spar cap is smaller than the two slab solution. More glass could be added to this design thus the optimizer demonstrates there is value to adding carbon. Figure 5.34a shows that a mix of carbon and glass is optimal at mid span locations. The results based on the 0.55m tip deflection (figure 5.34) are an extreme example. The tip deflection constraint is so small the blade is made from mostly carbon. The overall volume is much larger than any of the other blade designs. This shows the limitations for making stiffer blades economically from carbon.

Table 5.9: Glass-carbon blade optimization results

Deflection Constraint	1m	0.55m
Total Volume $[m^3]$	91.2	183.6
Carbon Volume $[m^3]$	58.7	132.1
Glass Volume $[m^3]$	32.5	51.6

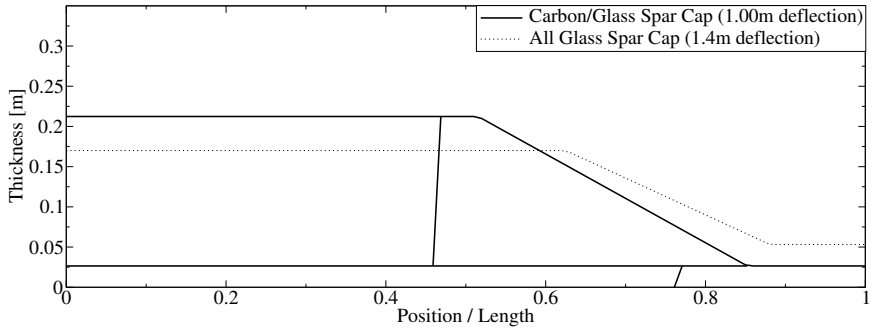

(a) 1.00m Tip Deflection

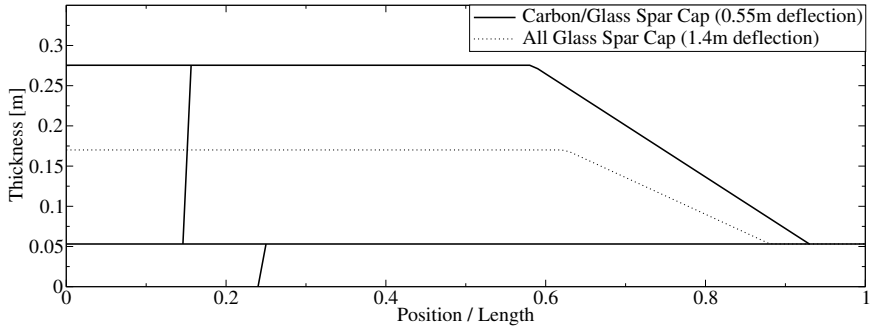

(b) 0.55m Tip Deflection

Figure 5.34: Glass-carbon spar cap thickness

5.4 MDO with Conventional LVD

The work presented in this section is adapted from a 2013 AIAA Annual Sciences Meeting joint publication between this author and Stephen Lawton:

Michael K. McWilliam, Stephen Lawton, and Curran Crawford. Towards a framework for aero-elastic multidisciplinary design optimization of horizontal axis wind turbines. In *AIAA Annual Sciences Meeting*, 2013

The results and discussion on the aerodynamic gradient noise and aerodynamic optimization is the work of Lawton. This thesis authors contribution to the aerodynamic optimization work is in the MDO code that was used to connect the optimization algorithm to the analysis code. The author of this thesis developed the coupled aero-elastic analysis and the coupling code that enabled aero-elastic optimization. The structural models were developed by the author and aerodynamic models were developed by Cline [268] and Lawton [87]. The author of this thesis performed all the aero-elastic optimization and aero-elastic gradient studies that are presented in the later half of the discussion.

MDO can imply the combination of many different disciplines such as aerodynamics, structural mechanics, aero-acoustics, electro-magnetics, controls, economics and many others. However, the aerodynamic and structural considerations bear the greatest impact on turbine performance and are also the most complicated to analyze. This section presents an initial step to developing an MDO framework that incorporates only aerodynamic and structural analysis capabilities.

For the aerodynamic analysis the conventional LVD simulation code developed by Cline [268] and Lawton [87] was used, for more details see section 2.3.3 in chapter 2. The structural calculations are performed with a GEBT code and VABS analysis developed by the author. The theory behind GEBT and VABS is discussed in chapter 2, sections 2.1.2 and 2.2.1 respectively.

The success of any MDO framework is highly dependent on the optimization algorithms applied. It is expected that the design space does not have multiple local minima, accordingly this problem is well suited for the more computationally efficient gradient based methods. The CFSQP optimization algorithm [202] was used for all the optimization in this section.

Gradient based optimization methods require coupled sensitivity information about the objective and constraints. For each of the two analysis codes several gradient algorithms were implemented. Lawton [87, 82] implemented the finite differencing and complex step algorithms into the aerodynamic analysis code, while the author implemented both a finite differencing and adjoint based sensitivity analysis in the structural models. Due to the circular dependency of the two disciplines the fully-coupled system derivatives can only be computed using finite difference techniques.

This work presents single discipline aerodynamic optimization using SDF framework and aero-structural optimization using the MDF framework. For more details on these optimization topics refer to section 2.4 of chapter 2. Chapter 4 gives two fixed point algorithms for converging the couple aero-structural model. At the time of this study the poor convergence properties of the co-evolving algorithm were not known. The aero-elastic analysis presented here is based on that algorithm due to the potential speed of the analysis.

5.4.1 Results and Discussion

The aerodynamic model relies on an explicit pseudo time-marching algorithm that has been found to have poor convergence behavior. This is likely owing to the explicit

convection scheme which is not based on a strict residual minimization of physical governing equations. The result is that the algorithm cannot be arbitrarily converged. This issue has persisted despite the use of 2nd order accurate advection schemes, viscous core models to avoid singularities, and various under-relaxation schemes. Numerical noise is therefore inherently present in the final aerodynamic solution. Obtaining converged optimization results with the aerodynamic model proved to be difficult primarily because of noise in the gradients. Despite the noisy gradients, pure aerodynamic optimization was achieved for a small rotor with a relaxed wake. Coupling the aerodynamic model with the structural model increased the numerical noise. To overcome this problem, aero-elastic optimization was performed with a fixed wake. Each of these topics are discussed in-turn.

Aerodynamic Gradient Noise

Finite differencing was used to calculate gradients of power in the aerodynamic model with respect to chord and twist. The gradient was found to be quite sensitive to the chosen step size. When the step size is too large, truncation error will dominate; when it is too small, round-off error will dominate. The optimal range of step sizes was found by taking the same gradient with different step sizes. Figure 5.35 shows the gradient results for a range of step sizes. The region between 10^{-7} and 10^{-12} where the gradient values are constant is where both truncation and round-off error is minimized. Within this region there was still some variation in gradient as the step size was changed.

The explicit algorithm used to solve the aerodynamic model is known to exhibit instabilities [13]. Initially small perturbations owing to numerical errors occur, after many iterations they begin to dominate the evolution of the flow and the results become unreliable. This prevents the aerodynamic model from being converged to an arbitrary level. It is difficult to determine the optimal number of iterations to converge the model in a general sense as the convergence behavior with number of iterations is not regular or monotonic. Figure 5.36 shows the large variation in relaxed wake gradient results from iteration to iteration. Furthermore, the simulation exhibited chaotic behavior where a small change in the design would result in significantly different levels of error at the same iteration. Since this error does not vary smoothly with the design parameters it violates the assumptions of the finite difference approximation which require at least C^1 continuity.

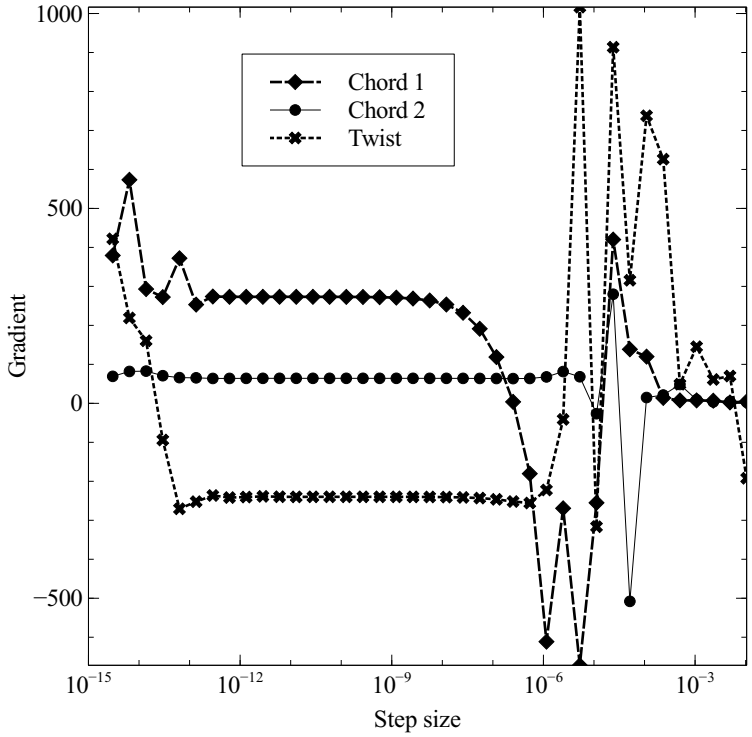

Figure 5.35: Example of gradients with respect to 3 different design variables

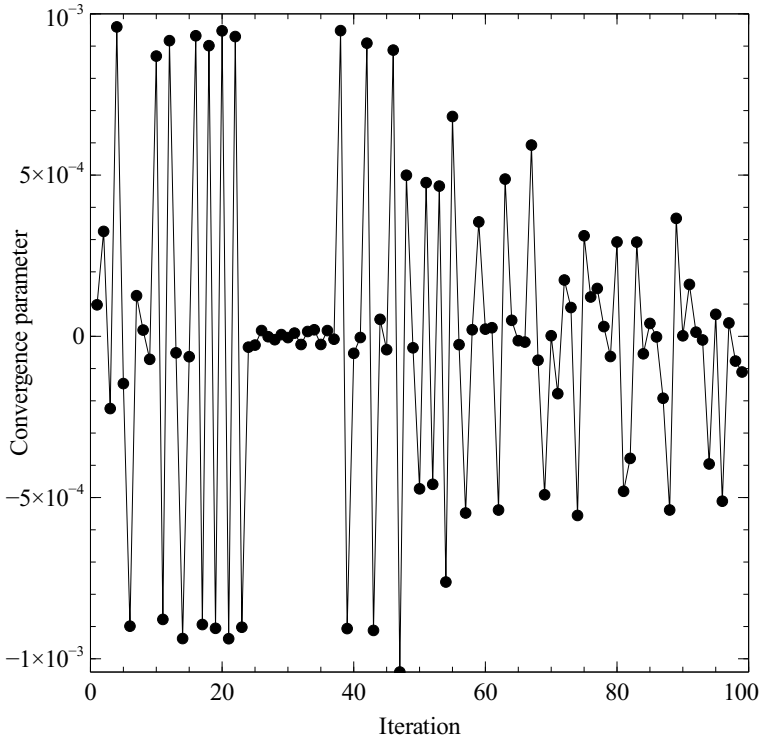

Figure 5.36: Sample convergence plot, showing how the error measure varies with iteration

Several attempts were made at trying to improve the gradient calculation. The chaotic oscillations can be attenuated by averaging the results of several iterations. To improve the gradient calculation this was applied separately to the objective values and the finite difference gradient values. However none of these approaches were able to reliably produce fully converged gradients.

The conventional first-order advection scheme was found to initially converge and then diverge after a sufficient number of iterations. To overcome this problem a second-order scheme was implemented that avoided the divergent behavior of the first order scheme. Unfortunately the second order scheme could not be converged to arbitrary levels. Instead these second order simulations would settle into a chaotic oscillations that would still have the same detrimental effects on the gradients.

Complex step aerodynamic derivatives were computed using the template functionality in the LibAero code. These gradients were somewhat better in terms of convergence to a fixed value, however the complex step derivatives were different than the mean finite difference gradients. In most cases, the difference was more than the standard deviation of the finite difference gradients. This suggests that the complex step derivative is in fact computing gradients in a complex numerical space quite different to the numerics of the real-number simulation. Note that the LibAero complex step derivatives were verified to be exact for fixed-wake test cases, so that these findings represent artifacts of the wake convection scheme.

Aerodynamic Optimization

Maximum coefficient of power optimization was performed with the aerodynamic model to assess the effect of the noisy gradients. A small 2.25m blade similar to the Mexico rotor [269] was optimized for a single operating point at a tip speed ratio of 7. The chord and twist distributions were represented with 4 design variables each. The optimal chord and twist distribution is shown in the table below. This blade achieved a coefficient of power of 0.541, an improvement on the original power coefficient of 0.458.

The step size for the gradients was varied between 10^{-3} and 10^{-15}. Many of the optimization attempts failed to converge due to poor gradient information. However the optimization with finite differencing step sizes between 10^{-9} and 10^{-6} did converge to solutions. In all cases the optimization was able to improve the original design, despite the issues with the gradients and convergence.

Table 5.10: Optimal aerodynamic solution

Blade r/R	Chord [m]	Twist [deg.]
0.142	0.1374	4.654
0.284	0.1432	12.56
0.429	0.1485	11.36
0.571	0.1435	11.43
0.714	0.1432	11.11
0.857	0.1256	9.56

Aero-Elastic Optimization

The aero-elastic optimization is based on the all-glass 100 m blade designed by Sandia National Laboratories [267]. The optimization maximized the ratio of the coefficient of power to blade volume by varying the chord, twist and spar cap thickness for a single wind speed. The blade design was constrained by a root bending stress with a safety factor of 10 to account for extreme loads and fatigue damage. The tip deflection was constrained to 1 m to avoid a tower strike under extreme loads. The chord was constrained to ±10% the original chord. The deviations from the original twist distribution was constrained to ±5°. The spar cap thickness was constrained to be greater than 5 mm and less than the maximum thickness that could be accommodated by the outer mold line.

The original Sandia 100 m blade had a third shear web at the in-board portion of the blade to limit panel buckling in edge-wise bending. The code used in this optimization cannot resolve buckling, so this constraint was ignored. Furthermore the design in this optimization did not include the third shear web and instead used the traditional box spar through the full length of the blade. The lay-up in the skin was tri-axial, ±45° was used in the shear-webs and uniaxial material was used in the spar caps. The blade was made with a S-Glass-epoxy laminate.

Numerical instabilities in the relaxed wake simulations prevented the optimization algorithm from converging. To overcome this challenge, optimization was performed with a fixed rotor wake. With a fixed wake, the location of the filaments is held constant throughout the whole optimization and is determined *a priori* according to a simple helical wake model, with first-order corrections for wake expansion and induction. Only the circulation along the blade and in the trailing filaments changes in the function evaluations.

Table 5.11 shows the optimal chord and twist distribution from the fixed wake optimization. The optimization improved the C_P to volume ratio from $1.51 \cdot 10^{-}3$ to $3.87 \cdot 10^{-}3$. This optimal coefficient of power is 0.37. While this is lower than the power coefficient of the initial design, the power per unit cost has increased. At the optimal solution no constraints are active. Figure 5.37 shows the convergence of the optimizer towards a solution, demonstrating good progress throughout.

Table 5.11: Optimal fixed wake aero-elastic solution

	Spar cap thickness [mm]	Chord [% original]	Deviation from initial twist [deg.]
Root	33.8	90	-5.0
Mid-span	26.5	90	1.880
Tip	5.0	110	0.779

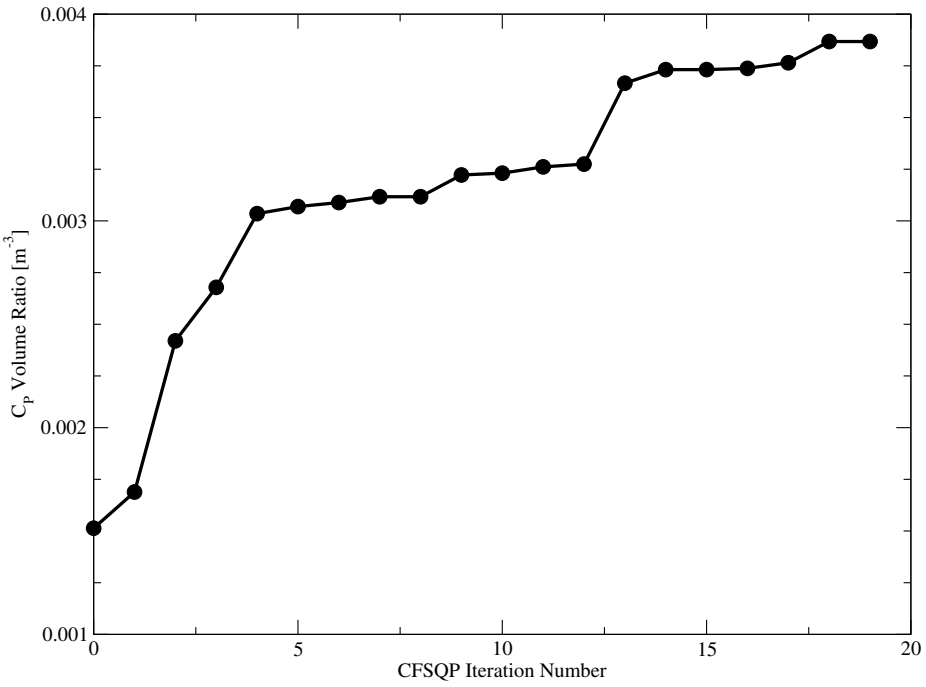

Figure 5.37: Plot of objective function value against CFSQP iteration

Fixing the wake dramatically accelerated the simulations and improved the gradients. A single relaxed wake function evaluation requires at least 10 minutes of CPU time at a reasonable resolution. The equivalent fixed wake simulation requires around

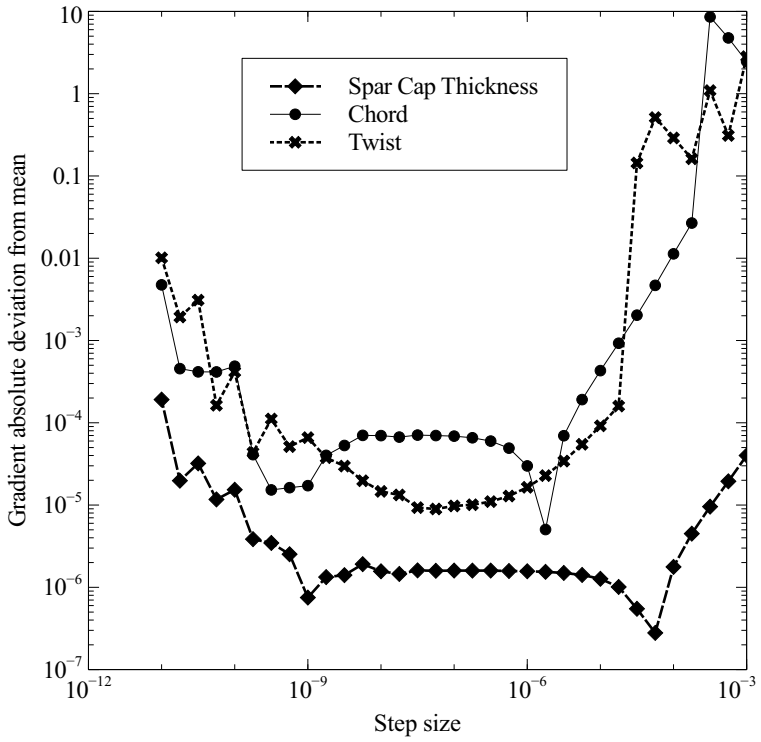

Figure 5.38: Aero-elastic gradient deviation from the mean

a minute of CPU time. Much of the instability was removed by fixing the wake, this indicates that most of the numerical issues arose from the relaxed wake.

Initially the aero-elastic optimization with a relaxed wake was based on the successful aerodynamic optimization. Accordingly these simulation used the same range of step sizes in the finite differencing algorithm. However all these optimization attempts failed. To understand the cause figure 5.38 shows how the gradient varies with step size with respect to three different design variables. Unlike in figure 5.35, there is not a broad region where the gradient values are stable.

The coupled fully relaxed wake aero-elastic optimization was repeated with the step size in the optimal range for that particular design variable. Under these conditions the optimization was able to improve the design. The optimizer was able to complete several iterations and improve the objective from $1.082 \cdot 10^{-}3$ to $1.793 \cdot 10^{-}3$. However it was unable to meet the optimization convergence criterion. The objective function values are shown in figure 5.39, it is clear after 10 iterations the optimization is stalled. This is a symptom of erroneous gradients, it is likely that the optimal step

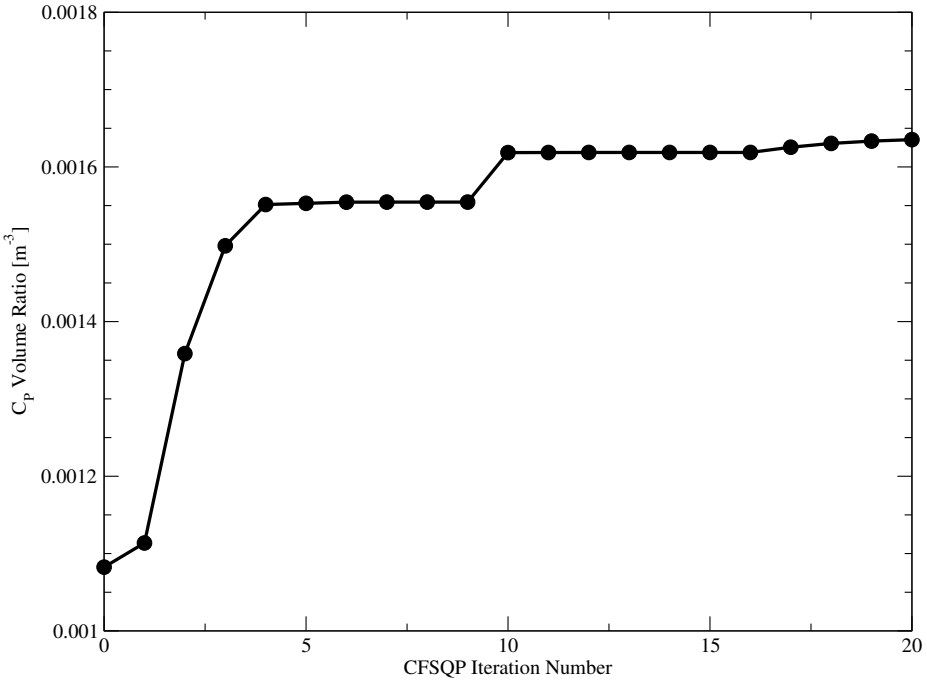

Figure 5.39: Plot of objective function value against CFSQP iteration

size is dependent on the design itself and when optimization improved the design it was no longer able to obtain reliable gradients.

The chord twist and spar-cap thickness distribution at the final CFSQP iteration is shown in table 5.12. The effect of erroneous gradients it clearly seen by the small spar-cap thickness in the root.

Table 5.12: Optimal relaxed wake aero-elastic solution

	Spar cap thickness [mm]	Chord [% original]	Deviation from initial twist [deg.]
Root	5.43	109	0.4273
Mid-span	26.9	110	-0.1759
Tip	46.5	109	-3.177

In summary one can obtain optimization results with a relaxed wake LVD simulation, albeit with some difficulty. However when the relaxed wake simulations are coupled to a structural model then optimization becomes impossible. The failure to obtain converged optimization results in this case shows the structural model has an adverse affect on the optimization. When the structural model is coupled to a fixed

wake aerodynamic simulation then optimization results can be obtained with little difficulty. Thus, the problem is due to an interaction between the structural model and the relaxed wake in the aerodynamic model. The fixed point iteration algorithm that is used to converged the coupled aero-structural simulation will generate changes to the blade shape each time the structural model is updated. This in-turn introduces a large perturbation in the wake. Distortions in the filament chain can be self-perpetuating as they exert an influence on itself and can lead to further instability. The affect of this instability is increased noise in the gradients that adversely affects the optimization.

These adverse interactions are confirmed in chapter 4. One solution would be to completely solve the aerodynamics after every beam update. For the linear beam model, the structural model converged after 4 updates. With a nonlinear beam model, this would require many iterations from both the aerodynamic and structural model. Without analytic gradients in the aerodynamic analysis, this would make the optimization very expensive in both function evaluations and sensitivity analysis.

Overall this demonstrates the difficulties of aero-elastic optimization with relaxed wake simulations. These problems are due to difficulties converging the wake of the aerodynamic model while simultaneously updating the beam configuration. These convergence issues will only be resolved with better algorithms. This has prompted research into the FEM-based LVD model. See chapters 3 and 4 for more details on this model and section 5.5 for it application in aero-elastic optimization.

5.5 MDO with FEM based LVD

The FEM-based LVD model was developed in response to the difficulties of aero-elastic optimization with conventional LVD outlined in section 5.4. Conventional LVD is limited in three way: it cannot be converged to arbitrary levels; it requires a fixed point iteration to converge the full aero-elastic solution; finally, the inability to converge conventional LVD to arbitrary levels caused erroneous gradients that interfered with aero-elastic optimization. Chapters 3 and 4 has demonstrated how the FEM-based LVD addressed the first two limitations respectively. This section outlines how the FEM-based LVD formulation leads to an analytic definition to the design sensitivities in section 5.5.1. Then section 5.5.2 demonstrates the FEM-based LVD and the analytic gradients in both aerodynamic and aero-elastic optimization.

5.5.1 Sensitivity Analysis

There are two components of the design sensitivity outlined in equation (5.60). The first term is the direct sensitivity of the objective to the design variable, the second term is the indirect sensitivity through variations of state.

$$\frac{d\boldsymbol{J}}{d\boldsymbol{Y}} = \frac{\partial \boldsymbol{J}}{\partial \boldsymbol{Y}} + \frac{\partial \boldsymbol{J}}{\partial \boldsymbol{X}} \frac{d\boldsymbol{X}}{d\boldsymbol{Y}} \tag{5.60}$$

Analytic design sensitivity cannot easily be defined for conventional LVD due to the difficulty of predicting how the state will change with respect to design variables (*i.e.* $d\boldsymbol{X}/d\boldsymbol{Y}$). By defining a convergence metric in equation (3.11) of chapter 3 one can calculate the sensitivity through state as shown in equation (5.61).

$$\frac{d\boldsymbol{X}}{d\boldsymbol{Y}} = -\left[\frac{\partial \boldsymbol{R}}{\partial \boldsymbol{X}}\right]^{-1} \frac{\partial \boldsymbol{R}}{\partial \boldsymbol{Y}} \tag{5.61}$$

Equation (5.60) and (5.61) are combined to give the final sensitivity in equation 5.62.

$$\frac{d\boldsymbol{J}}{d\boldsymbol{Y}} = \frac{\partial \boldsymbol{J}}{\partial \boldsymbol{Y}} - \left\{\frac{\partial \boldsymbol{J}}{\partial \boldsymbol{X}}\right\}^{T} \left[\frac{\partial \boldsymbol{R}}{\partial \boldsymbol{X}}\right]^{-1} \frac{\partial \boldsymbol{R}}{\partial \boldsymbol{Y}} \tag{5.62}$$

Equation (5.62) shows that four matrices need to be obtained to calculate the design sensitivity: $\{\partial \boldsymbol{J}/\partial \boldsymbol{Y}\}$, $\{\partial \boldsymbol{J}/\partial \boldsymbol{X}\}$, $\{\partial \boldsymbol{R}/\partial \boldsymbol{Y}\}$ and finally $[\partial \boldsymbol{R}/\partial \boldsymbol{X}]$. The definition of the last matrix is the Jacobian already given in section 3.1.3 of chapter 3. The remaining terms are specific to the objective and the design parameterization for a particular optimization formulation. However many objectives will rely on terms already defined in section 3.1.3 of chapter 3. For example the linearization of aerodynamic forces will depend on the linearized influence given in equation (3.10) in chapter 3. With the most of the complicated terms already defined in chapter 3, many of the analytic definitions can easily be obtained and will not be given here.

The reader should note that the definition in (5.62) is identical to the forward propagating version of design sensitivity given in equation (2.49a) of chapter 2. Similarly, one can define the adjoint version using the same four matrices used in equation 5.62. The relative advantage of the two approaches depend on the number of objectives vs. the number of design variables. When there are more objectives then the forward propagating approach is more attractive. In the optimization presented in this section the number of objectives and design variables was small and unlikely

to give either algorithm a significant advantage. Thus, equation (5.62) was used throughout.

5.5.2 Optimization Results

The optimization is presented in three parts. The first is a simple optimization study where the power was maximized by varying the chord. This study is meant to validate the FEM-based LVD model in optimization and to explore design variable parameterization. This section is followed by demonstrating aerodynamic optimization of the MEXICO and NREL 5 MW rotor. Finally this chapter closes by demonstrating the FEM-based LVD in aero-elastic optimization.

Power vs. chord optimization

An important aspect of optimal rotor design is developing a blade that produces the optimal axial thrust and axial induction. The amount of energy extracted from a given flow is proportional to the thrust, while too much thrust will deflect the wind away from the turbine and limiting the amount of energy available to the rotor. Axial Momentum Theory (AMT) suggests the optimal thrust coefficient is 8/9, with an induction factor of 1/3 and a coefficient of power of 16/27. A simple optimization study was conducted to determine whether optimization with the FEM-based LVD code would give similar solutions.

The study optimized the MEXICO rotor for maximum power by varying only the chord distribution. In all cases 8 elements were used on the blade, then 3 revolutions of the wake was simulated with 60 influencing elements and 15 basis sections in a Cartesian coordinate system. The wake terminated with a cylindrical far-wake model. The optimization maximized power by varying the chord distribution. Three optimization solutions will be presented here. The first represents the base case where the chord at each lifting line element is taken as a design variable. This optimization case produced an unexpected solution. Two additional test cases were explored to understand the best strategy for avoiding this anomaly. The second test case explored increased model fidelity, it used the same design variables as the base case but used 216 influencing elements to simulate 3 wake revolutions with basis sections defined in a cylindrical coordinate system. Additional test cases not shown here increased the wake length and far-wake model resolution, but these changes had a negligible affect on the optimization solution. The third test case looked at using quadratic

polynomials to control the chord with the same model model parameters as the base case.

Table 5.13 shows the final C_P, Karush-Kuhn-Tucker norm and the active constraints for each of the optimization solution. In all cases the optimization was able to improve the solution. The C_p estimation depends on the model accuracy and resolution, which means the C_P in the high fidelity optimization is not directly comparable. All the optimization solutions were able to achieve very small Karush-Kuhn-Tucker norm. The Karush-Kuhn-Tucker norm is dependent on the solution tolerance in the simulation code which itself is limited by the machine precision (Round-off error gives a lower limit on the final residual of solutions). The ability of FEM-based LVD model to converge to arbitrary levels allowed the optimization to achieve high levels of optimality.

Table 5.13: Power vs. chord optimization results

Case	C_P	K-T Norm	Notes
Original	0.473		
Base	0.523	$7.22 \cdot 10^{-3}$	Maximum Tip Chord Constraint Active
High Fidelity	0.491	$1.60 \cdot 10^{-2}$	
Spline	0.509	$5.35 \cdot 10^{-2}$	Chord Slope Constraint Active

Figure 5.40 shows the optimization results along the blade. All optimization cases found the original solution had too little thrust and increased the chord to maximize the power. The final solution show thrusts slightly greater than the optimal for AMT and the axial induction slightly less, yet all solution showed a coefficient of power close to the Betz limit. Overall optimization with FEM-based LVD reproduced solutions similar to those given by AMT, however the solutions appear to violate AMT. Unlike BEM theory, vortex methods take into account radial interactions so some local deviations are acceptable. However it is clear there is a small overall violation due to numerical errors, a detailed discussion is given below.

The base case and high fidelity case in figure 5.40a shows a strange solution where the tip chord is enlarged at the tip and then reduced at the next in-board station. This variation in the chord distribution causes the optimal solution to deviated from AMT near the tip. The constrained polynomial solution managed to reproduce the optimal solution without producing an un-realistic chord distribution. Constraining

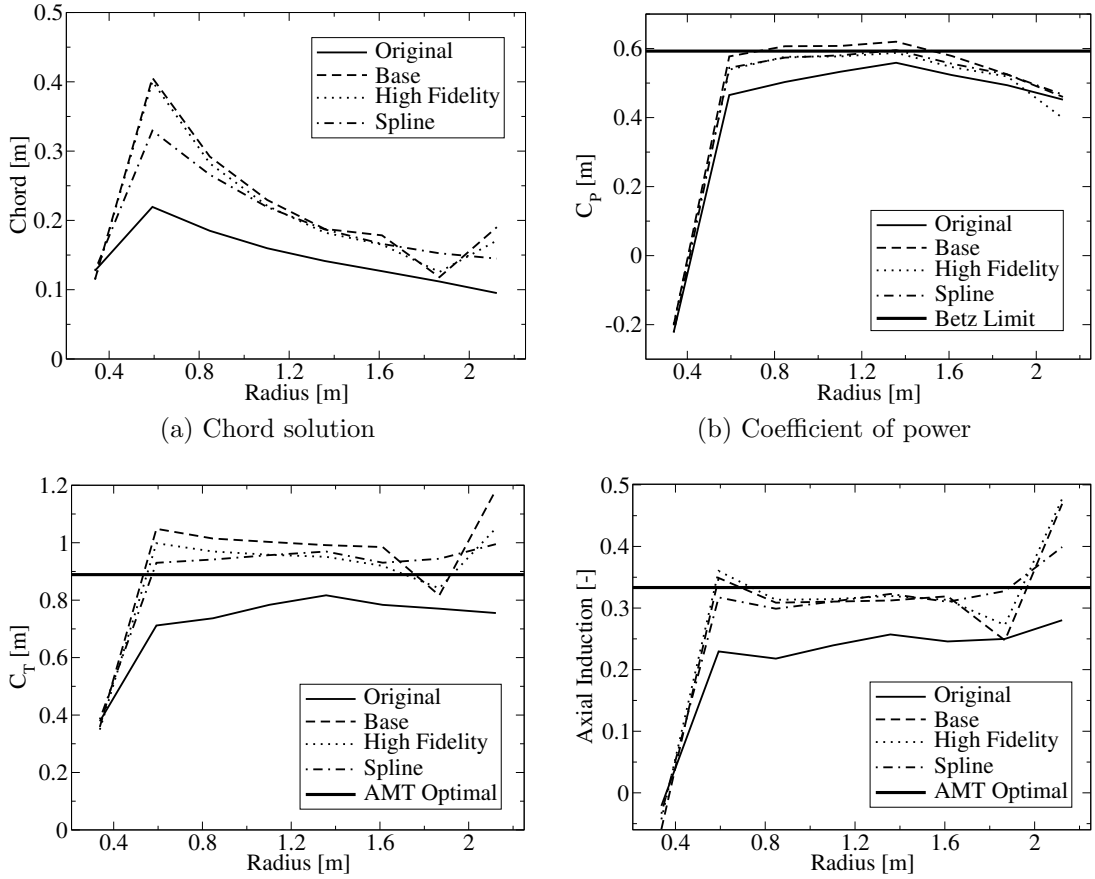

(a) Chord solution

(b) Coefficient of power

(c) Coefficient of thrust

(d) Axial induction

Figure 5.40: Power vs. chord optimization solution

the solution like this limits the predictive abilities of the optimization but is necessary to compensate for limitations in the analysis codes.

Sensitivity analysis was performed to understand why the optimization enlarged the tip chord. The sensitivity analysis was performed on the base case and only looked at the sensitivity of varying the tip chord. Figure 5.41 shows the results, it is clear by figure 5.41a that increasing the tip chord has a negative influence on power at the tip, but a positive influence on the rest of the blade. As expected figure 5.41b shows a large increase in strength at the tip due to the variation in chord. It also show an increase across the blade which can only be due to increased angle of attack from reduced inductions. The reduced induction is confirmed in 5.41d. It is clear these plots show increasing the tip chord improves the power at inboard stations by reducing the induction.

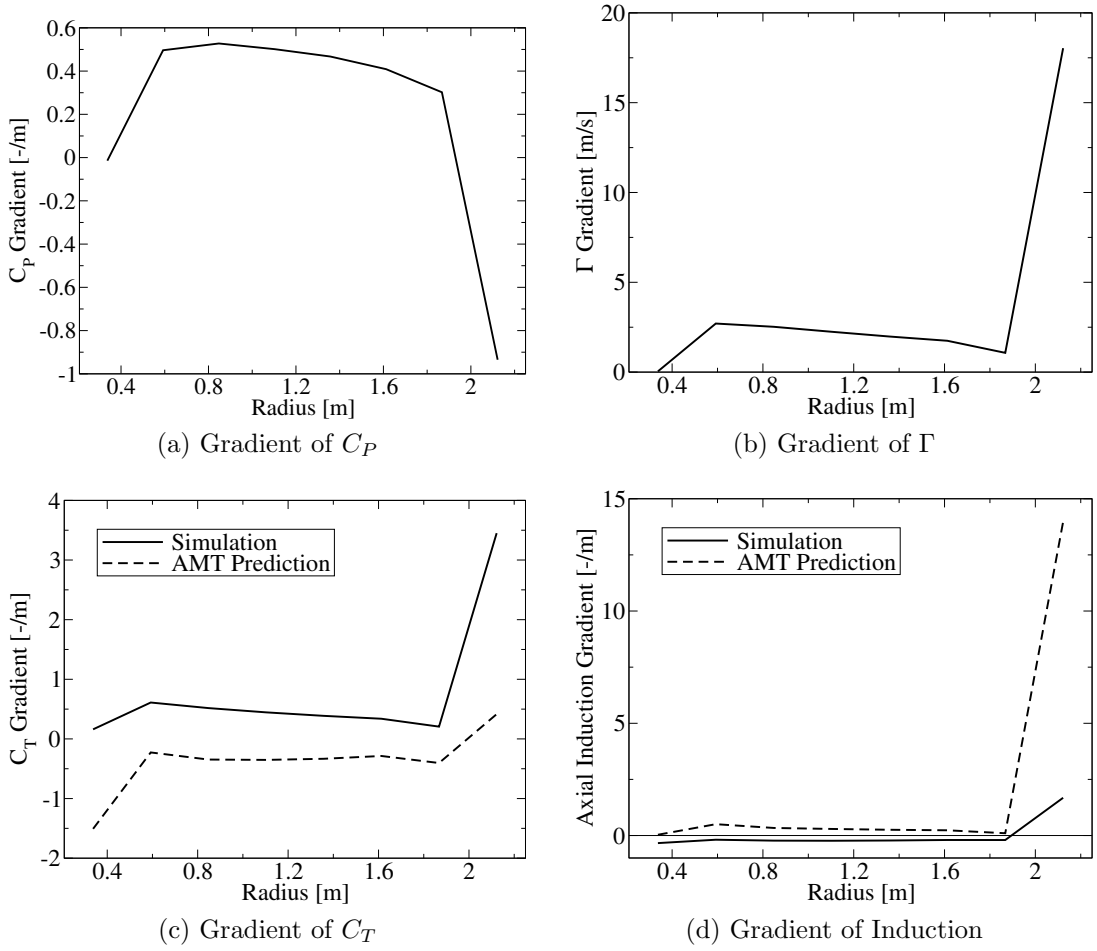

(a) Gradient of C_P

(b) Gradient of Γ

(c) Gradient of C_T

(d) Gradient of Induction

Figure 5.41: Power vs. chord sensitivity analysis

The conservation of axial momentum theory should be preserved in the sensitivity analysis. The gradient of AMT can be used to predict the sensitivity of thrust with respect to axial induction and vice versa. These predictions are plotted in figures 5.41c and 5.41d. Figure 5.41c shows an increase in thrust due to an increase in the angle of attack. AMT predicts this should lead to an increase in the axial induction, yet figure 5.41d shows the opposite trend. This shows that increasing the chord at only one station leads to a large deviation to AMT. This proves there is no benefit to increasing chord at the tip, and the perceived benefit is due to errors in the analysis.

Figure 5.41b gives some clues in understanding the source of the errors. Increasing the chord at the tip dramatically increases the circulation strength of that station relative to the rest of the blade. This would lead to a increased strength at the tip trailing filament which would have a positive contribution to axial induction, and decreased strength at the second inboard trailing filament which would have a

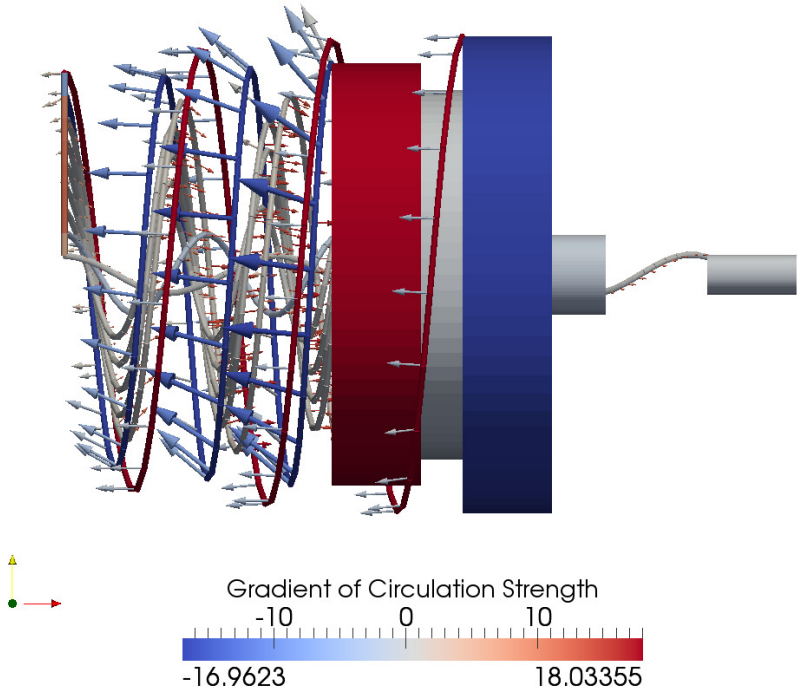

Figure 5.42: Wake configuration sensitivity

negative contribution to induction. In an infinite vortex cylinder the induction in any annular region is based on the sum of azimuthal circulation strength for all the outer cylinders. If helical vortex systems behave the same, the variation in induction from the two filaments should cancel, yet it is clear the affect of the second inboard filament is dominating.

The error in induction is not due to errors in the strength but in errors in how that strength contributes to induction. A helical filament will contribute to axial and tangential induction. With increased pitch, the axial induction is reduced, while the tangential induction is increased. Figure 5.42 shows how the wake configuration changes with changes in the tip chord. The arrows show how the influence changes with increasing tip chord. The results show that the second inboard filament has a large contraction relative to the rest of the wake. Due to the reduced axial induction inboard, the rest of the wake stretches out axially. The analysis shows that the pitch for the second inboard filament is being reduced too much from the tip filament. Since this filament has negative vorticity it contributes to a stronger negative induction when the pitch is small.

The source of this erroneous contraction is due to errors of lumping vorticity on a line element. In reality the trailed vorticity of this second inboard filament would

be distributed radially. Only the outer portion of this vorticity would experience the full effect of the tip filament. Further inboard, the affects of that tip filament would be attenuated by the distributed negative vorticity. Thus, it is more realistic that the pitch of the second trailing filament is only reduced by half of what is predicted here. This suggests the error can be reduced by increasing the resolution along the blade. However this usually leads to solver stall in FEM-based LVD.

Aerodynamic Optimization

The FEM-based LVD model was used in aerodynamic optimization of both the MEXICO rotor [217] and the NREL 5 MW wind turbine [228]. The objective was to maximize the power by varying the chord and twist. In both cases the chord and twist were represented by quadratic polynomials. To avoid the problems outlined above the chord control points were constrained to be monotonic. The inner-most stations of both blades have cylindrical cross-sections, since these cross-sections do not contribute to the power the chord there is kept constant.

The simulations were based on three different span-wise resolutions: 8, 16 and 32 elements. The wake was represented by 96 influencing elements per trailing filament with 96 basis sections with Hermite interpolating polynomials in a cylindrical coordinate system. The resolved wake was terminated with a cylindrical far-wake model. Optimization solutions were obtained for all cases except the NREL 5MW with 32 elements on the blade. This case appeared to run well but failed to complete due to time limits on the cluster.

Figure 5.43 shows the optimization solution for the MEXICO rotor with 32 elements. Figure 5.44 shows the optimization solution for the NREL 5 MW rotor with 16 elements on the blade. In both cases the optimizer found a blade geometry where the power generated on the blade approached the Betz limit across the aerodynamic region of the blade. For the MEXICO rotor the optimizer increased the chord at all regions to increase the thrust, while at the outboard region the optimizer decreased the twist to give higher angles of attack and lift. The optimizer made similar changes to the NREL 5 MW rotor, except the chord was only increased at the in-board stations and the twist was reduced by the same amount at all stations.

The smaller changes for the NREL 5 MW wind turbine are expected since this case is based on a commercial design that would have been extensively optimized. Despite this, the optimization was still able to improve the design because this optimization

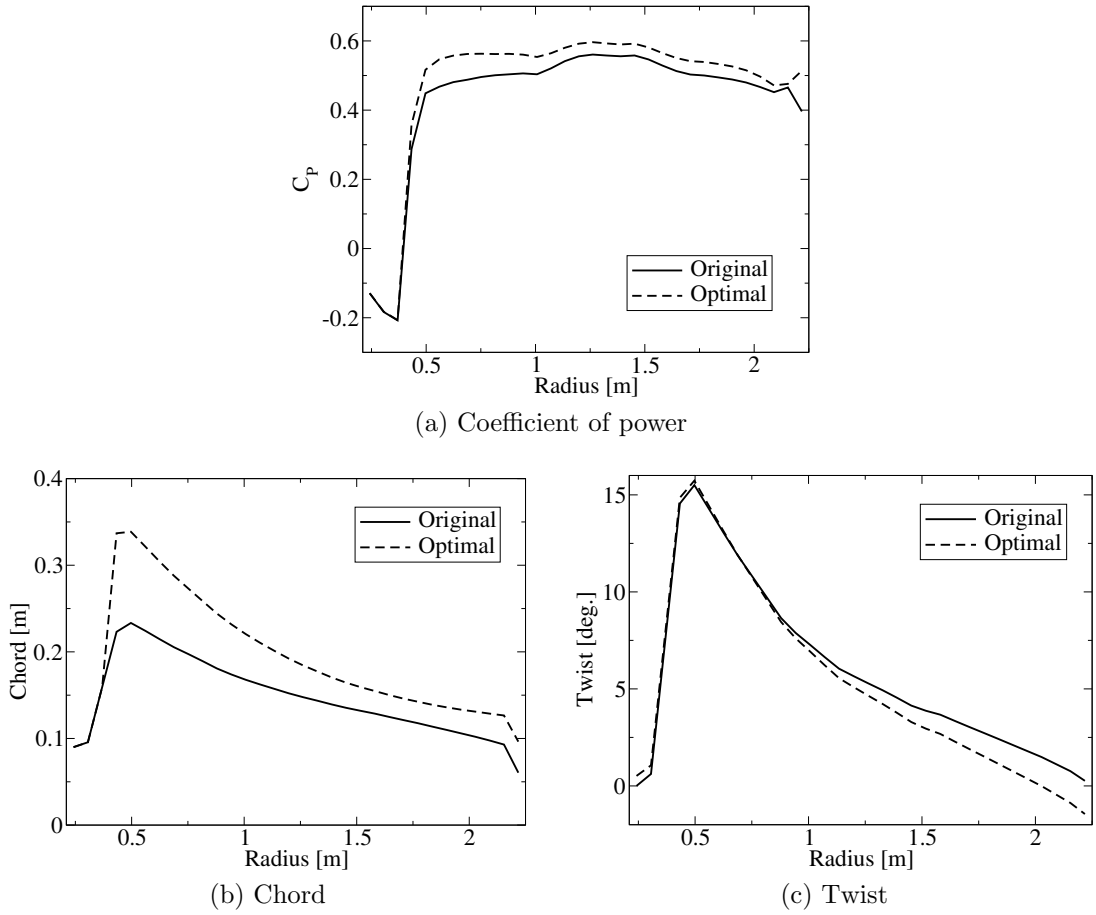

(a) Coefficient of power

(b) Chord

(c) Twist

Figure 5.43: 32 element MEXICO optimization solution

did not have to consider the economics, extreme loads and fatigue constraints that are required to produce a certified design. Figure 5.44a shows the benefit of a large root chord is small, however this larger chord would contribute significantly to higher costs. Furthermore the reduced twist would increase likelihood of stall in unsteady winds. To account for these effects the MDO framework would need to be extended to include economics and unsteady analysis. This will be a subject of future work.

The effectiveness of the FEM-based LVD model in optimization is demonstrated by showing how the CFSQP algorithm performed in the optimization. Figures 5.45 and 5.46 shows this performance for the MEXICO and NREL 5 MW cases respectively.

In both cases the figure 5.45a and 5.46a shows the optimization algorithm was able to make large improvements early in the optimization. Overall the final solution was obtained in a small number of iterations. It appears the optimization algorithm is stalling in the late stages, however figure 5.45b and 5.46b shows the optimization

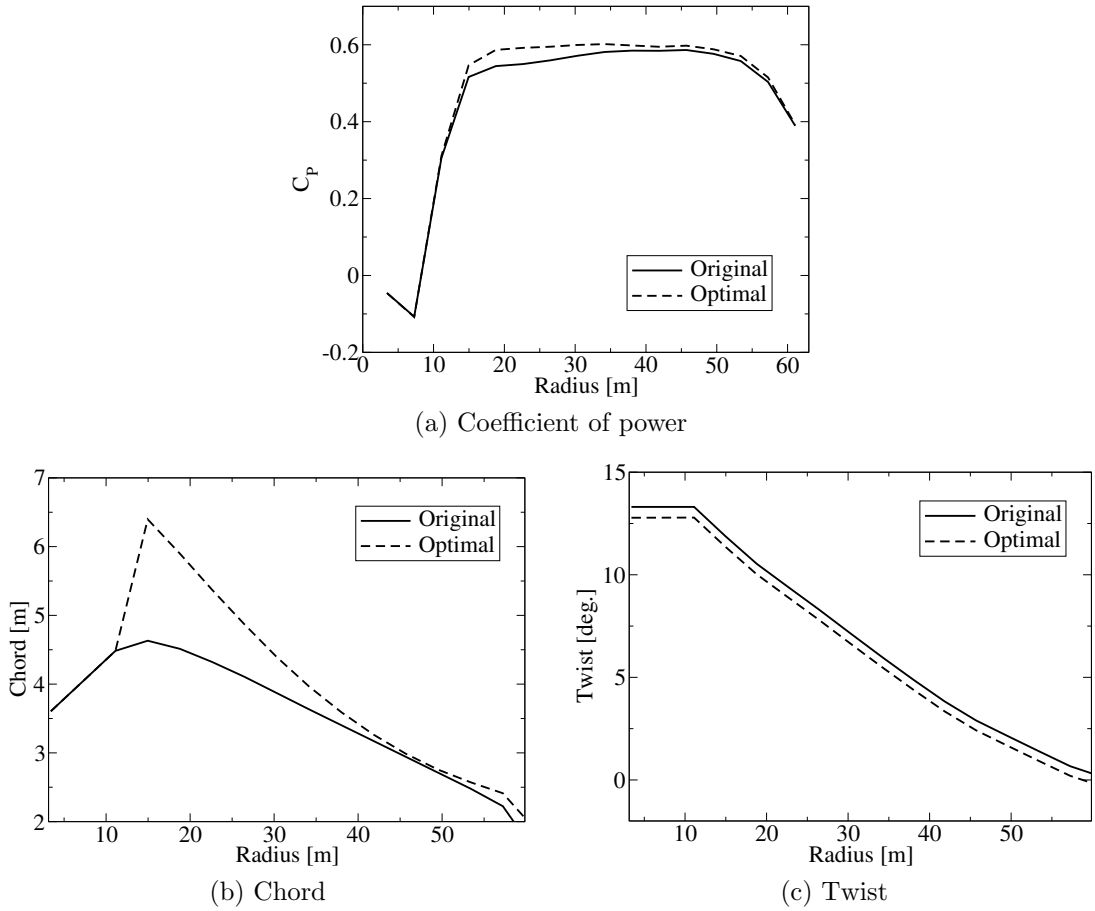

(a) Coefficient of power

(b) Chord

(c) Twist

Figure 5.44: 16 element NREL 5 MW optimization solution

is achieving very high levels of optimality during these iterations. This is something that would be difficult if there were errors in the gradients.

One advantage of the FEM-based LVD formulation is the ability to use previous solutions to accelerate the convergence. Figures 5.45c shows that FEM-based LVD solver became progressively faster as the optimization took smaller steps in the process. However the same plot (figure 5.46c) for the NREL 5 MW case demonstrates the challenges of the FEM-based LVD in optimization. In this case solver stall was more problematic and the solver had to be configured to use the strength stepping singularity avoiding strategy for all function evaluations.

Aero-elastic Optimization

This section demonstrates the FEM-based LVD model in aero-elastic optimization. The purpose of this section is to merely demonstrate the feasibility of using the

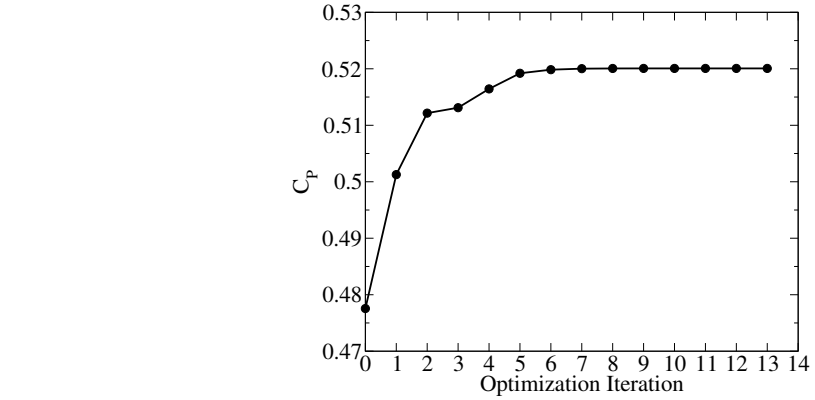

(a) Coefficient of power

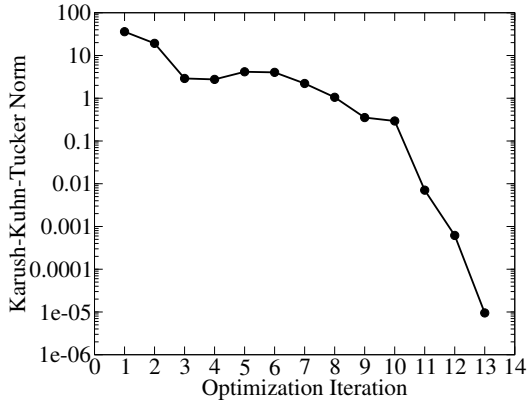

(b) KKT norm

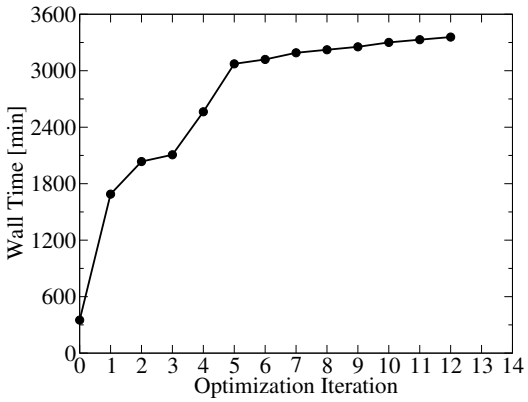

(c) Wall time

Figure 5.45: 32 element MEXICO optimization

FEM-based LVD in aero-elastic optimization. To avoid unnecessary complication, the GEBT and VABS models are not included in this study, instead the linear beam model is used for the structural deformation.

Cross section design aspects are still included in this optimization through a cross section scaling model. The model scales the geometric properties like area and moments of area according to chord c and a thickness parameter h as shown in equations (5.63). This model assumes the blade geometry remains similar with varying chord and the cross-section geometry is based on thin shells where $h \ll c$.

$$A = A_0 \left(\frac{h}{h_0}\right)\left(\frac{c}{c_0}\right)^2 \qquad (5.63a) \qquad I_y = I_{y0} \left(\frac{h}{h_0}\right)\left(\frac{c}{c_0}\right)^4 \qquad (5.63b)$$

$$I_z = I_{z0} \left(\frac{h}{h_0}\right)\left(\frac{c}{c_0}\right)^4 \qquad (5.63c) \qquad J = J_0 \left(\frac{h}{h_0}\right)\left(\frac{c}{c_0}\right)^4 \qquad (5.63d)$$

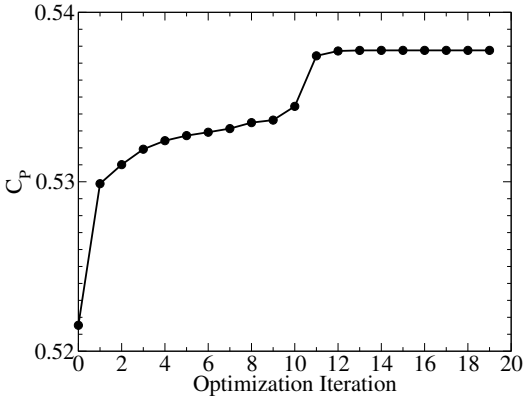

(a) Coefficient of power

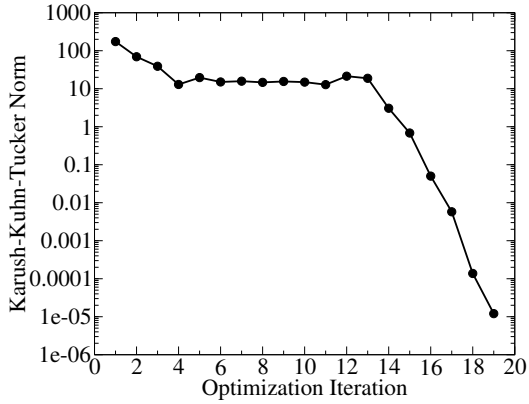

(b) KKT norm

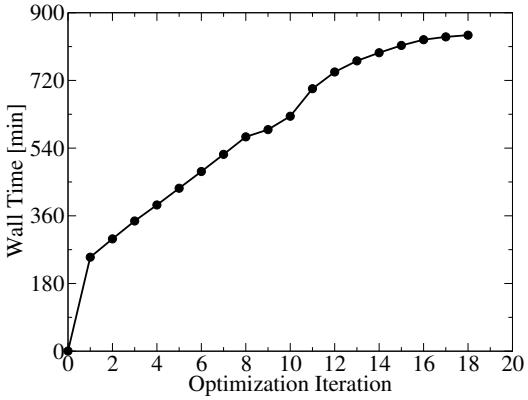

(c) Wall time

Figure 5.46: 16 element NREL 5 MW optimization

The real goal of optimal turbine design is to maximize power and minimize costs simultaneously. This is typically achieved by minimizing the COE [6]. COE minimization requires a suitable cost model to accurately reflect the costs of various design decisions. For the purpose of demonstrating the FEM-based LVD in aero-elastic optimization this optimization forgoes a cost model and introduces a pseudo cost metric based on the volume of the blade in equation (5.64). In equation 5.64 V is the volume of the blade and F is a fixed cost component, F is set to 4 times the original volume to reflect the fact that turbine blades typically represent 20% of the total turbine cost [8].

$$C = V + F \tag{5.64}$$

The NREL 5 MW wind turbine was used again in this optimization. The objective was to maximize the ratio of power to the pseudo cost metric. The optimization use

quadratic splines to vary the twist, chord and a thickness scaling parameter (*i.e.* h/h_0) along the length of the blade. An important consideration in turbine design is the thrust of the rotor, this can lead to excessive stresses on the drive-train and tower. To account for this limitation the rotor thrust was not allowed to exceed the thrust in the original design. In upwind wind turbines the tip of the blade can strike the tower and cause damage to both components if the blade is allowed to deflect too much. To avoid this problem the tip deflection was constrained not to exceed the deflection of the original design. The additional load calculations (*i.e.* root bending moment, unsteady loads, *etc.*) that would be required in commercial design have been neglected here for demonstration purposes.

The aerodynamic model used 16 elements on the blade with 96 15° influencing elements in the wake. Each filament was parameterized with 96 Hermite interpolating polynomials in a cylindrical coordinate system. The wake was terminated with cylindrical far-wake model.

The CFSQP optimization algorithm required many more function evaluations to navigate the tip deflection constraint. This prevented the optimization algorithm from reaching a converged solution within the maximum allowed time on the computing resources. However near the end of the computation the optimizer was only able to make a 0.005% improvement in the objective over the last 5 iterations. Thus, it is unlikely the optimization would have been able to make significant improvements if it was allowed to continue.

At the final iteration the optimization managed to improve the power to pseudo cost ratio from $7.89 \cdot 10^4$ to $8.08 \cdot 10^4$. The C_P improved from 0.528 to 0.532, while the biggest source of improvement was due to a reduction in volume from $1.712m^3$ to $1.558m^3$.

Figure 5.47 shows the optimal solution for the design variables. Due to the constraints the optimization was only able to make small changes to the chord. Figure 5.47c shows the biggest change was a reduction in the cross section thickness scaling at inboard stations. Figure 5.47b shows the inboard twist solution is similar to the aerodynamic optimization then at the tip the twist is increased. The reason for the increase is due to the tip deflection constraint explained below.

Figure 5.48 shows how the optimization improved the objective. Figure 5.48a shows the optimization had increased the C_P at inboard sections as it did in the aerodynamic optimization. Then figure 5.48b shows the majority of the volume reduction also occurred at the inboard sections.

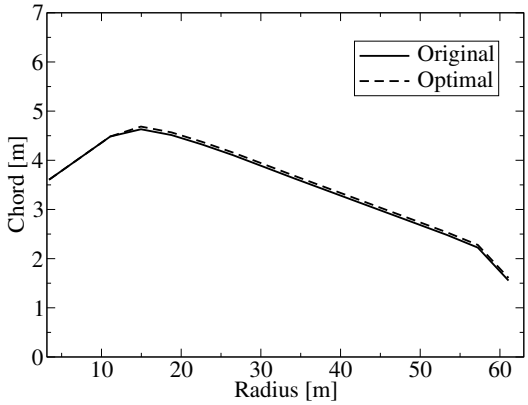

(a) Chord

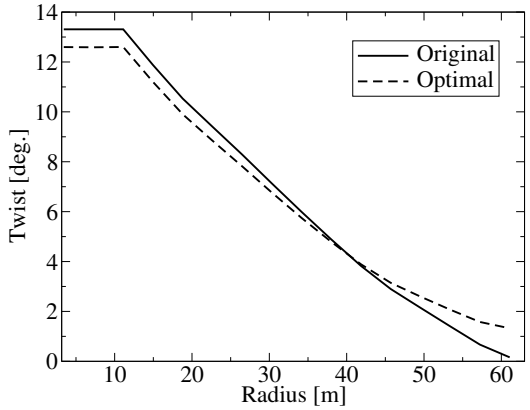

(b) Twist

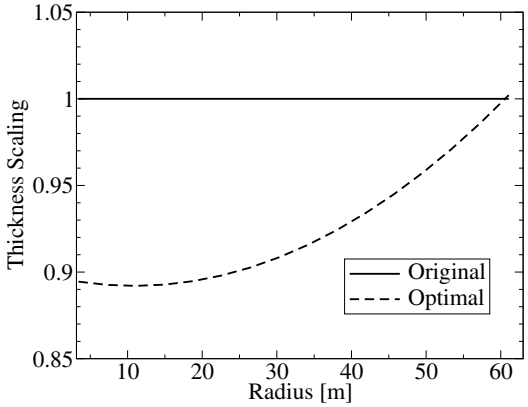

(c) Thickness scaling

Figure 5.47: 16 element NREL 5 MW aero-elastic optimization design variables

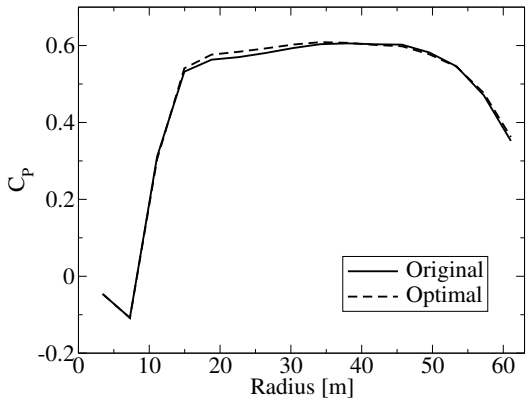

(a) Coefficient of Power

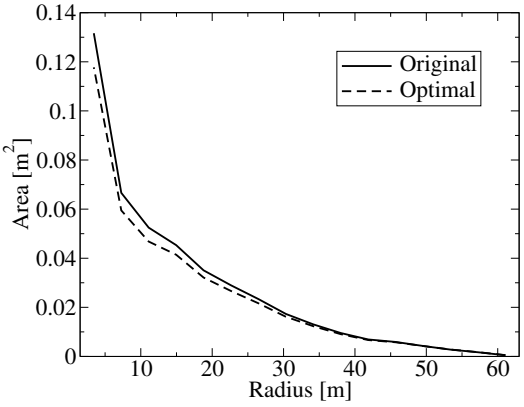

(b) Area

Figure 5.48: 16 element NREL 5 MW aero-elastic optimization objectives

In the optimization the tip deflection constraint was active and appeared to be the dominant constraint in the optimization. Figure 5.49 shows the important parame-

ters that affect the tip deflection. It is clear by the deflection shown in figure 5.49a and the flap-wise moment of area shown in figure 5.49b that the reduced thickness is making the blade more flexible at the inboard sections. Despite the reduced stiffness, figure 5.49c shows that the optimization is satisfying the tip deflection constraint by decreasing the axial force at the tip. The optimization managed to reduce the coefficient of thrust from 0.867 to 0.864[1]. Figure 5.48a shows the azimuthal forces are held constant. This explains why the optimization increased the twist at tip, by increasing the twist the angle of attack decreases. This would lead to lower lift and drag forces which both contribute to the axial forces, however drag has a negative affect while lift has a positive affect on the azimuthal forces. It seems that the reduction in drag is enough to compensate for the reduced lift forces and azimuthal forces are maintained. The optimization was able to reduce the thrust without affecting the power, leading to improved aerodynamic efficiency.

The final optimization solution is affected by the load constraints. This optimization ignored many of the constraints that would have been required. For example the reduced material near the root could have lead to increased stress. The improvements found here may not be possible when the full set of load constraints are included in the optimization.

Overall the aero-elastic optimization was able to find a better solution by improving the power and material usage near the root. The optimization was able to satisfy the tip deflection constraint by reducing the thrust at the tip with reduced twist.

[1]This indicates that only the tip deflection constraint was active. In this case it appears that only the tip deflection constraint is required to limit the thrust. Furthermore, the reduced thrust force at the tip shows the root bending moment is also reduced by the tip deflection constraint.

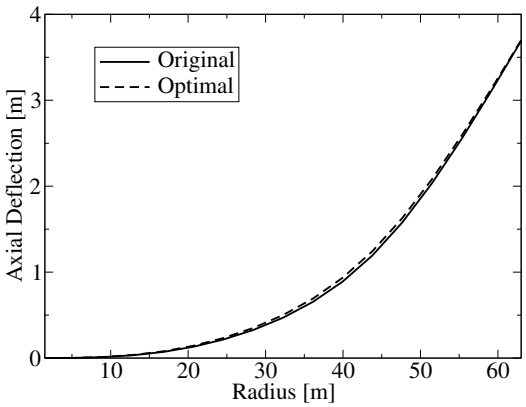

(a) Deflection

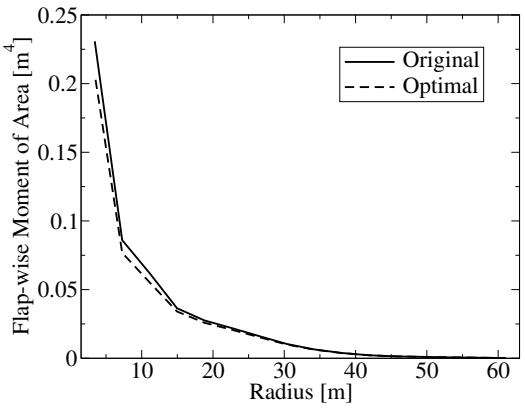

(b) Flap-wise moment of area

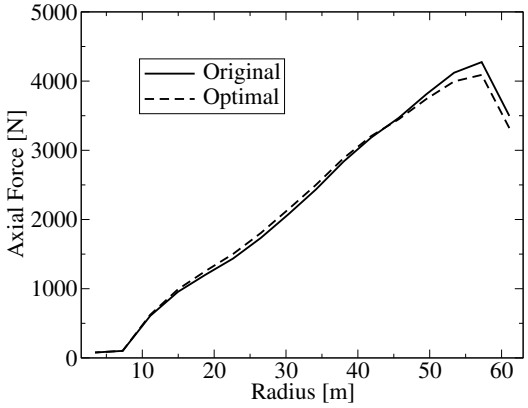

(c) Axial force

Figure 5.49: 16 element NREL 5 MW aero-elastic optimization deformation solution

Chapter 6

Conclusions

The research presented in this thesis expands the Multi-disciplinary Design Optimization (MDO) capabilities of Horizontal Axis Wind Turbine (HAWT) in many ways. Numerical optimization is a powerful tool to automatically navigate complicated problems, however optimization cannot tolerate faults and analysis tools need to be made robust enough for automatic analysis. Section 6.1 outlines work to improve the reliability of BEM models. This work contributed to a BEM model developed by Ning [146] with guaranteed convergence.

MDO is a field that involves expanding the scope of the optimization by including additional disciplinary models. One example is the wind farm siting model discussed in section 6.2. This model can be used to help design engineers identify the optimal design parameters for region-specific optimal designs.

Wind turbines continue to grow in scale, larger turbines benefit from economies of scale and better wind resources. To continue the growth of wind turbines, designs will need to incorporate load alleviation. Conventional design analysis tools like BEM and linear beams are not suitable for these advanced designs. This research explored the use of advanced tools like GEBT for nonlinear beam dynamics and VABS analysis for beam stiffness properties based on anisotropic materials. Section 6.3 discusses the development of adjoint-based gradients for the coupled GEBT-VABS analysis for use in gradient based optimization. To incorporate manufacturing effects section 6.4 summarizes the conclusions from a composite lay-up parameterization scheme based on the manufacturing process.

To improve the fidelity of the aerodynamic simulations, this work investigated LVD. Pure vortex systems are fundamentally chaotic, these chaotic effects cause conventional LVD simulations to exhibit erratic convergence and in some cases di-

vergence. The noise in the convergence leads to erroneous gradients. Despite the noise, aerodynamic optimization is possible, however aero-elastic analysis seems to amplify the noise and prevent aero-elastic optimization from converging. To overcome this problem this research developed a totally new formulation based on the Finite Element Method (FEM). This contribution is discussed in section 6.5.

This section closes with a discussion on future work given in section 6.6.

6.1 Numerical stability of BEM

BEM theory is an attractive aerodynamic model for wind turbine design because it is fast and gives accurate results. The model is based on converging two equations for the axial and the tangential momentum. The typical approach is to apply a fixed point iteration until the model converges. Despite the simplicity, there are cases where this approach will fail to produce a converged solution.

The research presented in section 2.3.1 of chapter 2 conducted an analytical and numerical investigation into the stability of both the fixed point algorithm and a Newton algorithm. The research found the BEM equations lead to numerical instabilities in the Newton algorithm when the blades elements approach stall. Where as the fixed point algorithm exhibited instabilities over a wide range of conditions. Furthermore this research identified many situations where multiple solutions existed and the solution would become indeterminate.

This research lead to a new development by Andrew Ning [146] where the BEM model was parameterized by the inflow angle and solved with an algorithm with guaranteed convergence.

6.2 Wind farm siting optimization

The profit generated by a wind turbine is based on the power generated, the costs of a wind turbine are dependent on the fatigue and extreme loads. Both of these outcomes depend on the site where the wind turbine will be built. Wind farm developers will select the best wind turbine for their site, for manufacturers to be successful their turbine needs to be optimized for that site. The problem of developing the optimal turbine is determining the properties of the sites *a-priori*. Section 5.1 of chapter 5 presents a wind farm-siting model capable of exploring provincial scale regions to help designers identify potential sites.

The model is sensitive to the local wind resource, transmission lines, the population density, the turbine density and noise regulations. Several case studies demonstrated how the model reacted to scenarios where AEP was prioritized, transmission costs were increased and where noise regulations became more stringent. The AEP seeking model successfully identified the region in Alberta where most wind turbines are built.

The model was based on coarse geographic data and a simple micro-siting model. Wind farm developers take advantage of fine-grained local effects to maximize the yield of the wind farm. To obtain an accurate representation of the optimal site conditions this model will need to include information at higher resolution to capture the same local effects used by wind farm developers.

6.3 Adjoint based gradients for coupled GEBT and VABS analysis

The coupled GEBT-VABS structural analysis starts with VABS to solve the cross section stiffness properties. These properties are fed to GEBT model to determine the nonlinear deformation for a given loading. The deformation in the beam is then fed back to the VABS analysis to recover the stress in the materials.

In section 5.2 of chapter 5 this research explored how adjoint based gradients could be incorporated into the coupled analysis. Despite the complexity, this research found a way in which the adjoint equations for both GEBT and VABS could be coupled together and solved to find the structural design sensitivities. These gradients were compared to finite difference and found to give good agreement. Both the finite difference and adjoint based algorithms solved the gradients in roughly the same time. This is due to the fact that the nonlinear beam solver only needs one iteration when the system is perturbed by a small step. The adjoint based gradients relied on finite differencing for many of the partial gradient terms. There is evidence that if these partial gradients are replaced by analytic gradients, the speed of the gradient calculation can be made nearly independent of the number of design variables.

Both the adjoint and finite difference gradients were applied in structural optimization. Both gradient algorithms lead the optimization to the same solution.

6.4 Composite lay-up optimization

Most structural optimization schemes in literature are based on cross section geometry at specific positions along the blade. The cross section design variables are then represented by splines defined along the length of the beam. This parameterization ignores the manufacturing process of wind turbines. In manufacturing, the cross-section geometry is built-up by stacking laminates of composite material along the length of the blade. The geometry and material properties between different span-wise locations are inherently coupled by this process. In section 5.3 of chapter 5 the composite lay-up optimization explored a parameterization scheme based on slabs of material defined along the blade in a similar way that the blade is manufactured.

The slab based parameterization was applied successfully in cross-section design optimization. The slab parameterization scheme was able to find an optimal thickness distribution that used less material than the spline based parameterization. For blades made with both glass and carbon fiber, it was used successfully to find the optimal mix. The parameterization can also include biased fibers in the parameterization. This configuration was used successfully to find the optimal amount of biased fibers for a prescribed bend-twist coupling.

When many slabs are introduced into the optimization, there are multiple ways the thickness can be increased and local minima are introduced. Due to the local minima this scheme cannot be used for high-fidelity optimization alone. A good starting point is required to avoid local minima, further research is needed to determine whether solutions from a convex parameterization scheme could be used as a starting point to a slab based optimization.

6.5 FEM-based LVD

The FEM-based LVD model was developed in response to the limitations of conventional LVD. At the heart of the problem is the lack of an objective convergence metric. The Galerkin projection is used to define an objective convergence metric for the wake and lifting line. The definition of an objective convergence metric solves many of the problems of conventional LVD. First noisy convergence is avoided because the model no longer needs to be evolved in time to obtain a solution. Instead, the Newton algorithm can be used to find a solution that eliminates the residual. The Newton algorithm is used in nonlinear FEM, by using the same solution algorithm

the FEM-based LVD model can be converged simultaneously with structural models. Finally, the convergence metric gives insights into how the state will change in response to changes in the design variables. This leads to an accurate definition of analytic gradients for optimization.

The FEM method was applied to develop a new parameterization scheme for the wake based on interpolating polynomials called basis sections. This parameterization scheme allows the user to locally increase the number of elements in the wake to improve the fidelity. Then to reduce the computational effort the user can independently reduce the number of control points and apply high-order basis functions.

There are three components to the FEM-based LVD research. First section 6.5.1 presents the conclusions from an extensive study into the aerodynamic analysis capabilities given in chapter 3. Then section 6.5.2 gives the conclusions from a study of the aero-elastic capabilities of both the conventional and FEM-based LVD given in chapter 4. Finally the main goal of this model was to obtain aero-elastic optimization results. Section 6.5.3 gives the conclusions from the optimization studies in section 5.5 of chapter 3 that applied FEM-based LVD in both aerodynamic and aero-elastic optimization.

6.5.1 Aerodynamic analysis

Conventional LVD typically relies on iterative convergence to indicate how well a simulation is converged. This metric could be misleading if the convergence happens to be slow. The FEM-based LVD defines an objective convergence metric that was applied to explore the convergence behavior of conventional LVD. The study explored multiple conventional configurations and found in all cases the error in conventional LVD models is increasing until the wake is truncated and the initial transients advect out of the system. After this point the error will drop off. Then after enough iteration one of two scenarios will arise. For smaller simulations the system will settle into a stable oscillation but never converge completely. In larger systems with many influencing elements the noise starts to increase and eventually dominates causing the simulation to diverge. The research found that in the region where the error does decay, an iterative convergence metric would under-predict the true error by a factor of approximately 250. Since conventional LVD cannot be converged to arbitrary levels, there is little one can do to compensate for errors in iterative convergence.

The FEM-based LVD model gives the aerodynamicist many options to configure the model. The classic approach to controlling fidelity and computational speed is to vary the size of the elements. In conventional LVD the computational costs scale according to the cube of the number of elements. However in FEM-based LVD the computational costs scale linearly. Due to the lack of an objective convergence metric in conventional LVD simulations it is difficult to compare the simulation times directly. The results in the convergence study suggest that FEM-based LVD model is faster than the conventional LVD model when the elements are less than 8° in size for wind turbine simulations.

FEM-based LVD is based on interpolating polynomials. Selecting the right type and the correct number can influence both the cost and the accuracy. For wind turbine simulations the interpolation should be performed in a cylindrical reference frame. In some cases cylindrical interpolation can be costly to solve. To suppress the distortions and avoid cylindrical interpolation, Hermite interpolating polynomials should be used to enforce C^1 continuity at the basis section end-points. Reducing the number of basis sections will reduce the computational cost. In wind turbine simulations, cubic basis sections larger than 60° started to introduce errors into the solution.

Without a far-wake model, there is a tendency for the wake to contract at the end. A far-wake model based on vortex cylinders will maintain monotonic expansion with little additional computational effort. With the far-wake models, the resolved wake can be as short as 3 rotor revolutions before significant error is introduced into the C_P solution.

In some cases the FEM-based LVD model can be highly sensitive to the number of elements on the span. This is due to singularities that tend to occur when elements are too close to one another. The problem of singularities is discussed further below. In cases where singularities do not occur, the computational load scales quadratically with the number span-wise elements. Convergence studies show that at least 16 elements are needed on the blade to get an accurate estimate for the coefficient of power. With 23 or more elements, tip-loss and wake roll-up effects are resolved.

The FEM-based LVD model was validated against the classic elliptically loaded wing. The simulation was able to reproduce the expected constant down-wash for most of the span. The solution deviated near the tip where there were not enough elements to properly resolve the elliptical distribution. The FEM-based LVD simulation was used to simulate a rectangular wind and a backward swept wing. In both cases the simulation showed good agreement with experimental measurement. The airfoil

coefficients for the rectangular wing were based on experiments, while the coefficients for the swept wing were based on XFoil. The improved agreement achieved with the rectangular wing demonstrates the importance of accurate airfoil coefficients for LVD simulations. Finally the FEM-based LVD was validated for wind turbine simulations using the MEXICO experiments. These experiments give the circulation strength on the blade along with the location of the tip-vortex. The FEM-based LVD model was used to simulate the MEXICO turbine in low-speed winds, design conditions and high-speed winds and demonstrated good agreement with measurements in all cases.

Solving the FEM-based LVD relies on solving a Jacobian. In some cases the Jacobian can become near singular and cause the solver to stall. This problem tends to occur more often when small elements are used on the lifting line. Small spanwise elements cause free-wake elements to be very close and strongly affected by the influence kernel function. Furthermore these singularities occur more often with longer wakes. Due to the connectivity, updates are integrated down the trailing filament and can lead to strange configurations in the far-wake.

Three strategies have proven successful for avoiding these problems. The first is to solve the strength and the wake configuration separately. This algorithm is similar to load stepping in structural FEM, in this case the strength is updated in small increments, then the wake is solved between updates. For problems with long wakes, singularities can be avoided by partitioning the wake by age. Updating the partitions in a downstream sequence has proven most effective at reducing the overall residual while avoiding singularities. Finally the singularity seems strongly associated with the Biot-Savart influence where the influence is strongest close to the element. Attenuating the near-field influence by increasing the core radius has been effective at removing singularities. The original small-core solution can still be obtained without singularities by using the large-core solution as a starting point to the small-core simulation.

The strategies to overcome solver stall require more computational time to complete the additional iterations. Some progress has been made in developing automatic algorithms to apply these strategies only when necessary. However they do not seem to work universally. To develop a solver algorithm that is both fast and robust more research is needed to properly identify the scenarios when these different strategies need to be applied.

The current FEM-based LVD is for steady state analysis. The same formulation could be extended for unsteady and periodic analysis. The unsteady aerodynamics

will be required to evaluate the extreme loads, while the periodic analysis can account for the effects of wind-shear and other periodic phenomenon.

6.5.2 Aero-elastic analysis

Both the conventional and FEM-based LVD models were used for aero-elastic analysis with a linear beam. Since the FEM-based LVD model uses the same solution algorithms used in structural FEM, it is straight-forward to simultaneously converge both the aerodynamic and structural models. The solution algorithm for conventional LVD is very different from structural models, to obtain mutually converged solutions the two models had to be converged in a fixed point iteration. There are two ways to apply the fixed point algorithm; in the first version the models are co-evolved, where the aerodynamic model completed a single update after each beam update; in the second configuration the aerodynamic model is reinitialized and solved completely after each beam update.

The research explored the convergence properties of the two aero-elastic algorithms for conventional LVD. It has already been shown that the convergence of conventional LVD for purely aerodynamic analysis leads to a erratic and sometimes divergent convergence. The research found that when the aero-structural models were co-evolved, the small motion caused by the beam updates were amplified in the wake and lead to increased noise. The only way to eliminate this effect was to reinitialize and completely solve the aerodynamics after each beam update. In this scenario the beam fully converged and noise in the wake was similar to the pure aerodynamic analysis. However, this approach took 4 times more iterations to adequately converge the beam than the co-evolution algorithm.

The analysis demonstrated that the FEM-based LVD algorithms was applied successfully to obtain coupled aero-structural solutions. Including the beam in the Newton algorithm did not introduce any difficulties in the solution algorithms, in fact the solution speed increased. The simulation showed how the deformation moves the wake back allowing the inboard sections to experience reduced induction and improved performance. However due to the same deformation, the outboard section were no longer normal to the flow and produced less power.

6.5.3 Aerodynamic and aero-elastic optimization

In section 5.4 of chapter 5 aero-elastic optimization was applied with conventional LVD. This study failed to obtain converged optimization results due to noise in the gradients. This difficulty was impetus to developing the FEM-based LVD model. An important advantage of the FEM-based LVD is the ability to obtain accurate analytic gradients.

An objective convergence metric is necessary to predict how the state will vary with changes to the design variables. Since the FEM-based LVD defines an objective metric, one can now define analytic gradients for LVD models. The analytic gradients were verified with finite difference. Several simple optimization studies were performed and in all cases the optimization showed excellent progress and managed to converge to levels with very small Karush-Kuhn-Tucker norms. This indicates the gradients are producing excellent sensitivity information to the optimization.

The LVD models are based on lumping the vorticity onto line elements. A consequence of this assumption is large amount of vorticity is sensitive to single influence calculations. In reality there would be a distributed vorticity, where some self-influence would attenuate the influence of other regions of vorticity. The optimizer was able to exploit this error to find unrealistic designs that only appeared to be an improvement. This error can be suppressed by using splines for the design variables and enforcing monotonic constraints on the control points.

The FEM-based LVD model was used in aerodynamic optimization of both the MEXICO rotor and the NREL 5 MW rotor. In both cases the optimization was able to find a converged solution with improved power output. This was achieved by enlarging the chord at inboard stations and decreasing the twist to give a more aggressive angle of attack.

Finally the FEM-based LVD model was used in aero-elastic optimization of the NREL 5 MW rotor. In this optimization the chord and twist were design variables. Structural aspects were introduced into the optimization through a cross section stiffness scaling model based on the chord and a 'thickness' design variable. The optimization did not include a cost model, instead a simple cost metric based on the blade volume was used in the optimization. This cost metric included a fixed cost component to reflect the other components of the wind turbine. The objective in the optimization was to maximize the ratio of power to cost. This optimization was

constrained to not increase the thrust and axial tip deflection beyond the original design.

The tip deflection constraint was active throughout the optimization. This required the optimization to make many more function evaluations than required in the aerodynamic optimization. The aero-structural optimization could not be fully converged in the time available on the cluster. Before the optimization was canceled the optimization was only making small improvements to the objective with every iterations. This suggests the optimization was close to a final solution when the calculation ended.

The final solution did manage to simultaneously improve the power output and reduce the volume of the blade. The tip constraint plays an important role in the optimization. The volume was reduced near the root. To compensate for the reduced stiffness, the optimization found a more aerodynamically efficient design at the tip that reduced the thrust forces while maintaining the same power.

Overall the FEM-based LVD was applied successfully in aero-elastic optimization. This proves the new FEM-based LVD has successfully overcome the problems of conventional LVD.

In this investigation the nonlinear beam model was not used. The purpose of the study was to validate the FEM-based LVD in aero-elastic optimization. One could argue the problems in the conventional LVD aero-structural optimization are due to the nonlinear beam model. Yet, chapter 4 showed that the linear beams will still increase the noise in the wake.

Further work is still needed to confirm whether the FEM-based LVD will give converged aero-elastic optimization solutions with the coupled GEBT-VABS analysis. The solver and gradient algorithm used in the FEM-based LVD optimization should work equally well with nonlinear beam models. Thus, it is expected that this model will still perform well with coupled GEBT-VABS analysis. This will be a topic of future research.

6.6 Future Work

The future work for this research is discussed in three broad categories. The FEM-based LVD solver algorithm; unsteady analysis with FEM-based LVD; further progress in the MDO framework.

The current solver algorithm for the FEM-based LVD was sufficient to obtain optimization results. However, due to singularities the algorithm can be quite slow when the singularity avoidance is required for every function evaluation. An important justification for using LVD is faster function evaluations when compared to grid based CFD. The solver algorithm needs to be improved for FEM-based LVD to be faster than grid based CFD in all cases. This is discussed in section 6.6.1.

Unsteady analysis is important in wind turbine design to evaluate fatigue damage and extreme loads. The medium fidelity analysis tools explored in this framework need to be upgraded for unsteady analysis for a complete MDO framework to be realized. Section 6.6.2 proposes how these tools can be upgraded.

Finally the final objective of this research is to create a MDO framework for HAWTs capable of optimizing advanced designs that exploit load alleviation strategies. Section 6.6.3 discusses what additional work is needed to expand the MDO capabilities further.

6.6.1 Improvements to the FEM-based LVD Solver

Solving the FEM-based LVD model is challenging due to singularities. It is desirable to simulate wind turbines with high span-wise resolution, however these singularities become more common in these cases. Strategies have been developed to avoid these problems, however the algorithms need further improvement.

First the source of the singularities is not fully understood. One of the factors could be locking in the basis sections. The highly nonlinear flow field of a Biot-Savart influence may require the basis sections to deform into configurations that are not possible with the basis functions. There have been some cases where the singularity was removed simply by adding more degrees of freedom. Further understanding into this issue will require detailed analysis of singular conditions. The basis section strongly associated with the singular modes need closer inspection to confirm how well the basis sections can approximate the local flow field.

Another potential source of singularities could be due to how the residual is integrated in the wake. When the residual is calculated in the wake, the influencing elements are shifted such that an element end-point lies on the integration point and self-influence is avoided. However, this approach produces a different flow field for each shifted configuration. Yet, a single basis section configuration needs to be aligned to each of these different flow fields. The same detailed analysis on the singular basis

section would shed light on this problem as well. Another approach would involve exploring different integration schemes. Instead of shifting the elements they could be held static, self influence could be removed by ignoring any connected elements in close proximity to an integration point. Ignoring the near field influence could be a solution on its own given the similarity to attenuation by an enlarged core-radius. Another integration scheme would eliminate the Van-Garrel elements completely and apply numerical integration on the Biot-Savart law in equation (2.39) directly.

The singularity seems to occur more often when the wake is pushed into strange configurations. These strange configurations are due to the line search where the residual will increase in a small local region because the solver is still able to decrease the system residual. These local increases could be avoided by modifying the line search algorithm. There are two possible approaches, the first is simply based on finding the minimum of higher-order residual norm. This approach would require little modification to the current line search algorithm. For aero-elastic solutions the residual is composed of force imbalances from the beam, circulation strength errors from the lifting line and velocity errors from the wake. Differences in the units makes the solver more or less sensitive to different components of error. A better strategy may involve making the line search sensitive to each of these domains independently. Instead of finding the system minimum, it may seeks out the smallest β where a domain minimum is found. Overall, these strategies aim to avoid strange configurations by developing a robust line search algorithm the ensures the residual is reduced over a wider region in the problem.

Enlarging the core radius in the influence calculation for the wake has proven successful for avoiding singularities. Furthermore, using large core-radius solutions as a starting point for small core-radius simulations has led to small core-radius solves without singularity problems. The current solver requires the user to manually run simulations with an enlarged core-radius. If the user desires the small core-radius solution a new simulations needs to be set-up and executed manually. This strategy could be automated and implemented in the solver so the core is automatically enlarged during difficult conditions and then reduced back to the original size before the solver finishes.

The problem of singularities was less of a problem in optimization because many of the function evaluations required only small changes to the system. In these cases the solver could be executed in a faster more aggressive configuration. In the cases where singularities arose, the solver would automatically invoke one or more of the

singularity strategies. However, there were situations where the solver was too aggressive and subsequent attempts to avoid singularities failed. Better methods are required to detect these situations early and avoid them automatically. All of the aforementioned solver improvements could contribute to the goal of a more robust automatic singularity avoidance algorithm.

Singularities occur more often when the solver must make large changes to the configuration. This suggests that the steady-state FEM-based LVD formulation is not ideal as a stand-alone solver. The FEM formulation solves the convergence problem of time marching schemes, but introduces solver stall. The advantages of both formulations could be combined. A time marching simulation could be used to get close to the steady state solution. Then when no further progress can be made with the time marching algorithm, the steady state FEM-based LVD could be used to finish the problem. Figure 3.10 shows the steady state FEM-based LVD solution algorithm can be faster than conventional algorithms with small elements due to improved scaling properties. This advantage can be maintained in a time marching code by developing a similar FEM formulation for unsteady LVD. More details on this are given in section 6.6.2.

6.6.2 Unsteady Analysis with Medium Fidelity Tools

Optimizing the performance of a wind turbine at a single operating point is not sufficient to produce optimal wind turbine designs for the real world. Wind turbines operate over a range of weather conditions and need to be optimized for the range of wind speeds that are most common. The current framework could easily be extended to solve steady state solutions over multiple wind speeds. These solutions could then be used to estimate the AEP for a given wind speed distribution.

Neglecting fatigue and extreme loads will produce overly optimistic designs. The IEC 61400 design standards requires manufacturers to design their wind turbines to withstand multiple load cases with different combinations of extreme gusts, extreme changes in direction and faults in the electricity grid. These events are transient and require unsteady analysis, which in-turn requires upgrades to the current set of analysis tools.

The cross section properties predicted by VABS are time-invariant, so only the nonlinear beam model needs to be updated for unsteady structural analysis. GEBT

is a mature model and several authors have already explored the best algorithm for unsteady analysis [245, 243, 244].

Updating the FEM-based LVD model for unsteady analysis is still an open and unexplored topic. First shed vorticity would need to be incorporated into the analysis, which should be straightforward. The FEM parameterization can be extended for unsteady analysis by adding time dependence to the finite element interpolation in equation (3.1). This transforms the 1 dimensional basis sections defined over space alone to 2 dimensional basis section defined over space and time.

Further considerations are required on how the FEM description is used to calculate the velocity of material points in the flow field. A Lagrangian interpretation assumes the fluid particles are attached to the basis section at a constant spatial position. In this interpretation the velocity of the fluid is merely the time rate of change of basis section. The simulation would be creating basis sections much in the same way that conventional time stepping algorithms create elements in a growing wake. The growing wake configuration in conventional LVD has proven to be the more efficient approach as oppose to solving pre-initialized wake. The growing wake approach in the FEM formulation could be the most efficient way of obtaining a good first guess for steady-state analysis.

An Eulerian interpretation is an alternative interpretation of the unsteady FEM formulation. This approach assumes spatial positions in the basis section correspond to a constant age in the trailing vortex filaments. In this interpretation the fluid is moving through the basis sections. The velocity of the flow is based on a combination of the time rate of change and the spatial tangent of the basis sections. This approach is most similar to the parameterization described in chapter 3. The parameterization could easily be extended for periodic analysis by defining the basis sections with sinusoidal functions in time. The periodic analysis can incorporate unsteady effects like wind shear and gravitational loads, this analysis could replace the steady state estimates of C_P and provide efficient surrogate models for other unsteady effects.

Majority of the fatigue damage in wind turbines is caused by small fluctuations in the wind speed during regular operation. The conventional approach to estimating the fatigue damage is to run unsteady simulations for 10 minutes of operation in a turbulent flow field. Since the magnitude of turbulent fluctuations vary with wind speed, multiple 10 minute solutions are required over a range of wind speeds. The turbulent flow fields are numerically generated based on turbulence statistics. These flow fields are not unique, multiple flow fields that each produce different fatigue

loads can be generated with the same statistics. To improve the fatigue estimate the analysis is conducted over multiple flow-fields. Overall, evaluating the fatigue damage is computationally expensive. Efficient alternatives are required to incorporate fatigue analysis into the optimization.

There are several approaches for incorporating fatigue loads into the optimization. The first example is given by Fuglsang and Madsen [57] where a simple surrogate model based on steady-state root bending loads was used to estimate fatigue. The model had to be updated and tuned with unsteady analysis at multiple points in the optimization. Another example is a multi-fidelity multi-level optimization approach is given by Bottasso *et. al.* [251] where unsteady analysis with high-fidelity tools is used to define the equivalent loads for low fidelity steady-state analysis within an inner optimization loop.

Each of these approaches rely on steady-state analysis as a surrogate for unsteady phenomenon. In these cases the optimizer is insensitive to how unsteady dynamics could affect the fatigue loads. These approaches would not be suitable for finding the optimal design for load alleviation strategies that rely on large unsteady nonlinear deformation. Efficient periodic analysis could incorporate the dynamics into the optimization without adding significant computational time. One approach is the nonlinear frequency domain technique developed by Jameson *et. al.* [60, 62, 61] for grid based CFD. This technique could be adapted for the periodic version of FEM-based LVD. These periodic solutions could then be used in a more accurate higher fidelity surrogate model for fatigue damage.

6.6.3 Progress towards the Complete MDO Framework

The MDO presented in this thesis only incorporated aero-structural design in the optimization. To fully realize the benefits of advanced wind turbine design the disciplinary scope of the optimization needs to be expanded. An obvious example is to combine all the tools presented in this thesis. First the optimal parameters from the wind farm siting model could be used to define the optimization formulation in the turbine design. The new FEM-based LVD model still needs to be coupled to the medium fidelity analysis tools. It is unlikely the nonlinear beam model will introduce further complications, yet this remains to be confirmed.

The aero-structural optimization relies on cost models to properly prioritize aerodynamic and structural improvements. The optimization presented here used a sim-

ple cost model based on the blade volume and a fixed cost for the remainder of the turbine. A better cost model is already provided by Fingersh *et. al.* [8] based on regression of existing turbine designs. This model is based on older designs and may not be suitable for advanced turbines. Furthermore, the loads for the rotor can affect the costs and performance of other components. A physics based cost model would have wider application to advanced wind turbine design optimization. The more sophisticated the cost model is, the more capable the optimization is for maximizing the system benefits.

Another important consideration in wind turbine design is the noise emissions. Regulations constrain noise emissions for the comfort of local residents. These constraints limit the maximum speed of the rotor and can lead to reduced performance. Accordingly aero-acoustics is an active area of research in wind energy [270, 271, 272], with several researchers developing noise models that can easily be incorporated into optimization [273, 274, 275].

The overall design could be improved by expanding the design space to additional components like the drive-train, tower and balance of plant. Each of these components would require physical models, component specific constraints and cost models. Another attractive application of MDO is offshore wind energy. For shallow waters specialized foundations must be included into the design. The high cost of these foundations could be reduced if the foundation design and costs were included in the optimization. The loads on these structures are affected by waves and would require additional models for the hydro-dynamics. For deeper waters, researchers are looking at developing floating wind turbines, in this case the foundation is replaced by buoys and mooring lines. For these turbines the hydro-dynamics take on greater importance as these effects have a greater influence on the turbine motion and loads.

Expanding the disciplinary scope of MDO can become very complicated with multiple models. To simplify the process there needs to be additional software to manage the MDO framework, the analysis and the gradient calculations in an efficient manner. Several researchers have already made progress in this area. The first example is pyMDO by Martins *et. al.* [276]. This inspired the OpenMDAO project by Gray *et. al.* [277]. The OpenMDAO framework has already been applied for wind turbine design optimization [278, 279]. The tools developed in this thesis need to be extended along with any additional tools to work with the OpenMDAO framework. The OpenMDAO-based WISEDEM framework developed by Dykes *et. al.* [279] is open source and openly available. Adapting the current tools to fit into this frame-

work would endow this MDO framework with the additional cost and disciplinary models that have already been incorporated into WISEDEM.

There is inherent uncertainty in the many of the numerical models used for wind turbine design analysis. One example is the airfoil coefficients that are used in the aerodynamic models. It is widely known that wind tunnel testing can produce slightly different results for the same airfoil [280], furthermore rotational effects can alter the performance further. Another source of uncertainty is the material properties. One example are composite materials that can be highly variable in stiffness and strength due to variations in fiber volume fraction. Finally defects can occur in the manufacturing. To incorporate these effects into the optimization, one can adopt uncertainty analysis and robust optimization techniques [281]. In this approach the performance of various designs are penalized based on the level of uncertainty. This leads to strong designs that will still perform well despite the different sources of variability.

Bibliography

[1] Flemming Rasmussen and Peter Hauge Madsen. Current Direction of Danish Wind Energy Research - The Researchers Point of View. *Journal of Solar Energy Engineering*, 126:1105–1109, 2004.

[2] Sven-Erik Thor and Patricia Weis-Taylor. Long-term Research and Development Needs for Wind Energy for the Time Frame 2000-2020. *Wind Energy*, 5:73–75, 2002.

[3] Manfred Lenzen and Jesper Munksgaard. Energy and CO2 life-cycle analyses of wind turbines-review and applications. *Renewable Energy*, 26:339–362, 2002.

[4] P. J. Tavner, J. Xiang, and F. Spinato. Reliability Analysis for Wind Turbines. *Wind Energy*, 10:1–18, 2007.

[5] Jeffery B. Greenblatt, Samir Succar, David C. Denkenberger, Robert H. Williams, and Robert H. Socolow. Baseload wind energy: modeling the competition between gas turbines and compressed air energy storage for supplemental generation. *Energy Policy*, 35(3):1474–1492, 2007.

[6] James L. Tangler. The Evolution of Rotor and Blade Design. In *American Wind Energy Association WindPower 2000, Palm Springs, California April 30-May 4, 2000*, 2000.

[7] David A. Spera. *Wind Turbine Technology*. American Society of Mechanical Engineers, New York, United States of America, 1994.

[8] L. Fingersh and M. HanM. Hand. Laxson. Wind turbine design cost and scaling model. Technical report, National Renewable Energy Laboratory, December 2006.

[9] K. Dykes and R. Meadows. Applications of Systems Engineering to the Research, Design, and Development of Wind Energy Systems. Technical report, National Renewable Energy Laboratories, 1617 Cole Boulevard, Golden Colorado, USA, December 2011. NREL/TP-5000-52616.

[10] Andrew R. Henderson, Colin Morgan, Bernie Smith, Hans C. Sorensen, Rebecca J. Barthelmie, and Bart Boesmans. Offshore Wind Energy in Europe-A review of the State-of-the-Art. *Wind Energy*, 6:35–52, 2003.

[11] D. C. Quarton. The Evolution of Wind Turbine Design Analysis - A twenty Year Progress Review. *Wind Energy*, 1:5–24, 1998.

[12] Gijs A. M. van Kuik. The Lanchester Betz Joukowsky Limit. *Wind Energy*, 10:289–291, 2007.

[13] M. O. L. Hansen, J. N. Sorensen, S. Voutsinas, N. Sorensen, and H. Aa. Madsen. State of the art in wind turbine aerodynamics and aeroelasticity. *Progress in Aerospace Sciences*, 42:285–330, 2006.

[14] Paul S. Veers, Thomas D. Ashwill, Herbert J. Sutherland, Daniel L. Laird, Donald W. Lobitz, Dayton A. Griffon, John F. Mandel, Walter D. Musial, Kevin Jackson, Michael Zuteck, Antonio Miravete, Stephen W. Tsai, and James L. Richmond. Trends in the Design, Manufacture and Evaluation of Wind Turbine Blades. *Wind Energy*, 6:245–259, 2003.

[15] K. J. Jackson, M. D. Zuteck, C. P. van Dam, K. J. Standish, and D. Berry. Innovative Design Approaches for Large Wind Turbine Blades. *Wind Energy*, 8:141–171, 2005.

[16] P. A. Joosse, D. R. V. van Delft, Chr. Kensche, D. Soendergaard, R. M. van den Berg, and F. Hagg. Cost Effective Large Blade Components by Using Carbon Fibers. *Journal of Solar Energy Engineering*, 124:412–418, 2002.

[17] Dayton A. Griffin and Thomas D. Ashwill. Alternative Composite Materials for Megawatt-Scale Wind Turbine Blades: Design Considerations and Recommended Testing. *Journal of Solar Energy Engineering*, 125:515–521, 2003.

[18] Daniel D. Samborsky, Timothy J. Wilson, Pancasatya Agastra, and John F. Mandell. Delamination at Thick Ply Drops in Carbon and Glass Fiber Lami-

nates Under Fatigue Loading. *Journal of Solar Energy Engineering*, 130, August 2008.

[19] Jeppe Johansen, Helge Aa. Madsen, Mac Gaunaa, Christian Bak, and Niels N. Sorensen. Design of a Wind Turbine Rotor for Maximum Aerodynamic Efficiency. *Wind Energy*, 12:261–273, 2009.

[20] Scott J. Schreck and Michael C. Robinson. Horizonal Axis Wind Turbine Blade Aerodynamics in Experiments and Modeling. *IEEE Transactions on Energy Conversion*, 22(1):61–70, 2004.

[21] T. K. Barlas and G. A. M. Van Kuik. Review of state of the art in smart rotor control research for wind turbines. *Progress in Aerospace Sciences*, 46:1–27, 2010.

[22] Scott J. Johnson, Jonathon P. Baker, C. P. Van Dam, and Dale Berg. An overview of active load control techniques for wind turbines with an emphasis on microtabs. *Wind Energy*, 13:239–253, 2010.

[23] Dale Berg, David Wilson, Jon Berg, Jon White, Brian Resor, and Mark Rumsey. Design, Fabrication, Assembly and Initial Testing of a SMART Rotor. In *49th AIAA Aerospace Sciences Meeting, 4-7 January 2011, Orlando, Florida*, January 2011.

[24] P. K. Chaviaropoulos, E. S. Politis, D. J. Lekon, N. N. Sorensen, M. H. Hansen, B. H. Bulder, D. Winkelaar, C. Lindenburg, D. A. Saravanos, T. P. Philippidis, C. Galiotis, M. O. L. Hansen, and T. Kossivas. Enhancing the Damping of Wind Turbine Rotor Blades, the DAMPBLADE Project. *Wind Energy*, 9:163–177, 2006.

[25] P. M. Jamieson and A. Jaffrey. Advanced Wind Turbine Design. *Journal of Solar Energy Engineering*, 119:315–320, 1997.

[26] Curran Crawford and Jim Platts. Updating and Optimization of a Coning Rotor Concept. *Journal of Solar Energy Engineering*, 130, August 2008.

[27] Curran Crawford. *Advanced Engineering Models for Wind Turbines with Application to the Design of a Coning Rotor Concept*. PhD thesis, Trinity College, Department of Engineering, University of Cambridge, October 2006.

[28] Tom Ashwill. Sweep-Twist Adaptive Rotor Blade: Final Project Report. Technical report, Knight & Carver Wind Group and Sandia National Laboratories, 2423 Hoover Avenue National City, California 91950 and PO Box 5800 Albuquerque New Mexico 87185 and Livermore California 94550, February 2010. SAND2009-8037.

[29] M. H. Hansen. Aeroelastic properties of backward swept blades. In *49th AIAA Aerospace Sciences Meeting, 4-7 January 2011, Orlando, Florida*, January 2011.

[30] Kyle Kristopher Wetzel. Wind turbine rotor blade with in-plane sweep and devices using same, and methods for making same, 2008.

[31] Beth Dwyer and Keith Bennett. Evaluation of Aeroelastically Tailored Small Wind Turbine Blades Final Project Report. Technical report, United States Department of Energy, Golden Field Office, 1617 Cole Boulevard, Golden, Colorado 80401, September 2005. DE-FG36-03G013133.

[32] Kyle K. Wetzel. Utility Scale Twist-Flap Coupled Blade Design. *Journal of Solar Energy Engineering*, 127:529–537, 2005.

[33] Alireza Maheri, Siamak Noroozi, and John Vinney. Decoupled aerodynamic and structural design of wind turbine adaptive blades. *Renewable Energy*, 32:1753–1767, 2007.

[34] J. F. Manwell, J. G. McGowan, and A. L. Rogers. *Wind Energy Explained, Theory, Design and Application*. John Wiley and Sons, Chichester, England, 2002.

[35] Martin O. L. Hansen. *Aerodynamics of Wind Turbines*. James & James, London, England, 2000.

[36] Xueyong Zhao, Peter Maiber, and Jingyan Wu. A new multibody modelling methodology for wind turbine structures using cardanic joint beam element. *Renewable Energy*, 32:532–546, 2007.

[37] Benjamin Yan. A Framework for Aerostructural Analysis of Wind Turbine Blades. Master's thesis, University of Toronto, Toronto Ontario Canada, January 2011.

[38] David J. Malcolm and Daniel L. Laird. Extraction of Equivalent Beam Properties from Blade Models. *Wind Energy*, 10:135–157, 2007.

[39] Alejandro D. Otero and Fernando L. Ponta. Structural Analysis of Wind-Turbine Blades by a Generalized Timoshenko Beam Model. *Journal of Solar Energy Engineering*, 132, February 2010.

[40] Dewey H. Hodges. *Nonlinear Composite Beam Theory.* American Institute of Aeronautics and Astronautics, 1801 Alexander Bell Drive, Reston, Virginia 20191-4344, 2006.

[41] Don W. Lobitz. Aeroelastic Stability Predictions for a MW-sized Blade. *Wind Energy*, 7:211–224, 2004.

[42] M. H. Hansen. Aeroelastic Instability Problems for Wind Turbines. *Wind Energy*, 10:551–577, 2007.

[43] Flemming Rasmussen, Morten Hartvig Hansen, Kenneth Thomsen, Torben Juul Larsen, Frank Bertagnolio, Jeppe Johansen, Helge Aagaard Madsen, Christian Bak, and Anders Melchoir Hansen. Present Status of Aeroelasticity of Wind Turbines. *Wind Energy*, 6:213–228, 2003.

[44] Gunjit Bir. Multi-Blade Coordinate Transformation and Its Application to Wind Turbine Analysis. In *2008 ASME Wind Energy Symposium, Reno, Nevada, January 7-10, 2008*, January 2008.

[45] M. H. Hansen. Aeroelastic Stability Analysis of Wind Turbines Using an Eigenvalue Approach. *Wind Energy*, 7:133–143, 2004.

[46] S. Schreck and M. Robinson. Blade Three-Dimensional Dynamic Stall Response to Wind Turbine Operating Condition. *Journal of Solar Energy Engineering*, 127:488–495, 2005.

[47] K. Pierce and A. C. Hansen. Prediction of Wind Turbine Rotor Loads Using the Beddoes-Leishman Model for Dynamic Stall. *Journal of Solar Energy Engineering*, 117:200–204, 1995.

[48] Ricardo Pereira, Gerard Schepers, and Marilena D. Pavel. Validation of the Beddoes-Leishman Dynamic Stall Model for Horizontal Axis Wind Turbines

using MEXICO data. In *49th AIAA Aerospace Sciences Meeting, 4-7 January 2011, Orlando, Florida*, January 2011.

[49] Morten Hartvig Hansen, Mac Gaunaa, and Helge Aagaard Madsen. A Beddoes-Leishman type dynamic stall model in state-space and indicial formulations. Technical report, Riso National Laboratories, Roskilde, Denmark, June 2004. Riso-R-1354(EN).

[50] Jesper Winther Larsen. *Nonlinear Dynamics of Wind Turbine Wings*. PhD thesis, Aalborg University, July 2008.

[51] Gunjit S. Bir. Computerized Method for Preliminary Structural Design of Composite Wind Turbine Blades. *Journal of Solar Energy Engineering*, 123:372–381, 2001.

[52] Elart von Collani, A. Binder, W. Sans, A. Heitmann, and K. Al-Ghazali. Design Load Definition by LEXPOL. *Wind Energy*, 11:637–653, 2008.

[53] Find M. Jensen, Amit S. Puri, John P. Dear, Kim Branner, and Andrew Morris. Investigating the impact of non-linear geometrical effects on wind turbine blades Part 1: Current status of design and test methods and future challenges in design optimization. *Wind Energy*, 2010.

[54] Andrew Halfpenny. A frequency domain approach for fatigue life estimation from Finite Element Analysis. In *International Conference on Damage Assessment of Structures*, 1999.

[55] Herbert J. Sutherland. On the Fatigue Analysis of Wind Turbines. Technical report, Sandia National Laboratories, Albuquerque, New Mexico, June 1999. SAND99-0089.

[56] T. G. Van Engelen. Frequency Domain Load Calculation for Offshore Wind Turbines (Turbu Offshore). In *European Wind Energy Conference, November 2004*, November 2004.

[57] P. Fuglsang and H. A. Madsen. Optimization method for wind turbine rotors. *Journal of Wind Engineering and Industrial Aerodynamics*, 80:191–206, 1999.

[58] Peter Fuglsang and Kenneth Thomsen. Site-specific Design Optimization of 1.5-2.0 MW Wind Turbines. *Journal of Solar Energy Engineering*, 123:296–303, 2001.

[59] P. Fuglsang, C. Bak, J. G. Schepers, B. Bulder, T. T. Cockerill, P. Claiden, A. Olesen, and R. van Rossen. Site-specific Design Optimization of Wind Turbines. *Wind Energy*, 5:261–279, 2002.

[60] Matther McMullen, Antony Jameson, and Juan Alonso. Demonstration of Nonlinear Frequency Domain Methods. *AIAA Journal*, 44(7):1428–1435, 2006.

[61] Farid Kachra and Siva K. Nadarajah. Aeroelastic Solutions Using the Nonlinear Frequency-Domain Method. *AIAA Journal*, 46(9):2202–2210, September 2008.

[62] Siva K. Nadarajah and Antony Jameson. Optimum Shape Design for Unsteady Three-Dimensional Viscous Flows Using A Non-Linear Frequency Domain Method. *Journal of Aircraft*, 44(5):1513–1527, September-October 2007.

[63] Wang Xudong, Wen Zhong Shen, Wei Jun Zhu, Jens Norkaer Sorensen, and Chen Jin. Shape Optimization of Wind Turbine Blades. *Wind Engineering*, 12:781–803, 2009.

[64] Soren Hjort, Kristian Dixon, Michael Gineste, and Anders S. Olsen. Fast Prototype Blade Design. *Wind Engineering*, 33:321–334, 2009.

[65] Curran Crawford and Luke Stack. Optimal Rotors for Distributed Wind Turbines. In *47th AIAA Aerospace Sciences Meeting*, 2009.

[66] Ernesto Benini and Andrea Toffolo. Optimal Design of Horizontal-Axis Wind Turbines Using Blade-Element Theory and Evolutionary Computation. *Journal of Solar Energy Engineering*, 124:357–363, 2002.

[67] G. R. Collecutt and R. G. J. Flay. The economic optimization of horizontal axis wind turbine design. *Journal of Wind Engineering and Industrial Aerodynamics*, 61:87–97, 1996.

[68] T. Diveux, P. Sebastian, D. Bernard, J. R. Puiggali, and J. Y. Grandidier. Horizontal Axis Wind Turbine Systems: Optimization Using Genetic Algorithms. *Wind Energy*, 4:151–171, 2001.

[69] Joaquim Martins and Gaetan K. W. Kenway. Aerostructural shape optimization of wind turbine blade considering site-specific winds. Energy, wind and water: algorithms for simulation, optimization and control, Aukland, New Zealand, February 2009. New Zealand Institute of Mathematics & its Applications.

[70] K. Thomsen, P. Fuglsang, and G. Schepers. Potential for Site-Specific Design of MW Sized Wind Turbines. *Journal of Solar Energy Engineering*, 123:304–309, 2001.

[71] K. Jockson, C. P. van Dam, and D. Yen-Nakafuji. Wind Turbine Generator Trends for Site-specific Tailoring. *Wind Energy*, 8:443–455, 2005.

[72] P. Giguere, M. S. Selig, and J. L. Tangler. Blade Design Trade-Offs Using Low-Lift Airfoils for Stall-Regulated HAWTs. *Journal of Solar Energy Engineering*, 121:217–223, 1999.

[73] R. Lanzafame and M. Messina. Fluid dynamics wind turbine design: Critical analysis, optimization and application of BEM theory. *Renewable Energy*, 32:2291–2305, 2007.

[74] M. J. Clifton-Smith. Wind Turbine Blade Optimisation with Tip Loss Corrections. *Wind Engineering*, 33(5):477–496, 2009.

[75] Michael McWilliam and Curran Crawford. The Behavior of Fixed Point Iteration and Newton-Raphson Methods in Solving the Blade Element Momentum Equations. *Wind Engineering*, 35(1):17–31, December 2010.

[76] Ye Zhiquan. Aerodynamic optimum design procedure and program for the rotor of a horizontal-axis wind turbine. *Journal of Wind Engineering and Industrial Aerodynamics*, 39:179–186, 1992.

[77] Jean-Jacques Chattot. Optimization of Wind Turbines Using Helicoidal Vortex Model. *Journal of Solar Energy Engineering*, 125:418–424, 2003.

[78] Kamoun Badreddinne, Helali Ali, and Afungchui David. Optimum project for horizontal axis turbines 'OPHWT'. *Renewable Energy*, 30:2019–2043, 2005.

[79] M. K. McWilliam, G. C. van Kooten, and C. Crawford. A method for optimizing the location of wind farms. *Renewable Energy*, 48:287–299, June 2013.

[80] Michael K. McWilliam and Curran Crawford. Adjoint Based Sensitivity Analysis for Geometrically Exact Beam Theory and Variational Asymptotic Beam Section Analysis with Applications to Wind Turbine Design Optimization. In *53rd AIAA Structures, Structural Dynamics and Materials Conference, April 23-26 2012, Honolulu Hawaii*, April 2012.

[81] Michael K. McWilliam and Curran Crawford. Composite lay-up optimization for horizontal axis wind turbine blades. In *AIAA 51st Aerospace Sciences Meeting*, 2013.

[82] Stephen Lawton and Curran Crawford. A comparison of complex step and finite difference approaches for gradient-based wind turbine blade optimization. Submited to Computers and Fluids, manuscript number CAF-D-15-00208, February 2015.

[83] Michael K. McWilliam, Stephen Lawton, and Curran Crawford. Towards a framework for aero-elastic multidisciplinary design optimization of horizontal axis wind turbines. In *AIAA Annual Sciences Meeting*, 2013.

[84] Michael K. McWilliam, Stephen Lawton, and Curran Crawford. An implicit model for lagrangian vortex dynamics for horizontal axis wind turbine design optimization. In *AIAA 2013 Structures, Dynamics and Materials conference*, 2013.

[85] Michael K McWilliam and Curran Crawford. Finite element based lagrangian vortex dynamics model for wind turbine aerodynamics. *Journal of Physics: Conference Series*, 524(1):012127, 2014.

[86] Shane Cline and Curran Crawford. Comparison of Potential Flow Wake Models for Horizontal-Axis Wind Turbine Rotors. In *48th AIAA Aerospace Sciences Meeting Including the New Horizons Forum and Aerospace Exposition, January 4th-7th 2010, Orlando Florida*, January 2010.

[87] Stephen Lawton and Curran Crawford. The development and validation of libaero, a potential flow aerodynamics library for horizontal-axis wind turbines. In *50th AIAA Aerospace Sciences Meeting*, 2011.

[88] Michael McWilliam and Curran Crawford. The Behavior of Fixed Point Iteration and Newton-Raphson Methods in Solving the Blade Element Momentum Equations. *Wind Engineering*, 35(1):17–31, December 2010.

[89] Daryl L. Logan. *A First Course in the Finite Element Method Fourth Edition*. Thomson, 1120 Birchmount Road, Toronto, Ontario, M1K 5G4 Canada, 2007.

[90] Ahmed A. Shabana. Flexible Multibody Dynamics: Review of Past and Recent Developments. *Multibody System Dynamics*, 1:189–222, 1997.

[91] Sung Nam Jung, V.T. Nagaraj, and Inderjit Chopra. Assessment of composite rotor blade modeling techniques. *Journal of the American Helicopter Society*, 44(3):188–205, 1999.

[92] Steen Krenk. *Non-linear Modeling and Analysis of Solids and Structures*. Cambridge University Press, Cambridge, England, 2009.

[93] Donald L. Kunz. Survey and comparison of engineering beam theories for helicopter rotor blades. *Journal of Aircraft*, 31(3):473–479, 1994.

[94] Ahmed A. Shabana and Refaat Y. Yakoub. Three Dimensional Absolute Nodal Coordinate Formulation for Beam Elements: Theory. *Transactions of the ASME*, 123:606–613, December 2001.

[95] Refaat Y. Yakoub and Ahmed A. Shabana. Three Dimensional Absolute Nodal Coordinate Formulation for Beam Elements: Implementation and Application. *Transactions of the ASME*, 123:614–621, December 2001.

[96] M. A. Omar and A. A. Shabana. A Two-Dimensional Shear Deformable Beam for Large Rotation and Deformation Problems. *Journal of Sound and Vibration*, 243(3):565–576, 2001.

[97] G. Gilardi, B. J. Buckham, and E. J. Park. Finite Element Modeling of a Slewing Non-linear Flexible Beam for Active Vibration Control with Arrays of Sensors and Actuators. *Journal of Intelligent Material Systems and Structures*, 20:1941–1958, November 2009.

[98] Marcello Berzeri, Marcello Campanelli, and Ahmed Shabana. Definition of the Elastic Forces in the Finite-Element Absolute Nodal Coordinate Formulation

and the Floating Frame of Reference Formulation. *Multibody System Dynamics*, 5:21–54, 2001.

[99] Ahmed A. Shabana. Computer Implementation of the Absolute Nodal Coordinate Formulation for Flexible Multibody Dynamics. *Nonlinear Dynamics*, 16:293–306, 1998.

[100] J. C. Simo. A finite strain beam formulation. The three-dimensional dynamic problem. Part I. *Computer Methods in Applied Mechanics and Engineering*, 49(1):55–70, 1985.

[101] J. C. Simo and L. Vu-Quoc. A three-dimensional finite-strain rod model. part II: Computational aspects. *Computer Methods in Applied Mechanics and Engineering*, 58(1):79–116, 1986.

[102] Dewey H. Hodges. A mixed variational formulation based on exact intrinsic equations for dynamics of moving beams. *International Journal of Solids and Structures*, 26(11):1253–1273, 1990.

[103] Dewey H. Hodges, Xiaoyang Shang, and Carlos E.S. Cesnik. Finite element solution of nonlinear intrinsic equations for curved composite beams. *Journal of the American Helicopter Society*, 41(4):313–321, 1996.

[104] Ignacio Romero. The interpolation of rotations and its application to finite element models of geometrically exact rods. *Computational Mechanics*, 34(2):121–133, 2004.

[105] John Argyris. An excursion into large rotations. *Computer Methods in Applied Mechanics and Engineering*, 32(1-3):85–155, 1982.

[106] Ignacio Romero. A comparison of finite elements for nonlinear beams: the absolute nodal coordinate and geometrically exact formulations. *MULTIBODY SYSTEM DYNAMICS*, 20(1):51–68, August 2008.

[107] Elisabet V. Lens and Alberto Cardona. A nonlinear beam element formulation in the framework of an energy preserving time integration scheme for constrained multibody systems dynamics. *Computers & Structures*, 86(1-2):47–63, 2008.

[108] I. Romero and F. Armero. An objective finite element approximation of the kinematics of geometrically exact rods and its use in the formulation of an energy momentum conserving scheme in dynamics. *International Journal for Numerical Methods in Engineering*, 54(12):1683–1716, 2002.

[109] P. Betsch and P. Steinmann. Frame-indifferent beam finite elements based upon the geometrically exact beam theory. *International Journal for Numerical Methods in Engineering*, 54(12):1775–1788, 2002.

[110] A. L. Schwab and J. P. Meijaard. Comparison of Three-Dimensional Flexible Beam Elements for Dynamic Analysis: Classical Finite Element Formulation and Absolute Nodal Coordinate Formulation. *Journal of Computational and Nonlinear Dynamics*, 5(1):11010–11010, 2010.

[111] Markus Dibold, Johannes Gerstmayr, and Hans Irschik. A Detailed Comparison of the Absolute Nodal Coordinate and the Floating Frame of Reference Formulation in Deformable Multibody Systems. *Journal of Computational and Nonlinear Dynamics*, 4(2):21006–21006, 2009.

[112] Adnan Ibrahimbegovic, Francois Frey, and Ivica Kozar. Computational aspects of vector-like parametrization of three-dimensional finite rotations. *International Journal for Numerical Methods in Engineering*, 38(21):3653–3673, 1995.

[113] Michael A. Crisfield and Gordan Jelenic. Objectivity of strain measures in the geometrically exact three-dimensional beam theory and its finite-element implementation. *Proceeding of the Royal Society of London A*, 455:1125–1147, 1999.

[114] G. Jelenic and M.A. Crisfield. Geometrically exact 3D beam theory: implementation of a strain-invariant finite element for statics and dynamics. *Computer Methods in Applied Mechanics and Engineering*, 171(1-2):141–171, 1999.

[115] Jing Li. Fortran programs for a 3-D four-noded curved beam element: ARCH-CODE version 1.0. Master's thesis, Virginia Polytechnic Institute and State University, December 2000.

[116] Dewey H. Hodges. Review of Composite Rotor Blade Modeling. *AIAA Journal*, 28(3):561–565, 1990.

[117] Michael W. Hyer. *Stress Analysis of Fiber-Reinforced Composite Materials*. WCB McGraw Hill, Boston, Massachusetts, USA, 1998.

[118] V. Giavotto, M. Borri, P. Mantegazza, G. Ghiringhelli, V. Carmaschi, G.C. Maffioli, and F. Mussi. Anisotropic beam theory and applications. *Computers & Structures*, 16(1-4):403–413, 1983.

[119] Eduardo N. Dvorkin, Diego Celentano, Alberto Cuitino, and Gustavo Gioia. A Vlasov Beam Element. *Computers & Structures*, 33(1):187–196, 1989.

[120] Wenbin Yu, Dewey H. Hodges, Vitali Volovoi, and Eduardo D. Fuchs. A generalized Vlasov theory for composite beams. *Thin-Walled Structures*, 43:1493–1511, 2005.

[121] D. H. Hodges and W. Yu. A Rigorous, Engineer-friendly Approach for Modelling Realistic, Composite Rotor Blades. *Wind Energy*, 10:179–193, 2007.

[122] Dewey H. Hodges, Ali R. Atilgan, Carlos E.S. Cesnik, and Mark V. Fulton. On a simplified strain energy function for geometrically nonlinear behaviour of anisotropic beams. *Composites Engineering*, 2(5-7):513–526, 1992.

[123] Bogdan Popescu and Dewey H. Hodges. On asymptotically correct Timoshenko-like anisotropic beam theory. *International Journal of Solids and Structures*, 37(3):535–558, 2000.

[124] Wenbin Yu, Dewey H. Hodges, Vitali Volovoi, and Carlos E. S. Cesnik. On Timoshenko-like modeling of initially curved and twisted composite beams. *International of Journal Solids and Structures*, 39(19):5101–5121, 2002.

[125] V. L. Berdichevskii. Variational-Asymptotic Method of Constructing a Theory of Shells. *PMM*, 43(4), 1979.

[126] Bogdan Popescu, Dewey H. Hodges, and Carlos E. S. Cesnik. Obliqueness effects in asymptotic cross-sectional analysis of composite beams. *Computer & Structures*, 76:533–543, 2000.

[127] Wenbin Yu and Dewey H. Hodges. Elasticity Solutions Versus Asymptotic Sectional Analysis of Homogeneous, Isotropic, Prismatic Beams. *Journal of Applied Mechanics*, 71:15–23, 2004.

[128] Wenbin Yu, Vitali Volovoi, Dewey H. Hodges, and Xianyu Hong. Validation of the Variational Asymptotic Beam Sectional Analysis. *AIAA Journal*, 40(10):2105–2112, 2002.

[129] V. V. Volovoi, D. H. Hodges, C. E. S. Cesnik, and B. Popescu. Assessment of beam modeling methods for rotor blade applications. *Mathematical and Computer Modelling*, 33(10-11):1099–1112, 2001.

[130] Hui Chen, Wenbin Yu, and Mark Capellaro. A critical assessment of computer tools for calculating composite wind turbine blade properties. *Wind Energy*, 13(6):497–516, 2010.

[131] Wenbin Yu, Dewey H. Hodges, and Jimmy C. Ho. Variational asymptotic beam sectional analysis - An updated version. *International Journal of Engineering Science*, 59(0):40–64, 2012.

[132] J. H. Ferziger and M. Peric. *Computational Methods for Fluid Dynamics*. Springer, Berlin Germany, 2002.

[133] Joseph Katz and Allen Plotkin. *Low-Speed Aerodynamics*. McGraw Hill Book Company, Inc., 1991.

[134] Ludwig Prandtl. Tragflugeltheorie. i. mitteilungu. *Nachrichten von der Gesellschaft der Wissenschaften zu Gottingen, Mathematisch-Physikalische Klasseo*, pages 451–477, 1918.

[135] Ludwig Prandtl. Tragflugeltheorie. i.i. mitteilungu. *Nachrichten von der Gesellschaft der Wissenschaften zu Gottingen, Mathematisch-Physikalische Klasseo*, pages 107–137, 1919.

[136] J. Weissinger. The lift distribution of swept-back wings. Technical report, National Advisory Committee for Aeronautics Technical report, 1947.

[137] W. F. Phillips and D. O. Snyder. Modern adaptation of prandtl's classic lifting-line theory. *Journal of Aircraft*, 37:662–670, 2000.

[138] Jean-Jacques Chattot. Extension of a Helicoidal Vortex Model to Account for Blade Flexibility and Tower Interference. *Journal of Solar Energy Engineering*, 128:455–460, 2006.

[139] Hugh D. Currin, Frank N. Coton, and Byard Wood. Dynamic Prescribed Vortex Wake Model for Aerodyn/FAST. *Journal of Solar Energy Engineering*, 130, August 2008.

[140] M. Roura, A. Cuerva, A. Sanz-Andres, and A. Barrero-Gil. A panel method free-wake code for aeroelastic rotor predictions. *Wind Energy*, 13:357–371, 2010.

[141] Mads Dossing. Vortex lattice modelling of winglets on wind turbine blades. Master's thesis, Riso National Laboratory and Technical University of Denmark, Roskilde Denmark, August 2007.

[142] Seongkyu Lee. Inverse design of horizontal axis wind turbine blades using a vortex line method. In *Aerospace Sciences Meetings*. American Institute of Aeronautics and Astronautics, 2012.

[143] J H Walther, M Gunot, E Machefaux, J T Rasmussen, P Chatelain, V L Okulov, J N Srensen, M Bergdorf, and P Koumoutsakos. A numerical study of the stabilitiy of helical vortices using vortex methods. *Journal of Physics: Conference Series*, 75(1):012034, 2007.

[144] V. L. Okulov. On the stability of multiple helical vortices. *Journal of Fluid Mechanics*, 521:319–342, 12 2004.

[145] A. van Garrel. Development of a wind turbine aerodynamics simulation module. Technical report, Energy research Centre of the Netherlands, 2003.

[146] Andrew Ning. A simple solution method for the blade element momentum equations with guaranteed convergence. *Wind Energy*, 17:1327–1345, 2014.

[147] R. Lanzafame and M. Messina. Design and performance of a double-pitch wind turbine with non-twisted blades. *Renewable Energy*, 34:1413–1420, 2009.

[148] Zhaohui Du and Michael S. Selig. A 3-D Stall-Delay Model for Horizontal Axis Wind Turbine Performance Prediction. In *AIAA 36th Aerospace Sciences Meeting and Exhibit*, 1998.

[149] James L. Tangler and Michael S. Selig. An Evaluation of an Empirical Model for Stall Delay due to Rotation for HAWTs. In *WINDPOWER '97 Conference Austin, Texas, June 15-18, 1997*, 1997.

[150] Wen Zhong Shen, Robert Mikkelsen, and Jens Norkaer Sorensen. Tip Loss Corrections for Wind Turbine Computations. *Wind Energy*, 8:457–475, 2005.

[151] K. Chaney and A. J. Eggers Jr. Expanding Wake Induction Effect on Thrust Distribution on a Rotor Disc. *Wind Energy*, 5:213–226, 2002.

[152] Helge Aa. Madsen, Christian Bak, Mads Dossing, Robert Mikkelsen, and Stig Oye. Validation and modification of the Blade Element Momentum theory based on comparisons with actuator disc simulations. *Wind Energy*, 13:373–389, August 2010.

[153] Wouter Haans, Tonio Sant, and Gijs Van Kuik Gerard van Bussel. Stall in Yawed Flow Conditions: A Correlation of Blade Element Momentum Predictions With Experiments. *Journal of Solar Energy Engineering*, 128:472–480, 2006.

[154] Curran Crawford. Re-examining the Precepts of the Blade Element Momentum Theory for Coning Rotors. *Wind Energy*, 9:457–478, 2006.

[155] D. J. Sharpe. A General Momentum Theory Applied to an Energy-extracting Actuator Disc. *Wind Energy*, 7:177–188, 2004.

[156] Tony Burton, David Sharpe, Nick Jenkins, and Ervin Bossanyi. *Wind Energy Handbook*. John Wiley and Sons, Chichester, England, 2001.

[157] Jaime Martinez, Luca Bernabini, Oliver Probst, and Ciro Rodriguez. An Improved BEM Model for the Power Curve Prediction of Stall-regulated Wind Turbines. *Wind Energy*, 8:385–402, 2004.

[158] M. J. Clifton-Smith and D. H. Wood. Further dual purpose evolutionary optimization of small wind turbine blades. In *Journal of Physics: Conference Series*, 2007.

[159] R. Reuss Ramsay, M. J. Hoffmann, and G. M. Gregorek. Effects of Grit Roughness and Pitch Oscillations on the S801 Airfoil. Technical report, National Renewable Energy Laboratories, 1617 Cole Boulevard, Golden, Colorado, United States of America, 1996. NREL/TP-442-7818.

[160] R. Reuss Ramsay, M. J. Hoffmann, and G. M. Gregorek. Effects of Grit Roughness and Pitch Oscillations on the S809 Airfoil. Technical report, National Renewable Energy Laboratories, 1617 Cole Boulevard, Golden, Colorado, United States of America, 1995. NREL/TP-442-7817.

[161] R. Reuss Ramsay, M. J. Hoffmann, and G. M. Gregorek. Effects of Grit Roughness and Pitch Oscillations on the S810 Airfoil. Technical report, National Renewable Energy Laboratories, 1617 Cole Boulevard, Golden, Colorado, United States of America, 1996. NREL/TP-442-7816.

[162] R. Reuss Ramsay and G. M. Gregorek. Effects of Grit Roughness and Pitch Oscillations on the S812 Airfoil. Technical report, National Renewable Energy Laboratories, 1617 Cole Boulevard, Golden, Colorado, United States of America, 1998. NREL/TP-442-8167.

[163] R. Reuss Ramsay and G. M. Gregorek. Effects of Grit Roughness and Pitch Oscillations on the S813 Airfoil. Technical report, National Renewable Energy Laboratories, 1617 Cole Boulevard, Golden, Colorado, United States of America, 1996. NREL/TP-442-8168.

[164] J. M. Janiszewska, R. Reuss Ramsay, M. J. Hoffman, and G. M. Gregorek. Effects of Grit Roughness and Pitch Oscillations on the S814 Airfoil. Technical report, National Renewable Energy Laboratories, 1617 Cole Boulevard, Golden, Colorado, United States of America, 1996. NREL/TP-442-8161.

[165] R. Reuss Ramsay, M. J. Hoffmann, and G. M. Gregorek. Effects of Grit Roughness and Pitch Oscillations on the S815 Airfoil. Technical report, National Renewable Energy Laboratories, 1617 Cole Boulevard, Golden, Colorado, United States of America, 1996. NREL/TP-442-7820.

[166] R. Reuss Ramsay, J. M. Janiszewska, and G. M. Gregorek. Effects of Grit Roughness and Pitch Oscillations on the S825 Airfoil. Technical report, National Renewable Energy Laboratories, 1617 Cole Boulevard, Golden, Colorado, United States of America, 1998.

[167] James Tangler and J. David Kocurek. Wind Turbine Post-Stall Airfoil Performance Characteristics Guidelines for Blade-Element Momentum Methods. Technical report, National Renewable Energy Laboratories, 1617 Cole Boulevard, Golden, Colorado, United States of America, October 2004.

[168] J. N. Sorensen, W. Z. Shen, and X. Munduate. Analysis of Wake States by a Full-field Actuator Disc Model. *Wind Energy*, 1:73–88, 1998.

[169] Jeppe Johansen and Niels N. Sorensen. Aerofoil Characteristics from 3D CFD Rotor Computations. *Wind Energy*, 7:283–294, 2004.

[170] Frank M. White. *Fluid Mechanics 5th Edition.* McGraw Hill Higher Education, New York, United States of America, 2003.

[171] Christian Masson and Arezki Smaili. Numerical Study of Turbulent Flow around a Wind Turbine Nacelle. *Wind Energy*, 9:281–298, 2006.

[172] Niels Troldborg, Jens N. Sorensen, and Robert Mikkelsen. Numerical simulations of wake characteristics of a wind turbine in uniform inflow. *Wind Energy*, 13:86–99, 2010.

[173] Stephen B. Pope. *Turbulent Flows.* Cambridge University Press, The Edinburgh Building, Cambridge, CB2 8RU, UK, 2000.

[174] L. J. Vermeer, J. N. Sorensen, and A. Crespo. Wind Turbine Wake Aerodynamics. *Progress in Aerospace Sciences*, 39:467–510, 2003.

[175] B. Sanderse, S.P. van der Pijl, and B. Koren. Review of computational fluid dynamics for wind turbine wake aerodynamics. *Wind Energy*, 14(7):799–819, 2011.

[176] Stefan Ivanell, Robert Mikkelsen, Jens N. Sorensen, and Dan Henningson. Stability analysis of the tip vortices of a wind turbine. *Wind Energy*, 13:705–715, 2010.

[177] Stefan Ivanell, Jens N. Sorensen, Robert Mikkelsen, and Dan Henningson. Analysis of Numerically Generated Wake Structures. *Wind Energy*, 12:63–80, 2009.

[178] Michael Shives and Curran Crawford. Mesh and load distribution requirements for actuator line cfd simulations. *Wind Energy*, 16:1183–1196, 2012.

[179] S. Gomez-Iradi, R. Steijl, and G. N. Barakos. Development and Validation of a CFD Technique for the Aerodynamic Analysis of HAWT. *Journal of Solar Energy Engineering*, 131, August 2009.

[180] A. Bechmann, N. N. Srensen, and F. Zahle. Cfd simulations of the mexico rotor. *Wind Energy*, 14(5):677–689, 2011.

[181] J. Johansen, H. A. Madsen, N. N. Sorensen, and C. Bak. Numerical Investigation of a Wind Turbine Rotor with an Aerodynamically Redesigned Hub-Region. Technical report, Riso National Laboratories, Roskilde, Denmark, 2005.

[182] Jeppe Johansen and Niels N. Sorensen. Aerodynamic investigation of Winglets on Wind Turbine Blades using CFD. Technical report, Riso National Laboratory, Roskilde, Denmark, February 2006.

[183] Danmei Hu, Ouyang Hua, and Zhaohui Du. A study on stall-delay for horizontal axis wind turbine. *Renewable Energy*, 31:821–836, 2006.

[184] Niels N. Sorensen. CFD Modelling of Laminar-turbulent Transition for Airfoils and Rotors Using the gamma-Re Model. *Wind Energy*, 12:715–733, April 2009.

[185] Gaetan K. W. Kenway and Joaquim Martins. Aerostructural shape optimization of wind turbine blades considering site-specific winds. In *12th AIAA Multidisciplinary Analysis and Optimization Conference*, Victoria, BC, Canada, September 2008.

[186] Georges-Henri Cottet and Petros D. Koumoutsakos. *Vortex Methods Theory and Practice*. Cambridge University Press, Cambridge, England, 2000.

[187] Manuel Fluck and Curran Crawford. A lifting line model to investigate the influence of tip features on wing performance. *Bioinspiration & Biomimetics*, 9, 2014.

[188] T. Sebastian and Matthew A. Lackner. Development of a free vortex wake method code for offshore floating wind turbines. *Renewable Energy*, 46:269–275, 2012.

[189] Ashish Bagai and J. Gordon Leishman. Rotor free-wake modeling using a pseudo-implicit technique - including comparisons with experimental data. *Journal of The American Helicopter Society*, 40:29–41, 1995.

[190] Mahendra J. Bhagwat and J. Gordon Leishman. Stability, consistency and convergence of time-marching free-vortex rotor wake algorithms. *Journal of The American Helicopter Society*, 46:59–71, 2001.

[191] Nestor Ramos-Garcia, Jens Norkaer Sorensen, and Wen Zhong Shen. Three-dimensional viscous-inviscid coupling method for wind turbine computations. *Wind Energy*, 2014.

[192] David Maniaci. *Wind Turbine Design Using a Free-wake Vortex Method with Winglet Application.* PhD thesis, Pennsylvania State University, May 2013.

[193] Herman Snel. Review of Aerodynamics for Wind Turbines. *Wind Energy*, 6:203–211, 2003.

[194] Stephen Lawton and Curran Crawford. An analysis of an implicit vortex method for wind turbine wake modelling. In *51st AIAA Aerospace Sciences Meeting*, Grapevine Texas, January 2013.

[195] Thomas Sebastian and Mathew A. Lackner. Offshore wind turbines - an aerodynamic perspective. In *49th AIAA Aerospace Sciences Meeting*, 2011.

[196] Thomas Sebastian and Mathew A. Lackner. A comparison of first-order aerodynamic analysis methods for floating wind turbines. In *48th AIAA Aerospace Science Meeting*, 2010.

[197] Sven Schmitz and Jean-Jacques Chattot. A Parallelized Coupled Navier-Stokes/Vortex-Panel Solver. *Journal of Solar Energy Engineering*, 127:475–487, 2005.

[198] Philippe Chatelain, Stphane Backaert, Grgoire Winckelmans, and Stefan Kern. Large eddy simulation of wind turbine wakes. *Flow, Turbulence and Combustion*, 91:587–605, 2013.

[199] Olivier de Weck and Karen Willcox. Multidisciplinary System Design Optimization, 2004. 16.888 Open Courseware Notes, Online Material Available http://ocw.mit.edu/OcwWeb/Aeronautics-and-Astronautics/16-888Spring-2004/CourseHome/index.htm.

[200] Garret N. Vanderplaats. *Numerical Optimization Techniques for Engineering Design. 3rd ed.* Vanderplaats Research & Development Inc., Colorado Springs, 2001.

[201] Magnus R. Hestenes. Multiplier and Gradient Methods. *Journal of Optimization Theory and Applications*, 4(5):303–320, February 1969.

[202] Craig Lawrence, Jian L. Zhou, and Andre L. Tits. User's Guide for CFSQP Version 2.5: A C Code for Solving (Large Scale) Constrained Nonlinear (Minimax) Optimization Problems, Generating Iterates Satisfying All Inequality Constraints. Technical report, Electrical Engineering Department and Institute for Systems Research, University of Maryland, College Park, MD 20742, April 1997. Institute for Systems Research TR-94-16r1.

[203] Gyung-Jin Park. *Analytic Methods for Design Practice*. Springer, 2007.

[204] Joaquim R. R. A. Martins. *A coupled-Adjoint Method for High-Fidelity Aero-Structural Optimization*. PhD thesis, Stanford University, October 2002.

[205] Jeffrey A. Fike and Juan J. Alonso. The Development of Hyper-Dual Numbers for Exact Second-Derivative Calculations. In *49th AIAA Aerospace Sciences Meeting, 4-7 January 2011, Orlando, Florida*, January 2011.

[206] Antony Jameson. Automatic Design via Control Theory. *Journal of Scientific Computing*, 3(3), 1988.

[207] Antony Jameson. Optimum Aerodynamic Design Using CFD and Control Theory. 1995.

[208] A. Jameson, L. Martinelli, and N. A. Pierce. Optimum Aerodynamic Design Using the Navier-Stokes Equations. *Theoretical and Computational Fluid Dynamics*, 10:213–237, 1997.

[209] M. B. Giles and N. A. Pierce. Adjoint Equations in CFD: Duality, Boundary Conditions and Solution Behaviour. In *Collection of Technical papers: 13th AIAA Computational fluid dynamics conference, Snowmass Village, Colorado,*, 1997.

[210] Michael B. Giles and Niles A. Pierce. An Introduction to the Adjoint Approach to Design. *Flow, Turbulence and Combustion*, 65:393–415, 2001.

[211] K. Ou and A. Jameson. Unsteady Adjoint Method for the Optimal Control of Advection and Burgers Equations using High Order Spectral Difference Method. In *49th AIAA Aerospace Sciences Meeting, 4-7 January 2011, Orlando, Florida*, January 2011.

[212] Gregory A. Wrenn. An Indirect Method for Numerical Optimization Using the Kreisselmeier-Steinhauser Function. Technical report, National Aeronautics and Space Administration, 1989. Nasa Contractor Report 4220.

[213] Siva K. Nadarajah and Antony Jameson. Comparison of the Continuous and Discrete Adjoint Approach to Automatic Aerodynamic Optimization. Technical report, American Institute of Aeronautics and Astronautics, 1999. AIAA-2000-0667.

[214] Alfonso Bueno-Orovio, Carlos Castro, Karthikeyan Duraisamy, Francisco Palacios, and Enrique Zuazua. When the exact discrete gradient is not the best choice in optimal shape design. In *49th AIAA Aerospace Sciences Meeting, 4-7 January 2011, Orlando, Florida*, January 2011.

[215] Sigurd D. Trier, Arne Marthinsen, and Ole Ivar Sivertsen. Design sensitivities by the adjoint variable method in nonlinear structural dynamics. In *Applied Modelling and Simulation, Proceedings of the 38th SIMS Simulating Conference, Trondheim, Norway*, June 1996.

[216] Qiqi Wang and Wenbin Yu. Sensitivity Analysis of Geometrically Exact Beam Theory (GEBT) Using the Adjoint Method with Hydra. In *52th AIAA/ASME/ASCE/AHS/ASC Structures, Structural Dynamics and Materials Conference, 4-7 April 2011, Denver, Colorado*, April 2011.

[217] H. Snel, J. G. Schepers, and B. Montgomeric. The MEXICO project (Model Experiments in Controlled Conditions): The database and first results of data processing and interpretation. *Journal of Physics: Conference Series*, 75:1–11, 2007.

[218] K. Levenberg. A method for the solution of certain problems in least squares. *The Quarterly of Applied Mathematics*, 2:164–168, 1944.

[219] D. Marquardt. An algorithm for least-squares estimation of nonlinear parameters. *The SIAM Journal on Applied Mathematics*, 11:431–441, 1963.

[220] Hassan K. Khalil. *Nonlinear Systems Third Edition*. Prentice Hall, 2002.

[221] K. W. McAlister and R. K. Takahashi. Naca 0015 wing pressure and trailing vortex measurements. Technical Report Technical Paper 3151, National Aeronautics and Space Administration, November 1991.

[222] Robert E. Sheldahl and Paul C. Klimas. Aerodynamic characteristics of seven symmetrical airfoil sections through 180-degree angle of attack for use in aerodynamic analysis of vertical axis wind turbines. Technical report, Sandia National Laboratories, 1981.

[223] Robert A. Mendelsohn and Jack D. Brewer. Comparison between the measured and theoretical span loading on a moderately swept-forward and a moderately swept-back semispan wing. Technical report, National Advisory Committee on Aeronautics, 1947.

[224] Zhaohui Du and M. S. Selig. The effect of rotation on the boundary layer of a wind turbine blade. *Renewable Energy*, 20:167–181, 2000.

[225] Alvaro Gonzales and Xabier Munduate. Three-Dimensional and Rotational Aerodynamics on the NREL Phase VI Wind Turbine Blade. *Journal of Solar Energy Engineering*, 130, August 2008.

[226] Guohua Yu, Xin Shen, Xiaocheng Zhu, and Zhaoui Du. An insight into the separate flow and stall delay for HAWT. *Renewable Energy*, 36:69–76, 2011.

[227] J. G. Schepers, K. Boorsma, T. Cho, S. Gomez-Iradi, P. Schaffarczyk, A. Jeromin, W. Z. Shen, T. Lutz, K. Meister, B. Stoevesandt, S. Schreck, D. Micallef, R. Pereira, T. Sant, H. A. Madsen, and N. Sorensen. Final report of iea task 29, mexnext (phase 1): Analysis of mexico wind tunnel measurements. Technical report, Energy Research Center of the Netherlands, 2012.

[228] J. Jonkman, S. Butterfield, W. Musial, and G. Scott. Definition of a 5-mw reference wind turbine for offshore system development. Technical report, National Renewable Energy Laboratory, 2009.

[229] D. Voivontas, D. Assimacopoulos, and A. Mourelatos. Evaluation of Renewable Energy Potential Using a GIS Decision Support System. *Renewable Energy*, 13(3):333–344, 1998.

[230] G. Quinonez-Varela, A. Cruden, C. Graham, B. Punton, L. Blair, and J. Thomson. A GIS/PSS planning tool for the initial grid connection assessment of renewable generation. *Renewable Energy*, 32:727–737, 2007.

[231] Serwan M. J. Baban and Tim Parry. Developing and applying a GIS-assisted approach to locating wind farms in the UK. *Renewable Energy*, 24:59–71, August 2001.

[232] Laura C. Rodman and Ross K. Meentemeyer. A geographic analysis of wind turbine placement in Northern California. *Energy Policy*, 34:2137–2149, 2006.

[233] P. Lejeune and C. Feltz. Development of a decision support system for setting up a wind energy policy across the Walloon Region (southern Belgium). *Renewable Energy*, 33:2416–2422, April 2008.

[234] Ignacio J. Ramirez-Rasado, Eduardo Garcia-Garrido, L. Alfredo Fernandez-Jimenez, Pedro J. Zorzano-Santamaria, Claudio Monteiro, and Vladimiro Miranda. Promotion of new wind farms based on a decision support system. *Renewable Energy*, 33:558–566, 2008.

[235] U Aytun Ozturk and Bryan A Norman. Heuristic methods for wind energy conversion system positioning. *Electric Power Systems Research*, 70(3):179–185, 2004.

[236] S.A. Grady, M.Y. Hussaini, and M.M. Abdullah. Placement of wind turbines using genetic algorithms. *Renewable Energy*, 30(2):259–270, 2005.

[237] N. O. Jensen. A Note on Wind Generator Interaction. Technical report, RISO National Laboratories, November 1983. RISO-M-2411.

[238] Jose Castro Mora, Jose M. Calero Baron, Jesus M. Riquelme Santos, and Manuel Burgos Payan. An evolutive algorithm for wind farm optimal design. *Neurocomputing*, 70(16-18):2651–2658, 2007.

[239] Grigorios Marmidis, Stavros Lazarou, and Eleftheria Pyrgioti. Optimal placement of wind turbines in a wind park using Monte Carlo simulation. *Renewable Energy*, 33(7):1455–1460, 2008.

[240] Canadian Wind Energy Atlas, 2008. http://www.windatlas.ca.

[241] Statistics Canada, 2010. http://www.statcan.gc.ca.

[242] Alberta Electric System Operator Long-term Transmission System Plan, 2009.

[243] J. C. Simo, N. Tarnow, and M. Doblare. Non-linear dynamics of three-dimensional rods: Exact energy and momentum conserving algorithms. *International Journal for Numerical Methods in Engineering*, 38(9):1431–1473, 1995.

[244] Adnan Ibrahimbegovic and Mazen Al Mikdad. Finite rotations in dynamics of beams and implicit time-stepping schemes. *International Journal for Numerical Methods in Engineering*, 41(5):781–814, 1998.

[245] Carlo L. Bottasso and Marco Borri. Integrating finite rotations. *Computer Methods in Applied Mechanics and Engineering*, 164(3-4):307–331, 1998.

[246] Wenbin Yu and Dewey H. Hodges. Generalized Timoshenko Theory of the Variational Asymptotic Beam Sectional Analysis.

[247] L. S. Blackford, J. Demmel, J. Dongarra, I. Duff, S. Hammarling, G. Henry, M. Heroux, L. Kaufman, A. Lumsdaine, A. Petitet, R. Pozo, K. Remington, and R. C. Whaley. An updated set of basic linear algebra subprograms (blas). *ACM Transactions on Mathematical Software*, 28:135–151, 2002.

[248] Patricio Lillo and Curran Crawford. Analysis of Fatigue Loads of Wind Turbine Blades Subject to Cold Weather Conditions Using a Finite Element Model. In *49th AIAA Aerospace Sciences Meeting, 4-7 January 2011, Orlando, Florida*, January 2011.

[249] Amendment 1 to IEC 61400-11: Wind Turbine generator systems - Part 11: Acoustic noise measurement techniques. Technical report, International Electrotechnical Commission, March 2006. IEC 61400-21 Ammendment 1 2nd Edition.

[250] C.L. Bottasso, F. Campagnolo, A. Croce, and C. Tibaldi. Optimization-based study of bend-twist coupled rotor blades for passive and integrated passive/active load alleviation. *Wind Energy*, 2011.

[251] C. Bottasso, F. Campagnolo, and A. Croce. Multi-disciplinary constrained optimization of wind turbines. *Multibody System Dynamics*, 27(1):21–53, 2012.

[252] Neil Buckney, Steven D. Green, Alberto Pirrera, and Paul M. Weaver. Wind Turbine Structural Efficiency. In *53rd AIAA Structures, Structural Dynamics and Materials Conference, April 23-26 2012, Honolulu Hawaii*, April 2012.

[253] Alberto Pirrera, Marco Capuzzi, Neil Buckney, and Paul M. Weaver. Optimization of Wind Turbine Blade Spars. In *53rd AIAA Structures, Structural Dynamics and Materials Conference, April 23-26 2012, Honolulu Hawaii*, April 2012.

[254] Joshua Paquette, Jeroen van Dam, and Scott Hughes. Structural Testing of 9 m Carbon Fiber Wind Turbine Research Blades. In *45th Aerospace Sciences Meeting and Exhibit, January 8-11, 2007, Reno Nevada*, January 2007.

[255] Don W. Lobitz and Paul S. Veers. Load Mitigation with Bending/Twist-coupled blades on Rotors using modern control strategies. *Wind Energy*, 6:105–117, 2003.

[256] Mark Capellaro. Design Limits of Bend Twist Coupled Wind Turbine Blades. In *53rd AIAA Structures, Structural Dynamics and Materials Conference, April 23-26 2012, Honolulu Hawaii*, April 2012.

[257] Hisao Fukunaga and Garretn Vanderplaats. Stiffness optimization of orthotropic laminated composites using lamination parameters. *AIAA Journal*, 29:641–646, 1991.

[258] Pizhong Qiao, Julio F. Davalos, and Ever J. Barbero. Design Optimization of Fiber Reinforced Plastic Composite Shapes. *Journal of Composite Materials*, 32(2):177–196, January 1998.

[259] Mark Walker and Ryan Smith. A methodology to design fibre reinforced laminated composite structures for maximum strength. *Composites Part B: Engineering*, 34(2):209–214, 2003.

[260] M. Bruyneel. A general and effective approach for the optimal design of fiber reinforced composite structures. *Composites Science and Technology*, 66(10):1303–1314, 2006.

[261] Tae-Uk Kim, Jeong Woo Shin, and In Hee Hwang. Stacking sequence design of a composite wing under a random gust using a genetic algorithm. *Computers & Structures*, 85(10):579–585, 2007.

[262] David Keller. Optimization of ply angles in laminated composite structures by a hybrid, asynchronous, parallel evolutionary algorithm. *Composite Structures*, 92(11):2781–2790, 2010.

[263] B. K. Choi and S. C. Park. A pair-wise offset algorithm for 2D point-sequence curve. *Computer-Aided Design*, 31:735–745, 1999.

[264] Tawfik T. El-Midany, Ahmed Elkeran, and Hamdy Tawfik. A Sweep-Line Algorithm and Its Application to Spiral Pocketing. *International Journal of CAD/CAM*, 2(1):23–28, 2002.

[265] Hyun-Chul Kim, Sung-Gun Lee, and Min-Yang Yang. A new offset algorithm for closed 2D lines with Islands. *International Journal of Advanced Manufacturing Technology*, 29:1169–1177, 2006.

[266] Xu-Zheng Liu, Jun-Hai Yong, Guo-Qin Zheng, and Jia-Guang Sun. An offset algorithm for poly curves. *Computers in Industry*, 58:240–254, 2007.

[267] D. Todd Griffith, Thomas D. Ashwill, and Brian R. Resor. Large Offshore Rotor Development: Design and Analysis of the Sandia 100-meter Wind Turbine Blade. In *53rd AIAA Structures, Structural Dynamics and Materials Conference, April 23-26 2012, Honolulu Hawaii*, April 2012.

[268] Shane Cline, Michael McWilliam, Stephen Lawton, and Curran Crawford. Validation of Potential Flow Aerodynamics for Horizontal-Axis Wind Turbines in Steady Conditions using the MEXICO Project Experimental Data. In *49th AIAA Aerospace Sciences Meeting, 4-7 January 2011, Orlando, Florida*, January 2011.

[269] Gerard Schepers, Koen Boorsma, and Herman Snel. Iea task 29 mexnext: Analysis of wind tunnel measurements from the eu project mexico. In *The Science of Making Torque from the Wind*, 2010.

[270] J. G. Schepers, W. Wuerz, A. Curves, A. Mantesanz, S. Oerlemans, L. Garcillan, K. Braun, M. Fischer, T. Lutz, K. Koegler, A. Herrig, and T. Maeder. SIROCCO: Silent rotors by acoustic optimization. Technical report, The Energy Research Center of the Netherlands (ECN), 1755 ZG Petten, Netherlands, July 2007. ECN-M07-064.

[271] Anthony L. Rogers and James F. Manwell. Wind Turbine Noise Issues. Technical report, Renewable Energy Research Laboratory, Center for Energy Efficiency and Renewable Energy, Department of Mechanical and Industrial Engi-

neering, University of Massachusetts at Amherst, Amherst, MA 01003, March 2004.

[272] John M. Prospathopoulos and Spyros G. Voutsinas. Noise Propagation Issues in Wind Energy Applications. *Journal of Solar Energy Engineering*, 127:234–241, 2005.

[273] P. Moriarty and P. Migliore. Semi-Emperical Aeroacoustic Noise Prediction Code for Wind Turbines. Technical report, National Renewable Energy Laboratories, 1617 Cole Boulevard, Golden, Colorado, United States of America, December 2003. NREL/TP-500-34478.

[274] Patrick Moriarty. NAFNoise User's Guide. Technical report, National Renewable Energy Laboratories, 1617 Cole Boulevard, Golden, Colorado, United States of America, July 2005.

[275] Wei Jun Zhu, Nicolai Heilskov, Wen Zhong Shen, and Jens Norkaer Sorensen. Modeling of Aerodynamically Generated Noise From Wind Turbines. *Journal of Solar Energy Engineering*, 127:517–528, 2005.

[276] Joaquim R. R. A. Martins, Christopher Marriage, and Nathan Tedford. pyMDO: An Object-Oriented Framework for Multidisciplinary Design Optimization. *ACM Transactions on Mathematical Software*, 36(4), August 2009.

[277] Justin Gray, Kenneth T. Moore, Tristan A. Hearn, and Bret A. Naylor. Standard platform for benchmarking multidisciplinary design analysis and optimization architectures. *AIAA Journal*, 51(10):2380–2394, Oct 2013.

[278] Frederik Zahle, Carlo Tibaldi, David Verelst, Christian Bak, Robert Bitsche, and Jose Pedro Albergaria Blasques. Aero-elastic optimization of a 10 mw wind turbine. In *Wind Energy Systems Engineering Workshop*, 2015.

[279] K Dykes, P Graf, G Scott, A Ning, R King, Y Guo, T Parsons, R Damiani, F Felker, and P Veers. Introducing wisdem: An integrated system model of wind turbines and plants. In *Third Wind Energy Systems Engineering Workshop, Boulder Colorado*, 2015.

[280] James L. Tangler. The Nebulous Art of Using Wind-Tunnel Airfoil Data for Predicting Rotor Performance: Preprint. In *21st ASME Wind Energy Conference, Reno Navada, January 14-17, 2002*, 2002.

[281] Dimitris Bertsimas, David B. Brown, and Constantine Caramanis. Theory and application of robust optimization. *SIAM Review*, 53(3):464–501, 2011.